



Experimental and numerical investigations of a continuous counter-current solid-liquid extraction process focusing on hydrodynamic phenomena

Dissertation

zur Erlangung des akademischen Grades

Doktoringenieurin (Dr.-Ing.)

von M.Sc. Annemarie Lehr

geb. am 24.09.1995 in Magdeburg

genehmigt durch die Fakultät für Verfahrens- und Systemtechnik der Otto-von-Guericke-Universität Magdeburg

Gutachter:

Prof. Dr.-Ing. Dominique Thévenin

Prof. Dr.-Ing. Andreas Seidel-Morgenstern

Prof. Dr.-Ing. Andreas Jupke

Promotionskolloquium am 10.07.2025

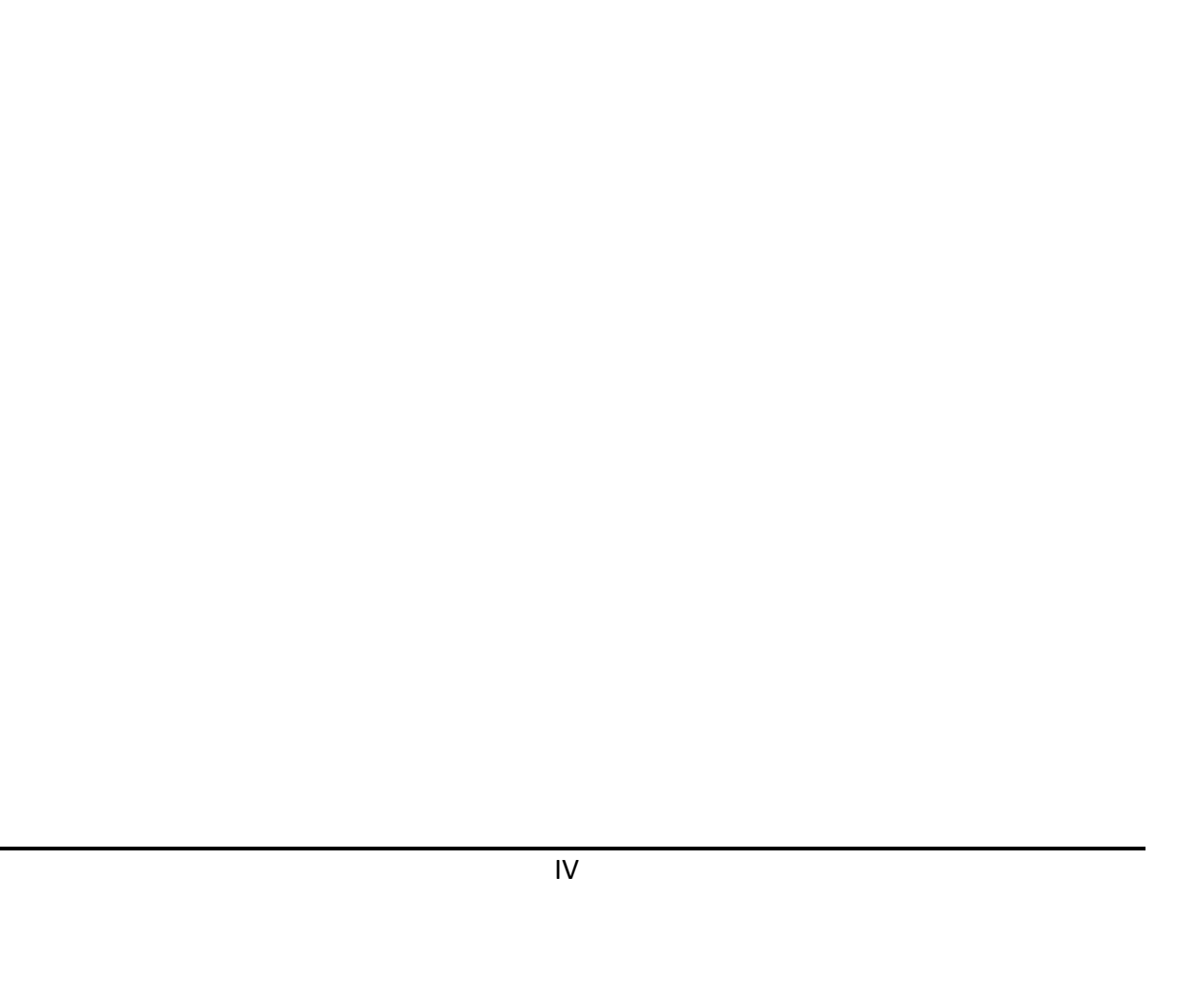
Abstract

Continuous counter-current extraction of natural products has gained increasing interest over traditional batch extraction methods due to its superior extraction efficiencies and larger productivity. This work investigates a complex three-phase counter-current extraction process in a horizontal screw-driven extractor, combining experimental studies, computational fluid dynamics (CFD) simulations, and simplified compartment model analysis. The objective is to understand phase behaviour, residence time distributions (RTD), and the effects of operating conditions, as well as to propose optimisation strategies.

Experimental characterisation used water as a solvent to enable optical observations and sampling and to provide detailed insights into operating conditions, material properties, and phase RTDs during steady-state operation. A partial filling of the extractor was detected, while the occurrence of a gas phase could not be prevented. A narrow operating window for stable process performance was identified, influenced primarily by the screw rotation speed, solid-liquid ratio, and dry leaf mass flow rate. Reducing the perforated disk hole size stabilised the pressure at the compression cake, improving solvent usage. The solid phase shows a near-plug flow reactor (PFTR) behaviour, while the solvent phase has a near-continuously stirred tank reactor (CSTR) behaviour which supports an efficient solvent exchange. These observations are transferable to toluene as the solvent when matching the corresponding Reynolds numbers.

To simulate the extraction process, various CFD approaches were applied. The Eulerian Multiphase (EMP) model, though theoretically suitable, was limited by mesh quality and computational cost. A Volume of Fluid (VOF) model represents the partly-filled flow, including solvent and gas phase, providing promising results. It can accurately predict liquid RTD and phase-specific mass flow rates. However, high computational costs remain a limitation.

Simplified coupling of CFD simulations with compartment models (CPT) reveal significant phase volume reductions on the way toward the extract outlet, contrary to previous assumptions made by Vu [Vu23]. Backflow rates for the solvent are about 50% of the forward flow, indicating near-CSTR behaviour and confirming the RTD results. Modified screw designs demonstrate potential for optimisation regarding these backflow effects. This work paves the way for more efficient and scalable extraction of natural products.

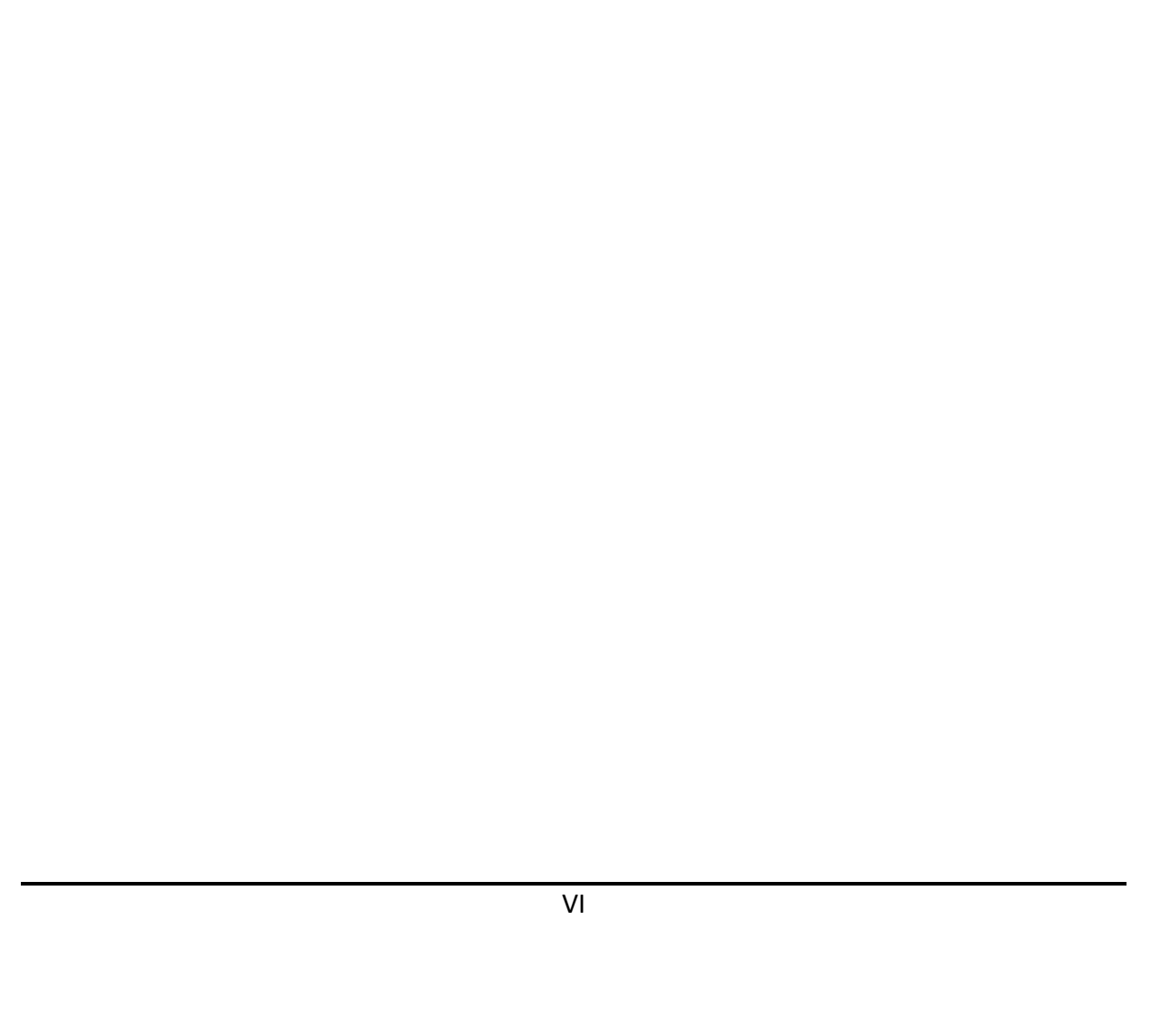


Zusammenfassung

kontinuierliche Gegenstromextraktion von Naturstoffen hat aufgrund ihrer Extraktionseffizienz und höheren Produktivität zunehmend an Bedeutung gegenüber Batch-Extraktionsverfahren gewonnen. Diese Arbeit untersucht Gegenstromextraktionsprozess in einem horizontalen, schneckengetriebenen Extraktor durch experimentelle Studien, Strömungssimulationen (CFD) und vereinfachte Kompartiment-Modelle (CPT). Ziel dabei ist das Phasenverhalten, die Verweilzeitverteilungen (RTD) und die Einflüsse der Betriebsbedingungen zu verstehen sowie Optimierungsstrategien zu entwickeln. Für die experimentelle Charakterisierung wurde Wasser als Lösungsmittel verwendet, um optische Beobachtungen und Probenentnahmen zu ermöglichen. Dies lieferte Einblicke in Materialeigenschaften und Betriebsbedingungen, Phasen-RTDs Bedingungen. Neben der Teilfüllung des Extraktors wurde ein schmales Betriebsfenster für einen stabilen Prozess identifiziert, beeinflusst von Schneckendrehzahl, Feststoff-Flüssigkeits-Verhältnis und Feststoff-Massenstrom. Die Verringerung der Lochdurchmesser in der Lochscheibe stabilisiert den Druck im Kompressionskuchen und verbesserte die Lösungsmittelnutzung. Die Feststoffphase zeigt das Verhalten eines Rohrreaktors (PFTR), während die Lösungsmittelphase einer Rührkesselkaskade (CSTR) ähnelt und einen effizienten Lösungsmittelaustausch unterstützt. Diese Beobachtungen sind bei Anpassung der Reynolds-Zahl auf Toluol als Lösungsmittel übertragbar.

Für die Simulation des Extraktionsprozesses wurden verschiedene CFD Ansätze genutzt. Das EMP Modell ist theoretisch geeignet, jedoch durch Gitterqualität und hohe Rechenkosten eingeschränkt. Das Volume-of-Fluid (VOF) Modell ist vielversprechend für den teilgefüllten Extraktor und kann die RTD der flüssigen Phase sowie phasenspezifische Massenströme vorhersagen. Seine Anwendbarkeit bleibt jedoch durch hohe Rechenkosten limitiert.

Eine vereinfachte Kopplung der CFD-Simulationen mit CPT-Modellen zeigt unterschiedliche Phasenvolumina entlang des Extraktors, entgegen früherer Annahmen von Vu [Vu23]. Die Rückflusseffekte des Lösungsmittels betragen durchschnittlich ca. 50% des Vorwärtsflusses und deuten wie die RTD Ergebnisse auf ein CSTR-Verhalten hin. Modifizierte Schneckendesigns bieten Optimierungspotenziale hinsichtlich der Rückflusseffekte. Zusammenfassend zeigt diese Arbeit verschiedene Möglichkeiten für eine effizientere und skalierbare Extraktion von Naturstoffen auf.



List of Abbreviations and Indices

A. annua Artemisia annua L.

ACT artemisinin-based combination therapy

API active pharmaceutical ingredient

ARTE artemisinin atmospheric ATS adaptive time step av. average value

CFD Computational Fluid Dynamics
CFL Courant-Friedrichs-Lewy

CPT compartment

CRE Chemical Reaction Engineering
DEM Discrete Element Model
DHAA dihydroartemisinic acid
DMP Dispersed Multiphase

ds dry leaves EC extraction cake

ELSD evaporate light scattering detector

EMP Eulerian Multiphase

eq. equilibrium exp experimental

ext extract

FDM Finite-Difference-Method FEM Finite-Element-Method FVM Finite-Volume-Method

g gas phase (air)

HPC high performance computing

HPLC high performance liquid chromatography

HRIC high-resolution interface capturing

liquid solvent

LL lower limit of the operation window

LLE liquid-liquid extraction
LSP lower sampling point
MMP Mixture Multiphase
MPI Max-Planck-Institute
MRT mean residence time

NIR near infrared num numerical

ODE ordinary differential equation

OS original screw PD perforated disk

raff raffinate

RD rotational domain

ref. reference ret. retention

s solvent-soaked leaves SD stationary domain SLA stereolithography SLE solid-liquid extraction

SP sampling point th theoretical tol toluene

TPTE Two-Phase Thermodynamic Equilibrium UL upper limit of the operation window

USP upper sampling point UV-VIS ultrared-visible VOF Volume of Fluid

List of Symbols

Operators

∇		Nabla operator	Eq. (4-1)			
$ abla^2$		Laplace operator	Eq. (4-5)			
∂		partial derivative	Eq. (4-1)			
Greek symb	ols					
α	[-]	phase volume fraction	Eq. (4-14)			
β	[°]	screw angle	Eq. (2-46)			
γ	[1/s]	shear rate	p. 35			
${\delta}_p$	[-]	solid packing limit	Eqs. (4-22),(4-23)			
ε	[-]	liquid phase mass fraction	Eqs. (2-13),(2-22)			
arepsilon'	[-]	liquid phase volume fraction	Eq. (3-24)			
ϵ	[%]	shear strain	p. 35			
η	[-]	transport efficiency	Eq. (2-45)			
μ	[Pa·s]	dynamic/shear viscosity	Eq. (3-1)			
μ_l , μ_s	[Pa·s]	dynamic/shear viscosity of liquid and solid phase	Eq. (4-10)			
ν	$[m^2/s]$	kinematic viscosity	Eq. (3-1)			
ν_l , ν_s	[Pa·s]	kinematic viscosity of liquid and solid phase	Eq. (4-10)			
$v_{\!\scriptscriptstyle A}$	[-]	stoichiometric coefficient of component A	Eq. (2-1)			
ho	[kg/m³]	density	-			
$ ho_{ds}$, $ ho_l$, $ ho_s$	[kg/m³]	density of dry A. Annua leaves, solvent (water)				
		and solvent-soaked leaves	p. 27			
σ	[s]	standard deviation	Eq. (2-32)			
σ^2	[s²]	variance	Eq. (2-32)			
$ar{ au}$	[s]	mean residence time	Eq. (2-31)			
$ar{ au}_l,ar{ au}_s$	[s]	mean residence time of liquid and solid phase	p. 56, 60			
$ar{ au}_s$ '	[s]	mean residence time of solid phase before PD	Eq. (3-17)			
χ	[-]	porosity	Eq. (4-23)			
Latin symbo	Latin symbols					
•						

Α	[m²]	cross-section of extractor	-
а	[m]	screw segment length	p. 23
a_{RTD} , b_{RTD}	[-]	signal constants of tracer concentration	Eq. (2-27)
B_1, B_2	[-]	constants in the counter-current model	Eq. (2-24)
B_3	[-]	constant in solid pressure model	Eq. (4-22)
\overline{b}	[-]	ratio between backward and forward volume flow	Eq. (5-4)
С	[mS/cm]	conductivity	p. 57

ΔC	[mS/cm]	change of conductivity	p. 55
x_l, x_s	[kg/kg]	mass fraction of liquid and solid phase (extraction)	Eqs. (2-14),(2-15)
\tilde{x}_l, \tilde{x}_s	[kg/kg]	modified mass fraction of segregated single	
		liquid and solid phase (extraction)	Eqs. (2-14),(2-15)
$ ilde{\chi}_l^{in}$, $ ilde{\chi}_S^{in}$	[kg/kg]	modified inlet mass fraction of liquid and solid	
		phase (extraction)	Eq. (2-18)
D	[m]	diameter	-
D_{ax}	[m²/s]	axial dispersion coefficient	Eq. (2-40)
D_{in}^{ax} , D_{out}	[m]	inner and outer screw diameter	p. 23
D_p	[m]	particle diameter	p. 27
E(t)	[1/s]	normalised RTD function	Eq. (2-28)
E_0	[-]	dimensionless normalised RTD function	Eq. (4-31)
e	[%]	error	-
F(t)	[-]	cumulative exit age distribution function	Eq. (2-29)
F_{ds}	[-]	filling degree of dry A. Annua leaves	Eq. (3-14)
f_p^{as}	[N]	porous medium force vector	Eq. (4-27)
f_{int}	[N]	solid pressure force	Eq. (4-22)
G	[Pa]	shear modulus	p. 35
G'	[Pa]	storage modulus (elastic component)	p. 35
G"	[Pa]	loss modulus (viscous component)	p. 35
g	[m/s ²]	gravitational vector	Eq. (4-4)
H	[wt.%]	bulk humidity in a batch and continuous reactor	Eq. (3-7)
H_{raff}	[wt.%]	bulk humidity of the raffinate (drying oven)	p. 35
$H_{raff,MB}$	[wt.%]	bulk humidity of the raffinate (mass flow balance)	p. 47
:-raff,мв i,j	[-]	component	-
K^{eq}	[-]	thermodynamic equilibrium	Eq. (2-6)
\widetilde{K}_{E}^{eq}	[-]	modified thermodynamic equilibrium for a	14. (2 0)
T E	LJ	pseudo-homogeneous phase (extraction)	Eq. (2-17)
k_{1}, k_{2}	[1/s]	reaction rate constant	Eq. (2-4)
k_1, k_2 k_E	[1/s]	extraction rate constant for heterogeneous phase	Eq. (2-16)
$ ilde{ ilde{k}}_{E}$	[1/s]	modified extraction rate constant for a pseudo-	Lq. (Z 10)
κ_E	[1/3]	homogeneous phase	Eq. (2-16)
L	[m]	total extractor length	p. 23
L_{ch}	[m]	characteristic length	Eq. (2-34)
L_{l}, L_{s}	[m]	flow length of liquid and solid phase	p. 25
L_{l}, L_{s} $L_{s,EC}$	[m]	flow length of the solid phase without the	Eq. (3-22)
≃ S,EC	r1	extraction cake	-y. (<i>5 22)</i>
dL	[m]	length vector connecting two cell centroids	p. 90
Μ	[-]	number of phases	Eq. (4-22)
m	[kg]	mass	-
m_{ds}, m_l, m_s	[kg]	mass of dry leaves, liquid, solvent-soaked leaves	p. 29
m_{tot}	[kg]	mass capacity of the total extractor	Eq. (2-1)
m_{ds}^1	[kg]	actual mass of dry leaves in one screw segment	Eq. (3-16)
$m_{ds,tot}^{1}$	[kg]	mass capacity of dry leaves in one screw segment	Eq. (3-16)
m_{int}	[kg]	mass of internal extract	Eq. (3-6)
\dot{m}	[kg/s]	mass flow rate	-
	. 0/ -1		

$\dot{m}_{ARTE} \ \dot{m}_{ds}, \dot{m}_{l}, \dot{m}_{s}$	[kg/s] [kg/s]	mass flow rate of ARTE in the extract mass flow rate of dry leaves, liquid and	p. 137
inds, inl, ins	[1/8/3]	solvent-soaked leaves	p. 39
$\dot{m}_{aut}, \dot{m}_{aaff}$	[kg/s]	mass flow rate of extract/raffinate (theory)	Eq. (3-12)(3-11)
\dot{m}_{ext} , \dot{m}_{raff} \dot{m}_{ext}^{exp} , \dot{m}_{raff}^{exp}	[kg/s]	mass flow rate of extract/raffinate (experiment)	p. 47
\dot{m}_{int}	[kg/s]	mass flow rate of internal extract	Eq. 39
N N	[-]	theoretical number of stages	Eq. (2-33)
NR	[-]	number of reactions	Eq. (2-1)
n	[-]	normal vector	Eq. (4-6)
n	[rpm]	screw rotation speed	Eq. (3-17)
P	[Pa/m]	porous resistance tensor	Eq. (3-17)
P _i		inertial (quadratic) resistance tensor	Eq. (4-27)
$\mathbf{P_{v}}^{i}$		viscous (linear) resistance tensor	Eq. (4-27)
$P_{v,x}, P_{v,y}, P_{v,z}$		components of the viscous resistance	Lq. (+ 27)
v, x, v, y, v, z	[1 4 3/111]	vector in x-,y-,z-direction	p. 105
p	[Pa]	pressure	p. 105 -
$ar{p}$	[Pa]	averaged pressure	p. 49
$p = p_{atm}$	[Pa]	atmospheric pressure	p. 49
p_{min}, p_{max}	[Pa]	minimal and maximal pressure	p. 52
p_{st}	[Pa]	pressure at the perforated disk for a steady state	p. 49
R	[kg _s /kg _l]	solid-liquid ratio	Eq. (3-9)
r	[m]	radius	Eq. (2-47)
r_{CRE}	[1/s]	reaction rate	Eq. (2-5)
S(t)	[-]	signal of tracer concentration	Eq. (2-27)
S_{H_2O}, S_{tol}	[-]	storage factor for water and toluene	Eq. (3-6)
So_{α}	[-]	user-defined source term	Eq. (4-19)
s σ _α	[-]	number of screw segments	p. 23
T	[Pa]	viscous stress tensor	Eq. (4-4)
\overline{T}	[°C]	temperature	p. 75
\overline{Tr}	[-]	transfer relation	Eq. (3-25)
t	[s]	time	
t_{eq}	[s]	kinetic equilibrium time between phases	p. 37
t_0	[-]	dimensionless time	Eq. (4-30)
t_{st}	[s]	stabilisation time in experiments	p. 46
Δt	[s]	discretized time step	Eq. (4-11)
u	[m/s]	velocity vector	Eq. (4-1)
$\mathbf{u_d}$	[m/s]	diffusion velocity vector	Eq. (4-19)
u _m	[m/s]	mixture velocity vector (mass-averaged)	Eq. (4-18)
$\mathbf{u}_{\mathbf{sf}}$	[m/s]	superficial velocity	Eq. (4-25)
u	[m/s]	characteristic velocity	Eq. (3-1)
u_{ax}	[m/s]	axial velocity (theory)	Eq. (2-46)
$u_{ax,exp}$	[m/s]	axial velocity (experiment)	-
u_x, u_y, u_z	[m/s]	velocity components in x-, y- and z-direction	Eqs. (4-7)-(4-9)
V	[m ³]	volume	-
V_f	[m³]	volume of a fluid phase	Eq. (4-23)
V_g	[m³]	volume of the gas phase	Eq. (3-23)
у	. ,	о r	1 1 -7

V_l, V_s	[m³]	volume of liquid and solid phase (experiment)	Eq. (3-20),(3-21)
V_p	$[m^3]$	particle volume	Eq. (4-20)
V_{tot}	[m³]	total extractor volume	p. 23
\dot{V}	[m ³ /s]	volumetric flow rate	-
\dot{V}_l , \dot{V}_S	[m ³ /s]	volumetric flow rate of liquid and solid phase	Eq.(3-20),(3-21)
$\dot{V}_{l,back}$	[m³]	volumetric flow rate of the liquid phase in	
,		backward and forward direction	Eq. (5-4)
\dot{V}_{th}	[m ³ /s]	theoretically possible volumetric flow rate	Eq. (2-45)
W_{EC}	[m]	width of the extraction cake	p. 45
$W_{1/2}$	[s]	examined widths of the distribution at half	
•		height of the $E(t)$ curve	Eq. (2-37)
x, y, z	[-]	cartesian coordinates	Eqs. (4-7)-(4-9)
x_A , x_B	[kg/kg]	mass fraction of phase A and B (CRE)	Eqs. (2-11),(2-12)
x_A^0 , x_B^0	[kg/kg]	inlet mass fraction of phase A and B (CRE)	Eq. (2-7)
Δx	[m]	mesh size	Eq. (4-11)

Dimensionless numbers

Во	Bodenstein number	Eq. (2-39)
CFL	Courant Friedrichs Lewy number	Eq. (4-11)
Da	Damköhler number	Eq. (2-10)
Da	modified Damköhler number in a batch reactor	Eq. (2-20)
$\widetilde{\mathrm{Da}}_{N}$	modified Damköhler number in a CSTR cascade	Eq. (2-21)
Pe	Péclet number	Eq. (2-39),(4-12)
Re	Reynolds number	Eq. (3-1)
Re _p	particle Reynolds number	Eq. (4-10)
Sc	Schmidt number	Eq. (4-13)

Table of Content

Αľ	ostra	Ct	III
Zι	ısam	menfassung	V
Li	st of	Abbreviations and Indices	. VII
Li	st of	Symbols	IX
Ta	ble	of Content	II
1	Intr	oduction	1
	1.1	Motivation	3
	1.2	Aims and structure of the thesis	5
2	Ext	raction of natural products	6
	2.1	Phytoextraction	6
	2.2	Analogy of extraction processes and reversible reactions	7
	2.3	Continuous operation modes described via a CSTR cascade	. 11
		2.3.1 Co-current mode	. 11
		2.3.2 Counter-current mode	. 12
	2.4	Residence time distribution and stage number	. 15
	2.5	Operation design of continuous screw extractors	. 20
3	Ехр	erimental investigations	. 22
	3.1	Design of the extraction device and counter current flow	. 23
	3.2	Characterisation of used materials	. 27
		3.2.1 Dry A. annua leaves	. 27
		3.2.2 Solvent	. 28
		3.2.3 Solvent-soaked A. annua leaves	. 29
	3.3	Selected results to estimate extraction kinetics in toluene	. 36
	3.4	Continuous steady-state operation	. 38
		3.4.1 Operation window	. 38
		3.4.2 Operation points for further investigations	. 44
		3.4.3 Pressure field	. 48
		3.4.4 Phases residence time distribution	. 54
		3.4.5 Efficiency of screw-driven transport	. 63
		3.4.6 Phase retention volume	65
	3.5	Influence of modified screw angles	. 68
	3.6	Transferability of the results to toluene as real solvent	. 74
		3.6.1 Hydrodynamics	. 74
		3.0.1 Tryar day names	. , ¬

		3.6.2 Continuous operation with toluene	77
	3.7	Summary	79
4	Nur	nerical simulations and validation	83
	4.1	Computational Fluid Dynamics	84
		4.1.1 Governing equations	84
		4.1.2 Boundary conditions	86
		4.1.3 Sliding mesh approach	87
		4.1.4 Characteristic dimensionless numbers	88
		4.1.5 Discretisation	89
		4.1.6 Numerical meshes	90
	4.2	Design of the computational geometry	92
	4.3	Flow simulation requirements	93
	4.4	Multiphase flow models – possibilities and limitations	94
		4.4.1 Overview of available models	94
		4.4.2 Volume of Fluid and Multiphase Mixture model	96
		4.4.3 Eulerian Multiphase model	100
		4.4.4 Viscous Multiphase model	102
		4.4.5 General options for region definition	103
	4.5	Mesh-independence study	106
	4.6	Multiphase flow simulations	110
		4.6.1 Eulerian Multiphase simulation	110
		4.6.2 Volume of Fluid simulation - Fully-filled reactor	114
		4.6.3 Volume of Fluid simulation - Partly-filled reactor	120
	4.7	Summary	131
5	CFD)-based compartment model	134
	5.1	Refinements of the reduced CPT model based on experimental investigations	137
	5.2	Compartmentalisation of the screw extractor for CFD-CPT coupling	141
	5.3	Simplified CFD-CPT coupling	144
	5.4	Summary	150
6	Con	nclusion	151
7	Out	:look	153
8	Ref	erences	156
Lis	t of	Figures	169
		Tables	
A.	App	pendix	174

1 Introduction

Counterflow extraction processes are widely used in the food industry, where they are applied, for example, in the solid-liquid extraction of beet sugar, vegetable oils from soybeans, rapeseed oil, or hop extract. With this method, higher final concentrations of the target substance in the solvent can be achieved compared to the direct current method. Additionally, the yield of the extraction process can be increased. This leads to a growing interest regarding counterflow processes in the pharmaceutical industry. In particular, high yields are required for the extraction of plant substances from natural materials, used further for the preparation of drugs [Lac85].

The Max-Planck-Institute for Dynamics of Complex Technical Systems (MPI) in Magdeburg has developed a continuous counterflow solid-liquid extraction process to gain artemisinin (ARTE) [Vu23]. Artemisinin-based combination therapies (ACT) are currently recommended by the World Health Organization as standard treatment against the infectious disease malaria [WHO24]. The World Malaria Report 2024 indicates that 263 million people in 83 countries were infected with malaria over the course of 2023, an increase of 11 million cases compared with 2022. Figure 1-1 illustrates the distribution of malaria cases globally, with the African and South-East Asian regions experiencing the highest incidence. Additionally, the data reveals that over 597 000 people died as a consequence of malaria, with 74% of these deaths affecting children below the age of 5 years.

In 2019, a malaria vaccination was developed and made available in the most affected countries, namely Ghana, Kenya and Malawi. A 13% reduction in all-cause early childhood mortality has already been obtained. However, the current supply of vaccines is insufficient to meet demand. A total of 18 million doses will be distributed to 12 countries between 2023 and 2025. It is estimated that four doses are required to provide optimal protection for vulnerable children, which allows for the treatment of only 4.5 million children. The objective of a reduction in malaria-associated mortality is presently not being achieved, with a discrepancy of 53% from the projected target [WHO24].

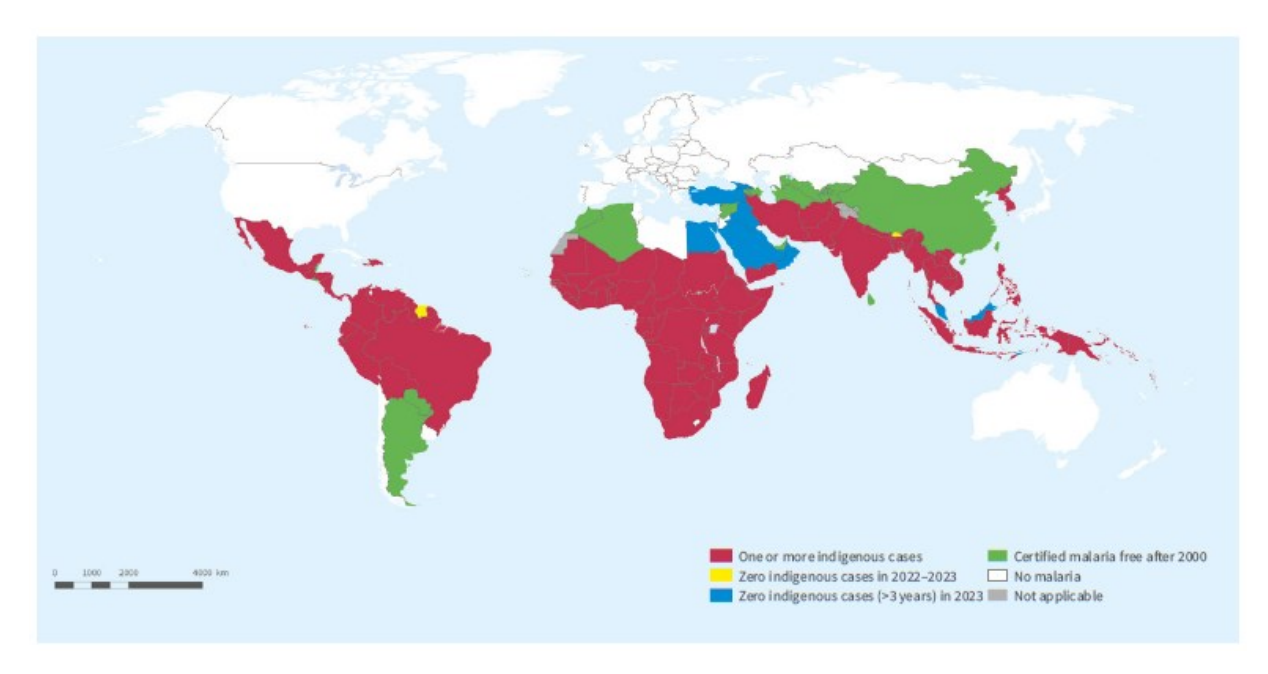


Figure 1-1: Countries with endemic status in 2000 and their status by 2023 [WHO24].

These facts demonstrate the need and importance of the standard treatment by ACTs. Their basic compound artemisinin is obtained from the *Artemisia annua L*. (Asteraceae) plant (Figure 1-2 a). It is an annual herb native to Asia, with origins in China and Vietnam. Today, it is cultivated in various nations, including Argentina, Bulgaria, France, and even tropical regions like Africa [FLD+05]. The plant's leaves are the primary source of active compounds like artemisinin which is located in the glandular trichomes of the upper younger leaves [DPE+94]. Chemically, ARTE is an odourless, non-volatile substance with chemical structure shown in Figure 1-2 (b) and formula C₁₅H₂₂O₅. It can be purified as white crystals [FLD+05]. The ARTE concentration in the plant depends strongly on growing conditions and geographical characteristics but also on genotype [CSW+90], harvesting time and plant tissues [GJM+96], [AEB99]. Typically, the concentration ranges from 0.5 to 1.5 wt.% based on the mass of dry leafs [LPC06], [You09], [FLD+05].

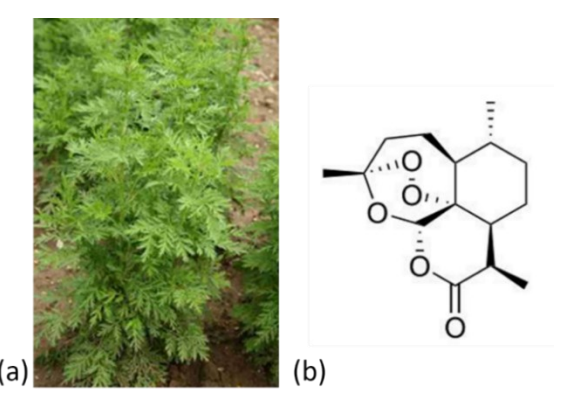


Figure 1-2: (a) Artemisia Annua L. plant, (b) chemical structure of Artemisinin [KFG+22].

1.1 Motivation

More than 210 million doses of ACTs have been supplied in affected regions in the year 2022. Nevertheless, the price of quality-assured ACTs is often higher than the recommended retail price by up to 57% [ONO+24] which renders them unavailable to the mostly poor population [HKR+07]. Reports of total syntheses of artemisinin by semi-synthetically pathways based on artemisinin acid [RPO+06], [TGG+14], [Noo10] and conversion of precursors like Dihydroartemisinic acid (DHAA) [TGV+18] are highly promising approaches but not economically feasible as a large-scale production yet [WSC+07]. In the conventional process, artemisinin is obtained by solid-liquid extraction, which is mostly performed in batch operation in the cultivating regions [LPC06]. In order to increase the production amounts, a conversion to continuous counterflow devices is increasingly applied [BP11]. With a fully continuous extraction process, which can be implemented cost-effectively in low-infrastructure areas by simple means, the global production of artemisinin could be significantly increased [Hal18].

Nevertheless, the performance of continuous extractors for solid-liquid extraction is only reported in few publications. Ferreira et al. reproduced a semi-continuous counter-current oil extraction of soybean by performing a three-stage batch extraction. While the soybeans have been placed in the extractor as a fixed bed, the solvent ethanol was heated and pumped in a closed circle through the fixed bed (percolation) [FGB+22]. Caré et al. studied solid-liquid phytoextraction of *Robinia pseudoacacia* combining static maceration and continuous flow at various solid-liquid ratios and flow rates. The process was performed semi-continuous, as well [CSB+23]. A completely continuous counter-current solid-liquid operation was performed by Neubauer et al. within a Taylor-Couette disk contactor to separate and purify a glycerol-salt mixture using ethanol as solvent. The performance was found to be comparable to two-stage cross-flow extraction by using only half the amount of solvent [NSV+23].

Recently, Vu developed a screw-type extractor to perform a completely continuous counter-current extraction of ARTE from the *Artemisia annua L.* plant (A. annua), coupled with the isolation of dihydroartemisinic acid (DHAA), a precursor to ARTE [Vu23]. The process is more efficient than traditional batch-wise extraction techniques commonly used in the pharmaceutical industry. The research provided data on distribution equilibria and extraction rates, enabling the development of a reduced compartment model for steady-state counter-

current solid-liquid extraction. Continuous extraction experiments with the solvent toluene have been performed in a steel extractor shown in Figure 1-3 [Vu23].

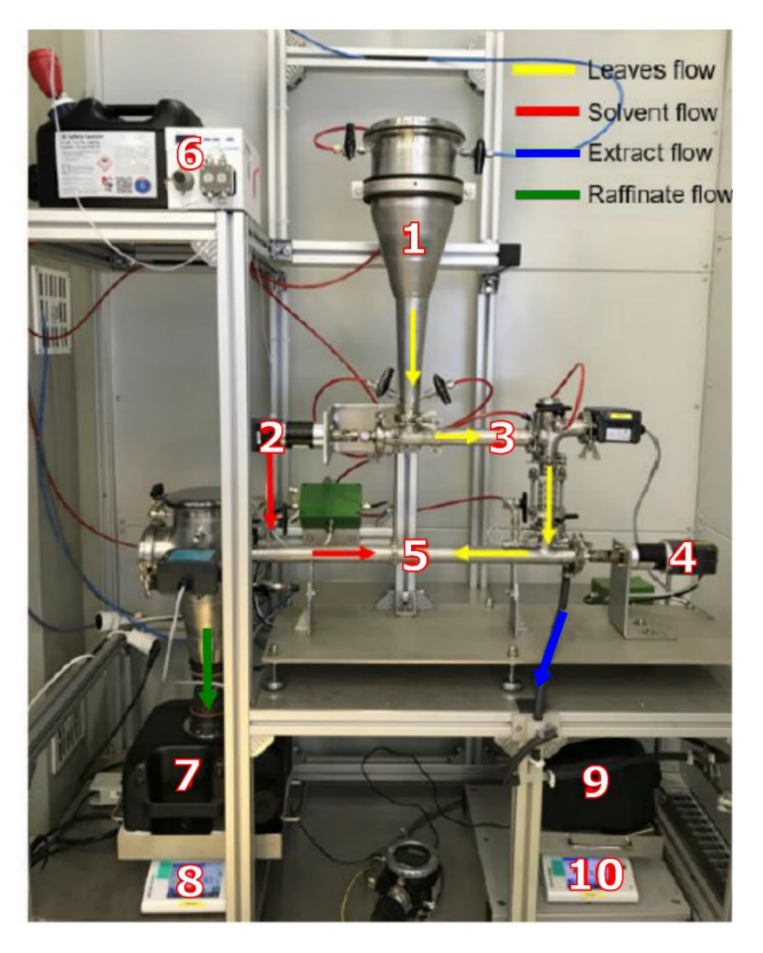


Figure 1-3: Extraction setup of the continuous counter-current apparatus (reproduced from [Vu23]), Steel extractor with 1- dried leaves storage, 2-motor for dry leaves feeding, 3-screw feeder, 4-motor extraction screw driving, 5-extractor, 6-solvent pump, 7-raffinate tank, 8-weighting scale for raffinate, 9-extract tank, 10-weighting scale for extract.

Since the organic solvent toluene is highly explosive when it comes into contact with oxygen, safety requirements are needed for this steel extractor. While the nitrogen gas is continuously flowing through the installation, several sensors measure the concentration of remaining oxygen and toluene at different locations. These sensors are connected to a control system. If the permitted thresholds are exceeded, the entire process is stopped immediately to prevent explosions. These facts require a completely closed steel extractor that can neither be opened during operation nor allow probes from inside the process. Furthermore, for safety reasons, the material of this extractor cannot be changed to a transparent material such as glass. As a result, the steel extractor offers very restricted possibilities for characterising the process and finding its limitations. Vu could only marginally observe the operating window,

the material properties during the process as well as the residence time distribution (RTD) of the phases involved [Vu23]. However, this information is essential for reactor characterisation and optimisation [Mar00], [SP02].

The application of a harmless solvent such as water in a similar reactor can provide useful information. It allows for optical observations of the process, since a transparent material such as glass can be used for the reactor. The interactions between velocity profiles and microscopic and macroscopic mechanisms of mass distribution can be additionally considered using Computational Fluid Dynamics (CFD). It also allows simple adjustments to the extractor design and solvent properties. However, CFD must first be properly validated using experimental data.

1.2 Aims and structure of the thesis

The thesis aims to enhance understanding of the continuous solid-liquid counter-current extraction process through simplified experiments in a glass extractor. Chapter 2 provides an overview of natural product extraction, including instructive chemical reaction engineering basics considering typical reactor systems. Chapter 3 details experimental investigations on a glass extractor constructed similarly to the steel setup reported by Vu [Vu23]. These experiments, focusing on material properties, steady-state operation, and phase residence time distribution, neglect mass transfer from the solid to the liquid phase but are essential for process understanding and CFD model development. Further, a transferability to real extraction considering mass transfer within the steel setup of Vu was performed. Based on these experimental observations and characterisations a numerical model is developed in chapter 4 using model simplifications to decrease computational costs. In chapter 5 this numerical model is further coupled with the existing compartment model of Vu [Vu23] including also the extraction kinetics to deliver a decision-support tool for improved process operation. This work is closed with conclusions and perspectives.

2 Extraction of natural products

Extraction basically exploits the mass transfer process of a desired compound from one phase into another. Here, liquid-liquid extraction (LLE) and solid-liquid extraction (SLE, also called leaching or maceration process) can be differentiated. When using natural products, so-called phytoextraction is performed from using mostly a solid starting material containing the valuable compounds while the extracting phase is usually a liquid (solvent).

2.1 Phytoextraction

Due to the growing demand in attractive bioactive compounds available in natural sources the development of efficient phytoextraction processes has recently received increasing interest [CRR+17]. These compounds are classified into primary and secondary metabolites. Primary metabolites result from the adaption of the plant to its surrounding, e.g., growth and reproduction of cells. They do not show any pharmaceutical effect. Secondary metabolites are bioactive compounds possessing an ecological role, e.g., defend the plant against predators. Typical secondary metabolites are, e.g., carotenoids, phenolic compounds and alkaloids. They are only found in specific plants inside capillaries, pores or single cells with much smaller amounts compared to primary metabolites [BP11], [APS+09].

The feed material can consist of leaves, flowers, branches, or seeds with a typical concentration of active pharmaceutical ingredient (API) ranging from 0.3 – 3 wt.%. The API concentration mainly depends on seasonal fluctuations and producing area. After receiving the raw material from agriculture, a pre-treatment is usually necessary for decreasing particle size and narrow particle size distribution. This enhances the mass transfer between the particles and the solvent. As a result, the extraction efficiency of APIs is increased. Nevertheless, too small particles can introduce bed compaction leading to blockage. The solid-liquid extraction is usually performed with a supercritical fluid (under high pressure) or a solvent [KJS+10]. Thereby, the solvent penetrates the feed material until reaching cellular structures by molecular diffusion. Here, the soluble compounds are dissolved and the solvent solution, or extract, returns back to the feed surface by molecular diffusion. Finally, the solvent is transferred from the feed material surface into the liquid phase by convection (Figure 2-1).

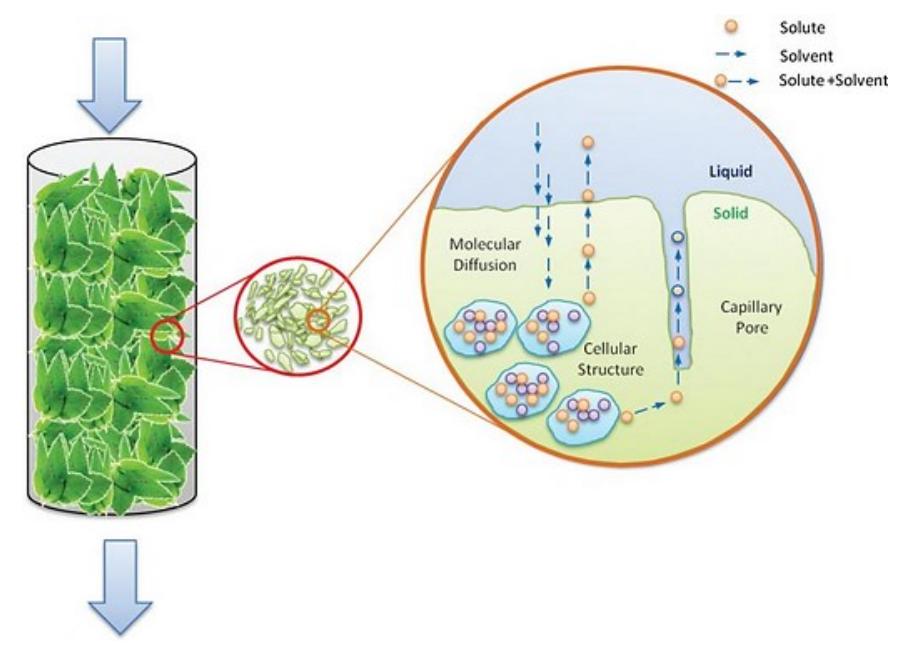


Figure 2-1: Phytoextraction of solute from solid leaves to liquid solvent, reprinted from [RP13].

For pharmaceutical applications a final purification of the extract solution is performed to achieve an ultrapure product which can be capsulised or pelletised. For an efficient extraction the selection of a suitable solvent is of high importance and a key component of the process.

2.2 Analogy of extraction processes and reversible reactions

The Chemical Reaction Engineering (CRE) community provides useful tools to describe reactions and to predict temporal and local concentration profiles in ideal reactors. These are namely the batch reactor (BR), the continuously stirred tank reactor (CSTR) and the plug flow tubular reactor (PFTR). Both, the CSTR and the PFTR represent limiting cases of continuously operated reactor systems as shown in Figure 2-2.

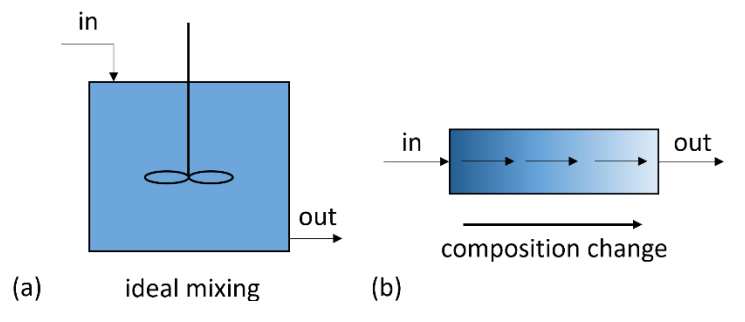


Figure 2-2: Ideal continuous tank reactor models, (a) CSTR, (b) PFTR.

A homogeneous and reversible reaction with the reaction rate r_j can generally be solved in a batch reactor by using the Eq. (2-1) where i denotes the number of components and j the

number of reactions. Here $v_{i,j}$ denotes the corresponding stoichiometric coefficient and m_{tot} the total mass capacity of the reactor including all components. In this thesis only mass balances instead of the generally used molar balances in CRE are implemented due to simplicity for later mass-based investigations. Considering a closed batch volume with NR reactions the following balance holds:

$$\frac{dm_i}{dt} = m_{tot} \sum_{j}^{NR} v_{i,j} r_j \qquad i = 1, M$$
 (2-1)

For the specific reversible reaction A $\rightleftarrows_{r_2}^{r_1}$ B with two characteristic reaction rates $r_j = [r_1, r_2]$ and a simple stoichiometric matrix $v_{A,j} = [-1,1]$ and $v_{B,j} = [1,-1]$, the specific mass fraction of component A, x_A , can be investigated by transferring Eq. (2-1) to Eq. (2-2).

$$\frac{dx_A}{dt} = -r_1 + r_2 \tag{2-2}$$

with a mass fraction of A:

$$x_A = \frac{m_A}{m_{tot}} \tag{2-3}$$

The reaction rates r_1 and r_2 are assumed to be of first order. The expressions contain rate constants k_1 and k_2 {Eq. (2-4)}.

$$r_1 = k_1 x_A$$
 and $r_2 = k_2 x_B$ (2-4)

Eq. (2-5) describes the final mass balance for component A. It contains for a reversible reaction also the mass fraction of component B, x_B . For large times after reaching equilibrium state, the thermodynamic equilibrium (eq) constant of the reaction, K^{eq} can be included, which provides Eq. (2-6).

$$\frac{dx_A}{dt} = -k_1 x_A + k_2 x_B = -k_1 \left(x_A - \frac{k_2 x_B}{k_1} \right) \tag{2-5}$$

for
$$t = t_{eq}$$
: $K^{eq} = \frac{k_1}{k_2} = \frac{x_B^{eq}}{x_A^{eq}}$ (2-6)

For a specific reaction of interest, the two corresponding parameters k and K^{eq} typically need to be determined experimentally.

The overall mass balance is expressed by Eq. (2-7) where x_A^{in} and x_B^{in} are the initial mass fractions of the two components, and $x_A(t)$ and $x_B(t)$ are the mass fractions at a specific reaction time t.

$$x_A^{in} + x_B^{in} = x_A(t) + x_B(t) (2-7)$$

The implementation of the total mass balance in Eq. (2-7) into Eq. (2-5) results in the following linear ordinary differential equation (ODE):

$$\frac{dx_{A}}{dt} = -k_{1} \left(x_{A} - \frac{x_{A}^{in} + x_{B}^{in} - x_{A}}{K^{eq}} \right) \tag{2-8}$$

With the initial conditions of $x_A(t=0)=x_A^{in}=1$ and $x_B(t=0)=0$ it holds:

$$x_B = 1 - x_A \tag{2-9}$$

In CRE often a dimensionless Damköhler number Da {Eq. (2-10)} is used to capture the ratio between the time t given for a reaction and a characteristic time quantifying the need of the reaction. The latter is for a first order reaction given by $1/k_1$.

$$Da = \frac{t}{1/k_1} \quad \text{or} \quad Da = k_1 \cdot t \tag{2-10}$$

Then, the solution can be expressed by Eqs. (2-11) and (2-12) for a batch reactor describing the time dependence of the mass fractions as a function of Da and K^{eq} :

$$x_{A}(t) = \frac{1}{1 + K^{eq}} \left(x_{A}^{in} + x_{B}^{in} \right) + \left(\frac{K^{eq}}{1 + K^{eq}} x_{A}^{in} - \frac{1}{1 + K^{eq}} x_{B}^{in} \right) e^{-\left(\frac{\text{Da}}{K^{eq}} + \text{Da} \right)}$$
(2-11)

$$x_{B}(t) = \frac{K^{eq}}{1 + K^{eq}} (x_{A}^{in} + x_{B}^{in}) - \left(\frac{K^{eq}}{1 + K^{eq}} x_{A}^{in} - \frac{1}{1 + K^{eq}} x_{B}^{in}\right) e^{-\left(\frac{Da}{K^{eq}} + Da\right)}$$
(2-12)

To quantify now extraction processes the equations given above and widely used in CRE can be adapted by defining mass fractions of a component i in the solid feed (raffinate) and in the product (extract), $x_{s,i}$ and $x_{l,i}$, respectively (index s for solid feed and l for liquid solvent). In this work only one component i is of interest, namely Artemisinin (ARTE). Since natural material soak a specific part of the solvent, two different liquid phases exist and need to be defined. These are often designated as internal and (the product containing) external solvent. To apply the introduced CRE model, the two phases can be considered as a pseudo-homogeneous mixture. The amounts initially segregated in two phases can be reformulated using new mass fractions (\tilde{x}_l and \tilde{x}_s), which characterise a hypothetical pseudo-homogeneous system. These fractions are defined in Eqs. (2-14) and (2-15), respectively. The application of these relations requires specifying a phase ratio of the amounts of the involved phases. This

can be done by introducing a liquid phase mass fraction ε as defined in Eq. (2-13) with interval [0,1]. The liquid phase external mass m_{ext} will be focused in subsection 3.2.3.

$$\varepsilon = \frac{m_{ext}}{m_l + m_s} \tag{2-13}$$

$$\tilde{x}_1 = x_1 \cdot \varepsilon$$
 (2-14)

$$\tilde{x}_s = x_s \cdot (1 - \varepsilon) \tag{2-15}$$

This approach, proposed first and implemented by Vu [Vu23], allows exploiting the classical Eqs. (2-11) and (2-12) derived by the CRE community for modelling extraction processes. These equations contain now the following two essential constants, which also take into account the phase ratio ε :

$$\tilde{k}_E = \frac{k_E}{1 - \varepsilon} \tag{2-16}$$

$$\widetilde{K}_{E}^{eq} = \frac{\varepsilon}{1 - \varepsilon} K_{E}^{eq} \tag{2-17}$$

The Eq. (2-16) contains the extraction rate constant, k_E , and Eq. (2-17) the extraction equilibrium constant, K_E^{eq} . Both constants are specific to the natural product, the component, and the used solvent. For ARTE extraction with toluene Vu already assumed both parameter as presented in chapter 5 [Vu23]. Finally, the following overall mass balance needs to be respected:

$$\tilde{x}_s^{in} + \tilde{x}_l^{in} = \tilde{x}_s(t) + \tilde{x}_l(t) \tag{2-18}$$

Continuous extraction

Moving now from batch to continuous extraction reactors the time t is equivalent to the mean residence time which can be defined for a tubular reactor with a mass capacity of m_{tot} as:

$$\bar{\tau}_m = \frac{m_{tot}}{\dot{m}} \tag{2-19}$$

The mass capacity is based on the total reactor volume V_{tot} and the phase specific density. This definition allows a simple integration to the proposed mass-based model.

The Damköhler number introduced above {Eq. (2-10)} can be easily adapted by using the residence time $\bar{\tau}_m$ instead of the time t as shown in Eq. (2-20):

$$\widetilde{\mathrm{Da}}(\tau) = \widetilde{k}_E \cdot \overline{\tau}_m \tag{2-20}$$

For a cascade of N sequentially connected and equally sized CSTR reactors, the Damköhler number needs to be adapted as follows:

$$\widetilde{\mathrm{Da}}_{N}(\tau) = \frac{\widetilde{k}_{E} \cdot \overline{\tau}_{m}}{N} \tag{2-21}$$

Further, the liquid phase mass fraction is now derived as a ratio of the mass flow rates focused on in section 3.4.

$$\varepsilon = \frac{\dot{m}_{ext}}{\dot{m}_l + \dot{m}_s} \tag{2-22}$$

The introduced equations can now be used to describe the extraction processes in continuous reactor systems as described in the next section.

2.3 Continuous operation modes described via a CSTR cascade

Continuous multi-phase processes are typically performed in co-current or counter-current mode [DLM99], [RL08], depending on the inlet positions and the flow directions. In extraction processes these refer to solid feed material and solvent. Due to its flexibility we will consider below a series of *N* sequentially connected CSTR reactors (units), which are a useful model to represent a tubular system.

2.3.1 Co-current mode

In co-current mode, the solid feed material (s) and the liquid solvent (l) are introduced at the same position and flow in the same direction through the reactor. Figure 2-3 shows the flow scheme for a theoretical stage number of N=2. This co-current flow is easy to implement in many configurations but always results in a lower extraction performance compared to the counter-current flow, under similar operating conditions [Tre80], [PP13].

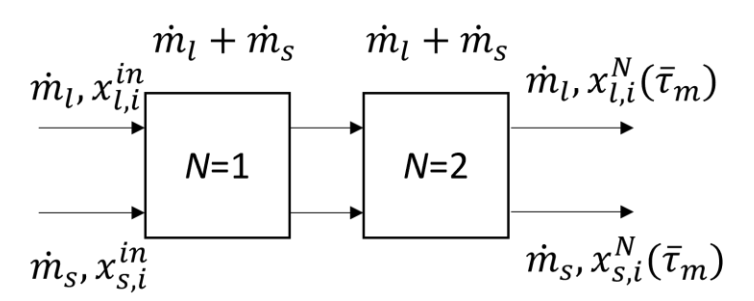


Figure 2-3: Process scheme of co-current extraction with two stages (N=2). The inlet mass fraction of liquid and solid phase $x_{l,i}^{in}$ and $x_{s,i}^{in}$ are introduced at the same position and flow in similar direction through the reactor. The most important mass fractions of the extract and raffinate phase exit at stage N with $x_{l,i}^N(\bar{\tau}_m)$ and $x_{s,i}^N(\bar{\tau}_m)$, reproduced from [Vu23].

2.3.2 Counter-current mode

In counter-current mode, the feed material contacts the solvent continuously for each stage over the whole reactor length. A separate injection is not performed. The fresh solvent introduced in stage N=1 ($x_{l,i}^{in}=0$) is contacted for a specific residence time τ with the most exhausted plant material. At the same time, the already enriched solvent at stage N is contacted with fresh plant material at $x_{s,i}^{in}$ (which represents the maximal solid phase mass fraction). A scheme of this process is shown in Figure 2-4. This procedure maximises the mass fraction differences between the solid and liquid phase and saves solvent compared to the cocurrent mode [BP11].

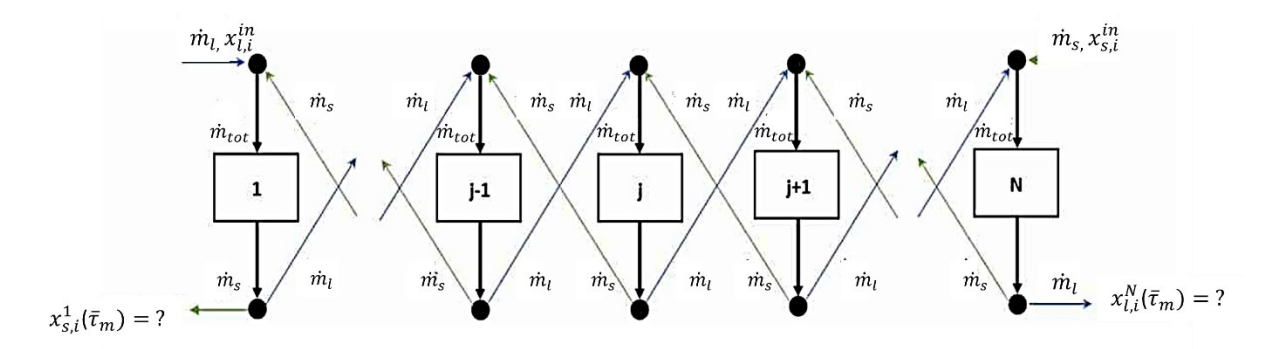


Figure 2-4: Process scheme of a counter-current extraction process with N stages. The mass fraction of the component i in the liquid phase (l) and solid phase (s) is changing in each stage while the most important mass fraction is in the extract $x_{l,i}^N(\bar{\tau}_m)$, at stage N. The raffinate exits at stage 1 with mass fraction $x_{s,i}^1(\bar{\tau}_m)$, reproduced from [Vu23].

For calculating the amount of the extracted component i= ARTE in the studied continuous counter-current process a linear equation system based on the equations defined in section 2.2 is applied. Here \tilde{x}_l^{in} and \tilde{x}_s^{in} are the known inlet mass fraction of the substance ARTE in the pseudo-homogeneous, single liquid and solid phase, respectively. The outlet mass fractions are defined with $x_{l,N}(\bar{\tau}_m)$, and $x_{s,1}(\bar{\tau}_m)$, depending on the residence time τ_m . The constants B_1 and B_2 include the theoretical number of stages N, the thermodynamic equilibrium \tilde{K}_E^{eq} and the Damköhler number \widetilde{Da}_N in Eq. (2-21) (depending on the extraction rate \tilde{k}_E).

$$j = 1 \qquad 0 = -B_{1} \tilde{x}_{l}^{in} + \tilde{x}_{l,1}(\bar{\tau}_{m}) - B_{2} \tilde{x}_{s,2}(\bar{\tau}_{m})$$
 (2-23)
$$j = 2...N - 1 \qquad 0 = -B_{1} \tilde{x}_{l,j-1}(\bar{\tau}_{m}) + \tilde{x}_{l,j}(\bar{\tau}_{m}) - B_{2} \tilde{x}_{s,j+1}(\bar{\tau}_{m})$$

$$j = N \qquad 0 = -B_{1} \tilde{x}_{l,N-1}(\bar{\tau}_{m}) + \tilde{x}_{l,N}(\bar{\tau}_{m}) - B_{2} \tilde{x}_{s}^{in}$$

$$j = N + 1 \qquad 0 = -\tilde{x}_{l}^{in} + \tilde{x}_{l,1}(\bar{\tau}_{m}) + \tilde{x}_{s,1}(\bar{\tau}_{m}) - \tilde{x}_{s,2}(\bar{\tau}_{m})$$

$$j = N + 2...2N - 1 \qquad 0 = -\tilde{x}_{l,j-1}(\bar{\tau}_{m}) + \tilde{x}_{l,j}(\bar{\tau}_{m}) + \tilde{x}_{s,j}(\bar{\tau}_{m}) - \tilde{x}_{s,j+1}(\bar{\tau}_{m})$$

$$j = 2N \qquad 0 = -\tilde{x}_{l,N-1}(\bar{\tau}_{m}) + \tilde{x}_{l,N}(\bar{\tau}_{m}) + \tilde{x}_{s,N}(\bar{\tau}_{m}) - \tilde{x}_{s}^{in}$$
 with
$$B_{1} = \frac{1 + \widetilde{Da}_{N}}{1 + \frac{\widetilde{Da}_{N}}{\widetilde{K}_{e}^{n}} + \widetilde{Da}_{N}} \qquad \text{and} \qquad B_{2} = \frac{\widetilde{Da}_{N}}{1 + \frac{\widetilde{Da}_{N}}{\widetilde{K}_{e}^{n}} + \widetilde{Da}_{N}}$$
 (2-24)

This structure of the linear equation system for a counter-current *N*-CSTR reactor is visualised in Figure 2-5. It can be solved numerically, e.g. by using the "linsolve" solver in the Matlab Toolbox [Mat24].

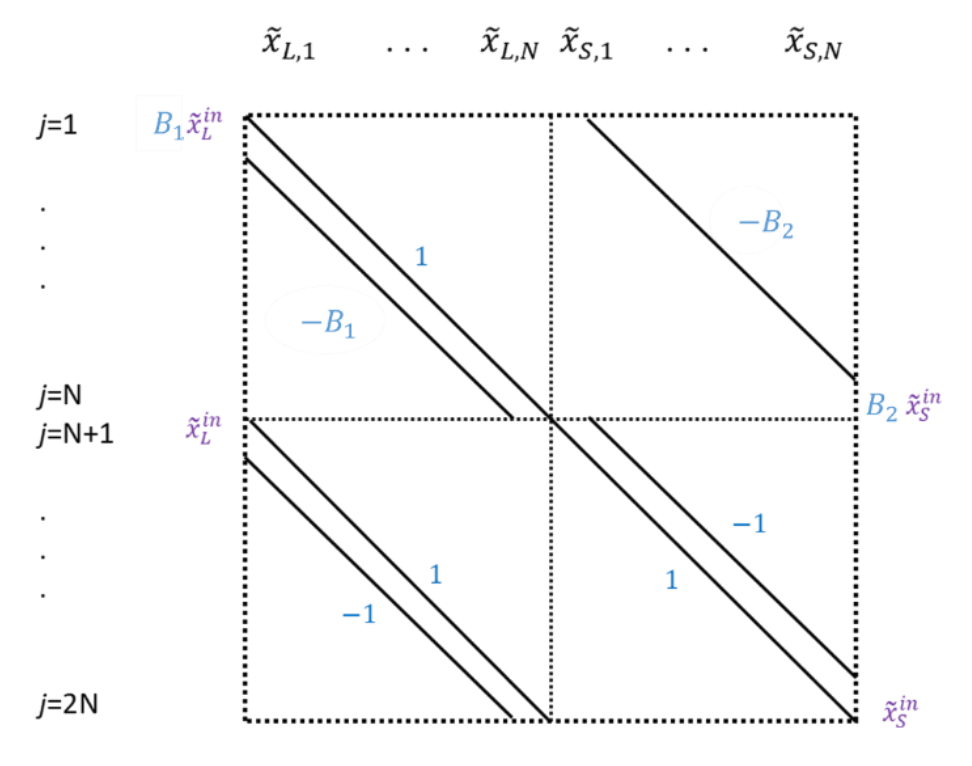


Figure 2-5: Linear equation system with 2N equations in the form of $0=\bar{B}\bar{y}+\bar{B}_0$. The vector \bar{y} describes the unknown variables $\bar{y}=\left[\tilde{x}_{l,1},...,\tilde{x}_{l,N},\tilde{x}_{s,1},...,\tilde{x}_{s,N}\right]$ while the vector \bar{B}_0 defines given variables: $\bar{B}_0=[-B_1\tilde{x}_l^{in},(2N-2)\cdot 0,-\tilde{x}_s^{in}]$. The linear system can be solved numerically, e.g. with the "linsolve" solver in the Matlab Toolbox [Mat24] (reproduced from [Vu23]).

To calculate finally the real effluent-mass fractions of ARTE in the solid and liquid phase the outlet mass fractions of the model $\tilde{x}_{l,N}$ and $\tilde{x}_{s,1}$ need to be transferred back from the pseudo-homogeneous system to the heterogeneous system according to Eqs. (2-25) and (2-26) by using ε :

$$x_{l,N}(\tau) = \frac{\tilde{x}_{l,N}(\bar{\tau}_m)}{\varepsilon}$$
 (2-25)

$$x_{s,1}(\tau) = \frac{\tilde{x}_{s,1}(\bar{\tau}_m)}{1 - \varepsilon} \tag{2-26}$$

For the implementation of this equation system it should be noted that extraction processes are typically irreversible reactions. Already extracted components cannot be reintroduced into the solid material in the manner described theoretically by the backward path formulated in the model. Thus, the model equations describe only situations for which holds $x_s > x_s^{eq}$.

This model was already successfully applied by Vu [Vu23] for ARTE extraction and by Fotovati [Fot23] for saffron extraction which makes it highly suitable for the coupling with CFD simulations, as desired in this work. The original parameters K_E^{eq} and k_E have been measured for ARTE extracted by the solvent toluene, as presented in section 3.3.

The stage number N could only be estimated theoretically. This stage number is essential to characterise the reactor and operating conditions. It needs to be estimated based on experiments which is one important purpose of the present work. It should be further mentioned, that the presented kinetic model assumes a pseudo-homogeneous system where the stage number for solid and liquid phases is equal. The actual heterogeneous system results in distinct flow behaviours for the solid (s) and liquid (l) phase. This discrepancy introduces differences in the residence time and the final theoretical number of stages for each phase. To address this model limitation, a mean theoretical number of stages $\overline{N}(N_s, N_l)$ should be employed to approximate the behaviour of both phases within the model.

The implementation of experimental investigations regarding this parameter will be performed in chapter 5.

2.4 Residence time distribution and stage number

The residence time distribution (RTD) is defined as a probability distribution of time in which a fluid stays inside one or more continuously operated units [GMI12]. In horizontal screw reactors, the RTD is mainly affected by the screw rotation speed, tube and screw geometry, phase throughputs, and their properties. It provides essential information for finding optimal operating conditions [SS18]. Consequently, it represents an important parameter for selecting suitable reactor models and is used in many industrial processes such as the continuous production of chemicals, plastics, polymers, food, catalysts, and pharmaceuticals [GMI12], [MGL92], [CG98], [GY94]. The general RTD theory assumes a homogeneous system where the involved phases share similar flow properties. For the heterogeneous system of the countercurrent solid-liquid flow, simplifications based on a homogeneous model must be considered. From the RTD analysis the mean residence time of a material in a system can be obtained. This is usually compared with the time required for a complete reaction in the system, based on the corresponding reaction kinetics. If the mean residence time is much shorter than the required reaction time, the reactor design is inadequate, and the extraction yield will be poor [GIM12]. Consequently, the RTD can be used for model discrimination and parameter estimation. The results of RTD measurement allow characterisation of the investigated reactor between the two ideal reactor designs, CSTR and PFTR.

RTD measurement is performed using the stimulus-response technique with pulse or stepwise tracer inputs. In the pulse-wise technique, a short-term marking is performed, saving tracer material compared to the step-wise technique, where a tracer is continuously added until the process ends. In the periodic variation technique, the tracer is added periodically to the process. The schematic input and output signals are illustrated in Figure 2-6. In this thesis the pulse-wise technique was used as described in chapter 3.

The tracer should share similar size and properties with the relevant phase to be able to follow the same path without disturbances. Further, the tracer should be easy to detect at the equipment outlet (e.g., by ultraviolet-visible (UV-VIS) spectroscopy, conductivity, online Near Infrared (NIR) spectroscopy, radioactive tracers etc.) [Rod21].

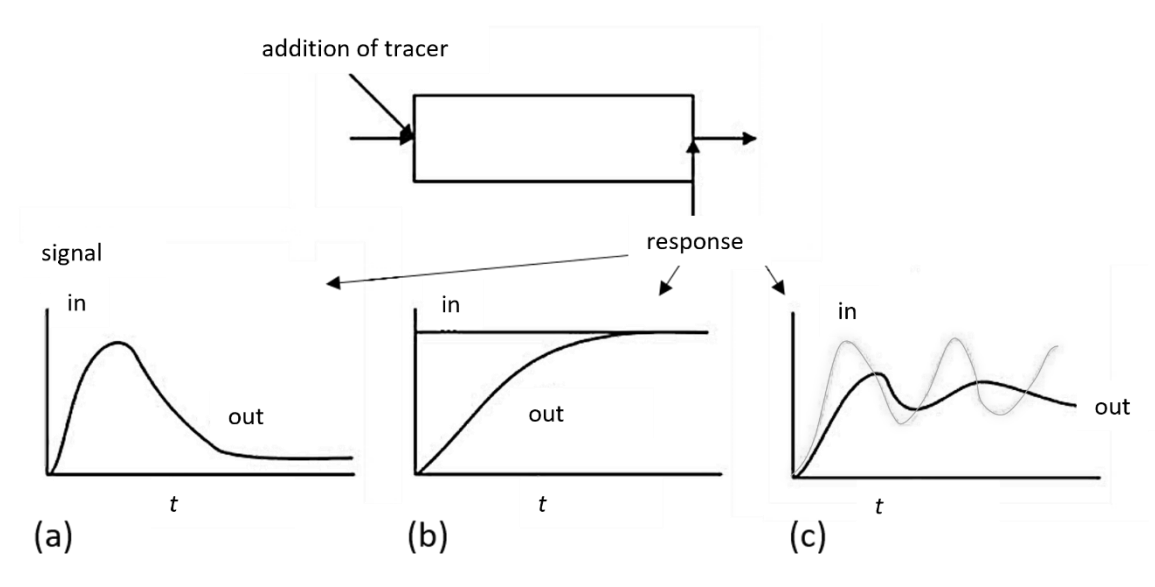


Figure 2-6: Methods of tracer input as a a) pulse-wise, b) step-wise and c) oscillating supply, reproduced from [SMW10].

The signal detected by the equipment S(t) is related to the tracer concentration c(t) by the model constants a_{RTD} and b_{RTD} {Eq. (2-27)}. They depend on the characteristics of the apparatus and the chemical composition of the system. The signal is equal to the tracer concentration for a constant volume flow rate through the apparatus, e.g. at steady-state as used in this work.

$$S(t) = a_{RTD} + b_{RTD}c(t) \qquad \xrightarrow{\dot{V} = const.} \qquad S(t) = c(t)$$
 (2-27)

The signal S(t) is used to calculate the normalised residence time distribution function E(t) {Eq. (2-28)}. This function can be transformed to the cumulative exit age distribution function F(t) {Eq. (2-29)} [Lev99].

$$E(t) = \frac{S(t)}{\int_0^\infty S(t) dt}$$
 (2-28)

$$F(t) = \int_0^t E(t)dt \tag{2-29}$$

The concentration measured at the outlet is normalised to the total concentration added to the process at the beginning. Consequently, the integral of all measured values for E(t) in a closed process has to be 1 {Eq. (2-30)}. As in experimental set-ups only discrete values can be measured, the RTD can be approximately determined by summation.

$$\int_0^\infty E(t)dt = 1 \implies \sum_j E(t_j) \Delta t = 1$$
 (2-30)

The mean residence time (MRT) $\bar{\tau}$ (first moment) and the variance σ^2 (second central moment) can be derived from E(t) according to Eqs. (2-31) and (2-32). They are typically shown in the unit [min] but transferred to the SI unit [s] for all calculations in this work. The standard deviation σ derives from the square root of the variance.

$$\bar{\tau} = \int_0^\infty t \cdot E(t) \ dt \tag{2-31}$$

$$\sigma^2 = \int_0^\infty (t - \bar{\tau})^2 \cdot E(t) dt \tag{2-32}$$

From the ratio between the square of the mean residence time τ and the variance σ^2 a corresponding number of theoretical stages N can be obtained by Eq. (2-33) [MW35]. This number is used with integer values.

$$N = \left(\frac{\bar{\tau}^2}{\sigma^2}\right) \tag{2-33}$$

While N=1 represents the flow behaviour of an ideal CSTR, a high value of N corresponds to the behaviour of an ideal plug flow tank reactor (PFTR), for which holds: $\sigma^2=0$ and $N\to\infty$. A general, simplified approach to determine the mean residence time is shown in Eq. (2-34). Here we consider a characteristic length of the flow geometry, L_{ch} , and \bar{u}_{ax} describing the flow velocity of the specific phase in axial flow direction.

$$\bar{\tau} = \frac{L_{ch}}{\bar{u}_{ax}} \tag{2-34}$$

For a constant flow area A inside the flow geometry, this equation can be extended to a volume-based approach, incorporating the total free volume of the extractor V_{tot} and the volume flow rate of the liquid solvent \dot{V} {Eq. (2-35)}. It aligns with the previously introduced mass-based residence time $\bar{\tau}_m$ in Eq. (2-19) assuming a completely filled reactor.

$$\bar{\tau} = \frac{L_{ch} \cdot A}{\bar{u}_{ax} \cdot A} = \frac{V_{tot}}{\dot{V}} \tag{2-35}$$

If the RTD resembles a Gaussian distribution, a fast estimation method is possible. It is frequently applied to analyse chromatographic peaks to estimate the number of theoretical stages N using investigated widths of the curve distribution at half height $w_{1/2}$ [SSS20]:

$$N = 5.54 \left(\frac{\bar{\tau}^2}{w_{1/2}^2} \right) \tag{2-36}$$

For describing back-mixing effects in tubular reactors (PFTR-behaviour dominates typically there) the dispersion model is frequently applied. It introduces an additional axial dispersion coefficient D_{ax} in a second-order term of the mass balance [Lev99]:

$$\frac{\partial c}{\partial t} = -u_{ax}\frac{\partial c}{\partial z} + D_{ax}\frac{\partial^2 c}{\partial z^2} \tag{2-37}$$

For the dispersion model the variance is defined by Eq. (2-38):

$$\sigma^2 = 2 \frac{D_{ax} \cdot L_{ch}}{\bar{u}_{ax}^3} \tag{2-38}$$

The extent of axial dispersion can be estimated by evaluating the Bodenstein number Bo (in the field of fluid dynamics also designated as a Péclet number Pe) defined in Eq. (2-39).

$$Bo = \frac{\bar{u}_{ax} \cdot L_{ch}}{D_{ax}}$$
 (2-39)

A rearrangement of Eq. (2-39) provides a definition of the axial diffusion coefficient:

$$D_{ax} = \frac{\overline{u}_{ax} \cdot L_{ch}}{\text{Bo}}$$
 (2-40)

To demonstrate the relation between the Bodenstein number Bo and the theoretical number of stages N for a PFTR, Eqs. (2-33) and (2-38) are used based on the variance σ^2 :

$$\sigma^2 = \frac{\bar{\tau}^2}{N} = 2 \frac{D_{ax} \cdot L_{ch}}{\bar{u}_{ax}^3}$$
 (2-41)

After reshaping Eq. (2-41) the Bodenstein number defined in Eq. (2-39) can be easily included:

$$\frac{\bar{\tau}^2}{N} = 2 \frac{D_{ax} \cdot L_{ch}^2}{\bar{u}_{ax} \cdot \bar{u}_{ax}^2 \cdot L_{ch}} = 2 \frac{L_{ch}^2}{\text{Bo} \cdot \bar{u}_{ax}^2}$$
(2-42)

Now, the MRT $\bar{\tau}$ according to Eq. (2-34) can be involved on the right-hand side:

$$\frac{\bar{\tau}^2}{N} = 2 \frac{L_{ch}^2}{\text{Bo} \cdot \bar{u}_{ax}^2} = 2 \frac{\bar{\tau}^2}{\text{Bo}}$$
 (2-43)

The MRT at both sides can be eliminated, showing a proportional behaviour between the Bodenstein number Bo, the theoretical number of stages N and the characteristic length L_{ch} in the Eq. (2-44) for constant flow velocities and mixing behaviour. In this case, also a constant relationship between the stage number and the characteristic length can be assumed.

Bo =
$$2 \cdot N = \frac{\overline{u}_{ax} \cdot L_{ch}}{D_{ax}}$$
 (2-44) for $u_{ax}, D_{ax} = \text{const.}$ Bo $\sim N \sim L_{ch}$, $\frac{N}{L_{ch}} = \text{const.}$

Large Bodenstein numbers (typically for values Bo > 100) indicate low axial dispersion and, thus, a flow behaviour as assumed in a PFTR [Lev12]. Such low degrees of dispersion enable high extraction efficiencies. Characteristic curves of E(t) and F(t) defining an ideal CSTR or PFTR, and a non-ideal, realistic reactor are shown in Figure 2-7.

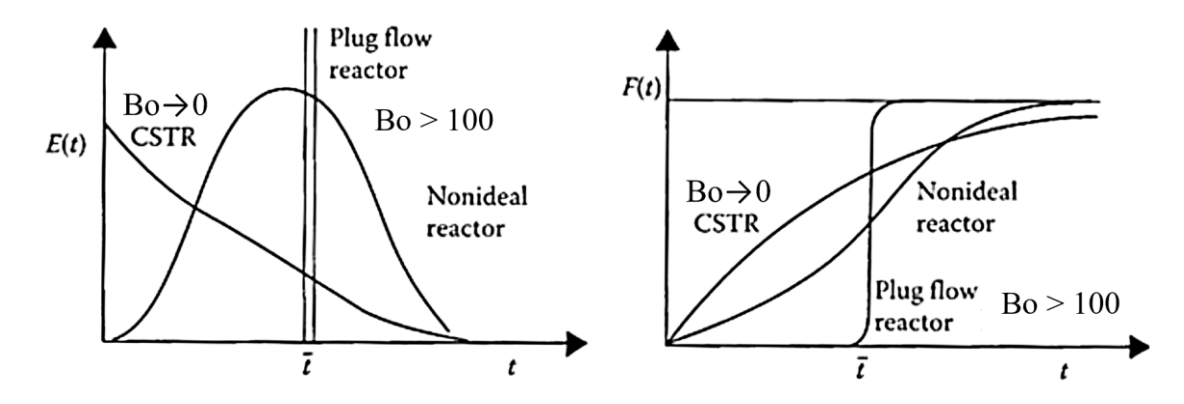


Figure 2-7: Typical RTD curves for CSTR, PFTR and non-ideal reactor for the (a) normalised residence time distribution function E(t) and (b) cumulative exit age function F(t). The Bodenstein number Bo characterises the limiting cases. Reproduced from [SMW10].

As mentioned previously, the flow behaviour of the solid and liquid phases in the investigated heterogeneous counter-current solid-liquid flow are assumed to differ, resulting in distinct RTD behaviours for each phase. Consequently, the mean residence time is not equal for both phases as proposed with the homogeneous model ($\bar{\tau}_s \neq \bar{\tau}_l$). This difference affects the theoretical number of stages N and the Bodenstein number Bo. Therefore, both phases must

be analysed independently in terms of their RTD behaviour to obtain reliable results for a combined reactor characterisation.

2.5 Operation design of continuous screw extractors

Continuous reactors have been mainly developed and used for extraction of oil or sugar. These are e.g. rotary reactors [CLT15], belt reactors [Riz13] and screw reactors [DSS24]. While the rotary reactors and belt reactors are based on percolation, the screw reactors are based on immersion. Since this thesis relies on the screw extractor constructed by Vu, only this operation design is discussed further.

Screw extractors use the advantages of screw machines. They are typically implemented in the plastic production and food industry where highly viscous fluids have to be transported against a pressure ramp. In this aspect, the screw extractors are also called extruders. High temperatures often play an important role. Furthermore, screw extractors perform tasks like plasticisation, homogenisation, mixing and granulation and are applied for degassing solvents and decreasing remaining humidity. For characterising screw extractors, the number and rotation direction of the implemented screws is of high importance. While one-screw extractors, as used in this thesis, are easier to produce and operate, twin-screw extractors have higher transport efficiencies and are often used for different production tasks during the transportation process of the product [Con08]. Figure 2-8 shows a general classification of screw extractors used for extrusion processes.

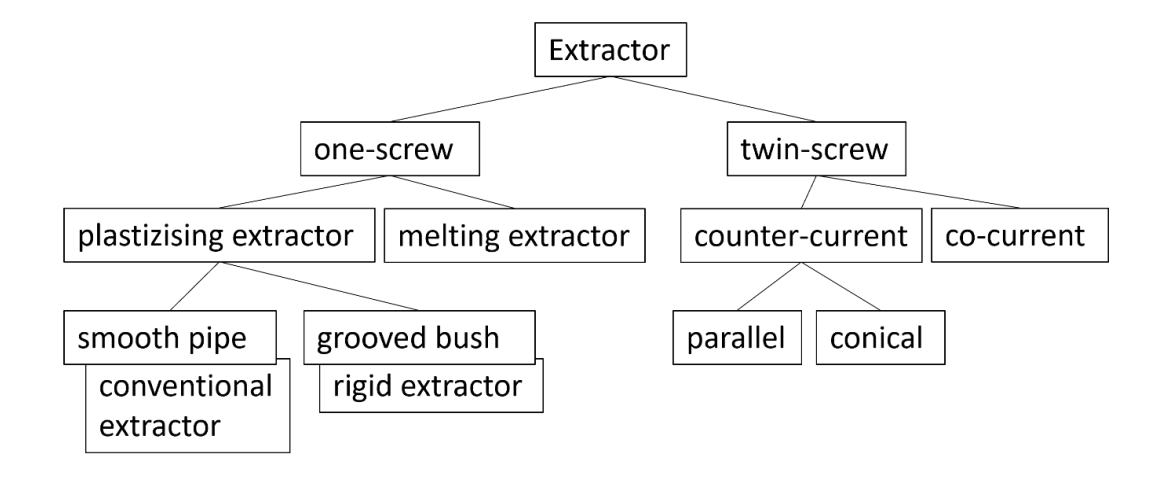


Figure 2-8: Classification of screw extractors, reproduced from [Con08].

For one-screw extractors as used in this thesis the transport efficiency η of solid materials can be estimated [RM94], [RMM93]. The transport efficiency describes the ratio between the actual volumetric flow along the length of the screw \dot{V}_s and the maximum theoretical volumetric flow \dot{V}_{th} following Eq. (2-45).

$$\eta = \frac{\dot{V}}{\dot{V}_{th}} = \frac{A \cdot \bar{\tau} \cdot \bar{u}_{ax,exp}}{A \cdot \bar{\tau} \cdot \bar{u}_{ax}} \tag{2-45}$$

The volume flow rate can be expressed by the cross-section area of the extractor A, the mean residence time $\bar{\tau}$ and the specific axial velocity of the material. While the actual volumetric flow \dot{V} can be calculated based on the experimentally examined material velocity $\bar{u}_{ax,exp}$, a characteristic theoretical axial velocity \bar{u}_{ax} of the investigated screw extractor is triggered by the screw angle β , its rotation rate n and the mean screw radius \bar{r} {Eq. (2-46)}. The mean screw radius results from the inner and outer screw diameter as defined in Eq. (2-47) and Figure 2-9.

$$\bar{u}_{ax} = n \cdot \bar{r} \cdot \tan(\beta) \tag{2-46}$$

$$\bar{r} = \frac{D_{out} + D_{in}}{4} \tag{2-47}$$

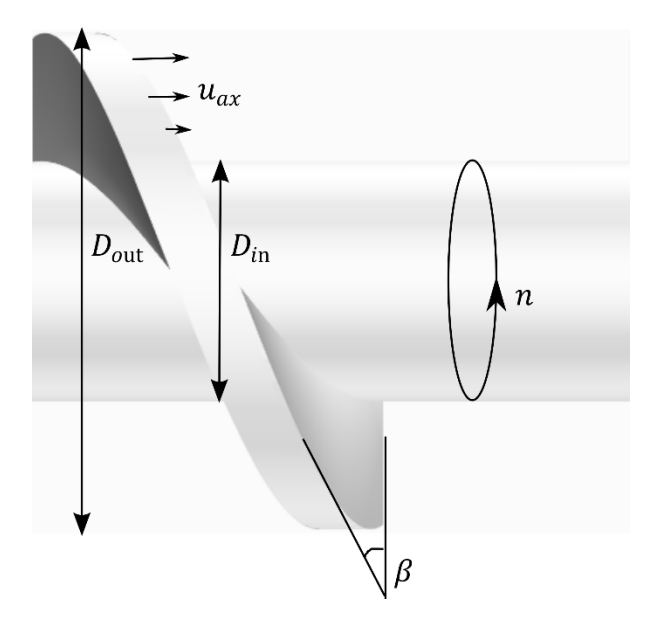


Figure 2-9: Theoretical axial velocity at one screw element.

The transport efficiency is an important quantity to evaluate the reactor design according to the transportation of solid material through the screw reactor.

3 Experimental investigations

The characterisation of the counter-current process is very important for the development and validation of a suitable CFD model. Material properties as well as process conditions and steady-state operating points are of high interest. Although Vu has already performed a steady-state operation with a steel extractor, optical observations as well as material sampling from inside the process could not be realised due to safety requirements coming with the solvent, toluene [Vu23]. This chapter presents the main results of experimental investigations in a self-constructed glass extractor, based on the steel setup of Vu. This glass extractor represents a simplified counter-current extraction process by using water as solvent. The main important scientific questions in this chapter are as follows:

Scientific questions:

- 1. How can a steady-state counter-current extraction process be operated and what are the material properties, phase distributions and possible optimisation potentials during this operation?
- 2. What are the residence time distributions for the phases involved in a steady-state operation and how do they characterise the reactor?
- 3. Are the hydrodynamic results obtained with water as solvent transferable to the extraction process using the solvent toluene?

3.1 Design of the extraction device and counter current flow

A screw-based solid-liquid extractor has first been developed at the Max-Planck Institute for Dynamics of Complex Technical Systems Magdeburg. This counter-current mode extractor enhances the extraction efficiency of the valuable substance artemisinin from A. annua leaves compared to conventional batch extraction methods. At the Otto von Guericke University, a second screw-based extractor has been constructed for detailed optical investigations, shorten in length by factor 2 (Figure 3-1). It consists of a transparent acrylic glass tube measuring a total length of L = 320 mm with an inner diameter of 29.7 mm, housing a screw. The screw is constructed from a central cylindrical rod with an inner diameter of D_{in} = 14 mm. The 3 mm thread is extending up to 14.5 mm from the rotation axis, spiralling around the rod at an original screw angle of β = 67.5°. This results in an outer screw diameter of D_{out} = 29 mm. The original screw (OS), used as the reference (ref.) case, consists of s = 9.14 screw segments with a pitch length of α = 35 mm. The screw geometry has been modified in this work according to its screw angle resulting in the modified screws MS 1 and MS 2 (Figure 3-2 and Table 3-1). The screw was produced using an in-house 3D stereolithography (SLA) printer (Form 3L, FormLabs, Berlin, Germany) and clear resin (V4, FLGPCL02, FormLabs, Berlin, Germany). For the curing process, the screw was exposed to ultraviolet light at a controlled temperature of 60°C for 30 min. Finally, the screw's surface was refined using various grades of sandpaper and cleaned with water. The identical design of all screw geometries results in a 0.35 mm gap between the screw's boundary and the reactor wall. The total fluid volume of the extractor excluding inlets, outlets and the screw geometry equals $V_{tot} = 1.59 \cdot 10^{-4} \,\mathrm{m}^3$ for OS.

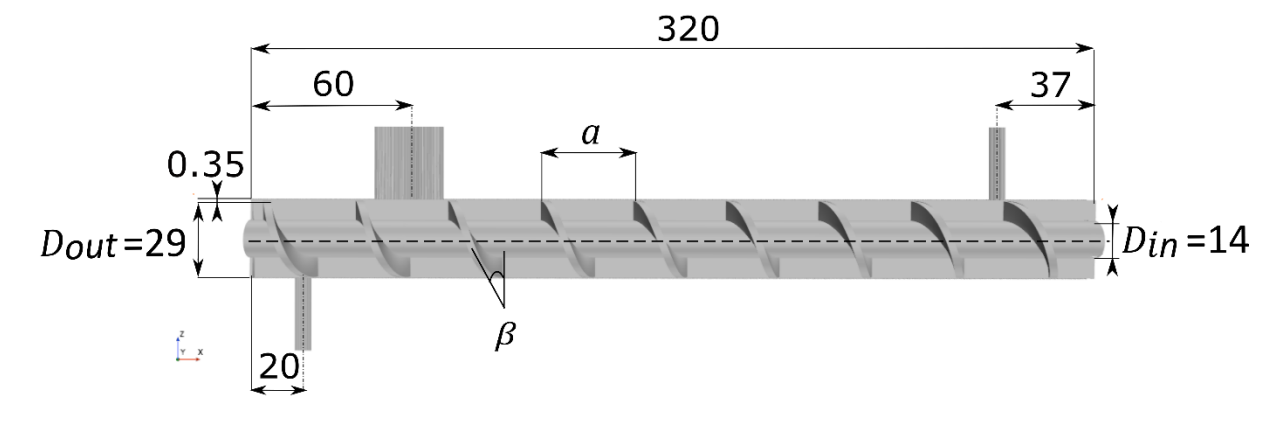


Figure 3-1: Dimensions of the screw extractor (in mm). The variable α denotes the segment length and β the specific screw angle, reproduced from [LVJ+23].

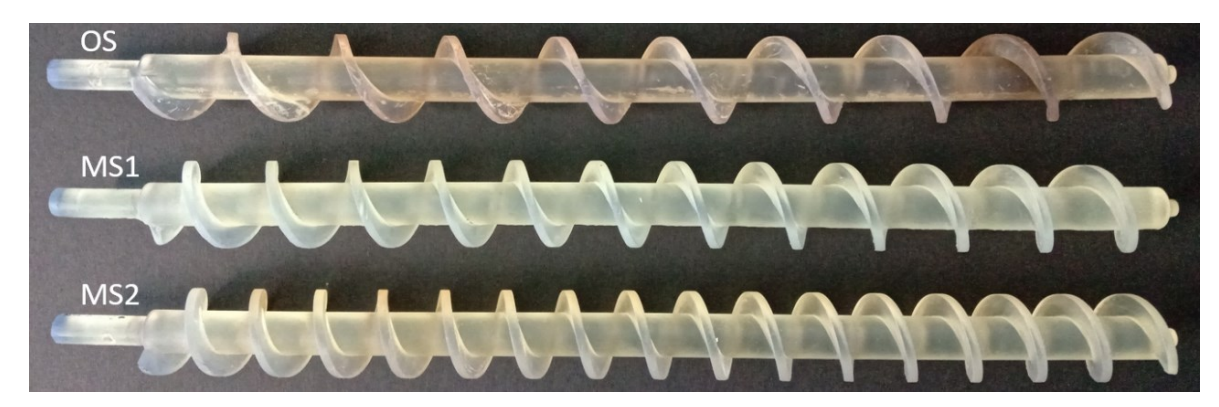


Figure 3-2: Original (OS) and modified screws (MS 1, MS 2). The modified screws result from a decrease of the screw angle, as shown in Table 3-1.

Table 3-1: Characterising parameters for the three screw geometries and resulting free volume in the extractor, excluding inlets and outlets.

	. 0				
Parameter		OS (ref)	MS 1	MS 2	Unit
screw angle	β	67.5	60.8	54	0
segment length	а	0.035	0.026	0.02	m
number of screw segments	S	9.14	12.31	16.00	-
free volume in the extractor	V_{tot}	1.59	1.54	1.49	· 10 ⁻⁴ m³

The extractor is sealed by a shaft seal at one end, which also centrally guides the extraction screw in the device. At the other end of the system, the screw is housed in a perforated disk (PD) including 18 holes with a diameter of 5.5 mm each (Figure 3-3 a). The exact dimensions are shown in the appendix, Figure A-1. The PD enables a counter-current flow of leaves and solvent as shown in Figure 3-3 b and described more detailed at the end of this section.

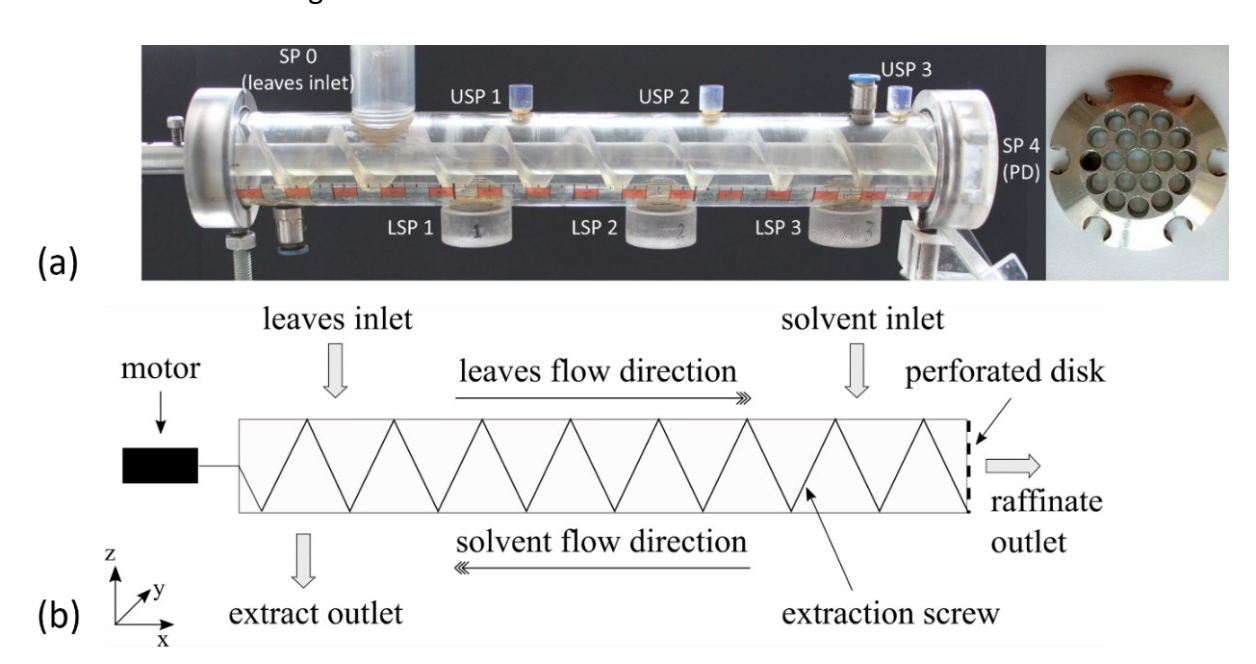


Figure 3-3: (a) Glass extraction device (left) and perforated disk (PD) in a front view (right). SP 0-leaves inlet, USP-upper sampling points, LSP-lower sampling points, SP 4- raffinate outlet at PD, (b) schematical representation of the process key features, reproduced from [LVJ+23].

To characterise the process conditions and the solvent-soaked material during a steady-state operation, the extraction device includes multiple sampling points (SP) positioned at the upper side (USP 1-3) and lower side (LSP 1-3) of the glass tube, as well as at the perforated disk (SP 4). While the USPs will later be used for pressure measurements, the LSPs enable material sampling and solid phase RTD measurements. Table 3-2 provides a summary of the diameter and position of each sampling point, including a dimensionless length x/L, where L is the total reactor length.

Table 3-2: Diameter and axial location of the upper and lower sampling points in the screw extractor. Location x = 0 defines the left wall of the extractor (shaft seal) and L characterises the total extractor length (L = 320 mm)

Upper sampling point	diameter D (m)	centre at x (m)	dimensionless length x/L
SP 0 (leaves inlet)	0.026	0.06	0.188
USP 1	0.008	0.12	0.375
USP 2	0.008	0.2	0.625
USP 3	0.008	0.28	0.875
SP 4 (PD)	0.005	0.32	1
Lower sampling point			
LSP 1	0.02	0.1	0.313
LSP 2	0.02	0.18	0.563
LSP 3	0.02	0.26	0.813

Based on the dimensions of the screw extractor in Figure 3-1 the flow length of solid material from leaves inlet (x = 0.06 m) to raffinate outlet (x = L = 0.32 m) equals a value of $L_s = 0.26$ m while the flow length of liquid solvent from solvent inlet (x = 0.32 - 0.037 = 0.283 m) to extract outlet (x = 0.02 m) equals $L_l = 0.263$ m.

The descripted glass extraction device operates continuously in a counter-current mode, with materials introduced at opposite ends. The experimental setup including all used devices is shown in Figure 3-4.

Solid material is introduced into the extractor using a separate screw feeder (DSR28, Brabender, Duisburg, Germany) (1) which is controlled by a monitor (2). Inside the feeder, an internal screw (1a) conveys the A. annua leaves axially, allowing them to fall into the extractor (3) under the influence of gravity. The transported mass flow rate of dry leaves varies slightly over time, as it is typical for solid materials, but stable on average within a range of ± 0.02 g/min. Subsequently, the screw within the extractor driven by a motor (4) (801495)

TNi21, Crouzet GmbH, Düsseldorf, Germany) located at one end of the device transports the leaves towards the perforated disk. The solvent, stored in a small tank (5), is injected here using a frequency-controlled peristaltic pump (6) (PD-5201, Heidolph, Kelheim, Germany). This pump allows a stepwise selection of flow rates.



Figure 3-4: Experimental setup for the glass extractor. 1 - screw feeder of leaves, 2 - monitor controlling the feeder, 3 - glass extractor, 4 - motor, 5 - solvent tank, 6 - peristaltic pump.

The screw transport of the leaves assists in solvent absorption along the entire length of the extractor. This process results in the formation of a compression cake at the perforated disk, which, in turn, increases the pressure at the raffinate outlet, preventing solvent outflow. As a result, the solvent flows counter-currently to the leaves, similar to the previously shown flow scheme (Figure 3-3 b). Details regarding the stability limits necessary to maintain steady-state operation will be discussed in section 3.4.

3.2 Characterisation of used materials

The investigated extraction process involves three distinct phases: dry A. annua leaves, water as the solvent, and a mixed phase of solvent-soaked A. Annua leaves formed during the steady-state process. This mixed phase possesses markedly different properties compared to the initial phases and requires a dedicated consideration.

3.2.1 Dry A. annua leaves

In this study, a 100 kg batch with dried A. annua leaves, a small amount of stems and no roots were provided by the Max Planck Institute Magdeburg, coming originally from Médiplant, Conthey (Switzerland). The raw material and the particle size distribution are shown in Figure 3-5.

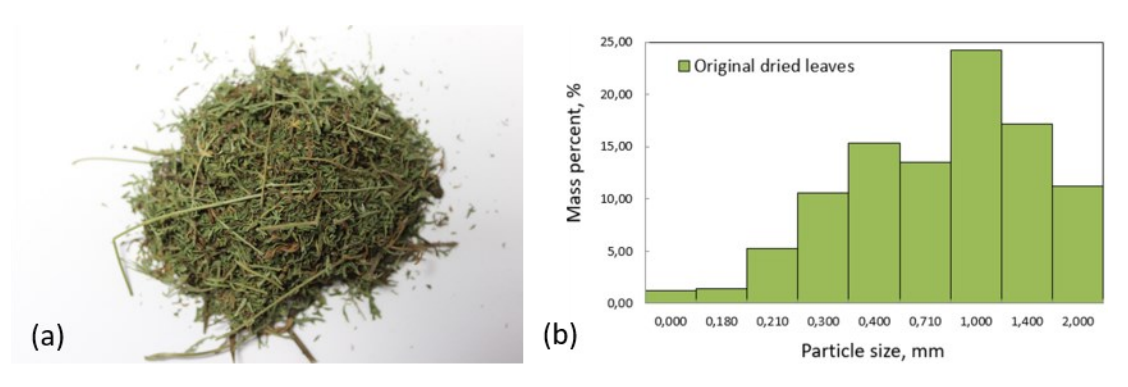


Figure 3-5: (a) A. annua leaves (raw material), (b) particle size distribution, reprinted from [Vu23].

Using a centrifugal milling machine (ZM-200, Retsch, Haan, Germany) the particles were pulverised (Figure 3-6 a). This reduction in particle size results in higher superficial areas while decreasing the inter-particle diffusion pathways due to rupture of organs, tissue and cell structures. Both facts enhance the extraction rate of active components. Too small particles should be avoided since they reduce the process efficiency again due to bed compression. Vu selected a particle size distribution of 0.09 - 0.4 mm with a mean particle size of D_p = 0.2 mm as appropriate range to assure mass transfer area, flow channelling and pressure drop [Vu23]. This particle size was kept in this work. As shown in Figure 3-6 (b) the relatively broad particle size range results from two peaks. A sufficient homogenisation of the material is obviously essential to obtain averaged material properties, as well as constant ARTE mass fractions. The averaged ARTE mass fraction in the leaves determined by Vu equals approx. x_s^{in} = 1.3 wt.%. The dry material density was found as ρ_{ds} = 260 kg/m³ [Vu23].

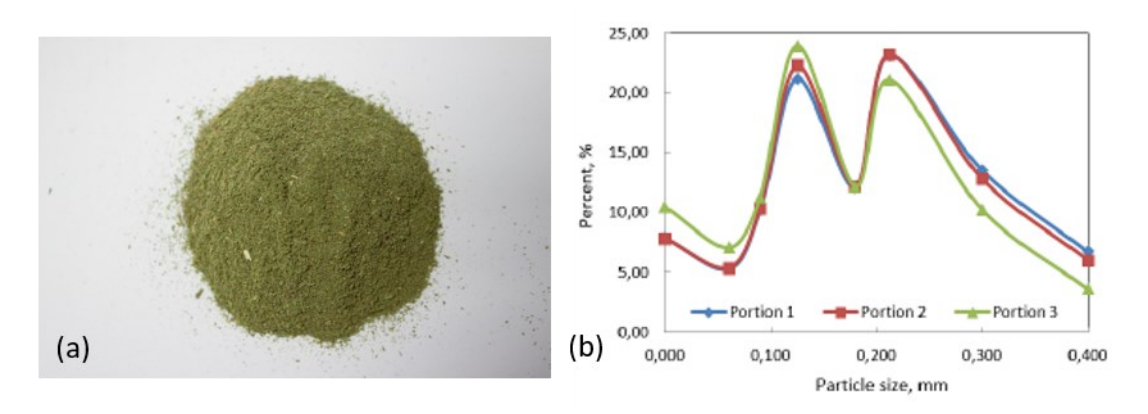


Figure 3-6: (a) grinded A. annua leaves, (b) particle size distribution, reprinted from [Vu23].

3.2.2 Solvent

The selection of the solvent is critically important for effectively extracting artemisinin. It should readily dissolve the compound, be easily available, cost-effective, and non-toxic, which is a crucial consideration in drug production [BP11]. Numerous studies have examined the solubility of ARTE in various solvents, and toluene has shown great promise [LIP09], [Hor19]. However, toluene is easily volatile and forms explosive mixtures in the presence of air [DGU23]. The required safety procedures do not allow for transparent glass setups.

Since the aim of experiments in this thesis is to get more knowledge about the material properties and residence time distribution during the extraction process by optical and hydrodynamical measurements, water has been selected as solvent for simplification.

Compared to toluene, the solubility of ARTE in water is significantly lower [WSC+07], [HFS+06] and extraction processes cannot be explored visually. A crucial factor influencing hydrodynamic characteristics is the Reynolds number Re {Eq. (3-1)}. Here, u is the characteristic velocity of the fluid, L_{ch} the characteristic length of the investigated geometry (reactor diameter), ρ the density of the fluid and μ the dynamic viscosity, or v the kinematic viscosity ($v = \mu/\rho$).

$$Re = \frac{u L_{ch} \rho}{\mu} = \frac{u L_{ch}}{v}$$
 (3-1)

When using equipment with identical diameter and screw rotation speeds, as in this work, the difference in Reynolds number between toluene and water as solvents is solely due to their distinct kinematic viscosities v. Specifically, at 20° C, toluene's kinematic viscosity $(0.68 \cdot 10^{-6} \text{ m}^2/\text{s})$ is only 32% less than that of water $(1.002 \cdot 10^{-6} \text{ m}^2/\text{s})$, as listed in Table 3-3. This indicates that hydrodynamic characteristics obtained using water as a solvent can still

provide a reliable approximation for evaluating real-world operations, where toluene serves as the primary solvent.

Table 3-3: Material properties of water and toluene at a temperature of 20°C [AP23].

Property		water	toluene	Unit
density	$ ho_l$	998	867	kg/m³
dynamic viscosity	μ_l	1	0.59	·10 ⁻³ Pa·s
kinematic viscosity	v_l	1.002	0.68	$\cdot 10^{-6} \text{m}^2/\text{s}$

In subsection 3.6.1 the hydrodynamic properties will even be completely equalised by heating up water to decrease its kinematic viscosity. A possible influence on the RTD behaviour will then be discussed.

3.2.3 Solvent-soaked A. annua leaves

The solvent-soaked leaves come with significantly different properties in density and viscosity compared to dry leaves and need to be considered in a dedicated study. The overall mass flow balance can be defined with Eq. (3-2). When contacting with a liquid solvent the mass of dry leaves m_{ds} absorbs a specific part of liquid solvent m_l into the capillaries. The solvent-soaked leaves named as raffinate (m_{raff}) and the external extract (m_{ext}) exit the process.

$$m_{ds} + m_l = m_{raff} + m_{ext} ag{3-2}$$

The solvent-soaked leaves consist of the dry leave mass and the so-called internal extract m_{int} {Eq. (3-3)}. Similarly, the external extract m_{ext} , containing the valuable substance ARTE, is derived by subtracting the internal extract from the total solvent amount {Eq. (3-4)}.

$$m_{raff} = m_{ds} + m_{int} ag{3-3}$$

$$m_{ext} = m_l - m_{int} ag{3-4}$$

The internal extract m_{int} is determined by a storage factor S_j which defines the amount of solvent j that can be stored in the dry leaves {Eq. (3-5)}.

$$m_{int} = m_{ds} \cdot S_i \tag{3-5}$$

The soaking process and amount of internal extract depend on the solvent and its chemical properties. Consequently, the definition of the storage factor is of high importance.

Storage factor

The storage factor quantifies the amounts of internal and external extract depending on the material properties of dry leaves (ds) and liquid solvent (l). The absorption rate of A. annua leaves was investigated using different masses of leaves m_{ds} ranging from 0.75 g to 6 g with equal amount of solvent $(30\,\mathrm{g})$. The materials have been contacted in a stirred batch reactor for two hours until equilibrium was reached. After phase separation by gravity, the free solvent (external extract) was collected using a syringe, and the amount of internal extract mass (m_{int}) was calculated for all batch processes. Using an interpolation between all measuring points, the storage factor S_j was calculated by the ratio of the internal extract m_{int} and the initial mass of dry leaves m_{ds} following Eq. (3-6), while j indicates the used solvent.

$$S_j = \frac{m_{int}}{m_{ds}} \tag{3-6}$$

As a result, the storage factor for the solvent water $(j = H_2 O)$, as used in this thesis) was determined with $S_{H_2 O} = 4.34$. This implies that one gram of dry leaves can store a mass of 4.34 g water (Figure 3-7). A similar procedure was conducted for the solvent toluene (j = tol) used by Vu, resulting in a storage factor of $S_{tol} = 2.25$, nearly half the value of water [Vu23].

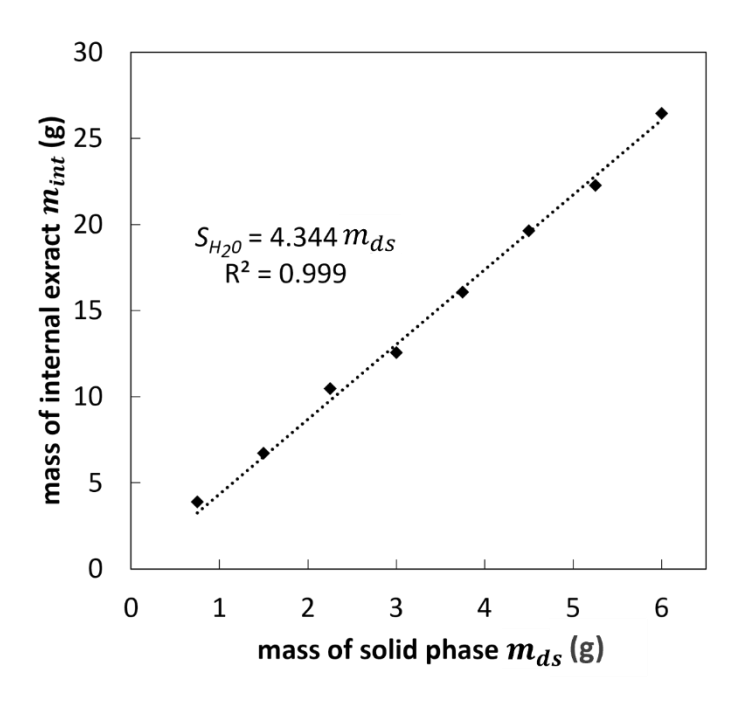


Figure 3-7: Absorption study of dry A. Annua leaves with the solvent water. The final storage factor depends linearly on the mass of internal extract m_{int} and the mass of the solid phase m_{ds} (R² = 0.999). It could be determined with S_{H_2O} = 4.34 according to the slope of the curve.

Density estimation

Understanding the density distribution in the single screw segments during a steady-state operation along the extractor and at the raffinate outlet is crucial for describing the hydrodynamics in later CFD simulations. The estimation of density from compressible bulk material with free pores is quite challenging and based on measurements of mass and volume for specific probes. Thereby, high amounts of probes are required to minimise the occurring measurement error. However, the volume of available sample material in the individual screw segments during a steady state is quite low due to the small reactor size. Consequently, an adjustment based on the bulk humidity H was first performed in the steady-state operation. This mass-based bulk humidity is calculated as a ratio between the internal extract m_{int} and the total mass of the solvent-soaked leaves (m_{raff}) and ranges within the interval [0,1]:

$$H = \frac{m_{int}}{m_{raff}} = \frac{m_{int}}{m_{int} + m_{ds}} \tag{3-7}$$

When the involved phases in a process reached their thermodynamic equilibrium after a long reaction time t_{eq} , Eq. (3-6) and (3-7) can be combined to estimate the solvent-specific bulk humidity of the solvent-soaked leaves H_i with the storage factor S_i .

$$H_j = \frac{S_j}{1 + S_j} \qquad \Rightarrow \qquad S_j = \frac{H_j}{1 - H_j} \tag{3-8}$$

For the solvent water with $S_{H_2\,O}$ = 4.34 the bulk humidity at equilibrium according to Eq. (3-8) equals a value of $H_{H_2\,O}$ = 81 wt.% while the bulk humidity for the solvent toluene with S_{tol} = 2.25 is slightly lower, with H_{tol} = 69 wt.%.

During the continuous counter-current extraction process, reaching thermodynamic equilibrium between the involved phases is highly important for obtaining high extraction efficiencies of ARTE. To quantify if and at which positions this equilibrium is reached, the bulk humidity was measured by sampling solvent-soaked leaves.

After maintaining a steady-state for 30 min (see later details in section 3.4), the solvent-soaked leaves were sampled behind the raffinate outlet for 10 min. The process was then stopped, and the inner material was sampled segment by segment by carefully extracting the screw. Nevertheless, solid material which did not stick to the screw (e.g. dry leaves) could not be sampled accurately since it cannot be assigned to any specific screw segment. This

especially applied for segment 1 where no material was sampled. The collected material of the continuous process and an additional sample of a batch process (2 hours contact time) were dried in a vacuum oven at 80°C for three days to ensure maximum evaporation of the liquid phase. The difference between the initial wet probe (mass of solvent-soaked leaves m_{raff}) and resulting dry mass m_{ds} determined the internal extract mass m_{int} , see Eq. (3-3). The bulk humidity per screw segment, behind the raffinate outlet and for one batch sample were then calculated using Eq. (3-7). They are compared in Figure 3-8.

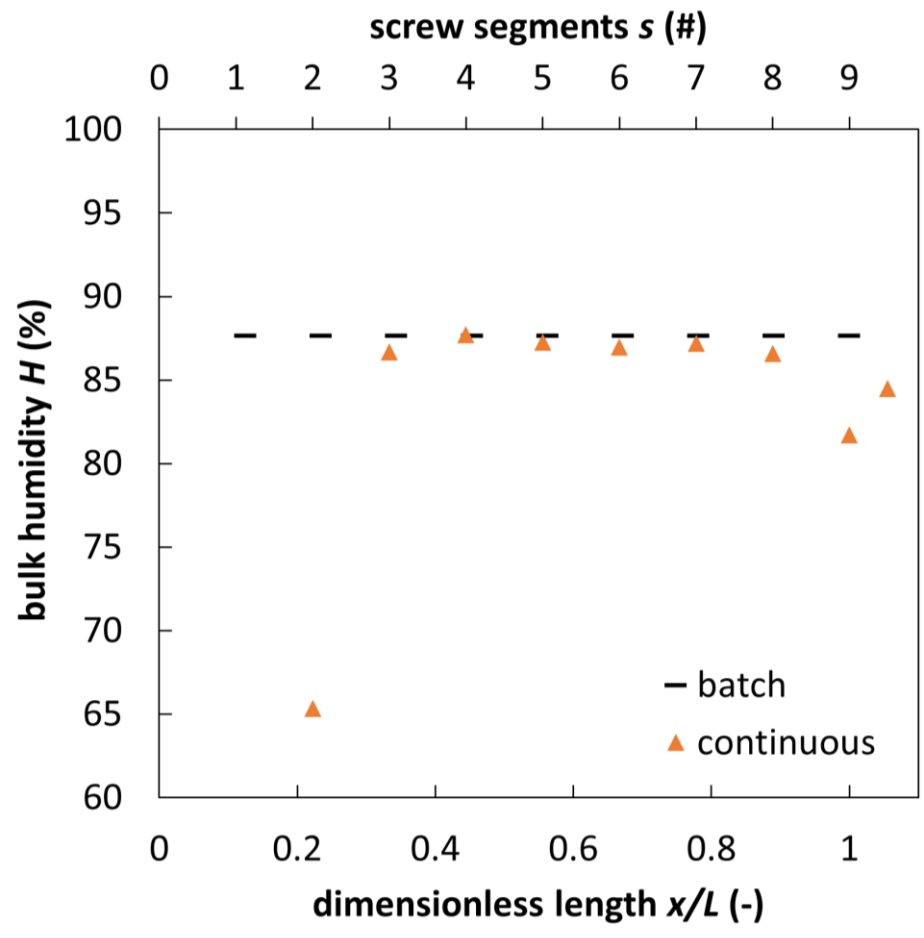


Figure 3-8: Bulk humidity in screw segments, behind raffinate outlet and for one batch process. Segment 1-9 represent the middle screw segments while the raffinate outlet is represented as segment 9.5. A continuous counter-current operation (orange) was compared with a single-stage batch process (black), showing high agreement.

The comparison between batch material and the inner screw material during a continuous process (segments 3-8) shows a high level of agreement (batch: 87.7 wt.%, continuous: 86.6 - 87.2 wt.%). Consequently, the solid leaves reach fast thermodynamic equilibrium with the solvent water when screw rotation and counter-current flow are present. In front of the perforated disk (segment 9) the bulk humidity decreases due to the compression at the

perforated disk resulting in a raffinate bulk humidity of 84.5 wt.% (represented as segment 9.5).

The measured batch bulk humidity of 87.7 wt.% is higher by \approx 8% compared to the previously calculated bulk humidity $H_{H_2\,0}$ based on the storage factor {Eq. (3-8): 81 wt.%}. This discrepancy can be explained by the fact that some of the water is trapped in the pores of the leaves during the drying process inside the oven, preventing it from evaporating. This makes an exact determination of the bulk humidity by drying the probe material unfeasible.

To overcome this, the calculated batch bulk humidity of 81 wt.% with Eq. (3-8) is considered as accurate. Since Figure 3-8 demonstrated that the continuous process bulk humidity is similar to this batch bulk humidity it is set at the same level ($H_{H_2,0} = H_{H_2,0}^{conti} = 81$ wt.%).

The raffinate bulk humidity can be assumed to have an equivalent error between drying oven measurement and reality of \approx 8%. It is estimated with H_{raff} = 84.5 wt.% · (100%– 8%) \approx 78 wt.%. This value for the raffinate is quite similar to the inner extractor value of 81 wt.%.

When assuming the same material bulk humidity for batch and continuous process, also the phase compositions can be considered equivalent. This allows the transfer of the batch density to the continuous process. To measure the batch density, a sample of solvent-soaked leaves with the batch bulk humidity of $H_{H_2\,O}$ = 81 wt.% was placed in cylinders of known volume. The mass of the solvent-soaked A. annua leaves was measured three times, resulting in a mean equilibrium density of $\bar{\rho}_s$ = 922 kg/m³ (Table 3-4).

Table 3-4: Measuring data of soaked-leaves density in a batch process using water as solvent.

mass of dry	mass of	volume of	mass of soaked	density of soaked
leaves m_{ds} (g)	water m_l (g)	cylinder V (cm 3)	leaves m_{raff} (g)	leaves $\bar{ ho_s}$ (kg/m³)
4.6	20	11.8	10.87	921.2
4.6	20	15.3	14.12	922.9
4.6	20	15.6	14.40	923.1

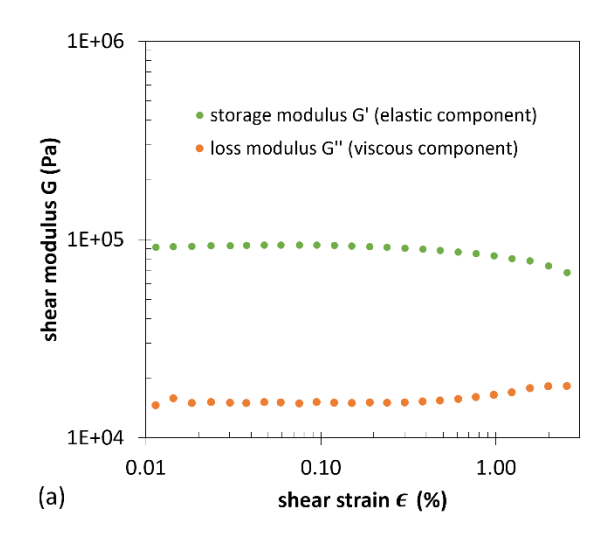
Although sensitive to the bulk humidity, knowing this density is important for later CFD simulations.

Shear viscosity measurement

The dynamic viscosity μ , also known as shear viscosity, is an important parameter for the characterisation of fluids. It is significant in this work in terms of CFD simulations representing the actual solid-liquid flow, where the solvent-soaked leaves are represented as a highly-viscous fluid.

Samples were collected at the raffinate outlet and inner material during a 30-minute steady-state run. Given the stable composition inside the extractor indicated by bulk humidity and density measurements, specific segment sampling was not necessary. The samples were analysed using a KINEXUS pro+ rotational rheometer (NETZSCH, Selb, Germany), with the material placed between a rotating and a stationary plate with a 1 mm gap. Solvent-soaked leaves exhibit intermediate behaviour between ideal elastic solids and ideal viscous fluids, similar to natural materials like soil [GO01]. The amplitude test measures the shear modulus to determine whether liquid or solid properties dominate. Figure 3-9 (a) presents the elastic component G' of the shear modulus with $\approx 10^5$ Pa which is significantly higher than the viscous component $G'' \approx 1.5 \cdot 10^4$ Pa. This indicates that the solvent-soaked leaves behave more like a solid material [Mez14]. This will have consequences for our later numerical model in chapter 4.

The complex component for shear viscosity is calculated by the computerised driver of the rheometer using a frequency test with a range from 0.1 to 50 Hz. According to Mas et al. [MM97], these frequencies correspond to the shear rate γ in the system. The process temperature was set to 20°C. Figure 3-9 (b) shows non-Newtonian shear thinning behaviour for both inner material and raffinate, as shear viscosity μ decreases from $4\cdot10^5$ Pa·s (γ = 0.1 1/s) to 413 Pa·s (γ = 150 1/s) for the inner material. The raffinate viscosity is higher due to lower humidity. For the extraction process, small screw rotation rates below 1/s are needed for fitting extraction kinetics, resulting in very high shear viscosity values for the soaked leaves (μ > 10^3 Pa·s for both raffinate and inner material), comparable to molten glass at its working point [Tes13].



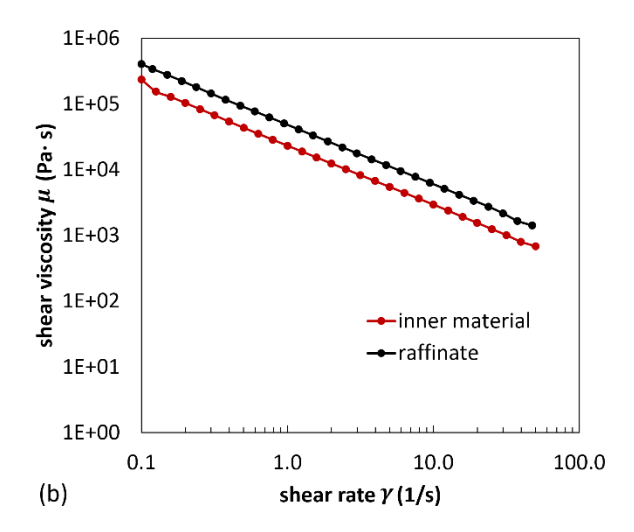


Figure 3-9: Rheological measurements for the solvent-soaked leaves, (a) shear modulus components, (b) shear viscosity of inner material and the raffinate.

As an intermediate conclusion, the viscosity measurements show that the solvent-soaked leaves have primary solid-phase properties. Nevertheless, as a simplification the solvent-soaked leaves can alternatively be represented as highly-viscous fluid in CFD, with a viscosity taken as $\mu_s = 1\cdot 10^3$ Pa·s, also reported in literature [LW12]. Note that higher viscosities generally lead to a divergence of the CFD solver and cannot be considered. Table 3-5 summarises the estimated material properties for dry leaves (ds), solvent-soaked leaves (s) and liquid solvent (l).

Table 3-5: Summary of material properties at $T = 20^{\circ}$ C.

Parameter	Symbol	Value	Unit
particle mean diameter of dry leaves	D_{p}	0.0002	m
density of dry leaves	$ ho_{ds}^{\cdot}$	260	kg/m³
storage factor of water	S_{H_2O}	4.34	kg_l/kg_{ds}
storage factor of toluene [Vu23]	S_{tol}	2.25	kg _l /kg _{ds}
mean density of solvent-soaked leaves	$ar{ ho}_{\scriptscriptstyle S}$	922	kg/m³
bulk humidity of solvent-soaked leaves	$H_{H_2 O}$	81	wt.%
(equilibrium = continuous)	1120		
bulk humidity of raffinate	H_{raff}	78	wt.%
shear viscosity of solvent-soaked leaves	$\mu_{\scriptscriptstyle S}$	1·10 ³	Pa∙s

3.3 Selected results to estimate extraction kinetics in toluene

As stated previously, the solvent water used for the hydrodynamic experiments and later CFD model validation cannot extract artemisinin efficiently. For the actual extraction of ARTE the solvent toluene is suitable and used by Vu [Vu23]. The extraction kinetics between the feed material and the solvent can be measured in simplified batch experiments. These experiments deliver the required contact time for reaching equilibrium between the materials. In a continuous process, the mean residence time of the phases must be adapted to this equilibrium time. If the mean residence time is too short to allow for sufficient extraction, the yield will be poor [GWB00]. Consequently, the knowledge about the residence time is important for adapting the reactor design. This will be discussed later.

The extraction kinetics were determined in cooperation with Vu by repeating several batch processes with the immersion method [Vu23]. While the solvent mass of toluene m_l has been set constant to 30 g, the mass of solid leaves m_{ds} has been varied resulting in solid-liquid ratios R {Eq. (3-9)} between 0.05 and 0.3. The maximum limit is restricted by the reciprocal of the soaking factor 1/S {Eq. (3-6)}. When the solid phase absorbs all the liquid solvent (internal extract), there will no longer be any external extract and the extraction cannot be performed efficiently. Since S is solvent-specific as described in subsection 3.2.3 the limit of R for toluene (S_{tol} = 2.25) must be lower 0.4 and for water ($S_{H_2,O}$ = 4.34) lower than 0.2.

$$R = \frac{m_{ds}}{m_l} = \frac{\dot{m}_{ds}}{\dot{m}_l} \tag{3-9}$$

During the extraction process with the solvent toluene, samples with volume of 1 ml have been collected at specific times (after 2, 5, 10, 30, 60, 120, 180 min). Finally, a probe was taken after a total time of 18 hours (1080 min) assuming complete extraction. These samples have been later analysed by a HPLC-ELSD system (Agilent 1100 High Performance Liquid Chromatography (HPLC) system with Evaporative Light Scattering Detector (ELSD) combined with gradient mobile phase, Agilent Technologies). Figure 3-10 shows the ARTE mass fraction in the extract. After a reaction time of 10 min the mass fraction is nearly stable for all curves indicating an equilibrium. With increasing solid-liquid ratio the content of extracted artemisinin increases. Simultaneously, the amount of external extract which can be collected becomes lower due to the soaking of leaves with solvent. A solid-liquid ratio of 0.1 was defined as optimum by Vu [Vu23]. The maximum extractable amount of ARTE, assumed after the total

runtime of 18 h, was used to estimate the extraction rate by a second-order kinetic model resulting in k_E = 0.05 1/min [Vu23]. The thermodynamic equilibrium constant from the (equilibrium) extract and raffinate mass fractions was calculated as K_E^{eq} = 0.4 using Eq. (2-6) [Vu23]. Both constants are applied in the kinetic model discussed in chapter 5.

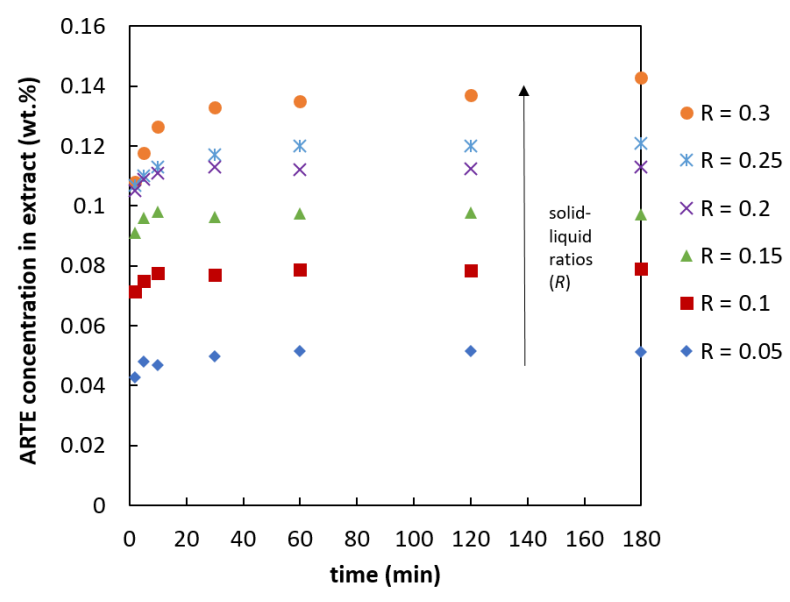


Figure 3-10: Mass fraction of ARTE in the extract during batch extraction with toluene. A range of solid-liquid ratios R was examined from 0.05 to 0.3. The extraction rate and thermodynamic equilibrium constant resulted as $k_E = 0.05$ 1/min and $K_E^{eq} = 0.4$, reproduced from [Vu23].

Table 3-6 quantitatively normalises the maximum extractable amount of ARTE using a range of the solid-liquid ratio of R = 0.05 - 0.15. After 10 minutes, already more than 90% of extractable ARTE is reached in batch extraction for all values of R. For the optimal solid-liquid ratio R = 0.1, 97.4% is reached. These experiments suggest an equilibrium time of $t_{eq} \approx 10$ min, crucial for matching ARTE-toluene extraction kinetics. This contact time must be reached in continuous extraction as a mean residence time for optimal process design.

Table 3-6: Normalised extraction efficiency of artemisinin in %. Measurements have been performed in batch processes with A. annua. leaves and toluene as solvent. Reference (ref) mass fractions of extractable artemisinin $x_l(R)$ = 0.052 (0.05), 0.080 (0.1), 0.098 (0.15) [Vu23].

time t (min)	solid-liquid ratio R {Eq. (3-9)} (kg/kg)			
	0.05	0.1	0.15	
2	82.8	89.7	92.6	
5	92.8	94.1	97.7	
10	90.5	97.4	99.7	
30	96.3	96.6	98.0	
60	99.4	98.9	99.2	
120	99.4	98.5	99.5	
180	99.0	99.2	99.0	
1080 (ref)	100.0	100.0	100.0	

3.4 Continuous steady-state operation

This section is partly based on:

[LVJ+23]

Lehr, A.; Vu, G. T.; Janiga, G.; Seidel-Morgenstern, A.; Thévenin, D.: Experimental investigation of the residence time distribution in a screw-type apparatus designated to extract artemisinin. Chemical Engineering and Processing - Process Intensification 187, 109337, pages 1 - 10, 2023.

Optimising the counter-current flow requires a deeper understanding of steady-state process conditions. Therefore, it is essential to identify continuous steady-state operation points as well as the key influencing parameters. Particularly, it is important to ensure that the phase residence times align with the extraction kinetics studied in the batch method (section 3.3).

3.4.1 Operation window

The stability of the examined process is a major advantage over batch processes. The definition of an operating window provides important information about the process sensitivity and helps to optimise the process. Before achieving a steady-state process, a start-up procedure must be performed to build up the extraction cake on the perforated disk. This step is essential for enabling the solvent to flow counter-current to the leaves, which is a critical aspect of the process in this project. The start-up procedure was developed by Vu [Vu23], as follows.

Starting procedure

To ensure correct inlet conditions, the mass flow of leaves transported by the feeder is always calibrated for 10 minutes before experiments are started. After three segments were completely filled with dry A. annua leaves by hand, the feeder and motor were started. When the dry leaves reach the solvent inlet position, the solvent pump is started incrementally at low solvent mass flow rate (12.9 g/min) for five seconds at 30 s intervals. This allows the leaves to slowly soak the solvent and build up an extraction cake on the perforated disk. After all holes in the disk are blocked by soaked leaves (detected after 5 min of pumping), the solvent pump is started continuously at the desired mass flow rate.

Continuous operation

The continuity of the investigated process is a main advantage compared to batch process. The observation of hydrodynamics inside the counter-current extraction process is performed during a steady-state where the mass flow rate balance of incoming solid and liquid phases $(\dot{m}_{ds}, \dot{m}_l)$ matches the combined outlets for raffinate and extract $(\dot{m}_{raff}, \dot{m}_{ext})$. The mass flow balance is similar to the previously introduced mass balance in a batch process {Eqs. (3-2) to (3-5)}. The mass fluxes are visualised in Figure 3-11 by neglecting the compression process at the perforated disk.

For an ideal steady-state operation, the mass flow rates of extract and raffinate at equilibrium can be calculated based on the inflow rates and the internal extract \dot{m}_{int} using Eqs. (3-11) and (3-12). The internal extract results from the solvent-specific storage factor (for water $S_{H_2\,0}=4.34$) and the mass flow of the dry leaves \dot{m}_{ds} {Eq. (3-13)}, as already introduced in subsection 3.2.3. It has to be noticed that due to the compression at the perforated disk the bulk humidity H_{raff} and thus the storage factor inside the extraction cake at the perforated disk is decreasing. This effect leads to discrepancies between the actually measured raffinate mass flow and the calculated value by Eq. (3-11). According to Table 3-5 the batch bulk humidity inside the extractor ($H_{H_2\,0}=81$ wt.%) and the raffinate bulk humidity ($H_{raff}=78$ wt.%) are quite similar, so that this effect can be neglected in further investigations.

$$\dot{m}_{ds} + \dot{m}_l = \dot{m}_{raff} + \dot{m}_{ext} \tag{3-10}$$

$$\dot{m}_{raff} = \dot{m}_{ds} + \dot{m}_{int} \tag{3-11}$$

$$\dot{m}_{ext} = \dot{m}_l - \dot{m}_{int} \tag{3-12}$$

$$\dot{m}_{int} = \dot{m}_{ds} \cdot S_j \tag{3-13}$$

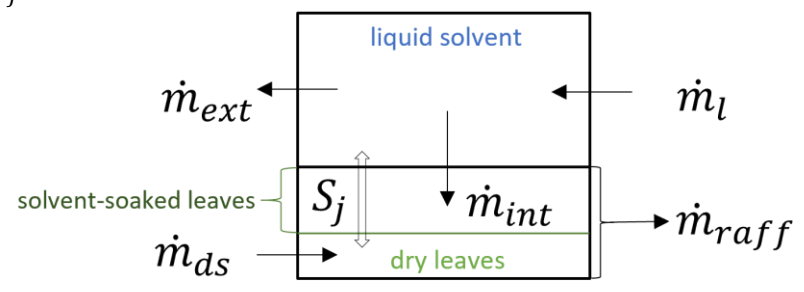


Figure 3-11: Mass fluxes in a continuous steady-state process, neglecting the extraction cake. The incoming dry leaves (\dot{m}_{ds}) soak a specific part of the liquid solvent (\dot{m}_l) according to the solvent-specific storage factor (S_j) , forming the internal extract (\dot{m}_{int}) . The raffinate mass flow (\dot{m}_{raff}) is the sum of dry leaves and the internal extract. The extract mass flow (\dot{m}_{ext}) is the external extract representing the solvent inlet flow \dot{m}_l reduced by the internal extract.

For reaching a stable counter-current flow, two critical regions inside the extractor have to be considered (Figure 3-12). These are: (1) the region in front of the perforated disk, where the extraction cake forms due to compression, and (2) the area below the leaves inlet, where dry leaves are introduced into the process and agglomerate as a result of the soaking process.

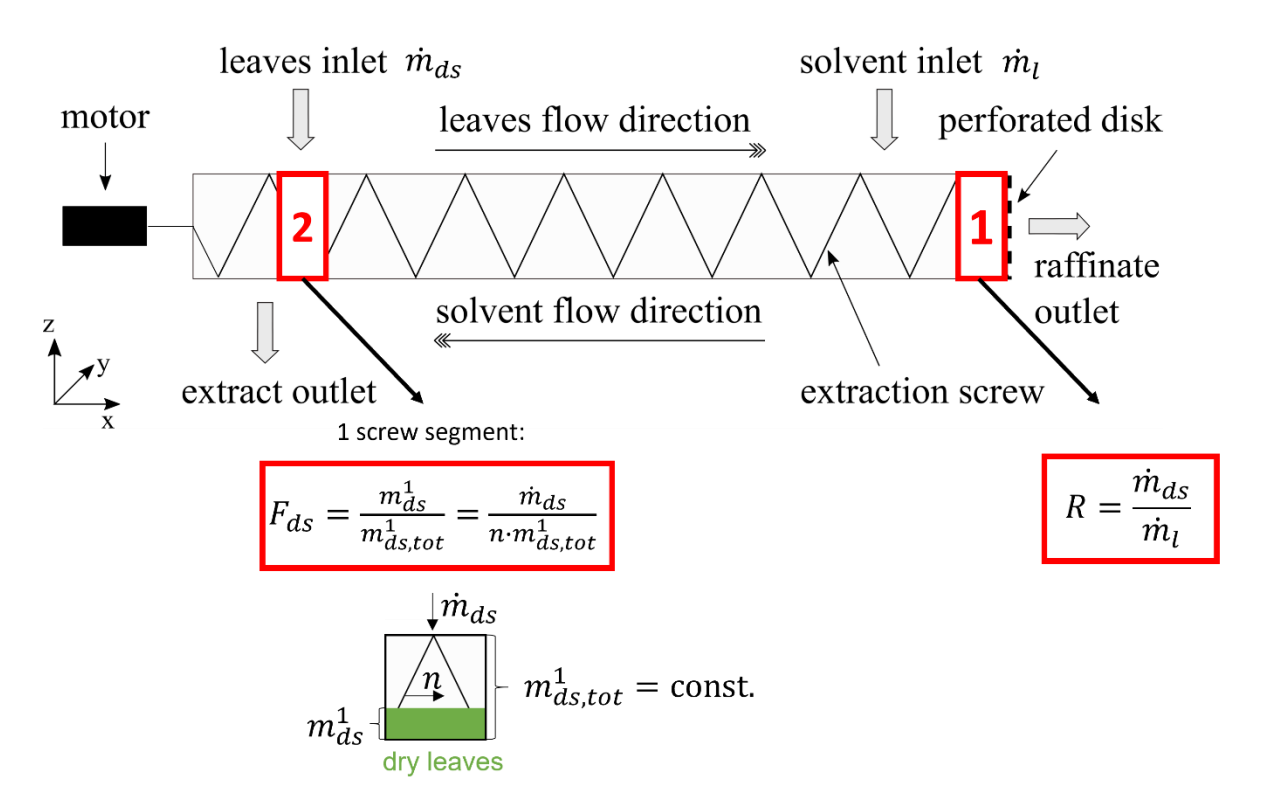


Figure 3-12: Critical regions in the extractor influencing the stability of the continuous process, (1) in front of the perforated disk, quantified by the solid-liquid ratio R, (2) below the area of the leaves inlet quantified by the filling degree of dry leaves F_{ds} .

The stability at the critical region (1) can be quantified using the previously defined **solid-liquid** ratio R {Eq. (3-9)}.

$$R = \frac{\dot{m}_{ds}}{\dot{m}_{t}}$$

It significantly influences the establishment and stability of the extraction cake forming at the perforated disk. On the one hand, high values of R indicate an excess of leaves compared to solvent. This results in a too low bulk humidity of the extraction cake compared to stable operation conditions. Consequently, a compact dry cake is formed, leading to a blockage at the PD which will stop the continuous process. Additionally, the amount of extract is reduced. On the other hand, low values of R indicate an excess of solvent compared to leaves. The resulting high bulk humidity level at the PD leads to liquid-like properties of the extraction

cake, preventing the formation of a stable cake. Additionally, the mass fraction of extracted artemisininin the resulting high extract mass flow rate is low. In batch processes using toluene as solvent, the solid-liquid ratio was found to be optimal at a value of 0.1.

Nevertheless, process stability is not automatically achieved by fixing the solid-liquid ratio at its optimal value. Instead, it also depends on the screw rotation rate n and the inserted mass of dry A. Annua leaves \dot{m}_{ds} . Difficulties arise especially in the critical region (2) when a large mass of leaves is introduced at a low screw rotation rate n (e.g. for a full-filling of the extractor). Upon contact with the solvent, the excess leaves become solvent-soaked, accumulate, and pile up near the inlet, ultimately blocking the process. Similarly, a lack of solid material inside the extractor due to low solid mass flow rates at higher screw rotation rates prevents an appropriate build-up of the extraction cake near the PD. Consequently, there is a need for defining a relation between the mass flow rate of dry leaves introduced to the process and the screw rotation rate.

The geometrically based **filling degree of dry leaves** F_{ds} quantifies the stability in the critical region (2) (Figure 3-12) by considering this relation based on one screw segment (s=1) and normalising it to the total screw segment capacity $m_{ds,tot}^1$. It ranges within the interval [0,1]: For s=1:

$$F_{ds} = \frac{m_{ds}^1}{m_{ds,tot}^1}$$
 (3-14)

with

$$m'_{ds} = \frac{\dot{m}_{ds}}{n}$$
 $[n] = 1/s$ for $n = 1$: $m^1_{ds} = m_{ds}$ (inlet mass of dry leaves) (3-15)

The total mass capacity $m^1_{ds,tot}$ in one screw segment can be derived from the total extractor volume V_{tot} , the number of screw segments s (both in Table 3-1) and the dry leaves density ρ_{ds} (Table 3-5). For OS this value becomes a constant of $m^1_{ds,tot}$ = 4.52·10⁻³ kg according to Eq. (3-16).

$$m_{ds,tot}^1 = \frac{V_{tot} \cdot \rho_{ds}}{s} \stackrel{os}{\Rightarrow} \frac{1.59 \cdot 10^{-4} \text{ m}^3 \cdot 260 \text{ kg/m}^3}{9.14} = 4.52 \cdot 10^{-3} \text{ kg}$$
 (3-16)

Based on Eq. (3-17), the screw rotation speed n depends linearly on the mass flow rate of dry leaves \dot{m}_{ds} while the filling degree of dry leaves in one screw segment F_{ds} represents the inverted slope.

$$n = \frac{1}{F_{ds} \cdot m_{ds,tot}^1} \cdot \dot{m}_{ds} \qquad m_{ds,tot}^1 = \text{const.}$$
(3-17)

The parameter F_{ds} is exclusively employed as a measure of stability in the critical region (2), rather than for the characterisation of the extractor.

By varying these parameters for more than 30 experimental runs within bounds listed in Table 3-7, a range of continuous operation at steady-state was identified, which corresponds to the black-marked points in Figure 3-13. The red-marked points represent failed operation, at which either an unstable compression cake or a full blockage was obtained. Therefore, continuous operation is only possible for a specific range of solid-liquid ratio R (x-axis), mass flow rate of leaves \dot{m}_{ds} (depending on R) (y-axis), and screw rotation speed n (depending on F_{ds}) (z-axis). This area is shown with a green cylinder limited by unsuccessful operation points on all sides. The extractor should be preferably operated near the centre of the green volume. The continuous operation point used in further experiments is marked with a black circle and will be discussed further in subsection 3.4.2.

Table 3-7: Range of experiments for finding steady-state operation. The dependency of mass flow rate of leaves and screw rotation speed through the constant mass of dry A. annua leaves in one segment $\{m_{ds,tot}^1 = 4.52 \cdot 10^{-3} \text{ kg, Eq. (3-17)}\}$ needs to be kept in mind.

<u> </u>	Ο/ I \	,,		
Parameter		Value		Unit
		lower limit	upper limit	
mass flow rate of dry leaves	\dot{m}_{ds}	0.08	0.25	$\cdot~10^{-4}~\text{kg/s}$
mass flow rate of solvent	\dot{m}_l	1.75	4.42	$\cdot~10^{-4}~ ext{kg/s}$
solid-liquid ratio	R {Eq. (3-9)}	0.03	0.1	kg/kg
screw rotation speed	n	1	3.1	rpm
filling degree of dry leaves in	E (Fa (2.14))	0.044	0.265	
one segment	F_{ds} {Eq. (3-14)}	0.044	0.265	-

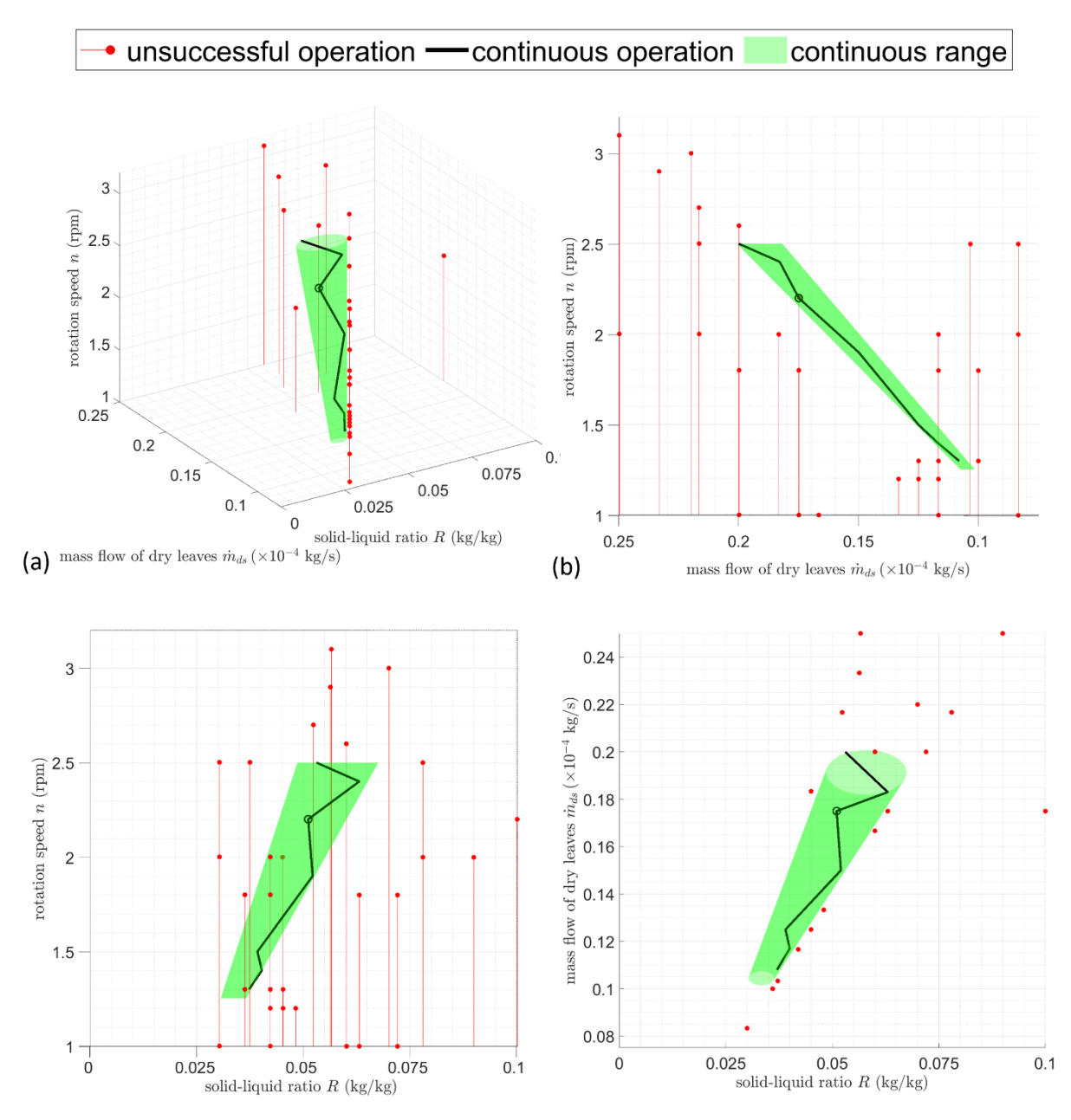


Figure 3-13: Operation window for the counter-current process. Successful continuous operation (black line) and unsuccessful operation (red points) of the extractor as function of (a) solid-liquid ratio R (x-axis), mass flow of dry A. annua leaves \dot{m}_{ds} (y-axis), and screw rotation speed n (z-axis), projection along (b) y-z-axis, (c) x-z-axis and (d) x-y-axis. The identified exploitable operation window is marked by the green area and a reference point used for further experiments in the following sections is marked with a black circle.

The upper (UL) and lower limit (LL) of the defined cylinder-shaped operation window are listed in Table 3-8. The limits for steady-state operation are interdependent. For example, operating the process at all explored lower limits may not necessarily result in a steady-state process. As explained previously, the mass flow rate of dry leaves \dot{m}_{ds} and the screw rotation speed n are connected by Eq. (3-17). The filling degree of dry leaves in a screw segment F_{ds} appears

to be very low at $\approx 0.11 = 11$ %. This value is only used as a measure of stability and not to characterise the extractor filling degree. It does not take into account the occupied mass of solvent, the solvent-soaked leaves or the compression at the PD, which all affect the total retention volume in the extractor. This retention volume will be analysed in section 3.4.6.

Table 3-8: Identified exploitable limits for successful steady-state operation. The dependency of mass flow rate of leaves and screw rotation speed through the constant mass of dry A. annua leaves in one segment $\{m_{ds,tot}^1 = 4.52 \cdot 10^{-3} \text{ kg}, \text{Eq. (3-17)}\}$ needs to be kept in mind. Due to this dependency the table can only be read from left to right and not from top to bottom.

Parameter		Value		Unit
		lower limit	upper limit	
		(LL)	(UL)	
mass flow rate of dry leaves	\dot{m}_{ds}	0.108	0.200	$\cdot~10^{-4}~\text{kg/s}$
mass flow rate of solvent	\dot{m}_l	1.75	4.42	$\cdot~10^{-4}~{ m kg/s}$
solid-liquid ratio	R {Eq. (3-9)}	0.037	0.063	kg/kg
screw rotation speed	n	1.3	2.5	rpm
filling degree of dry leaves	E (Fa (2.14))	0.101	0.110	
in one segment	F_{ds} {Eq. (3-14)}	0.101	0.110	-

The lower limit of the leaves mass flow is not related to stability, but rather corresponds to the minimum capacity of the screw feeder used to convey the dry leaves to the extractor. Since high productivities of the extraction process can only be reached with a high throughput of A. annua leaves, the lower region has not been further explored, being irrelevant.

3.4.2 Operation points for further investigations

For investigating a steady-state process in more details three operation conditions with parameters shown in Table 3-9 have been selected. Based on the mass flow rate of dry leaves the operation point (OP) 1 equals the defined lower limit (LL) of the operation window concerning the mass flow rate of dry leaves while OP 3 represents the upper limit (UL). OP 2 is preferentially used in this thesis due to its central position in the defined operation window as shown in Figure 3-13 (black circle). It is called as reference (ref) case. It has to be noted that the solid-liquid ratio R was found to be lower for OP 1 compared to OP 2 and OP 3 indicating a higher amount of the liquid solvent. Based on the screw rotation speed n, the theoretical axial velocity $\bar{u}_{ax,th}$ can be calculated by Eq. (2-46) and is included in Table 3-9.

Table 3-9: Selected operating parameters for RTD measurements.

Parameter		Operation p	Operation point (OP)		
		1	2 (ref)	3	
mass flow rate of dry leaves	\dot{m}_{ds}	0.108 (LL)	0.175	0.2 (UL)	$\cdot10^{-4}$ kg/s
mass flow rate of solvent	\dot{m}_l	2.898	3.465	3.767	$\cdot~10^{-4}~$ kg/s
solid-liquid ratio	R {Eq. (3-9)}	0.037	0.051	0.053	kg/kg
screw rotation speed	n	1.3	2.2	2.5	rpm
theoretical axial velocity	\overline{u}_{ax} {Eq. (2-46)}	5.62	9.52	10.8	· 10 ⁻⁴ m/s
filling degree of dry leaves in one segment	F _{ds} {Eq. (3-14)}	0.110	0.106	0.106	-

The steady-state process for OP 2 (only with the lower sampling points) is shown in Figure 3-14. The solvent-soaked leaves and the water phase are distributed similarly across each screw segment from LSP 1 to the solvent inlet. The extraction cake (EC) on the right maintains a stable thickness of $w_{EC} \approx 5 \cdot 10^{-3}$ m. While the A. annua leaves adhered to the transportation screw, the water phase fills the lower-right part of each screw segment. A clear interface between the two phases is evident. A gas phase fills up the segments on the top, but plays a minimal role in the process. The water phase drains out at the extract outlet in varying flow rates, depending on the blockage by leaves. On average, the flow rate stabilises over time. In summary, the process can be described as a three-phase multiphase flow while the central segments appear as equally distributed.

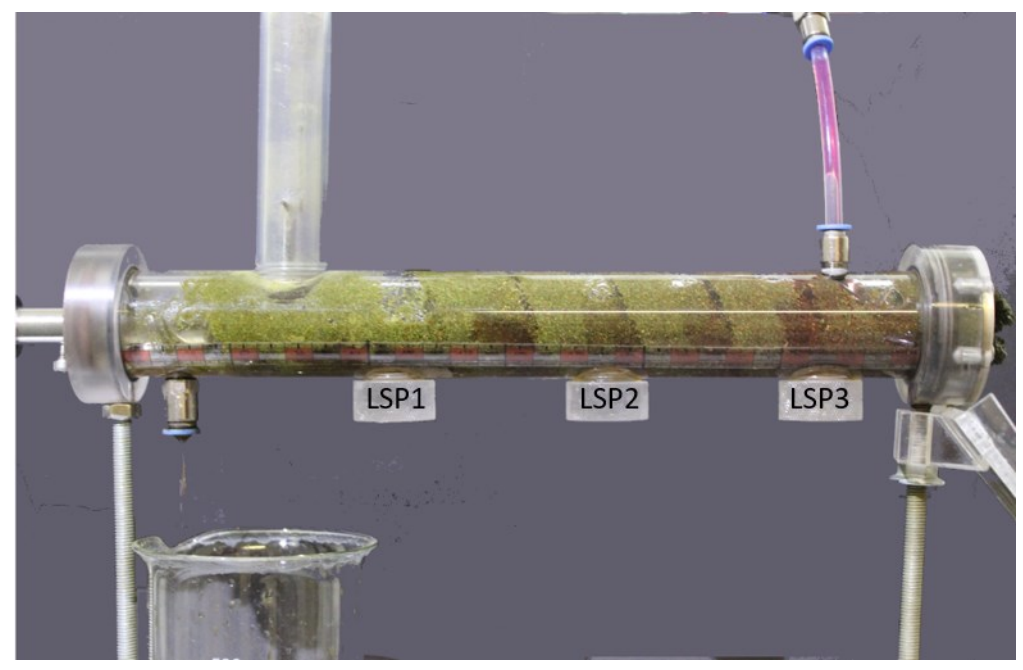


Figure 3-14: Steady-state operation of the counter-current solid-liquid extraction process with OP 2. The solvent water is red-coloured for improved visibility.

To ensure also quantitatively a continuous operation of the process, the compliance of the mass flow rate balance according to Eq. (3-10) should be checked. The mass flow rates of extract and raffinate have been measured in three identical repetitions for every two minutes in a total time of 45 minutes (Figure 3-15). The mass flow rates are given in the unit of gram/minute (g/min) in the following part. Nevertheless, for all calculations the unit needs to be transferred to the SI unit (kg/s) again.

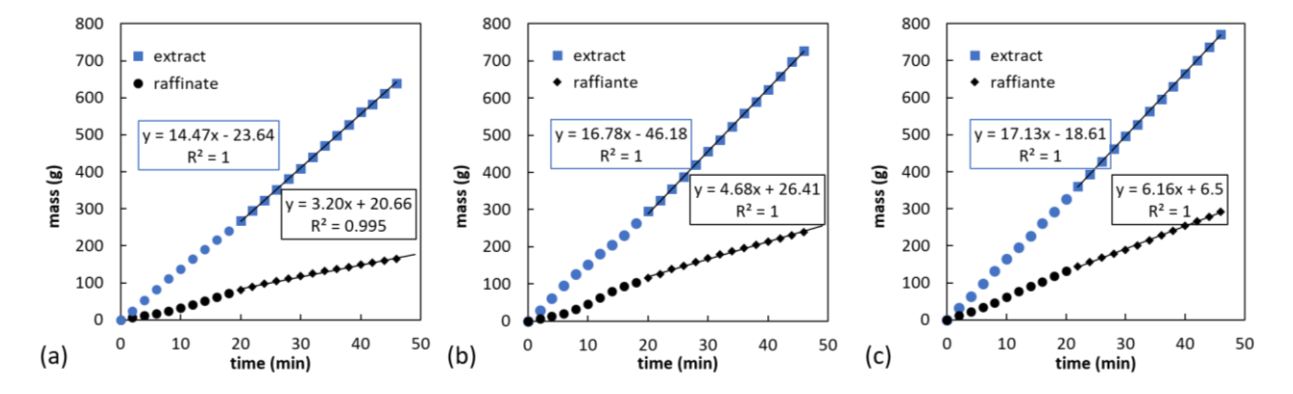


Figure 3-15: Mass flow rates in three identical repetitions of steady-state. The defined operation point is (a) OP1 with n = 1.3 rpm, (b) OP2 with n = 2.2 rpm and (c) OP3 with n = 2.5 rpm according to Table 3-9. After a stabilisation time of 20 min a linear interpolation of the measurements points shows a very good fit (coefficient of determination $R^2 \approx 1$).

According to Figure 3-15 the raffinate mass flow rate stabilises after a specific time, around $t_{st}=20$ min. Consequently, the mean mass flow rates have been determined after this time by linear interpolation. The very good fit is proved by the R-squared value of ≈ 1 , which defines the proportion of variability in the data described by a (linear) model ($0 \le R^2 \le 1$) [Mon17]. Measurements during the steady-state operation, e.g., RTD measurements, should start after this stabilisation time t_{st} . From OP 1 to OP 3, the extract mass flow \dot{m}_{ext} increases from 14.47 g/min (OP 1) to 17.13 g/min (OP 3), indicating the potential for higher artemisinin flow rates at higher operation points. Comparing the specific outlet mass flow rates of extract and raffinate between theory (th) {Eqs. (3-11) and (3-12)} and experiments (exp), a very good agreement can be found for all three OPs (e.g., OP 1: th: 14.57 g/min, exp: 14.47 g/min) (Table 3-10). The error e between the input mass flow rates and output mass flow rates in experiments (exp) given by Eq. (3-18) and based on the total mass flow balances shown in Eq. (3-10) ranges around 2% for all OPs (Table 3-10).

$$e = \left(1 - \frac{\dot{m}_{ext} + \dot{m}_{raff}}{\dot{m}_{ds} + \dot{m}_{l}}\right) \tag{3-18}$$

Table 3-10: Input and output mass flow rates for steady-state operation. Theoretical assumptions are compared with experimental (exp) investigations. Note that the employed units are not the same as in Table 3-9.

Parameter		Operati	Operation point (OP)		
Input		1	2 (ref)	3	
mass flow rate of dry leaves	\dot{m}_{ds}	0.65	1.05	1.2	g/min
mass flow rate of solvent	\dot{m}_l	17.39	20.79	22.6	g/min
Theory output					
th. mass flow rate of extract	\dot{m}_{ext} {Eq. (3-12)}	14.57	16.23	17.39	g/min
th. mass flow rate of raffinate	\dot{m}_{raff} {Eq. (3-11)}	3.47	5.61	6.41	g/min
Experimental output					
mass flow rate of extract	\dot{m}_{ext}^{exp}	14.47	16.78	17.13	g/min
mass flow rate of raffinate	\dot{m}_{raff}^{exp}	3.20	4.68	6.16	g/min
error of mass balance	e^{exp} {Eq. (3-18)}	-2.1	-2.0	-2.1	%

During the experimental measurements the extraction cake for OP 3 was visually more wet than for OP 2 even if the solid-liquid ratios are almost identical (Table 3-9). To quantify this observation the cake humidity was evaluated based on the raffinate mass flow rate in the experiments and their mass balance (MB). This raffinate humidity differs from the bulk humidity inside the extractor (measured in subsection 3.2.3 with $H_{H_2\,O}=81$ wt.%) because a certain amount of water has been removed from the leaves by compression at the PD.

An analytical separation of the raffinate phase into a single liquid phase (internal extract) and a solid phase is required. For the example of OP 2, the total raffinate mass flow of \dot{m}_{raff}^{exp} = 4.68 g/min comprises a solid part $\dot{m}_{raff,s}^{exp}$ = 1.05 g/min (input mass of dry leaves) and a liquid part $\dot{m}_{raff,int}^{exp}$ = 3.63 g/min. Using Eq. (3-7) the bulk humidity of the raffinate corresponds to a value of 76.5 wt.% at OP 2. Applying this method to the other OPs reveals slight variations between OP 1 to OP 3 (Table 3-11). The highest bulk humidity is found at OP 3, reaching 80.5 wt.%, which aligns with the visual observations.

Table 3-11: Bulk humidity of the steady-state operation points.

Parameter			Operation (OP)		Unit
		1	2 (ref)	3	
Raffinate bulk humidity – mass balance	$H_{raff,MB}$ {Eq. (3-7)}	79.7	76.5	80.5	wt.%

This slight variation in cake consistency remains within a range that ensures stable operation. However, the higher bulk humidity at OP 3 results in increased solvent waste compared to OP 2, making OP 2 optimal for further process characterisation and subsequent analysis.

3.4.3 Pressure field

The pressure field inside the extractor provides information about the extraction conditions of artemisinin. Since the investigated extractor is open to atmosphere through the leaves inlet, with an air layer on top of the liquid and solid phase, the pressure is almost atmospheric. A noticeable increase is only possible directly at the position of the perforated disk, influencing the stability of the extraction cake. Consequently, the pressure value is important to obtain steady-state conditions. An optimisation of the perforated disk and its induced pressure could possibly stabilise the extraction cake and increase the narrow operation window.

Pressure distribution in the extraction device

The pressure distribution during a steady-state process is measured at the three upper sampling points USP 1, USP 2, USP 3 as well as at the solid inlet (SP 0) and the raffinate outlet (SP 4) (Figure 3-3). An ultra-compact, gel-filled digital pressure sensor (MS5837-02BA, TE connectivity Corporation, Berwyn, PA, USA) has been attached to the corresponding SP after reaching steady-state with OP 2 (Table 3-9). For the perforated disk (SP 4) the sensor has been attached to one single hole. This single hole is completely blocked by the sensor, which could influence the conditions slightly. Figure 3-16 shows the single pressure sensor, the adapters for the USP and the perforated disk with attached sensor.

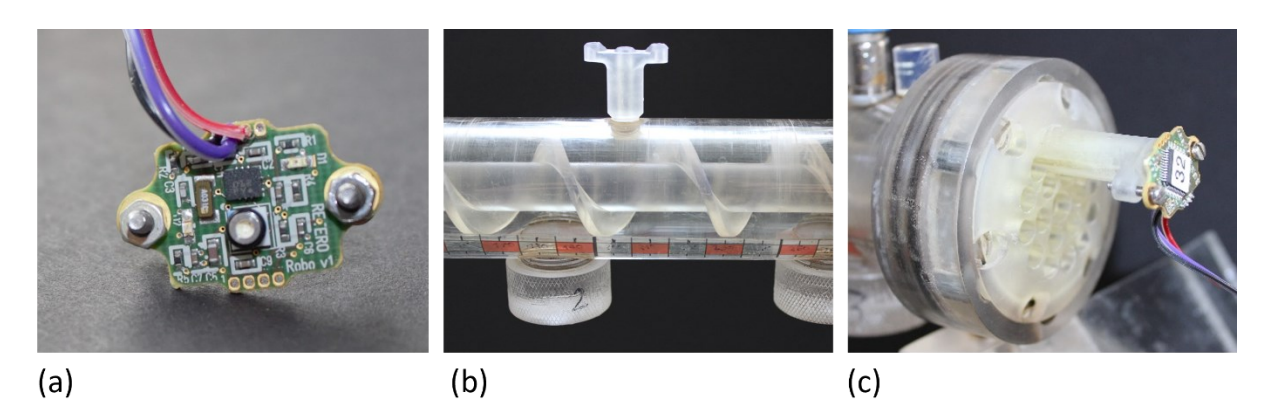


Figure 3-16: Pressure measurement device, (a) digital pressure sensor in detail, (b) adapter for pressure sensor at one USP of the extractor, (c) perforated disk with attached sensor.

After attachment of the sensor the pressure has been measured three times at the five positions in 5 minutes intervals. The mean pressure and standard deviation have been calculated and are listed in Table 3-12. Further the difference of the calculated mean pressure \bar{p} to the present atmospheric pressure $p_{atm} = 1.005 \cdot 10^5$ Pa at every SP has been determined.

The pressure distribution is graphically shown in Figure 3-17.

T 11 0 40 D	11			r		
Table 3-12: Pressure	dictribution	in the	CCTOW DVTractor	tor	Oneration	naint ()P /
Table 5 IZ. I I C33ul C	uisti ibutioii	111 1111	JULEW CALLACION	101	opciation	point or Z.

			G / 1 C C C C C C C C C C		· « • • • • • •		-
Parameter		SP 0	USP 1	USP 2	USP 3	SP 4	Unit
		(leaves inlet)				(PD)	
position x		0.06	0.13	0.21	0.29	0.32	m
dimensionless length	x/L	0.19	0.41	0.66	0.91	1	-
mean pressure	\bar{p}	1.005	1.008	1.012	1.015	1.187	· 10 ⁵ Pa
		$(=p_{atm}^{})$					
standard deviation	σ	-	0.002	0.005	0.001	0.022	$\cdot10^5$ Pa
difference to p_{atm}	е	0	0.30	0.70	1.00	18.11	%

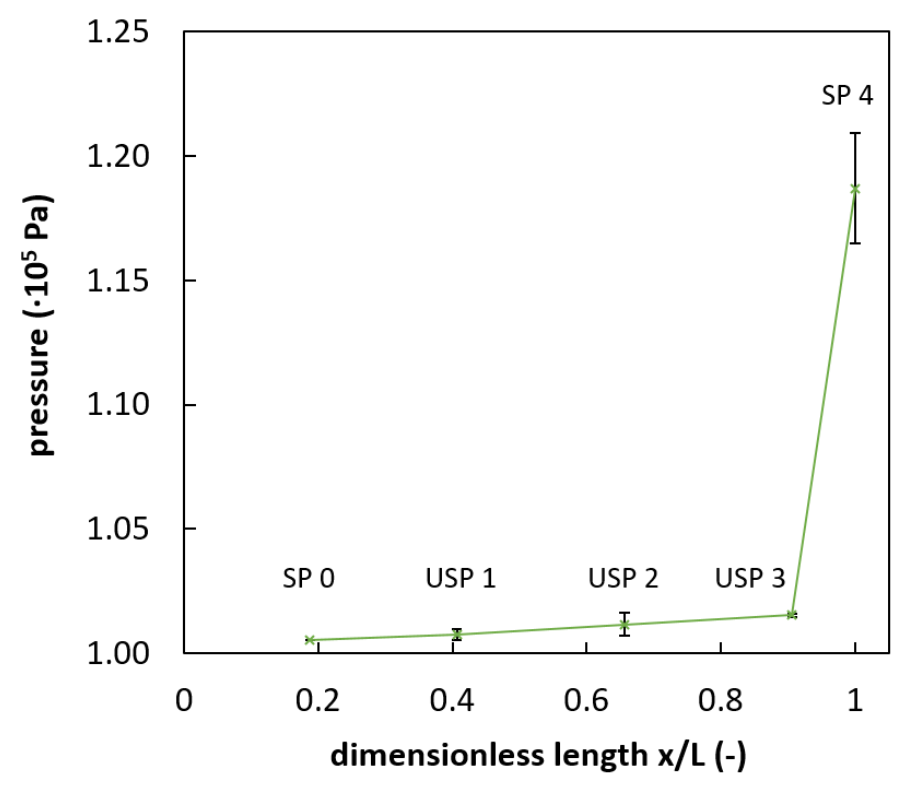


Figure 3-17: Pressure distribution in the screw extractor at steady-state for OP 2. Pressure measurements have been repeated three times (error bars with the green line) at SP 0, USP 1, USP 3, and SP 4 (perforated disk), from left to right.

The measured data show that the highest increase of pressure in the extractor is located as expected at SP 4 (perforated disk). Here, the mean pressure equals $1.187 \pm 0.022 \cdot 10^5$ Pa, which is an increase of 18.11% compared to atmospheric pressure. The increase of pressure inside the device from SP 1 - SP3 remains lower than 1% compared to the atmospheric pressure. The pressure increase at the perforated disk is important for a sufficient cake formation which is crucial for the success of a continuous process operation.

Steady-state pressure

In a next step only the pressure at the PD was measured for all three steady-state operation points (Table 3-9) at a time t = [0, 5, 10] min after sensor attachment to define a steady-state pressure. Measurement data are provided in Table 3-13.

Table 3-13: Pressure at the perforated disk for three steady-state operation points.

Parameter		Operation point (OP)			Unit
		1	2 (ref)	3	
measuring time:	0 min	1.187	1.171	1.224	· 10 ⁵ Pa
	5 min	1.134	1.219	1.104	$\cdot~10^5$ Pa
	10 min	1.434	1.173	1.225	$\cdot~10^5$ Pa
mean pressure	$ar{p}$	1.252	1.187	1.184	$\cdot10^5$ Pa
standard deviation	ι σ	0.131	0.022	0.057	$\cdot10^5$ Pa

During the measurement, the pressure for OP 1 rises sharply after 10 min. The blocked hole in the perforated disk has a greater impact on OP 1 compared to OP 2 and OP 3. Additionally, the slow screw rotation speed of only 1.3 rpm increases the system's sensitivity to process fluctuations.

Despite these variations, the mean pressure \bar{p} remains stable across all steady-states, ranging between $1.252 \cdot 10^5$ and $1.184 \cdot 10^5$ Pa. The total standard deviation remains below 10% for OP 1 and below 5% for OP 2 and OP 3, indicating overall stable pressure conditions.

In conclusion, a nearly constant steady-state pressure of $p_{st} \approx 1.2 \cdot 10^5$ Pa is maintained within the defined operation window.

Definition of a pressure operation window at the PD

To optimise the stability of the steady-state process, identifying the upper and lower pressure limits at the PD is essential.

The *lower pressure limit* was determined by stopping the leaves inflow rate after reaching steady-state operation (OP 2). As a result, the solid-liquid ratio R {Eq. (3-9)} decreases, gradually dissolving the extraction cake and ultimately causing flooding at the perforated disk. The minimal pressure required to maintain a stable extraction cake, as shown by the red line in Figure 3-18, was found to be $p_{min} \approx 1.082 \cdot 10^5$ Pa.

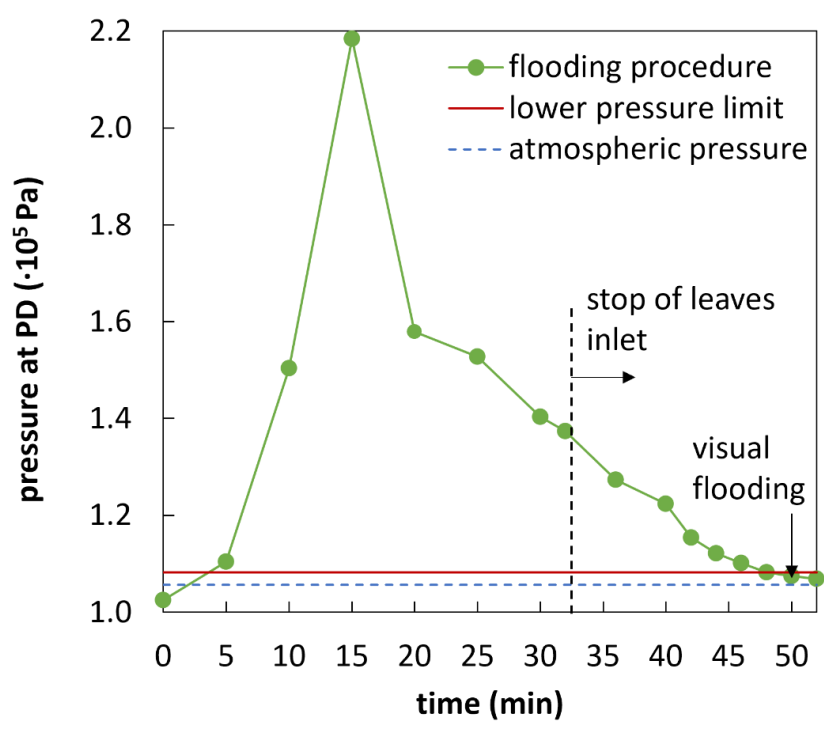


Figure 3-18: Flooding pressure measurement. First a steady state with attached sensor is performed for 30 min (OP 2) measuring the pressure distribution (green line). Then, the leaves inlet is stopped (dashed black line) which forces a flooding at the perforated disk due to the absence of solid material. The pressure is measured at the PD during this procedure until reaching a complete dissolution of the extraction cake (marked as "visual flooding"). The pressure right before the dissolution of the extraction cake is defined as lower pressure limit (red line). This limit is slightly higher than the atmospheric pressure (dashed blue line).

The *upper pressure limit* was measured by increasing the solid-liquid ratio R {Eq. (3-9)} by a factor two right from the start of the measurement. Operation parameters resulting from this adaption are shown in Table 3-14.

Table 3-14: Upper pressure limit operating conditions.

Parameter		Values	Unit
mass flow rate of dry leaves	\dot{m}_{ds}	1.05	g/min
mass flow rate of solvent	\dot{m}_l	10.5	g/min
solid-liquid ratio	<i>R</i> {Eq. (3-9)}	0.1	kg/kg
screw rotation rate	n	2.2	rpm

The pressure sensor is attached to the PD from the start of the experiments to estimate the pressure evolution. Simultaneously, the mass of extract and raffinate have been weighted every 2 min to identify blockage. Figure 3-19 (a) shows an increase of pressure at the beginning of the measurement from atmospheric to $2.1 \cdot 10^5$ Pa. Between 5 and 10 min, the pressure stabilises at $2.2 \cdot 10^5$ Pa, then increases to $2.46 \cdot 10^5$ Pa after 15 minutes. At this time

the weighted mass at the raffinate converged polynomial, indicating a full blockage of material at the level of the perforated disk (Figure 3-19 b). The experiment was stopped to prevent damage at the extraction device. The maximal pressure was measured as $p_{max} \approx 2.2 \cdot 10^5$ Pa.

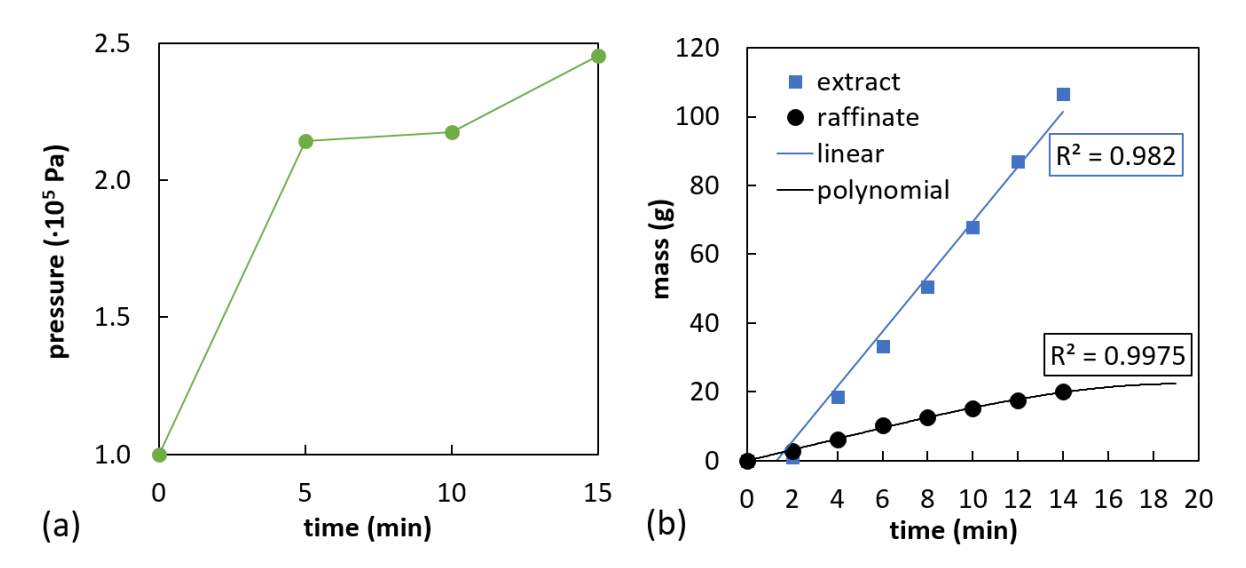


Figure 3-19: Upper pressure limit measurement, (a) pressure evolution until reaching blockage, (b) mass of extract (linear interpolation) and raffinate (polynomial interpolation).

Finally, the pressure field is found between $[p_{min}, p_{max}] = [1.1, 2.2] \cdot 10^5$ Pa for continuous operation. The pressure measured for all selected operation points $(p_{st} = 1.2 \cdot 10^5 \text{ Pa})$ is close to the lower pressure limit. For optimising the operation window this pressure should be increased by modifying the shape of the perforated disk.

Optimisation of the perforated disk inside the pressure operation window

The hole diameters for two re-designed perforated disks have been decreased from initially 5.5 mm (noted PD 5.5) to 5 mm (PD 5) and 4.5 mm (PD 4.5). The implementation of PD 5 for the operation conditions of OP 2 (Table 3-9) resulted in a stable process with stable mass flow rates (Figure 3-20) and a slight increase of pressure at the PD 5 (1.5 \pm 0.25·10⁵ Pa) compared to the initial PD 5.5 ($p_{st}=1.2\cdot10^5$ Pa), as expected. The increased pressure has an effect on the extract mass flow rate by approx. +10% while the raffinate flow rate is simultaneously decreased by 50 - 60% resulting in lower solvent waste compared to PD 5.5 (Table 3-15).

Table 3-15: Comparison of mass flow rates for original (PD 5.5) and modified disk (PD 5).

Parameter		PD5.5 (initial)	PD 5	Unit
mass flow rate of extract	\dot{m}_{ext}	16.29 - 17.02	18.53	g/min
mass flow rate of raffinate	\dot{m}_{raff}	3.58 - 5.06	1.83	g/min

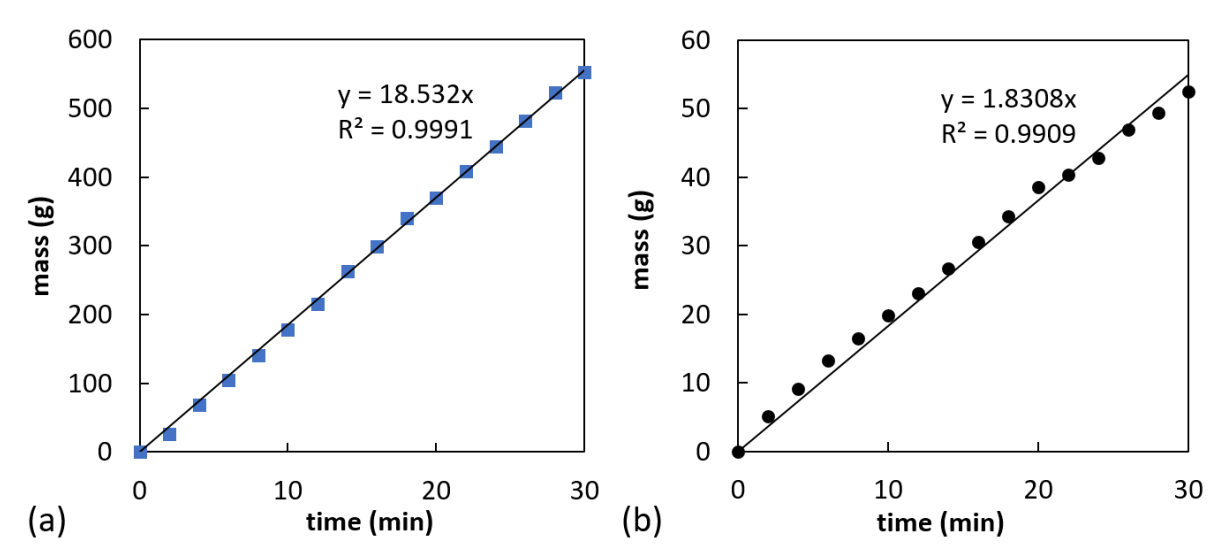


Figure 3-20: Mass flow rates of steady-state operation with the modified disk PD 5, (a) extract and (b) raffinate.

A further pressure increase with PD 4.5 could not be realised since the smaller hole diameter resulted in a blockage at the PD for all investigated conditions (Figure 3-21).

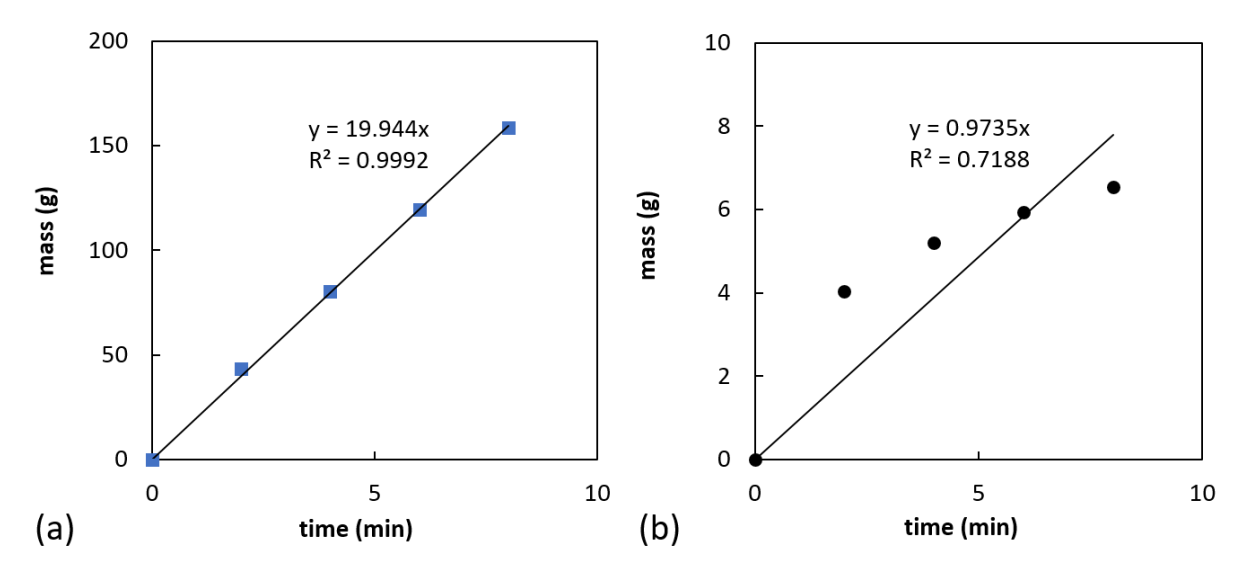


Figure 3-21: Mass flow rates of OP 2 with PD 4.5 for (a) extract and (b) raffinate. The raffinate mass flow rate curve shows a non-linear behaviour, indicating a blockage at the perforated disk preventing steady-state operation.

Regarding the hole diameter, 5 mm was identified as the optimal geometric configuration for the perforated disk. While further optimisation of the perforated disk is possible, it falls outside the scope of this thesis and is considered a topic for future work. The initial perforated disk, with 5.5 mm hole diameters, is used for subsequent experimental observations, as it was previously employed in extraction experiments with the steel setup at the local MPI, allowing for direct comparisons.

3.4.4 Phases residence time distribution

For measuring the RTD behaviour of **solvent** and **solvent-soaked A. annua leaves**, the extractor was operated continuously at operation point 2 (Table 3-9) for at least 20 minutes, ensuring steady state. During this time, the caps covering all sampling ports completely sealed the extractor wall, so that the process was not affected. The process takes place at room temperature (20°C).

The RTD of the **solvent** was measured using a 10 wt.% solution of sodium chloride in water (99.5 % purity, Sigma-Aldrich, Merck, Darmstadt, Germany). According to a calibration study of Vu [Vu23], this was defined as the optimal operation point of the employed conductivity meter (FiveEasy Conductivity, Mettler Toledo, Columbus, USA). A volume of 30 ml of the tracer solution was introduced as a pulse injection after reaching steady-state operation. Then, samples with a volume of 10 ml were collected every minute at the extract outlet only and their conductivity was measured.

For investigating the RTD of **solvent-soaked A. annua leaves**, black mustard seeds have been used as tracer particles to track the behaviour of the pulverised leaves. Mustard seeds have a spherical shape with a mean diameter of 1.6 \pm 0.4 mm and stable material properties [WR01]. A pulse injection of 1.5 g of tracer particles was introduced by gravity at the solid inlet (SPO, see Figure 3-3). The tracer particles stick immediately to the neighbouring soaked leaves already present within the reactor. Samples were taken every minute at each of the three lower sampling points (LSP 1, LSP 2, or LSP 3) and at the raffinate outlet (SP 4), see Figure 3-3. Three identical runs have been repeated to measure the RTD behaviour at all lower sampling points. When sampling the solid tracer particles, the solvent pump has been stopped, to avoid solid displacement due to solvent flow. The cap of the specific sampling point has been removed. In one-minute intervals also the motor of the screw was stopped and the material appearing at the position of the opened cup was scraped out of the extractor, before restarting the motor. The procedure has been repeated until all tracer particles had passed the sampling point. The tracer particles have been separated from the leaf particles afterwards using a sieve and dried at the air for one day. Finally, the sampled and dry mustard seeds have been weighted.

RTD of the liquid phase (related to \dot{m}_l)

The sodium chloride concentration in the samples used to calculate the normalised residence time distribution curve E(t) converges to small values after 12-14 min of measurement time, but does not reach a value of zero. This results from the soaking of concentrated solvent to the leaves phase. To eliminate the effect of solvent soaking from the RTD analysis, a stop criterion for this concentration measurement is defined. The change of concentration between two samples $\Delta C(t)$ has been set in relation to the maximum change between two samples $\Delta C_{max}(t)$. If this ratio is below 5% for two consecutive samples, the conductivity is assumed to be zero and not used for RTD analysis (Table 3-16).

Table 3-16: Conductivity measurement of OP 2. As a stop criterion for the conductivity measurements the change of conductivity between two sampling times $\Delta C(t)$ was set in relation to the maximum concentration change $\Delta C_{max}(t)$ (bold). The measurements stop when this ratio $\Delta C(t)/\Delta C(t)$ is lower than 5% for two consecutive sampling times (red) – in the presented measurement table this is the case after a time of 12 min.

time t (min)	conductivity $C(t)$ (mS/cm)	$\Delta C(t)$	$\Delta C(t)/\Delta C_{max}(t)$ (%)
0	0	0	0
1	15.12	15.12	99.60%
2	30.3	15.18 = $\Delta C_{max}(t)$	100.00%
3	31.1	0.8	5.27%
4	28.5	2.6	17.13%
5	22	6.5	42.82%
6	17.32	4.68	30.83%
7	13.47	3.85	25.36%
8	10.17	3.3	21.74%
9	7.48	2.69	17.72%
10	5.55	1.93	12.71%
11	4.66	0.89	5.86%
12	3.69	0.97	6.39%
13	3.07	0.62	4.08% <5%
14	3.45	0.38	2.50% < <mark>5%</mark>

Results of three repetitions with mean value and deviations between the trials are given in Figure 3-22. Visually, the tracer concentration curve shows a peak after approx. three minutes (dotted line) and a slow subsequent decrease. The mean residence time has been calculated to be $\bar{\tau}_l$ = 4.5 min using Eq. (2-31) which corresponds to 1.5 times the read value of the peak. This is a reasonable relation for mixed flows approaching CSTR behaviour [Lev12]. The determined, slow decay of the conductivity signal can be attributed to the holdup of the solvent by the soaked leaves. The tracer absorbed by the leaves upon injection is slowly released back into the liquid after the peak of the tracer has already passed.

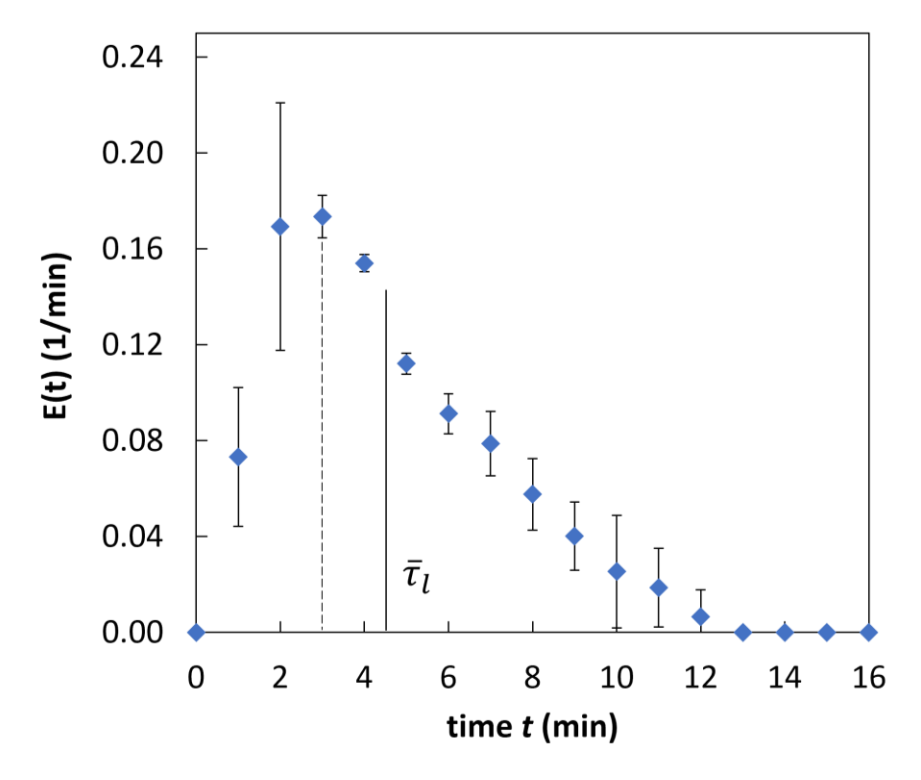


Figure 3-22: Experimentally determined RTD curve of the liquid phase (water). The dotted line shows the visual value of residence time according to the concentration peak while the continuous line shows the actually measured solvent mean residence time (MRT) $\bar{\tau}_I$.

The measured MRT ($\bar{\tau}_l$ = 4.5 min) can be compared with the general assumption of Eq. (2-35), where the MRT results from the ratio of the total free volume V_{tot} (= 1.59· 10^{-4} m³) and the volume flow rate of solvent \dot{V} (= 20.79 cm³/min = 3.47· 10^{-7} m³/s). This volume-based assumption leads to a MRT of 7.6 min which is by 3.1 min higher compared to the experimental value. This difference comes from the fact, that the solvent is not filling the total volume of the extractor (due to the presence of the gas phase), as assumed in the general definition of Eq. (2-35).

$$\bar{\tau} = \frac{V_{tot}}{\dot{V}} = \frac{1.59 \cdot 10^{-4} \text{ m}^3}{3.47 \cdot 10^{-7} \text{m}^3/\text{s}} = 458 \text{ s} = 7.6 \text{ min}$$

The calculated variance σ_l^2 for the RTD curve in Figure 3-22, averaged between the three trials, equals a value of 6.3 min² with the resulting standard deviation $\sigma_l = \sqrt{6.3} = 2.5$ min {Eq. (2-32)}. The first and second moment of the E(t) curve $(\bar{\tau}_l, \ \sigma_l^2)$ have been used to estimate the theoretical number of stages {Eq. (2-33)} which results in a value of $N_l = 3$ for OP 2. This value is very low and corresponds to a near-CSTR-behaviour for the liquid solvent. According to Eq. (2-40) the Bodenstein number for the solvent equals $\mathrm{Bo}_l = 6$ indicating a rather high degree of axial molecular diffusion and back-mixing. The behaviour close to CSTR

corresponds well to the shape of the curve [Lev12]. It is influenced by the low solvent residence time which ensures fast exchange of artemisinin-loaded solvent with fresh solvent, thus maintaining high concentration gradients during the continuous process.

Changes of the screw rotation speed to evaluate the steady-state OP 1 and OP 3 revealed a slight decrease of the MRT and standard deviation for higher rotation rates (Table 3-17). The theoretical number of stages and, simultaneously, the Bodenstein number increase slightly from $N_l=3$ (Bo $_l=8$) for OP 2 to a value of $N_l=4$ (Bo $_l=8$) for OP 1 and OP 3 which is still in the same order of magnitude and predicts the desired near-CSTR behaviour for all operation points. As a result, increasing the screw rotation rate from 1.3 rpm (OP 1) to 2.5 rpm (OP 3) has no significant impact on the axial diffusion of the solvent phase, which flows countercurrent to the screw rotation. A mean value of the stage number can be taken with $\overline{N}_l=4$. This contrasts with reports in the literature, where screw rotation consistently shows an increasing impact on the stage and Bodenstein number and consequently, on axial diffusion [WPT+07], [NvR+15]. However, these studies only examined materials transported with the screw, flowing in the same direction. The counterflow of the liquid phase against the screw rotation appears to be an exception. It is presumed that at higher screw rotation rates, there might be an influence on the liquid phase. However, as this lies outside the system's operating window (subsection 3.4.1), it is not explored further.

Table 3-17: Effect of the screw rotation speed on the liquid-phase Bodenstein number. Three steady-state operation points have been examined.

operation point	screw rotation speed n (rpm)	mean residence time and standard deviation $\bar{ au}_l \pm \sigma_l$ (min) Eqs. (2-31), (2-32)	<i>N_l</i> Eq. (2-33)	Bo _l (-) Eq. (2-41)
1	1.3	5.5 ± 2.8	4	8
2 (ref)	2.2	4.5 ± 2.5	3	6
3	2.5	4.4 <u>+</u> 2.1	4	8

RTD of the solvent-soaked A. annua leaves (related to \dot{m}_s)

Three identical measurement campaigns have been repeated to obtain the solid-phase RTDs at the lower measurement points LSP 1, LSP 2, LSP 3 - and simultaneously behind the perforated disk (SP 4). This leads to a total of 12 RTD curves, shown in Figure 3-23 (a): green for original measurement, black for first repetition, red for second repetition. Relatively large variations are detected, highlighting the importance of repeating the measurements to get reliable information. This variability is due to the complex behaviour of the pulverised leaves, leading to local compaction and accumulation effects depending on the exact size, shape, and bulk humidity of the solid particles. The RTD curves at all four sampling points show a decrease of the peak value with time, together with an increasing spread of the curves. At the level of the perforated disk (outlet of the leaves from the compression cake), a mean residence time of $\bar{\tau}_s$ = 15.5 min has been measured for the extraction process during steady-state operation, using Eq. (2-31). The mean residence time at sampling point LSP 3 in front of the PD equals 7.3 min. According to the reaction kinetics of artemisinin with the solvent toluene discussed in section 3.3, a contact time of $t_{eq} \approx 10$ min already leads to a 97.4 % normalised extraction efficiency based on the extractable mass fraction. Consequently, the length of the glass extractor of L = 0.32 m for the employed operation conditions is sufficient when using toluene as solvent.

Figure 3-23 (b) shows the RTD curve for the sampling point SP 4 (PD) in detail. The deviations between all three trials are represented by error bars. Tracer particles are detected from 9 to 26 minutes after pulse injection, with relatively large deviations between repeated measurements. This can be attributed to the compression of leaves and tracer particles by the PD, leading to stochastic, alternating flooding or blockage of the material at this level.

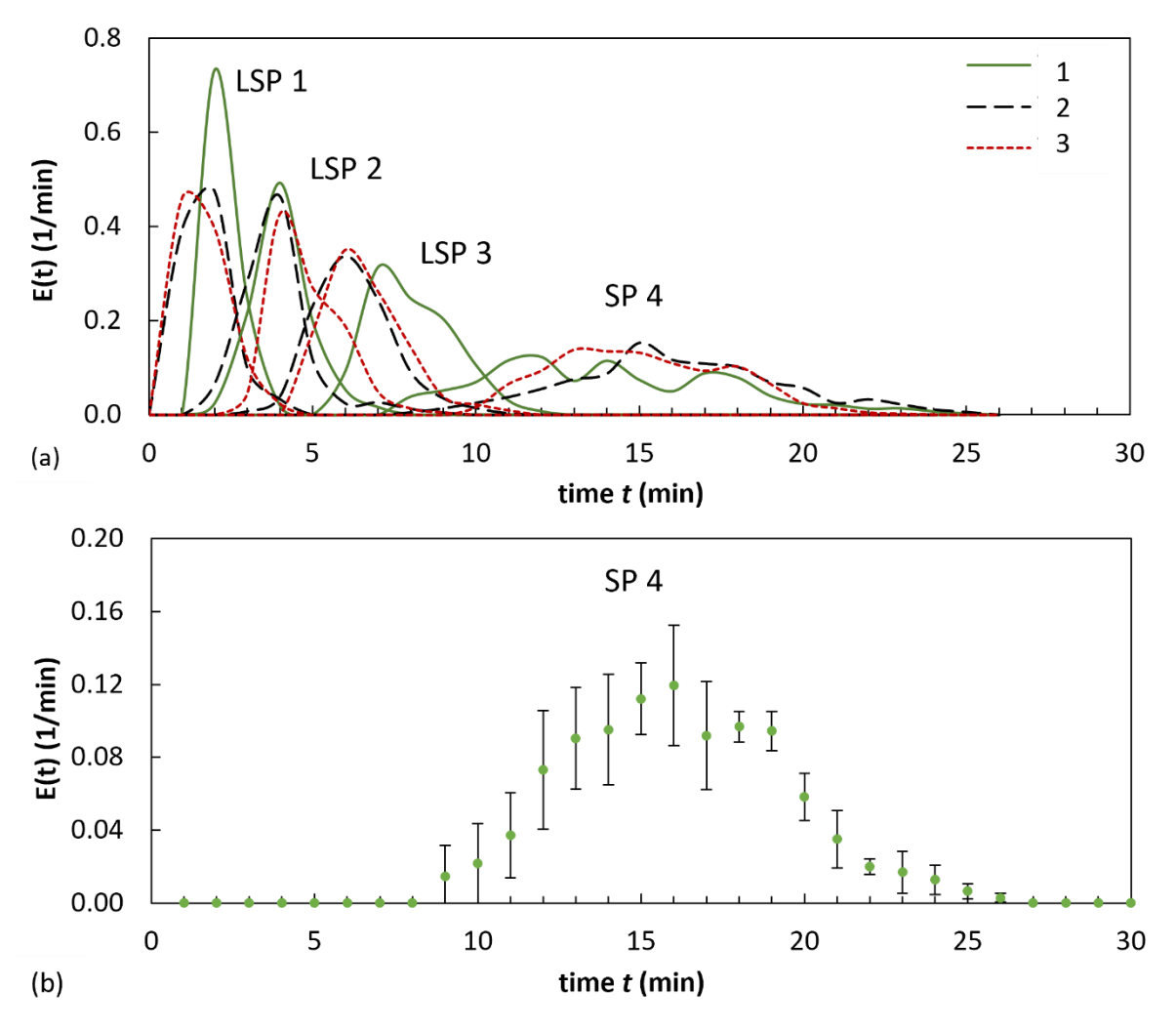


Figure 3-23: Experimental RTD curve for the solvent-soaked leaves. Three identical trials (1-3) have been examined with OP 2 for (a) all four sampling points (LSP 1, LSP 2, LSP 3, SP 4), (b) sampling point SP 4 (PD), with deviations between three repeated measurements illustrated by error bars.

In order to characterise the RTD behaviour for the solvent-soaked leaves in the steady-state process and to analyse the extent of axial dispersion, the first moment $\bar{\tau}_s$ (MRT) and the second moment σ_s^2 (variance) of the E(t) function are analysed for all sampling points (Figure 3-24). Both moments increase almost linearly with the dimensionless length x/L from LSP 1 to LSP 3, with the MRT increasing faster than the variance. At SP 4, both moments and their variation across trials 1–3 are significantly higher, likely due to the influence of the perforated disk and the extraction cake.

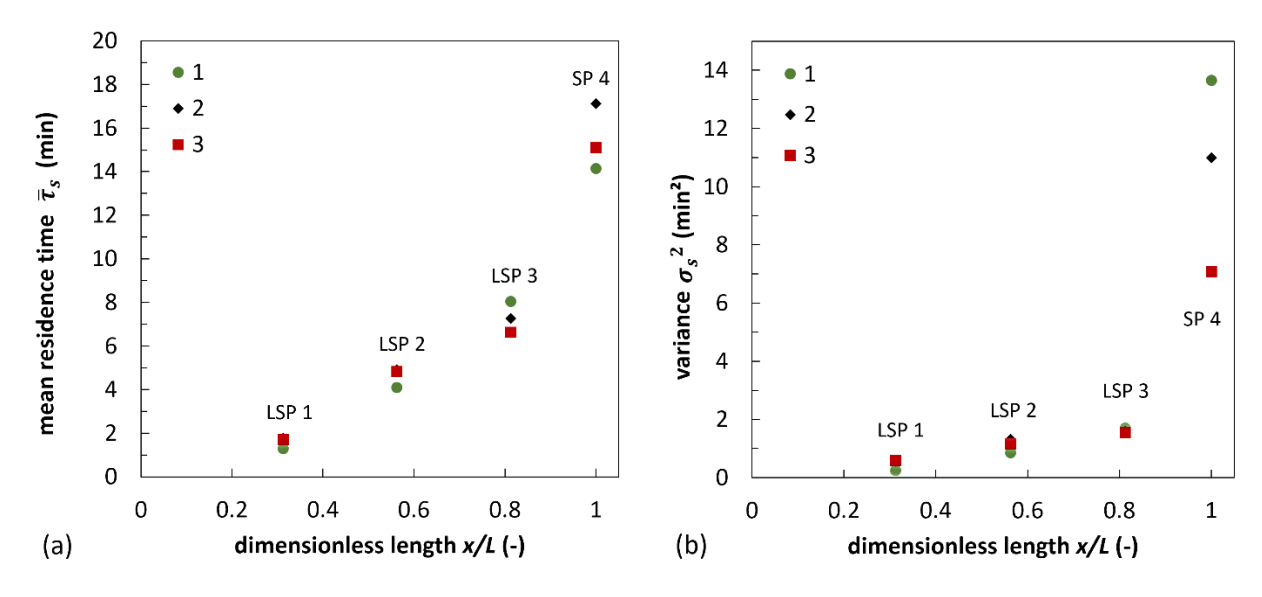


Figure 3-24: (a) Mean residence time and (b) variance for the solvent-soaked leaves. Three identical trials (1-3) have been investigated with OP 2 for sampling points LSP 1, LSP 2, LSP 3, SP 4.

Based on the first and second moment, the theoretical number of stages N_s {Eq. (2-33)} and simultaneously the Bodenstein number Bo_s {Eq. (2-44)} can be analysed for each sampling point. Figure 3-25 depicts an increase of N_s (and Bo_s) with increasing transportation length in the extractor (e.g., for trial #2: from N_s = 5 at LSP 1 to N_s = 33 at LSP 3). At SP 4 the average number of stages and Bodenstein number decreases again to a value of N_s = 23 and Bo_s = 46 caused by the compression process at the perforated disk which reduces axial diffusion and the spread of the RTD curve. Since the extraction process at this position can be neglected these values are not relevant for reactor characterisation.

A linear interpolation of the averaged (av.) values for LSP 1 – LSP 3 shows a perfect fit ($R^2 = 1$) confirming the constant relation between stage number N_s and characteristic length L_{ch} of the extractor, as given in Eq. (2-44). This indicates a constant transport velocity of the leaves by the screw and a consistent diffusion coefficient throughout the reactor, as described by the dispersion model [Lev99]. This leads to more narrow peaks with higher transportation length, which are advantageous for this extraction process, as they reduce elution volumes and yield higher ARTE mass fractions [SSS20].

For extractor characterisation the values at LSP 3 are used which defines the total transportation length of the leaves (\overline{N}_s = 33). The Bodenstein number of Bo_s = 66 is ≈ 10 times higher compared to the liquid solvent. Since it indicates an ideal PFTR for values Bo > 100 [Lev12], the extractor exhibits near-PFTR behaviour for the solvent-soaked leaves.

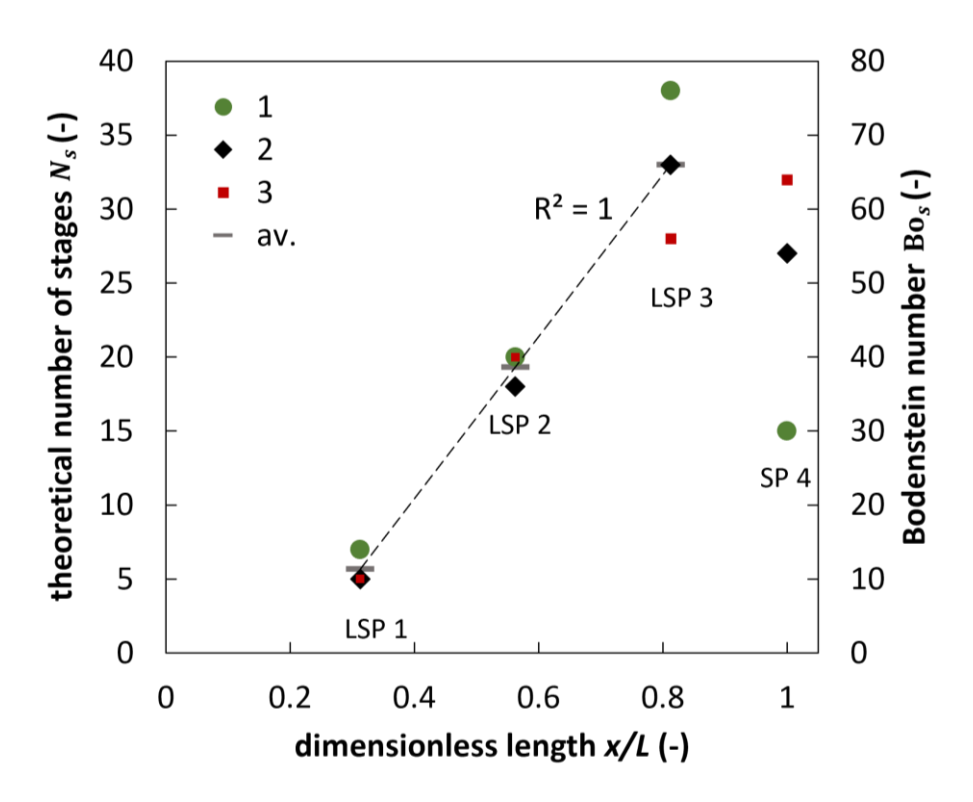


Figure 3-25: Stage number and Bodenstein number for solvent-soaked leaves along the extractor at OP 2. Three identical experimental runs have been performed (shown with 1-3 and different markers) by taking samples at LSP 1-SP 4. A linear interpolation of the averaged (av.) values for each run reveals a perfect fit, proving constant transport velocities and diffusion coefficients as defined in Eq. (2-44). The parameters are plotted as function of dimensionless length x/L (L = 0.32 m).

A similar analysis was performed for the two other limiting steady-state operation points OP 1 and OP 3 (see operation conditions in Table 3-9). While generally, higher mass flow rates of feed material increase the stage number, higher screw rotation rates decrease the stage number [WPT+07], [NvR+15]. Results of the stage and Bodenstein numbers for the countercurrent extraction process at LSP 3 are compared to steady-state OP 2 in Table 3-18. The stage number N_s decreases from 41 (OP 1) to 20 (OP 3) by a factor 2, indicating a spread of the curves and higher axial diffusion. Consequently, the effect of the increased screw rotation rate is higher compared to the increased feed material, which fits to literature [WPT+07], [NvR+15]. This effect indicates undesired back-mixing effects. Consequently, the reactor should preferably be used with lower screw rotation rates of OP 1 or OP 2.

Table 3-18: Stage number N_s and Bodenstein number Bo_s for solvent-soaked leaves for three steady-state operation points OP 1, OP 2 and OP 3 have been examined at LSP 3 (in front of the PD). Operation conditions are listed in Table 3-9.

Parameter			Operation point (OP)		
		1	2 (ref)	3	
screw rotation rate	n	1.3	2.2	2.5	rpm
theoretical number of stages	$N_{\rm s}$ (LSP 3) {Eq. (2-33)}	41	33	20	-
Bodenstein number	Bo_{s} (LSP 3) {Eq. (2-44)}	82	66	40	-

Based on the phases RTD analysis the extractor shows different flow behaviour for liquid and solid phases. The liquid solvent exhibits a stage number of \overline{N}_l = 4 indicating a near-CSTR behaviour with significant back-mixing. In contrast, the solvent-soaked leaves show a high stage number of N_s = 33 for OP2, reflecting a near-PFTR behaviour with minimal back-mixing. This behaviour is advantageous for the extraction process, as the solvent maximises the contact area with the leaves while the exhausted leaves are efficiently transported out of the extractor. Nevertheless, for using the RTD analysis for a simplified compartment model as described in subsection 2.3.2 and applied in chapter 5 only one parameter for N must be determined. Therefore, a mean number of stages \overline{N} (\overline{N}_l , N_s) = \overline{N} (4,33) = 18 is defined.

3.4.5 Efficiency of screw-driven transport

The residence time of the solvent-soaked A. annua leaves is mainly influenced by the screw transportation process. The efficiency of the screw transport η , meaning the ratio of the actual volumetric flow rate along the screw divided by the maximum theoretical volumetric flow rate of material according to Eq. (2-45), is obviously always below 1 [RMM93], [RM94]. For constant cross-sectional areas of the screw this relation is also valid for axial velocities. The difference between actual flow and theoretical flow can be explained by two reasons: (1) high shear of the bulk solid in the gaps along the screw during its rotational motion, (2) slippage and backflow in the clearance between screw and extractor walls.

Information about the transport efficiency η of the implemented screw provides a correction factor between theoretical and experimental axial material velocities. This allows an estimation of the residence time of solvent-soaked A. annua leaves which depends on the axial material velocity and the overall transportation length L_s = 0.26 m (section 3.1) starting at the inlet of dry A. annua leaves {Eq. (2-34)}. The theoretical axial velocity of leaves \bar{u}_{ax} is determined using Eq. (2-46) based on the screw rotation speed n. It has been calculated in Table 3-9 for all operation points (OP 2 as a reference: $\bar{u}_{ax} = 9.52 \cdot 10^{-4}$ m/s ≈ 1 mm/s). Figure 3-26 shows the experimentally derived axial velocities of the solvent-soaked A. annua leaves with a rotational speed of n = 2.2 rpm for each lower sampling point (LSP 1 – LSP 3) and for the perforated disk (SP 4), considering again three repetitions of the same experiment for OP 2. The average value (av.) changes only slightly between LSP 1 (4.28·10⁻⁴ m/s) and LSP 3 (4.59·10⁻⁴ m/s) which amounts to only 7%, as expected in the previous section 3.4.4. Its value decreases significantly at the location of the perforated disk (x/L = 1). This decrease of axial velocity is caused by the higher pressure at this location (subsection 3.4.3), which inhibits the transport of the leaves. Therefore, this position is excluded from the determination of the overall transport efficiency. Finally, the experimentally measured average axial velocity of the solvent-soaked leaves in OP 2 can be determined as $\bar{u}_{ax.exp} \approx 4.41 \cdot 10^{-4}$ m/s.

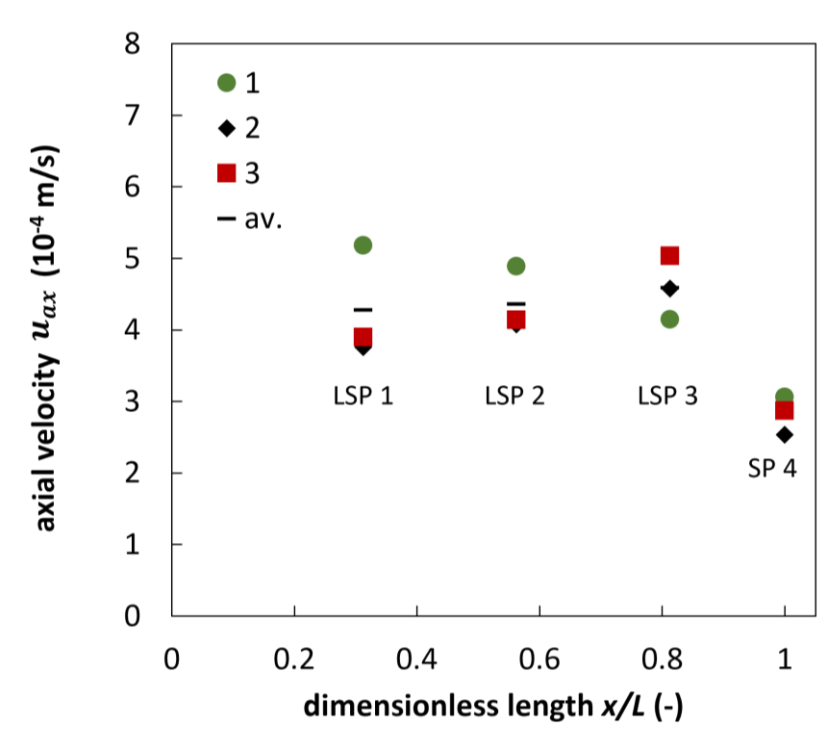


Figure 3-26: Evolution of the axial velocity for leaves along the extractor at OP 2. Three identical experimental runs have been performed (shown with the different markers) by taking samples at LSP 1 - SP 4. The axial velocity is plotted as function of the dimensionless length x/L (L = 0.32 m).

The transport efficiencies η {Eq. (2-45)} for the three examined operation points are shown in Table 3-19. This table indicates similar transport efficiencies for all three operation points, with a mean value $\bar{\eta} \approx 0.46$, corresponding also to the value for the reference case OP 2.

Table 3-19: Transport efficiency by the screw for three different operation points (conditions are listed in Table 3-9).

Parameter			Operation point (OP)		
		1	2 (ref)	3	
screw rotation speed	n	1.3	2.2	2.5	rpm
experimental axial velocity	$\bar{u}_{ax,exp}$	2.82	4.41	4.36	$\cdot~10^{-4}~{ m m/s}$
theoretical axial velocity	\bar{u}_{ax} {Eq. (2-46)}	5.62	9.52	10.81	$\cdot~10^{-4}~\mathrm{m/s}$
transport efficiency	η {Eq. (2-45)}	0.502	0.463	0.403	-

Keeping this constant value, a simple conversion into the mean residence time $\bar{\tau}_s$ of solvent-soaked A. annua leaves using Eq. (3-19) {based on Eq. (2-34)} can be performed.

$$\bar{\tau}_{s}' = \frac{L_{s}}{\bar{u}_{ax\,exp}} = \frac{L_{s}}{\bar{\eta} \cdot \bar{u}_{ax}} \tag{3-19}$$

Using this approach, the experimental residence time of solvent-soaked A. annua leaves in the extractor can be assessed in advance for a variety of steady-state operation points without any necessity of performing additional experiments. This is extremely valuable for the preliminary design of corresponding process units.

3.4.6 Phase retention volume

The retention (ret.) volume of liquid solvent V_l and solvent-soaked leaves V_s inside the extractor provides information about the liquid phase volume fraction ε' . This volume fraction is necessary for adapting analytical models describing the extraction process. Further, the retention volume of liquid and solid phase provides information for setting up CFD simulations and validation.

The phase retention volume can be calculated based on the experimentally measured phase residence times. Since the derived number of stages for the liquid solvent \bar{N}_l = 4 (Bo $_l$ = 8) indicates a near-CSTR behaviour, the liquid volume V_l inside the extractor can be calculated as a function of solvent residence time $\bar{\tau}_l$ and volume flow rate \dot{V}_l , following Eq. (2-35). Thereby, only the extract mass flow rate excluding the internal extract, and the liquid density ρ_l are used. This extract mass flow rate was experimentally investigated in several operation points (subsection 3.4.2). Nevertheless, the final mass flow rate balance included small errors coming from experimental accuracy limitations (Table 3-10). These errors could affect the resulting retention volume. Consequently, the extract mass flow rate is theoretically calculated assuming equilibrium state between the involved phases to ensure complete mass conservation using Eq. (3-12). The solvent residence time $\bar{\tau}_l$ comes from residence time distribution measurements (subsection 3.4.4) while the liquid phase (water) density equals ρ_l = 998 kg/m³ (Table 3-5).

$$V_l = \dot{V}_l \cdot \bar{\tau}_l = \frac{\dot{m}_{ext} \cdot \bar{\tau}_l}{\rho_l} \tag{3-20}$$

Similarly, the retention volume of the solvent-soaked leaves V_s is distributed over the total length of the extractor and can be calculated according to Eq. (3-21) by using the density of solvent-soaked leaves $\rho_s = 922 \text{ kg/m}^3$ (Table 3-5).

$$V_{s} = \dot{V}_{s} \cdot \bar{\tau}_{s}' = \frac{\dot{m}_{raff} \cdot \bar{\tau}_{s}'}{\rho_{s}} \tag{3-21}$$

To ensure mass conservation the raffinate mass flow rate is calculated according to Eq. (3-11). Regarding the MRT, the experimental value $\bar{\tau}_s$ at SP 4 (PD) describes the final outcome at the perforated disk. Previous measurements at several sampling points inside the extractor showed that the axial velocity of leaves is nearly constant in the extractor but decreases significantly at the perforated disk due to the compression process (Figure 3-26). This effect influences the residence time of leaves significantly, by nearly a factor 2 (subsection 3.4.4). Since the extraction cake does not play a significant role for the extraction efficiency the residence time of leaves in front of the extraction cake $\bar{\tau}_s$ was calculated based on Eq. (3-19), neglecting the width of the extraction cake (w_{EC} = 5·10⁻³ m) (Table 3-20). The resulting transportation length equals:

$$L_{s,EC} = L_s - w_{EC} = 0.26 \text{ m} - 0.005 \text{ m} = 0.255 \text{ m}$$
 (3-22)

Table 3-20: Calculated mean solid-phase residence times. The mean residence time is calculated based on Eq. (3-19) using the experimental and theoretical axial velocities from Table 3-19, the transport efficiency $\bar{\eta}$ = 0.46 and the transportation length L_{SEC} = 0.255 m.

Parameter	Operati	Unit			
		1	2 (ref)	3	
exp. axial velocity	$\bar{u}_{ax,exp}$	2.82	4.41	4.36	$\cdot~10^{-4}~{ m m/s}$
th. axial velocity	$ar{u}_{ax}$ {Eq. (2-46)}	5.62	9.52	10.81	$\cdot~10^{-4}~\text{m/s}$
mean residence time (in front of extraction cake)	$ar{ au}_{\scriptscriptstyle S}$ $^{\prime}$ {Eq. (3-19)]	16.44	9.70	8.55	min

The final retention volumes for the solvent-soaked A. annua leaves and the liquid phase are listed in Table 3-21 using the unit (min) for the MRT. The free volume in the extractor filled by the gas phase (air) results from Eq. (3-23), using the total volume of the extractor $V_{tot} = 15.9 \cdot 10^{-5} \text{ m}^3$.

$$V_a = V_{tot} - V_l - V_s \tag{3-23}$$

The solid phase retention volume of the A. annua leaves is very constant (< 5% variation). This implies constant filling degrees of the screw segments for different operation conditions, as desired. The liquid phase retention volume V_l varies slightly (\approx 20%) caused by the difference in solvent MRT for the operation points, as discussed in subsection 3.4.4. The gas phase is present in all operation points, which fits to the experimental observations. A total filling of the extractor is not possible due to the defined operation window and the limiting parameters

(subsection 3.4.1). The retention volumes are important for later validation procedures of the CFD simulations.

Based on the volume of liquid and solid phase a liquid phase volume fraction ε' can now be calculated, similar to the previously defined mass flow-based definition in section 2.2 {Eqs. (2-13) and (2-22)}. This allows simple adaption to the CFD model later developed in chapter 4.

$$\varepsilon' = \frac{V_l}{V_l + V_s} = \frac{\dot{V}_l}{\dot{V}_l + \dot{V}_s} \tag{3-24}$$

The liquid phase volume fraction for the examined experiments ranges between 0.55 (OP 2) and 0.61 (OP 3). This implies that overall, the three operation points correspond to quite similar conditions in this respect. This liquid phase volume fraction is applied in the compartment model in chapter 5.

Table 3-21: Retention volume and phase ratio of solid and liquid phases. The phase densities are constant with solvent density ρ_l = 998 kg/m³ (Table 3-3) and A. Annua density ρ_s =922 kg/m³ (Table 3-5). The MRT needs to be transferred to unit [s] when calculating the retention volumes.

Parameter		Opera	tion point	: (OP)	Unit
		1	2 (ref)	3	_
mass flow rate of extract	\dot{m}_{ext} {Eq. (3-12)}	24.28	27.05	29.98	$\cdot~10^{-5}~{ m kg/s}$
liquid phase MRT	$ar{ au}_l$ (Table 3-17)	5.9	4.5	5.1	min
liquid phase ret. volume	V_l {Eq. (3-20)}	8.61	7.32	9.19	$\cdot~10^{-5}~\mathrm{m^3}$
mass flow rate of raffinate	\dot{m}_{raff} {Eq. (3-13)}	5.78	9.35	10.68	$\cdot~10^{-5}~{ m kg/s}$
solid phase MRT	$ar{ au}_{\scriptscriptstyle S}{}'$ {Eq. (3-19)}	16.44	9.70	8.55	min
solid phase ret. volume	V_s {Eq. (3-21)}	6.18	5.90	5.94	$\cdot~10^{-5}~\mathrm{m^3}$
gas phase ret. volume (air)	V_g {Eq. (3-23)}	1.11	2.68	0.77	$\cdot~10^{-5}~\mathrm{m^3}$
liquid phase volume fraction	ε'_{exp} {Eq. (3-24)}	0.58	0.55	0.61	-

3.5 Influence of modified screw angles

The screw geometry is a central component of the investigated extractor. The screw angle β defines the segment length α and the number of screw segments s. As described in subsection 3.4.1 the small operation window for continuous steady-state operation allows only further process optimisation concerning geometrical components.

In this section the two modified screws MS 1 and MS 2 are analysed (Figure 3-2 and Table 3-1). They represent a decreased screw angle by 10% and 20%, respectively, based on the original screw (OS), used so far. The influence of this modification on the steady-state operation as well as on the RTD behaviour of the solvent-soaked leaves is investigated and compared to OS. This work was strongly supported by Riem Al-Hamadi during her Bachelor's thesis [AlH24].

Steady-state behaviour

The measurements of extract and raffinate mass during three identical repetitions of steadystate operation point 2 (see operation conditions in Table 3-9) showed a linear increase over time proving a stable operation (Figure 3-27).

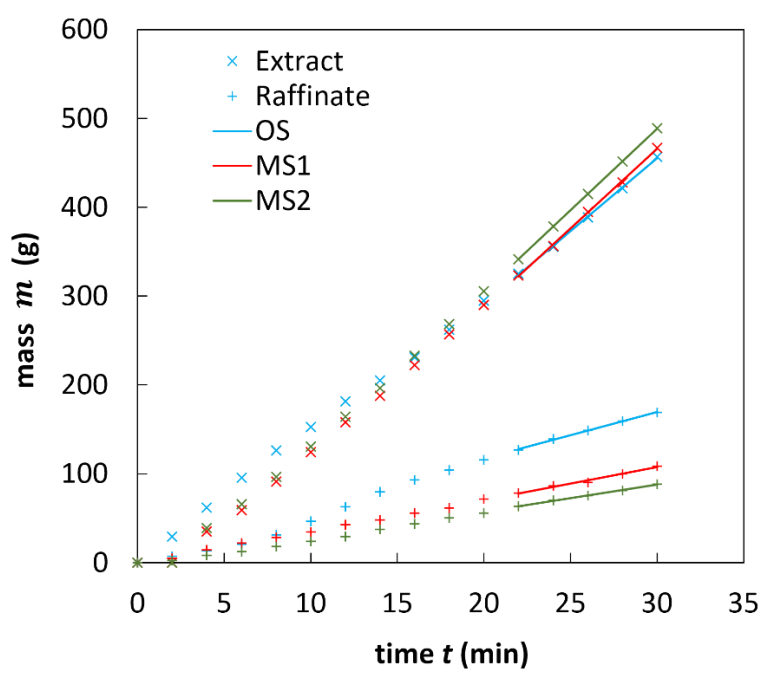


Figure 3-27: Mass of extract and raffinate over time for OS, MS 1 and MS 2 at OP 2. Operation conditions are listed in Table 3-9. Three repetitions are averaged. Mass flow rates are calculated between 20 and 30 min, reprinted from [AlH24].

Analysing the final mass flow rates, the decrease of the screw angle β results in a decrease of the raffinate mass flow rate of 20.9% (OS: 4.68 g/min, MS 2: 3.07 g/min) with a simultaneous

increase of extract mass flow rate by 8% (OS: 16.78 g/min, MS 2: 18.38 g/min) (Table 3-22). The resulting raffinate bulk humidity is decreased by 12 wt.% (OS: 78 wt.%, MS 2: 66 wt.%) and differs strongly from the batch bulk humidity inside the extractor which is always constant with 81 wt.% (subsection 3.2.3).

Table 3-22: Mass flow rates of extract and raffinate for OS, MS 1 and MS 2. The operation conditions of the used OP 2 are listed in Table 3-9.

Parameter		OS	MS 1	MS 2	Unit
extract mass flow rate	\dot{m}_{ext}^{exp}	16.78	17.93	18.38	g/min
raffinate mass flow rate	\dot{m}_{raff}^{exp}	4.68	3.72	3.07	g/min
bulk humidity of raffinate	H_{raff} {Eq. (3-7)}	78	72	66	wt.%

The change of the screw angle β influences the size of one screw segment and consequently the filling degree of dry leaves in one segment F_{ds} . For reaching a continuous process operation this parameter increases from 10.6% for OS up to 18.5% for MS 2 (Table 3-23). It needs to be noted that this filling degree is only a measure of stability by excluding the internal extract in solvent-soaked leaves or the compression at the PD. It cannot be used to evaluate the actual retention volume in the continuous process. This retention volume is calculated at the end of this section for MS 1 and MS 2.

Table 3-23: Filling degree of dry leaves in one screw segment for OS, MS 1 and MS 2. The calculation is based on OP 2 (n = 2.2 rpm, $\dot{m}_{ds} = 1.05$ g/min)

	1 , us c.				
		OS	MS 1	MS 2	Unit
mass in one screw segment	m_{ds}^{1} {Eq. (3-15)}	0.48	0.48	0.48	g
total capacity in one screw segment	$m_{ds,tot}^{1}$ {Eq. (3-16)}	4.52	3.4	2.6	g
filling degree of dry leaves	F_{ds} {Eq. (3-14)}	0.106	0.141	0.185	-

RTD of the solvent-soaked A. annua leaves

The RTD for solvent-soaked leaves was measured as described in subsection 3.4.4. RTD curves for LSP 1 - SP 4 for three repetitions (in total 12 curves) are shown in Figure 3-28 while the averaged curves are presented in Figure 3-29. These averaged RTD curves show similar maximum peaks for OS, MS 1 and MS 2. Especially for MS 2 a second smaller peak is visible for LSP 2 - SP 4. This double peak is very present in the actually measured RTD curves in Figure 3-28 (b). It comes from flow in parallel paths due to channelling, causing a higher amount of back-mixing inside the extractor compared to OS. This effect results from the higher filling degree in MS 2 changing the flow pattern inside the screw reactor [WPT+07], [NvR+15].

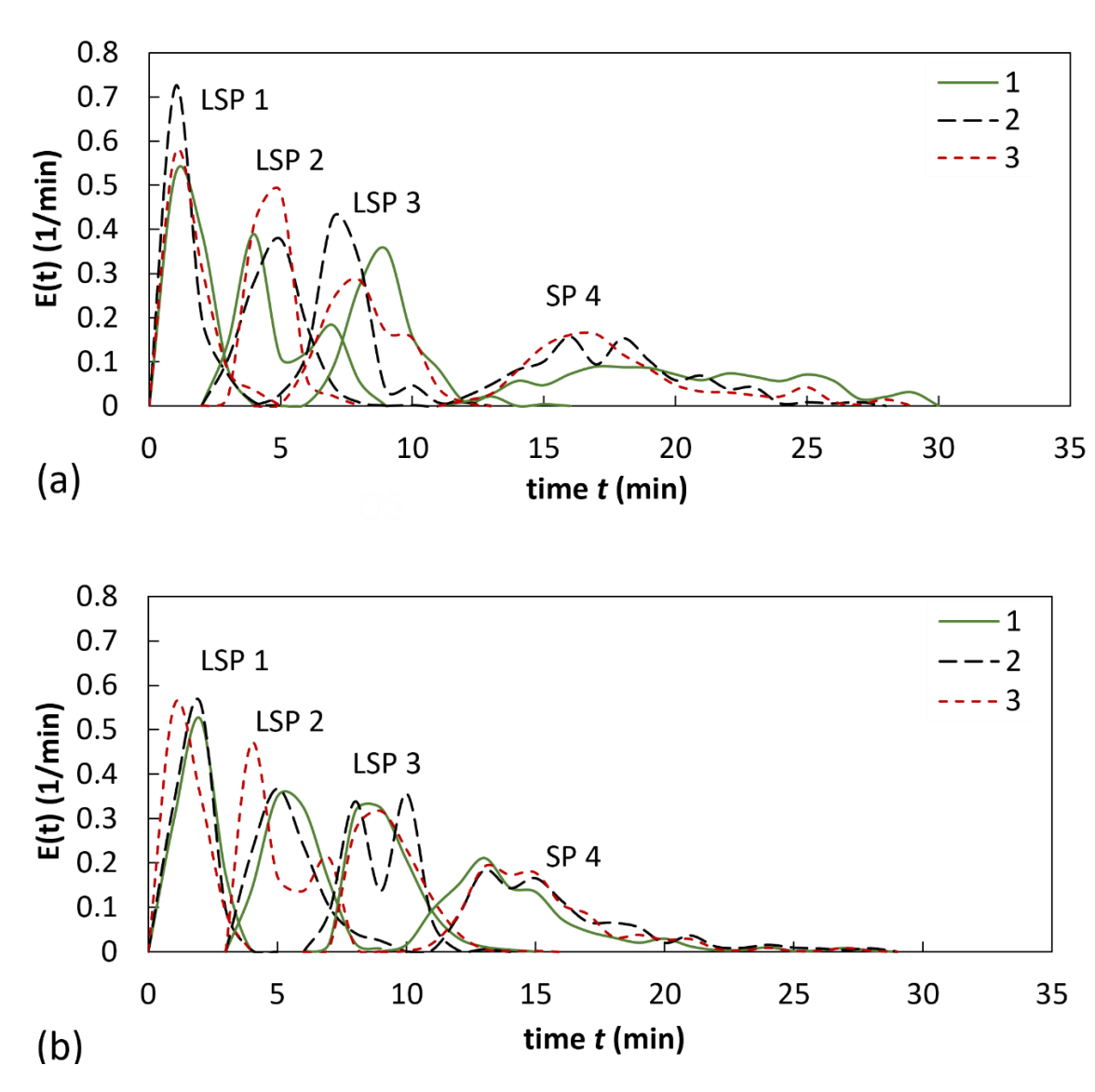


Figure 3-28: RTD curves for (a) MS 1 and (b) MS 2 for sampling points LSP 1 - SP 4, showing three identical repetitions of the same experiment (reproduced from [AlH24]).

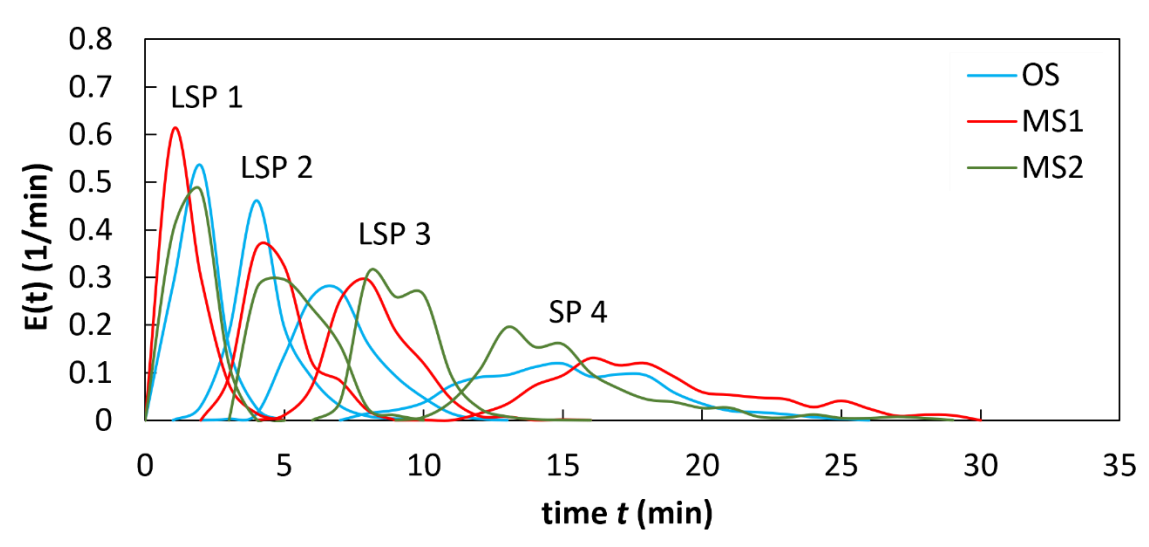


Figure 3-29: Averaged solid phase RTD curves with screw designs OS, MS 1 and MS 2. Results are based on three identical runs (reproduced from [AlH24]).

Back-mixing effects usually increase the mean residence time (MRT) and the standard deviation [WPT+07], [CBD+23]. This expected increase for a decreased screw angle is visible in Table 3-24 (at LSP 3 from OS: 7.31 min to MS 2: 9.18 min). The expected increase of standard deviation due to the apparent second peak is not significant and only appears at LSP 2 (OS: 1.05 min; MS 2: 1.16 min). Furthermore, at SP 4 the MRT increases from OS (15.45 min) to MS 1 (18.53 min) but decreases again to MS 2 (15.17 min). This can be related to the change of bulk humidity at the raffinate outlet. As shown in Table 3-22 the bulk humidity decreases from OS to MS 2, which would be expected to lead to higher cake compaction and consequently higher residence times. The inconsistency at MS 2 could be caused by a higher transport efficiency of the screw geometry leading to a lower residence time as theoretically expected.

The number of stages N_s for the modified screws still increase from LSP 1 to LSP 3, as already investigated with OS. For the averaged RTD curves, the theoretical number of stages N_s at LSP 3, located inside the extractor, increases from 33 (OS) to 57 (MS 2) (Table 3-24). The corresponding Bodenstein numbers increase from 66 (OS) to 114 (MS 2) as shown in Figure 3-24 and support the characterisation of a PFTR behaviour (Bo > 100) [Lev12]. Nevertheless, MS 1 should be used in preference to MS 2, since the application of MS 2 introduces back-mixing effects for the solvent-soaked leaves (as seen in Figure 3-24), leading to a channelling of the flow.

Table 3-24: Mean residence time and standard deviation for OS, MS 1 and MS 2. The operation conditions of the used OP 2 are listed in Table 3-9.

Parameter			Pos	sition		Unit
		LSP 1	LSP 2	LSP 3	SP 4	
			0	S		
mean residence time	$ar{ au}$ {Eq. (2-31)}	1.59 ±	4.61 ±	7.31 ±	15.45 ±	min
standard deviation	$\pm \sigma$ {Eq. (2-32)}	0.68	1.05	1.27	3.25	min
theoretical number of stages	$N_{_S}$ {Eq. (2-33)}	5	19	33	23	
	MS 1					
mean residence time	$\bar{\tau}$ {Eq. (2-31)}	1.50 ±	4.81 ±	8.20 ±	18.53 ±	min
standard deviation	$\pm \sigma$ {Eq. (2-32)}	0.69	1.14	1.28	3.56	min
theoretical number of stages	$N_{_S}$ {Eq. (2-33)}	5	18	41	27	
	MS 2					
mean residence time	$\bar{\tau}$ {Eq. (2-31)}	1.73 ±	5.39 ±	9.18 ±	15.17 ±	min
standard deviation	$\pm \sigma$ {Eq. (2-32)}	0.66	1.16	1.22	3.08	min
theoretical number of stages	N _s {Eq. (2-33)}	7	22	57	24	

Table 3-25: Stage number and Bodenstein number for OS, MS 1 and MS 2 of the solvent-soaked leaves at LSP 3 with operation conditions of OP 2 (see Table 3-9).

		OS	MS 1	MS 2	Unit
theoretical number of stages	N_s {Eq. (2-33)}	33	41	57	-
Bodenstein number	Bo_s {Eq. (2-44)}	66	82	114	-

Efficiency of screw-driven transport

After the discussion for design OS in subsection 3.4.5, Table 3-26 shows that the decrease of the screw angle β results in an increase of the transport efficiency from 46% (OS) to 69% (MS 2). These values are quite high compared to literature (only 24 - 32% in [WPT+07]).

Table 3-26: Screw-driven transport efficiency for OS, MS 1 and MS 2 for OP 2.

			,		
Parameter		OS	MS 1	MS 2	Unit
exp. axial velocity	$\bar{u}_{ax,exp}$	4.41	4.26	3.74	· 10 ⁻⁴ m/s
th. axial velocity	$ar{u}_{ax}$ {Eq. (2-46)}	9.52	7.05	5.43	· 10 ⁻⁴ m/s
transport efficiency	η {Eq. (2-45)}	0.46	0.60	0.69	-

A high transport efficiency ensures a smooth and sharp transportation of leaves through the extractor. This allows a good exchange of exhausted leaves with fresh leaves. Nevertheless, a balance between transport efficiency and back-mixing behaviour introduced by the higher filling degree of the screw needs to be found.

Phase retention volume

Based on the previously derived information the solid phase retention volume inside the extractor can be estimated for MS 1 and MS 2. For these calculations the mass flow rate of raffinate \dot{m}_{raff} in front of the perforated disk is of interest {Eq. (3-11)}. This mass flow rate is constant for all screw geometries, as the operating conditions are identical. The MRT in front of the perforated disk $\bar{\tau}_s$ is of importance for estimating the retention volume as stated in subsection 3.4.6. It can be calculated with Eq. (3-19) using the screw-specific transport efficiency and theoretical axial velocity in Table 3-26.

The retention volume is calculated according to Eq. (3-21) with the density of the solvent-soaked leaves ($\rho_s = 922 \text{ kg/m}^3$, Table 3-5). The results show that the retention volume increases from OS to MS 2 by 17% (OS: 5.90· 10^{-5} m³, MS 2: 7.04· 10^{-5} m³), as expected, providing higher extractor loading with increased screw angle (Table 3-27).

Table 3-27: Retention volume of solid leaves with OS, MS 1 and MS 2. The density of the solvent-soaked leaves is $\rho_s = 922 \text{ kg/m}^3$ (Table 3-5).

Parameter		OS	MS 1	MS 2	Unit
mass flow rate of solid leaves	\dot{m}_{raff} {Eq. (3-11)}	9.35	9.35	9.35	$\cdot10^{-5}~\text{kg/s}$
MRT of solid leaves	$\bar{\tau}_{s}$ ' {Eq. (3-19)}	9.70	10.24	11.57	min
solid phase ret. volume	$V_{\rm s}$ {Eq. (3-21)}	5.90	6.23	7.04	$\cdot~10^{-5}~{ m m}^{ m 3}$

This section demonstrates that decreasing the screw angle, resulting in smaller screw segments, reduces the bulk humidity and thereby increases the extract mass flow rates. This effectively reduces solvent waste. While mean residence times decrease, the standard deviation remains nearly constant, enhancing the near-PFTR behaviour of the extractor regarding the leaves transportation process. However, the higher filling degree of MS 2 leads to increased back-mixing within the extractor, making it unsuitable for further application. Nevertheless, the screw design of MS 1 was found to be promising and should be tested in future studies.

3.6 Transferability of the results to toluene as real solvent

The results of the continuous steady-state operation presented so far characterise the process without actually extracting artemisinin with an appropriate solvent — since only water is used. This major assumption was necessary due to safety restrictions with toluene. In this way more information about the process hydrodynamics by using a glass extractor and taking probes from inside the process could be received. This information is essential for a better understanding and the basis for developing a CFD model. Similar experiments by using an efficient solvent, e.g., toluene are not possible due to safety requirements.

Nevertheless, the transferability of the results with water to toluene is now examined (1) hydrodynamically by adapting the kinematic viscosity, and (2) experimentally with real extraction in a steel-setup without probe taking by observing only steady-state operation points.

3.6.1 Hydrodynamics

Regarding hydrodynamics, the only difference between water and toluene results from their difference in kinematic viscosity (at 20°C: 32%, see Table 3-28). By adapting the kinematic viscosity of water to toluene thanks to a water temperature of 38°C the hydrodynamic properties become identical, since the Reynolds number is the same {Eq. (3-1)}. The process temperature of water was regulated in these experiments with a temperature control unit (93704220122 VT2, ANTON PARR GmbH, Graz, Austria), maintaining a stable temperature over time. As water flows from the inlet to the outlet, the temperature drops by only 5%, ensuring stable operation conditions.

Table 3-28: Adaption of kinematic viscosity of water to the efficient solvent toluene [AP23].

Parameter		toluene	water	Unit
kinematic viscosity	υ	0.68 (20°C)	1.002 (20°C) 0.683 (38°C)	· 10 ⁻⁶ m²/s · 10 ⁻⁶ m²/s

RTD of the solvent (water) at 38°C

The residence time distribution of water as solvent with an increased temperature of 38°C was measured at the extract outlet as described in subsection 3.4.4 for OP 2. The resulting tracer concentration curve is used to calculate the residence time distribution {Eq. (2-28)}. Compared to the RTD curve of water at 20°C (subsection 3.4.4), the RTD curve at a temperature of 38°C is very similar (Figure 3-30). The peak of the curve is slightly shifted to the right, but its maximum is at the same level. The deviations between the three replicates, visible as error bars, are very small, indicating high reproducibility. Table 3-29 demonstrates that the standard deviation is identical (20°C and 38°C: 2.5 min), while the mean residence time is lower by only 3% (0.1 min = 6 s). The resulting Bodenstein number equals a value of 6 for both setups. This proves that the hydrodynamic behaviour of toluene or water as solvent is almost the same and water can safely be used to investigate the process.

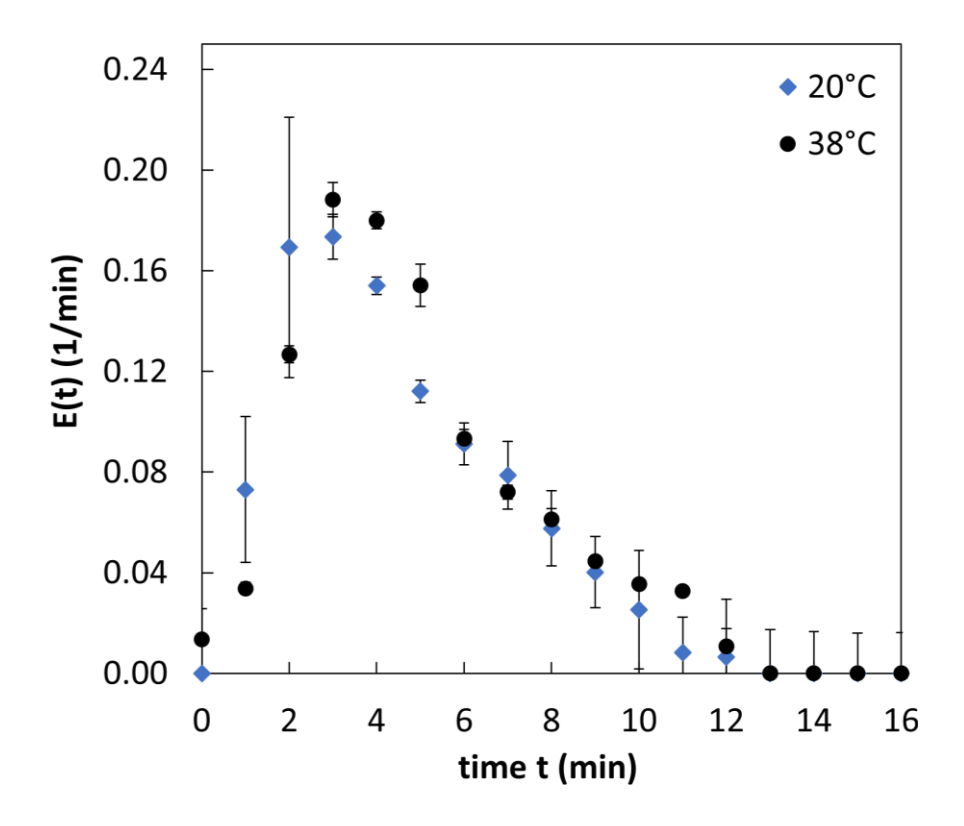


Figure 3-30: RTD curves of the solvent (water) at $T = 20^{\circ}$ C (blue) and at $T = 38^{\circ}$ C (black).

Table 3-29: Residence time distribution of the solvent water at $T = 20^{\circ}$ C or 38°C.

Parameter		<i>T</i> = 20°C	<i>T</i> = 38°C	Unit
mean residence time	$\bar{ au}_{l}$ {Eq. (2-31)}	4.5	4.4	min
standard deviation	σ_l {Eq. (2-32)}	2.5	2.5	min
theoretical number of stages	N_l {Eq. (2-33)}	3	3	-
Bodenstein number	Bo _{l} {Eq. (2-41)}	6	6	-

RTD of the solvent-soaked leaves (with water at 38°C)

The solid phase RTD curves were measured in three identical trials at all four sampling points, similar to subsection 3.4.4. For comparison with the RTD curves measured at 20°C, the average curves from the three trials were used. Figure 3-31 shows a very good shape match between the two curves for LSP 1 and LSP 3, but deviations for LSP 2 and SP 4. The largest difference appears at LSP 4 with 23%, behind the perforated disk. This difference may be due to slight variations in extraction cake humidity. However, for LSP 3 in front of the extraction cake, an excellent agreement between the two RTD curves can be detected with variations below 5% for the mean residence time (Table 3-30). The resulting stage number N_s differs slightly for the two temperatures (at LSP 3: $20^{\circ}\text{C} - 33$, $38^{\circ}\text{C} - 28$) but represents similar flow characteristics.

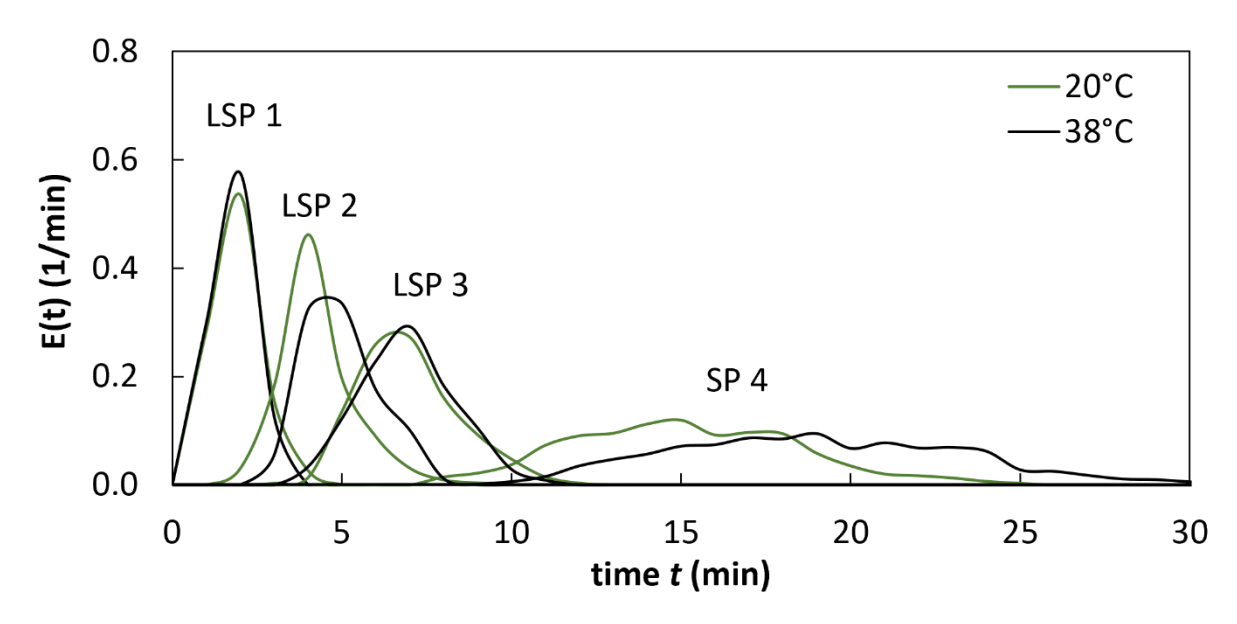


Figure 3-31: Averaged solid phase RTD curves for a process temperature of $T = 20^{\circ}\text{C}$ (green) and 38°C (black). The values were calculated by averaging over three identical trials for each sampling point (LSP 1 – SP 4).

Table 3-30: RTD of the A. annua leaves with water as solvent at $T = 20^{\circ}$ C or 38°C.

T	Parameter	LSP 1	LSP 2	LSP 3	SP 4	Unit
20°C	$\bar{\tau_s} \pm \sigma_s$ {Eqs. (2-31), (2-32)}	1.6 ± 0.7	4.6 ± 1.0	7.3 ± 1.3	15.5 ± 3.2	min
	N_s {Eq. (2-33)}	5	21	33	23	
38°C	$\bar{\tau_s} \pm \sigma_s$ {Eqs. (2-31), (2-32)}	1.8 ± 0.6	5.0 ± 1.0	6.9 ± 1.3	18.9 ± 3.9	min
	N_s {Eq. (2-33)}	9	25	28	23	

In conclusion the presented RTD measurements show only small deviations between water at a temperature of 20°C and 38°C. From a hydrodynamic point of view, similar results can therefore be expected when using either water or toluene as solvent. This allows the

transferability of the presented experimental results in section 3.4 and 3.5 (based on water) to the real extraction process using toluene.

3.6.2 Continuous operation with toluene

The glass extractor used in this work with the solvent water has identical dimensions but is shorter by a factor 2 compared to the steel extractor developed at the MPI Magdeburg. This steel extractor was used by Vu to perform real extraction of artemisinin from A. Annua leaves with the solvent toluene [Vu23]. A transfer of the characterised operation points 2 and 3 from the glass extractor defined in subsection 3.4.2 to the real extraction process in the steel setup with toluene is now to be attempted. The lower limit, OP 1, is irrelevant since only small amounts of A. annua leaves are introduced to the process, resulting in minimal ARTE extraction.

This transfer requires a consideration of the different storage factors for water ($S_{H_2\,O}=4.34$) and toluene ($S_{tol}=2.25$, see again subsection 3.2.3). This storage factor influences the solid-liquid ratio R since the A. Annua leaves soak more water compared to toluene, resulting in less free (external) solvent mass in the extractor. This affects the hydrodynamics and stability of the process. To compare both setups the transfer relation Tr between solid-liquid ratio R and the storage factor S_i is used, where j denotes the solvent material:

$$Tr = R \cdot S_j = \text{const.}$$
 (3-25)

Transfer to reference operation point 2

Vu already reported a steady-state of the steel setup by using toluene as solvent and a rotation rate of 2.2 rpm [Vu23]. This operation point is similar to the defined reference OP 2 in this thesis (subsection 3.4.2). Table 3-31 shows similar input mass flow rates of dry leaves by using the solvent water or toluene (water: $0.175 \cdot 10^{-4}$ kg/s, toluene: $0.2 \cdot 10^{-4}$ kg/s). The small deviation may be due to measurement uncertainties in the closed steel setup: while the leaf mass flow in the glass extractor can be measured correctly before each experiment, the mass flow in the steel setup was calibrated once before the extractor was completely closed (see Figure 1-3). Re-validation is not possible, which can lead to errors. Nevertheless, the dimensionless transfer relation Tr {Eq. (3-25)} resulting from the product of solid-liquid ratio

R and storage factor S_j is nearly identical (water: 0.22, toluene: 0.23). The estimated filling degree of one screw segment with dry leaves F_{ds} also differs only slightly (water: 11%, toluene: 12%). The final extract mass flow rate with the solvent toluene was detected with \dot{m}_{ext}^{OP2} = 10.1 g/min, which is lower than the measured water mass flow rate with the glass extractor (16.78 g/min) due to differences in the solid-liquid ratio R. The applicability of OP 2 for both, water and toluene is proved.

Table 3-31: Steady-state operation conditions with n = 2.2 rpm using water or toluene. The operation conditions for using toluene [Vu23] are similar to OP 2 in this thesis.

Parameter		Operation point 2 (ref)			
		water	toluene		
		Value		Unit	
mass flow rate of dry leaves	\dot{m}_{ds}	0.175	0.20	$\cdot 10^{-4} \text{ kg/s}$	
mass flow rate of solvent	\dot{m}_l	3.465	1.95	$\cdot~10^{-4}~$ kg/s	
solid-liquid ratio	R {Eq. (3-9)}	0.05	0.10	kg/kg	
screw rotation speed	n	2.2	2.2	rpm	
filling degree of dry leaves in one	F_{ds} {Eq. (3-14)}	0.11	0.12	-	
segment		0.11	0.12		
transfer relation	$Tr\{ Eq. (3-25) \}$	0.22	0.23	-	

Transfer to the upper limit operation point 3

For finding more steady-state operation points with the steel setup, the upper limit of the defined operation window in this thesis (OP 3 with n=2.5 rpm, see subsection 3.4.1) has been reproduced using toluene as solvent. This process could be run for more than two hours, proving stability (Table 3-32). The slightly higher solid-liquid ratio R for toluene of 0.105 compared to 0.1 (OP 2, Table 3-31) results from limitations of the solvent pump steps. This affects the transfer relation for toluene Tr showing a slightly higher value than for water (water: 0.22, toluene:0.24). Overall, similar operation conditions for a steady-state are proved.

Table 3-32: Steady-state operation conditions with n = 2.5 rpm using water or toluene. The operation conditions for using toluene are similar to OP 3.

Parameter			Operation point 3			
		water	toluene			
		Value		Unit		
mass flow rate of dry leaves	\dot{m}_{ds}	0.2	0.21	$\cdot~10^{-4}~$ kg/s		
mass flow rate of solvent	\dot{m}_l	4.0	2.0	$\cdot~10^{-4}~$ kg/s		
solid-liquid ratio	R {Eq. (3-9)}	0.05	0.105	kg/kg		
screw rotation speed	n	2.5	2.5	rpm		
filling degree of one screw segment	F_{ds} {Eq. (3-14)}	0.11	0.11			
transfer relation	<i>Tr</i> {Eq. (3-25)}	0.22	0.24	-		

The averaged extract mass flow rate was measured as \dot{m}_{ext}^{OP3} = 9.9 g/min. This value is slightly lower compared to OP 2 (\dot{m}_{ext}^{OP2} = 10.1 g/min), despite an increased solvent mass flow rate. This indicates a higher bulk humidity for the extraction cake and higher solvent waste for this operation point 3 compared to OP 2. Similar trends were observed with the glass extractor using water as solvent (subsection 3.4.2). The higher screw rotation rate in OP 3 of 2.5 rpm obviously affects both, leaf transport and solvent flow, pushing the solvent toward the perforated disk and diluting the cake. Although the process remains stable, the higher raffinate bulk humidity leads to a lower extract mass flow rate. This cannot be considered an optimal operating point compared to OP 2; therefore, OP 3 is not recommended.

To conclude, the transferability of the steady-state operating points 2 and 3 found in the glass extractor using water as solvent could be demonstrated when using the real solvent, toluene. This shows again that it is possible to carry out extensive experimental campaigns with water in order to get a better understanding of the process.

3.7 Summary

A continuous solid-liquid counter-current extraction process has been experimentally characterised in a horizontal screw-driven glass extractor by neglecting any mass exchange processes. The use of water as solvent instead of an efficient but highly explosive solvent like toluene allows optical observations as well as sampling from inside the process. In this way, the counter-current process could be analysed in detail to improve the understanding of operating conditions, material properties and phase residence time distributions during steady-state operation. This information will also support model development and validation using CFD. Nevertheless, the A. Annua leaves behave differently with the solvent water compared to toluene used for efficient extraction, in particular regarding the storage factor. This introduces deviations.

The operating window leading to a stable, steady-state extraction process has been identified. Such a continuous process already improves the extraction efficiency of artemisinin by reducing loading and unloading time and solvent waste. Unfortunately, this window is quite small and is limited by the screw rotation speed, the ratio of pulverised A. annua leaves to solvent, and the mass flow rate of dry leaves entering the extractor. Three operating points within the operation window (upper limit, lower limit, centre) were used for further

investigations, while the central point was used as reference operation point (OP 2). The key results are summarised in Table 3-33.

Table 3-33: Summary of important parameters after experimental investigations of the steady state operations. The examined operation points OP 1, OP 2 and OP 3 with parameters listed in Table 3-9 are taken from the identified operation window with limits listed in Table 3-8.

Parameter		OP 1	OP 2 (ref)	OP3	Unit
Steady state operation - OS					
operation pressure	p_{st}		1.2		·10 ⁵ Pa
pressure window	p_{min}, p_{max}		[1.1, 2.2]		·10⁵ Pa
RTD analysis - OS					
stage number liquid phase	N_l	4	3	4	-
average stage number liquid phase	\overline{N}_l		≈ 4		
stage number solid phase	N_s (LSP 3)	44	33	20	-
total average stage number	$\overline{N}\;(\overline{N}_l,N_s)$	-	≈ 18	-	-
Apparatus - OS					
transport efficiency	η	0.502	0.463	0.403	-
average transport efficiency	$ar{\eta}$		≈ 0.46		-
liquid phase volume fraction	$arepsilon_{exp}'$	0.58	0.55	0.61	-
RTD analysis - MS 1					
stage number solid phase	N_s (LSP 3)	-	41	-	-
RTD analysis - MS 2					
stage number solid phase	N_s (LSP 3)	-	57	-	-

The pressure distribution inside the extractor was measured using sensors at several sampling points. As expected, a noticeable pressure increase compared to atmospheric pressure occurs at the level of the perforated disk with $p_{st} \approx 1.2 \cdot 10^5$ Pa. The disk influences the stability of the induced compression cake formed by solvent-soaked leaves. Reducing the diameter of the holes in the disk from 5.5 mm (initial) to 5 mm slightly increases the pressure at this level. This stabilises the compression cake, resulting in a smoother extraction process and a reduction in solvent waste.

Then, the residence time distributions (RTDs) of the solid and liquid phases were measured, which differ significantly for this heterogeneous system. An increasing stage and Bodenstein number with axial length confirms a constant relation, indicating a consistent diffusion coefficient. The high Bodenstein number at LSP 3 reflects narrower RTD curves, approaching near-PFTR behaviour, which reduces elution volumes and enhances extraction efficiency.

The same parameter for the solvent phase is quite low, indicating a near-CSTR behaviour with high axial mixing. This supports high contact surfaces between leaves and solvent. For model development where a pseudo-homogeneous system is assumed as simplification, only one value for the stage number can be applied. Here, a mean value of \overline{N} (\overline{N}_l, N_s) = 18 between liquid and solid phase (at LSP 3) is assumed. Overall, the operation of the current apparatus with a shorter length compared to the steel setup seems to be already well designed.

Observations at three steady-state operating points revealed a consistent transport efficiency of the soaked leaves through the rotating screw, with $\bar{\eta} \approx 0.46$. Partial filling, including a gas phase (air) on the top is detected, significantly affecting hydrodynamic flow properties due to the solvent's free surface. A complete filling of the extractor was unattainable in steady-state operation due to the described operation constraints.

The process conditions can be slightly influenced by increasing the screw angle, leading to higher transport efficiency and higher retention volumes. Also the Bodenstein number of the solid phase becomes higher, strengthening the near-PFTR behavior. However, at higher filling degrees, back-mixing of solvent-soaked leaves occurs.

Finally, it was demonstrated that the obtained process information is hydrodynamically transferable to the solvent toluene by heating the water phase to adjust the Reynolds numbers. Extraction experiments in the steel setup showed consistency in operating points and similar process limits.

Answers:

- 1. How can a steady-state counter-current extraction process be operated and what are the material properties, phase distributions and possible optimisation potentials during this operation?
 - Only a relatively small operation window was examined depending on the solid-liquid ratio, the filling degree and the screw rotation speed. This operation window could not be extended significantly by geometrical or material variations. The solvent-soaked leaves share similar material properties to their equilibrium state in a batch reactor. An assumption as highly viscous fluid is acceptable, though the real behaviour corresponds more to a solid.
- 2. What are the residence time distributions for the phases involved in a steady-state operation and how do they characterise the reactor?
 - > The solid-phase residence time fits the extraction kinetics determined in batch

experiments. A near-PFTR behaviour is found for the leaves. The solvent residence time is significantly smaller and corresponds to a near-CSTR behaviour. To model the heterogeneous system with the proposed pseudo-homogeneous model, a mean stage number of \overline{N} (\overline{N}_l , N_s) = 18 can be specified based on experimental investigations.

- 3. Are the hydrodynamic results obtained with water as solvent transferable to the extraction process using the solvent toluene?
 - An adapted Reynolds number for water shows nearly identical RTD behaviour. The steady-state operation points are similar, confirming a good transferability of results.

4 Numerical simulations and validation

The experimental investigations of the previous chapter provide important information about the counter-current extraction process in steady-state operation. Thanks to the improved understanding of the complex process a numerical model is developed in this chapter using Computational Fluid Dynamics (CFD). The major goal is to represent the RTD behaviour of solid and liquid phase and provide a model for later optimisation.

First, requirements on flow simulation based on experimental observations are summarised as a basis for model selection. After mesh generation and an intensive mesh independence study a simplified single-phase flow is represented and compared with experimental measurements. Subsequently, multiphase models available in the software Simcenter STAR-CCM+ (2302 Build 18.02.008) are compared regarding their options and limitations in respect to hydrodynamics. Based on these available options, two multiphase flow simulations have been performed to represent the counter-current flow and the phase residence times. A validation with experiments is finally performed for the three steady-state operation points, as defined in subsection 3.4.2. For all numerical simulations the high-performance computing (HPC) cluster "Sofja" was used (292 nodes with an InfiniBand-connection; 2 x 16 cores Ice Lake Xeon 6326 with 256 GB RAM, peak performance: > 0.7 PFlops).

Scientific questions:

- 1. Which multiphase flow models are available to simulate the complex counter-current screw-driven process in terms of hydrodynamics?
- 2. What is the specific distribution of the involved phases at steady-state?
- 3. Is it possible to accurately represent the residence time behaviour of both solid and liquid phases using CFD?

4.1 Computational Fluid Dynamics

Computational Fluid Dynamics (CFD) use digital computers to simulate fluid flow processes. With the exception of certain special cases, like the laminar flow over a flat plate, real-world fluid flow problems, such as the considered extraction process studied in this thesis, are incredibly intricate and cannot be solved through analytical methods. In these situations, CFD is employed to find a solution. This involves solving a system of differential equations, becoming algebraic equations after a discretisation step. They are summarised as governing equations. This approach allows for a deeper understanding of the flow processes and the generation of quantitative results. Numerical solutions are often more cost-effective than experimental ones and are implemented in various applications of process engineering, environmental sciences, and physics [LO18]. However, discretisation involves various approximations, making validation an essential component of the research.

4.1.1 Governing equations

For characterising a hydrodynamic system, it is necessary to analyse and preserve its governing equations consisting of mass, momentum (in three dimensions) and energy. Since the extraction process in this thesis operates at constant temperature, the energy conservation equation is not considered. The general mass and momentum equations are presented below, with further derivations provided, e.g., in [Wen08], [FP20], [LO18].

Mass conservation

A basic assumption for describing the mass conservation is an estimated control volume in cartesian coordinates. This control volume is permeated by a fluid with a specific mass flow rate which enters or exits through the side surfaces. This mass conservation equation, also called continuity equation, can be described with:

$$\frac{\partial \rho}{\partial t} + \nabla \cdot (\rho \mathbf{u}) = 0 \tag{4-1}$$

where the term $\nabla \cdot (\rho \mathbf{u})$ represents the divergence, with ρ indicating the density of the fluid and \mathbf{u} the velocity vector in three dimensions (u_x, u_y, u_z) . Based on the investigated control volume, Eq. (4-1) can also be expressed by an integral form using the side area A:

$$\frac{\partial}{\partial t} \int_{V} \rho \ dV + \oint_{A} \rho \mathbf{u} \ dA = 0 \tag{4-2}$$

For incompressible flows with constant density as water in this thesis Eq. (4-1) can be further simplified to Eq. (4-3).

$$\nabla \cdot \mathbf{u} = 0 \tag{4-3}$$

Momentum conservation

The momentum of a material system changes due to the action of external forces. The resulting momentum equations can be described in their coordinate-free form as follows:

$$\rho \frac{D\mathbf{u}}{Dt} = \rho \mathbf{g} - \nabla p + \nabla \cdot \mathbf{T} \tag{4-4}$$

Thereby, \mathbf{g} represents the gravitational vector, p the pressure and \mathbf{T} the viscous stress tensor. Using a viscous flow with an isothermal, incompressible Newtonian fluid as in this thesis leads to:

$$\rho \frac{D\mathbf{u}}{Dt} = \rho \mathbf{g} - \nabla p + \mu \nabla^2 \mathbf{u} \tag{4-5}$$

or in integral form:

$$\rho \int_{V} \frac{D\mathbf{u}}{Dt} dV = \rho \int_{V} \mathbf{g} \, dV - \oint_{A} p \, dA + \oint_{A} \mathbf{T} \cdot \mathbf{n} \, dA \tag{4-6}$$

with $\bf n$ defining the normal vector vertical to the area $\bf A$.

This equation is the simplest form of the so-called Navier-Stokes equation. Its final form can be presented as a three-scalar equation in a Cartesian coordinate system:

$$\rho\left(\frac{\partial u_x}{\partial t} + v_x \frac{\partial u_x}{\partial x} + v_y \frac{\partial u_x}{\partial y} + v_z \frac{\partial u_x}{\partial z}\right) = \rho g_x - \frac{\partial p}{\partial x} + \mu \left(\frac{\partial^2 u_x}{\partial x^2} + \frac{\partial^2 u_x}{\partial y^2} + \frac{\partial^2 u_x}{\partial z^2}\right)$$
(4-7)

$$\rho\left(\frac{\partial u_{y}}{\partial t} + v_{x}\frac{\partial u_{y}}{\partial x} + v_{y}\frac{\partial u_{y}}{\partial y} + v_{z}\frac{\partial u_{y}}{\partial z}\right) = \rho g_{y} - \frac{\partial p}{\partial y} + \mu\left(\frac{\partial^{2} u_{y}}{\partial x^{2}} + \frac{\partial^{2} u_{y}}{\partial y^{2}} + \frac{\partial^{2} u_{y}}{\partial z^{2}}\right)$$
(4-8)

$$\rho\left(\frac{\partial u_z}{\partial t} + v_x \frac{\partial u_z}{\partial x} + v_y \frac{\partial u_z}{\partial y} + v_z \frac{\partial u_z}{\partial z}\right) = \rho g_z - \frac{\partial p}{\partial z} + \mu \left(\frac{\partial^2 u_z}{\partial x^2} + \frac{\partial^2 u_z}{\partial y^2} + \frac{\partial^2 u_z}{\partial z^2}\right) \tag{4-9}$$

4.1.2 Boundary conditions

Solving the Navier-Stokes equations requires a definition of boundary conditions. These are conditions for the flow velocity components (u_x,u_y,u_z) and the pressure which are typically defined at the in-/ outlet surfaces and at the wall of the flow system. Stationary flows consist of a set of differential equations and boundary conditions, and are also called boundary value problems. The unsteady flow of the described extraction process with screw rotation further requires an initial condition, leading to an initial boundary value problem. Only the correct number of boundary conditions can lead to a unique solution of the simulation.

For viscous fluids the relative velocity at a stationary surface or wall becomes zero due to friction. This is called a *no-slip* condition. For moving walls (e.g., a rotating screw), the flow velocity becomes equal to the wall velocity. Numerical boundary conditions are calculated during the computation and connect the walls with the inner flow field. This becomes important if the field of integration is not equal to the boundaries of the flow field. The number of physical and numerical boundary conditions needs to match the number of conserved variables.

4.1.3 Sliding mesh approach

To represent the screw rotation of the extractor an efficient option in unsteady flows is the sliding mesh approach [DP90]. It requires a separate definition of moving and stationary geometry. In this method the mesh vertices are moved during every time step relative to the remaining stationary geometry. The transfer of flow variables is performed through an interface, connecting both parts. These should be as similar as possible concerning the cell size to ensure an accurate transfer of flow parameters. Full conformity is advisable but not required [Sie23]. Figure 4-1 shows two cells before the connection through the interface with small inconsistencies and different cell areas between them. When the cell faces are intersected to find a common face shared by the volumes centred at P and P_j, a volume change will occur on one side. Consequently, the moving surface or the faces of the moving volumes should be used as the reference. In this way, the faces of the rotating cells are projected onto the stationary surface to form new common faces, ensuring that the moving volumes stay unchanged [BAB04].

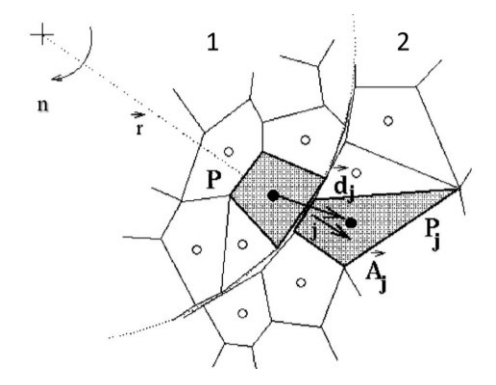


Figure 4-1: Unstructured mesh blocks before connection through interface. The flow direction is from the rotating geometry (1) with rotation rate n, radius vector \vec{r} and cell P to the stationary geometry (2) with cell P_j, cell area vector \vec{A}_j and cell centred distance vector to cell P of \vec{d}_j , reproduced from [BAB04].

In Simcenter StarCCM+ this approach can be implemented by defining a "rotating motion" with a user-defined axis direction and rotation rate. This approach is used for the investigated screw extractor to consider also the gap between screw and wall which is significant for the solvent flow. To ensure a feasible resolution of the gap cells, at least two cell layers should be defined. Due to the small gap thickness of 0.35 mm (section 3.1) this results in very small layer cells. A refinement of the adjacent rotating mesh towards the screw gap is required to ensure high mesh quality. Further details are presented in section 4.2 and 4.5.

4.1.4 Characteristic dimensionless numbers

For the classification of flows characteristic dimensionless numbers are widely used in fluid dynamics. A central parameter controlling hydrodynamic features is the **Reynolds number Re** which indicates the ratio between inertia forces and friction forces in a specific flow. Its general definition was already presented in subsection 3.6.1, Eq. (3-1).

$$Re = \frac{u L_{ch} \rho}{\mu} = \frac{u L_{ch}}{v}$$

For pipe flows a Reynolds number up to a value of 2 300 indicates a laminar flow behaviour. For larger Reynolds numbers the flow is considered as transitional, then turbulent [BS13].

For flows involving a solid phase as the A. Annua leaves, a **particle Reynolds number Re**_p can be defined. It involves the difference between the particles velocity u_s and the surrounding fluid u_l , presented in Eq. (4-10), where D_p is the particle diameter and u_l the fluid kinematic viscosity.

$$Re_{p} = \frac{D_{p}|u_{l} - u_{s}|}{v_{l}} \tag{4-10}$$

For particle Reynolds numbers below 1 the flow surrounding the particles is in a so-called Stokes regime. With an increase of Re_p a separation of the flow occurs while values of Re_p > 500 characterises turbulent flows [SB23]. For the present problem, all single-phase and multiple flows take place in the laminar regime.

The **Courant number** (or CFL number for Courant-Friedrichs-Lewy-number) is an import reference value regarding the discretisation of time-dependent partial differential equations and is defined with Eq. (4-11):

$$CFL = \frac{u \Delta t}{\Delta r}$$
 (4-11)

The variable u indicates the flow velocity, Δt the discretized time-step and Δx the mesh size. It is therefore a measure of how fast a fluid flows in relation to the specified mesh size. In order to achieve a stable simulation, the time step needs to be sufficiently small so that the calculated information can be transferred accurately from one mesh cell to the neighbouring

one. At the same time the computational costs significantly depend on the time step size. Explicit methods require a limit of $CFL \le 1$ for reaching accurate and stable results, while in fully-implicit methods, as used in this work, accurate solutions can still be reached with much higher CFL numbers [MW12], [HC97].

In continuum mechanics the dimensionless **Péclet number Pe** is relevant for studying transport phenomena. It defines the ratio between advective and diffusive transport rates. The Péclet number is derived by the product of Reynolds number Re and Schmidt number Sc or by a relation between the flow velocity u, the characteristic length L_{ch} and the axial diffusion coefficient D_{ax} , following Eq. (4-12) [Rap17].

$$Pe = Re \cdot Sc = \frac{u L_{ch}}{D_{ax}}$$
 (4-12)

Here, the **Schmidt number** Sc defines the ratio between the viscous diffusion rate and the axial diffusion rate of mass:

$$Sc = \frac{v}{D_{ax}}$$
 (4-13)

For a pipe flow the Péclet number is identical with the dimensionless Bodenstein number in Eq. (2-39) which serves as an alternative in the field of Chemical Reaction Engineering. In this thesis only the Bodenstein number, introduced in Eq. (2-39) will be used.

4.1.5 Discretisation

Apart from special cases such as the flat plate, no analytical solutions are known for the governing equations of fluid mechanics [Lec11]. Therefore, a differential equation system must be created, which can finally be solved numerically. The partial derivatives (differentials) are converted into finite differences or fluxes and transformed into discontinuous quantities. This method is called discretisation. Consequently, the flow variables can only be determined at the grid points or in the discrete cells [LO18]. For the solution of the partial differential equations, three main methods are distinguished which are the Finite-Difference-Method (FDM), the Finite-Volume-Method (FVM) and the Finite-Element-Method (FEM). The software Simcenter StarCCM+ used in the present thesis mainly applies the FVM. This method solves the governing equations in integral form for a defined control volume. The specific values of flow quantities like velocity or pressure are defined in the centre of the volume cells (cell-centred method) [Wil03].

4.1.6 Numerical meshes

A numerical computational mesh covers the investigated flow field. It consists of a specific number of grid points or cell volumes in space at which the flow quantities are calculated based on the selected discretisation method [LO18]. The quality of the computing mesh is highly important for the accuracy of the solution. There are several parameters to quantify the mesh quality, e.g. the volume change, face validity and the skewness angle. Especially the skewness angle θ is an important quality measure in this thesis. It represents the angle between a vector connecting the centroids of two adjacent cells dL and the (normal) face area vector \mathbf{n} of the connecting face (Figure 4-2). A skewness angle of zero defines a perfectly orthogonal mesh while angles <90° occur in concave cells, often leading to solver convergence issues. For a robust simulation a skewness angle <85° is recommended [Sie23].

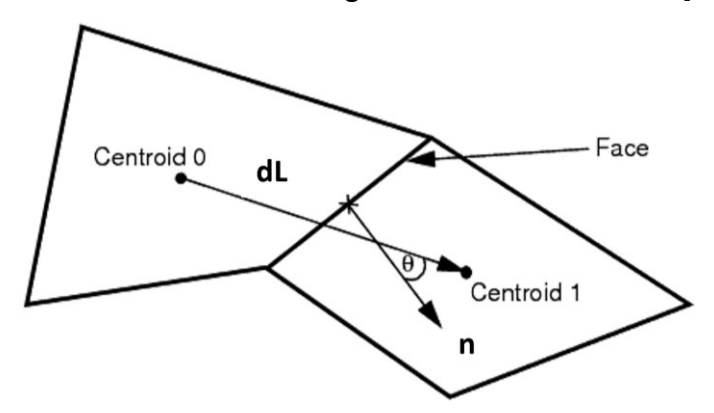


Figure 4-2: Scheme of the skewness angle θ between two adjacent cells. The vector \mathbf{dL} connects centroid 0 with centroid 1 while \mathbf{n} is the (normal) area vector of the connecting cell face. The skewness angle θ is the angle between these two vectors and should be < 85° to avoid solver instabilities. [Sie23].

The computational meshes can be categorised into structured, unstructured and block-structured meshes (Figure 4-3) [Kun12].

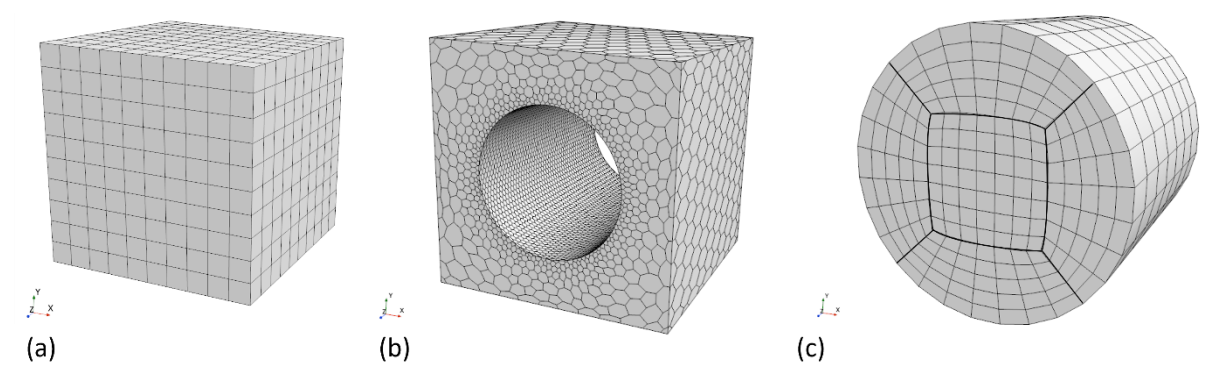


Figure 4-3: Types of numerical 3D meshes. (a) structured mesh, (b) unstructured mesh with polyhedral cells, (c) block-structured mesh with marked blocks.

In this thesis, only 3D simulations will be performed. A structured 3D mesh consists of hexahedral cells with a well-defined topology as presented in Figure 4-3 (a). They can only be applied to relatively simple solution areas but require a low cell number and introduce small numerical diffusion [MKK+20], [Lec11]. Unstructured meshes are often used for highly complex geometries and consist of tetrahedral, hexahedral or polyhedral cells. The meshes can be locally refined in certain areas at any time as presented in Figure 4-3 (b) with polyhedral cells. This allows very high flexibility. A disadvantage is the higher storage space requirement and lower accuracy compared to the structured mesh [Kun12]. Block-structured meshes consist of several composite structured mesh blocks as presented in Figure 4-3 (c) with bold lines. The combination of different mesh structures reduces the skewness of the mesh cells and results in a smaller termination error and a higher accuracy of the solution. Block-structured meshes can therefore also be used for more complex composite geometries [Lec11]. In the present study a block-structured mesh is employed despite the high complexity of the screw geometry involving tiny gaps between screw and wall.

4.2 Design of the computational geometry

The computational three-dimensional geometry is a virtual representation of the real experimental setup (see Figure 3-1). The screw rotation motion is described by the sliding mesh approach (subsection 4.1.3), separating the computational geometry into two parts, namely a Rotational domain (RD) and a Stationary domain (SD) connected by an in-place internal interface (Figure 4-4). Through this interface the flow variables are transferred for each rotation step between the RD and the SD. The SD results in a very small layer geometry encasing the RD. It has nevertheless an important role for the transition of the flow inside the extractor to the inlets and outlets. Mesh refinements were applied at the interface between the domains to accurately capture any leakage flows. The mesh design and resolution were determined based on a mesh-independence study (see section 4.5). The boundary conditions are adapted for each simulation setup.

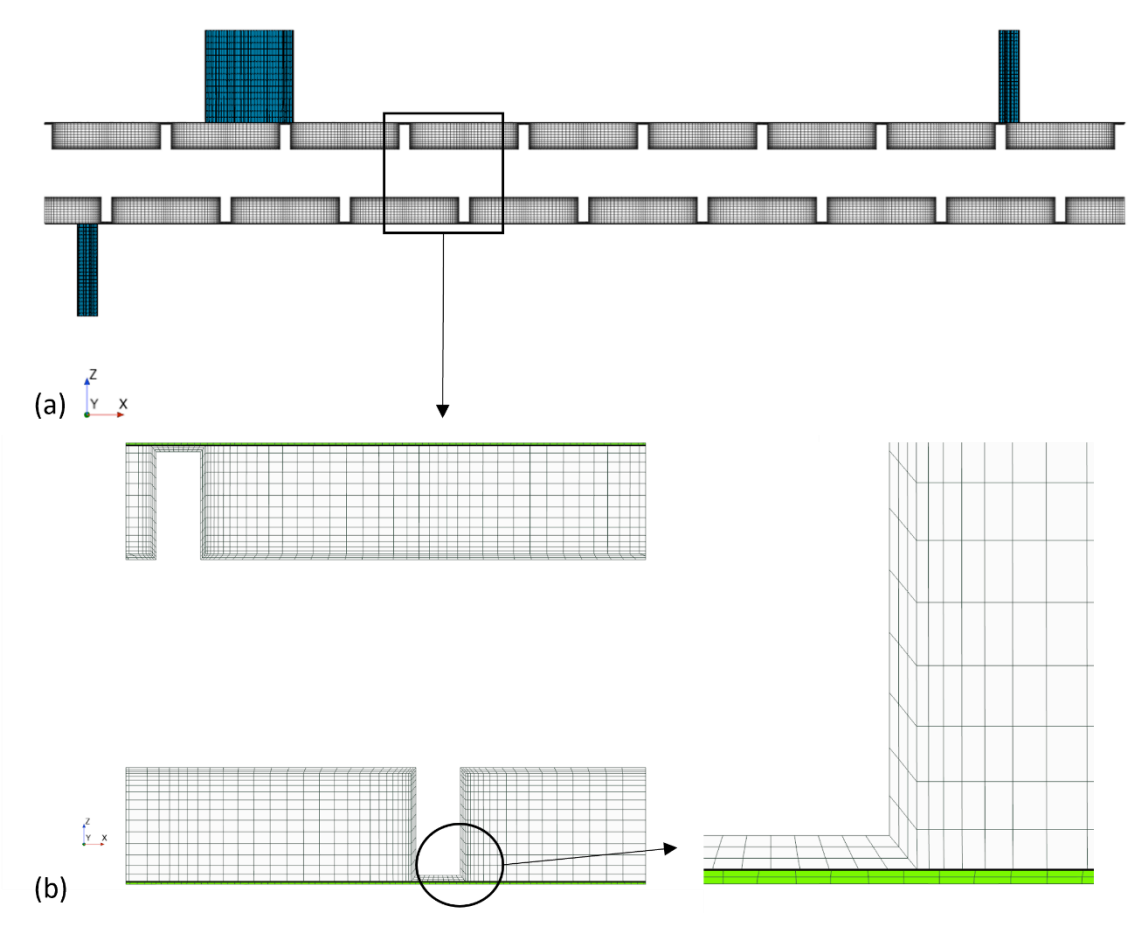


Figure 4-4: Screw extractor in xz-plane. (a) The in- and outlet geometries (blue) are connected to the Stationary domain (SD, green) by three internal interfaces, respectively, (b) A detail of one screw segment shows the connection of the Rotational domain (RD, white) and Stationary domain (SD, green) by one internal interface (black line).

4.3 Flow simulation requirements

For choosing appropriate simulation models representing the counter-current extraction process, information from the experimental investigations in chapter 3 are crucial. The process was examined as a three-phase multiphase flow. Besides the artemisinin-loaded A. annua leaves and the penetrating solvent, a gas phase (air) appears inside the extractor forming a free surface. The gas phase has no significant role in the extraction process. Nevertheless, a complete loading of the extraction device is not possible due to stability limits of the continuous process, as described in subsection 3.4.1. For validation of the CFD simulations, water is further used as solvent, as in all experiments.

The pressure inside the extractor equals nearly atmospheric pressure and only increases at the location of the extraction cake to a maximum of $p_{max} = 2.2 \cdot 10^5$ Pa (Figure 3-19). The characterisation of the solvent-soaked A. annua leaves showed a behaviour in-between solid and highly viscous non-Newtonian fluid (subsection 3.2.3). Optical observations showed that the particles agglomerate to a continuous phase during the wetting process. This continuous phase sticks at the screw pitch and is constantly transported forward by the screw.

The fluid Reynolds number {Eq. (3-1)} can be approximated according to a velocity derived from the solvent mean residence time for steady-state at OP2 of $\bar{\tau}_l$ = 4.5 min (subsection 3.4.4) and equals Re = 28. This low value shows that the process is laminar. This behaviour can be assumed for all steady-state processes inside the defined operation window. The screw rotation rate defines the particle Reynolds number. The maximum rotation rate of 2.5 rpm results in a particle Reynolds number of $\mathrm{Re}_p = 0.1$ using Eq. (4-10). This value is far below 1 resulting in a laminar (Stokes) flow regime. Consequently, turbulence models can be safely neglected in the simulation setup.

A significant process parameter for achieving efficient extraction is the mean residence time of the solvent-soaked A. annua leaves. This time should roughly equal t_{eq} = 10 min to fit the extraction kinetics determined in batch experiments by Vu as discussed in section 3.3. This long physical time is a high challenge for CFD simulations since it dramatically increases the computational effort. Consequently, simplifications are necessary to find accurate results within reasonable calculation times.

As a major simplification, mass exchange processes occurring in the actual extraction process are neglected in all CFD models to reduce computational costs. This assumption prevents the simulation of the actual artemisinin output mass fraction in the extract, but allows the

observation of all hydrodynamic phenomena. The extraction process will be later included back to the simulation by a coupling with a compartment model.

4.4 Multiphase flow models – possibilities and limitations

Multiphase flows comprise a mixture of fluids, including gases, liquids, and solids, occurring simultaneously within a single flow. Their prominence in numerous industrial applications highlights the significance of acquiring a comprehensive understanding of these phenomena. The complexity of the numerical representation of such multiphase flows is very high compared to single-phase flows since the apparent phase interface needs to be represented accurately where a jump in fluid properties, but also mass, momentum and energy transfer occurs. Several modelling approaches are available, which are summarised in this section.

4.4.1 Overview of available models

For modelling multiphase flows, they need to be classified according to their increasing spatial scales of interfaces of the involving phases into dispersed (bubbly flow, droplet flow), mixed/intermittent (slug flow, churn flow) and separated/stratified (film flow, annular flow, horizontal stratified flow). Often several flow regimes can occur in one multiphase flow domain as shown in Figure 4-5 [Sie23].

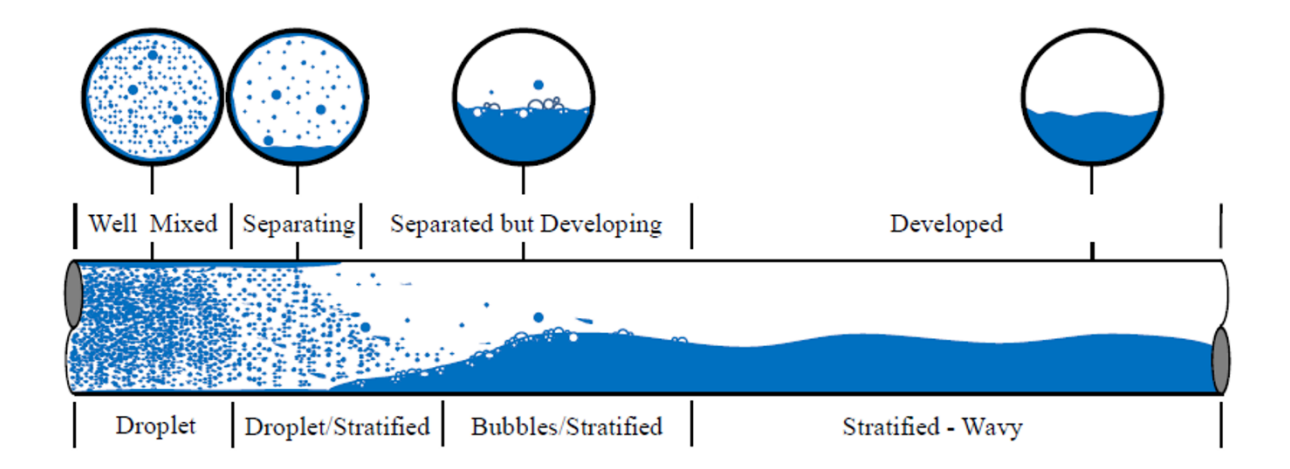


Figure 4-5: Example of several flow regimes in one domain, reprinted from [Sie23].

The research concerning simulations of multiphase flows is not finished. Some decisive physical mechanisms and complex flow dynamics cannot be represented yet. This complicates reaching a general agreement. Therefore, a thorough understanding of the flow properties to be simulated is essential for selecting the appropriate models. Numerical errors may still arise, particularly in the pressure correction method, due to algorithmic limitations. Simulation results should, therefore, always be validated with experimental results [Sie23], as done in the present study.

Simcenter StarCCM+ provides several multiphase flow models and options to consider all relevant flow properties of the investigated flow (Figure 4-6). These models are based on FVM or FEM, differing in their concept for describing the involved phases.

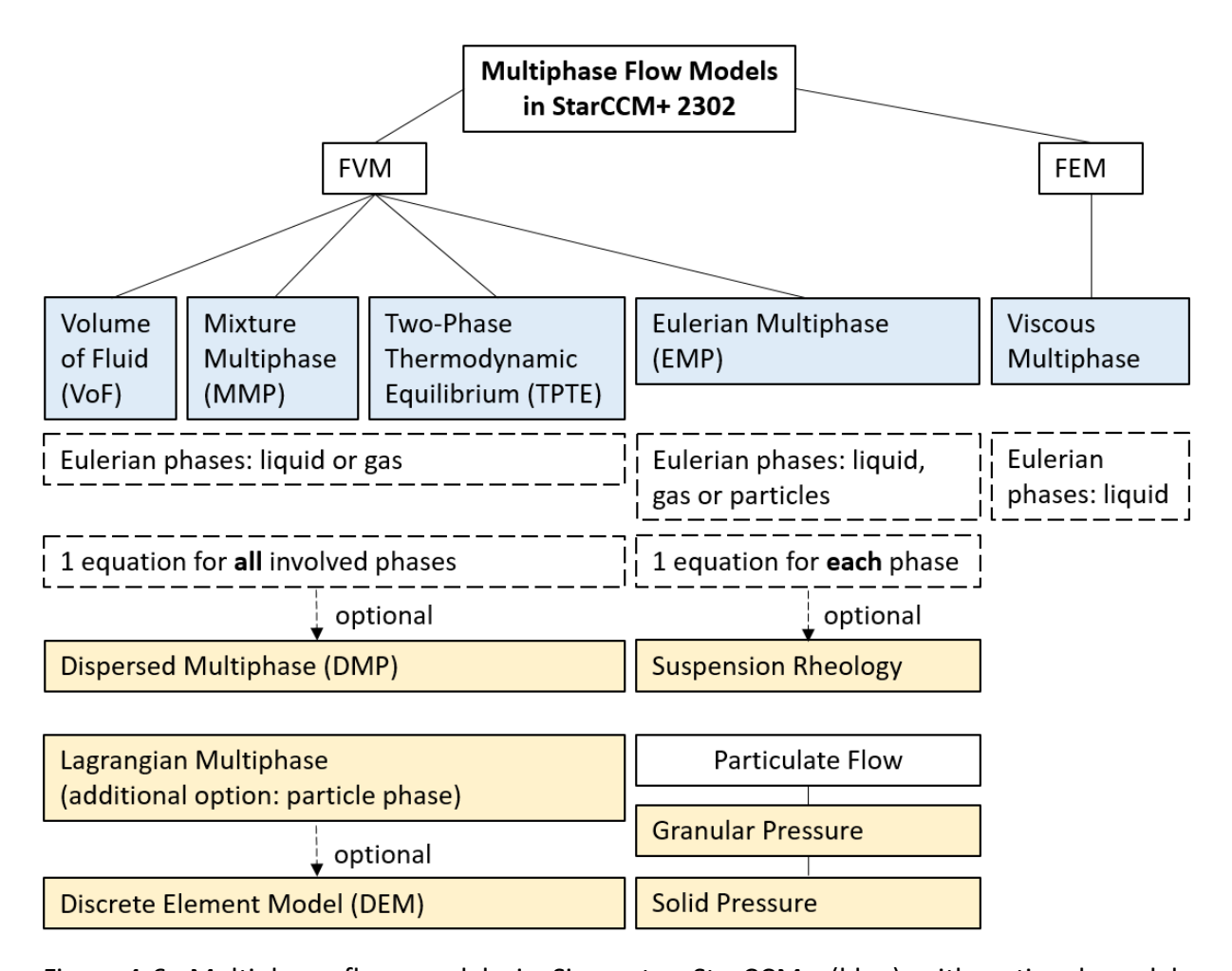


Figure 4-6: Multiphase flow models in Simcenter StarCCM+ (blue) with optional models (yellow).

Based on the FVM method, the Volume of Fluid (VOF), the Mixture Multiphase (MMP) model, the Two-Phase Thermodynamic Equilibrium (TPTE) model and the Eulerian Multiphase (EMP) model are available. These four main multiphase models are Eulerian-based approaches.

While the first three listed models allow for a definition of gas and liquid phases only, the EMP model also provides the selection of a particle phase. Furthermore, it solves one separate momentum equation for each defined phase while the VOF, MMP and TPTE model solve one common momentum equation for all involved phases. Thereby, the TPTE model is a simplified Mixture Multiphase model. It is restricted to two phases of the same substance which are in thermodynamic equilibrium e.g., the boiling process of water. Since our flow consists of several substances and operates at constant temperature of 20°C the TPTE model was removed from the model selection process.

Optional models for an increased accuracy of the flow simulation depend on the basic multiphase model and can be chosen as the Dispersed Multiphase (DMP), Lagrangian Multiphase, Discrete Element Model (DEM), Suspension Rheology, Granular Pressure and Solid Pressure. The FEM method provides the Viscous Multiphase model which can deal with highly viscous liquid phases, only.

For model selection the characterisation of the multiphase models was compared with flow simulation requirements as summarised in section 4.3.

4.4.2 Volume of Fluid and Multiphase Mixture model

The Volume of Fluid (VOF) and Multiphase Mixture (MMP) models are multiphase models based on the Eulerian approach. As stated, they allow for a definition of gas and liquid phases but no particle phases. The momentum equation is solved for all defined phases and is based on the volume fraction of the fluid i with α_i defined in the centre of each control volume cell (FVM) according to Eq. (4-14) [FP20]. The sum of the volume fractions of all present phases M in one cell equals one {Eq. (4-15)}.

$$\alpha_i = \frac{V_i}{V} \tag{4-14}$$

$$\sum_{i=1}^{M} \alpha_i = 1 \tag{4-15}$$

Volume of Fluid (VOF) model

The Volume of Fluid model (VOF) was initially developed by Hirt and Nichols [HN81] to calculate free surfaces. It is highly suitable for simulating stratified, immiscible multiphase flows characterised by a large-scale interface. The distribution of the phases and the position

of the interface depends on the value of the volume fraction α_i . If the value equals 0, the cell is completely void of the fluid while a value of 1 indicates a complete filling with the fluid. For a volume fraction between 0 and 1, the respective cell is part of an interphase and therefore contains several fluids.

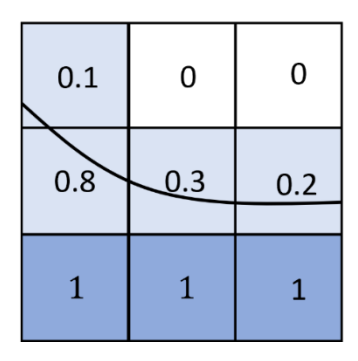


Figure 4-7: Interface capturing with the Volume of Fluid model illustrated on a 2D grid. The interface (black line) divides the fluid phase i (dark blue, $\alpha_i=1$) from the fluid phase j (white, $\alpha_i=0$). Each cell through which the interface extends (light blue) is called an interphase cell with an assumed mixed fluid ($0<\alpha_i<1$).

The fluids present in the interphase are treated as a mixture. Their properties are a combination of both single fluids by using the liquid volume fraction as a weighting factor.

$$\rho_m = \sum_{i=1}^M \rho_i \alpha_i \tag{4-16}$$

$$\mu_m = \sum_{i=1}^M \mu_i \alpha_i \tag{4-17}$$

$$\mathbf{u_m} = \frac{1}{\rho_m} \sum_{i=1}^{M} \mathbf{u_i} \alpha_i \rho_i \tag{4-18}$$

Here, ρ_i denotes the density, μ_i the dynamic viscosity and $\mathbf{u_i}$ the velocity vector of the respective phase i. The variables ρ_m , μ_m and $\mathbf{u_m}$ define the respective mixture properties. The VOF-model can only be used with an unsteady solver. The transport of the phase i is driven by the phase mass conservation equation resulting in a volume fraction transport equation:

$$\frac{\partial}{\partial t} \int_{V} \alpha_{i} dV + \oint_{A} \alpha_{i} \mathbf{u_{m}} \cdot d\mathbf{A} = \int_{V} \left(So_{\alpha_{i}} - \frac{\alpha_{i}}{\rho_{i}} \frac{D\rho_{i}}{Dt} \right) dV - \int_{V} \frac{1}{\rho_{i}} \nabla \cdot \left(\alpha_{i} \rho_{i} \mathbf{u_{d,i}} \right) dV$$
(4-19)

where \pmb{A} is the surface area vector, $\pmb{u}_{\mathbf{d},\mathbf{i}}$ is the diffusion velocity vector, So_{α_i} is a user-defined source term of phase i and $\frac{D\rho_i}{Dt}$ is the material derivative of the phase densities ρ_i [Sie23].

The total mass conservation equation and momentum equation for all phases is equal to the general form in Eq. (4-1) and Eq. (4-4). If two phases are present in one cell, the volume fraction transport is calculated for the first phase i only. The volume fraction of the second phase j is adjusted to fit the sum of 1 in each cell [Sie23]. Consequently, the VOF method has a high numerical efficiency, which enables its use in flow simulations where a large-scale separation of phases exists, with a relatively small total contact area between them. Especially for free-surfaces, additional modelling of the interface interactions is not required and the surface tensions can be neglected when considering large surface areas [BS13]. For analysing the motion of the interface an iterative system in two steps is performed until convergence is received: (1) an initial position of the interface is defined or the position at the last time step is used, where the continuity equation and the momentum equation are solved, (2) based on this calculated velocity field the transport equation {Eq. (4-19)} is solved. With the received values and gradients of α_i the progress of the interface is determined.

When solving the transport equation, the correct order of the discretisation scheme, a sufficient fine mesh resolution and a corresponding time step are significant for receiving a sharp presentation of the interface. Low order discretisation schemes lead to strong numerical diffusion resulting in a smearing of the interface while high orders can introduce oscillations. The mesh resolution around the position of the free surface should be fine enough to ensure that the interphase (0 < α_i < 1) includes not more than three cells normal to the interface. A possibility to further increase the sharpness of the interface is the High-Resolution Interface Capturing (HRIC) scheme. This uses a 2nd order discretisation to simulate the convective transport. In this case, the value of the CFL number has to be < 0.5 (with explicit discretisation). The complete resolving of the interface can become prohibitively expensive when applied to multi-scale flows, where a precise modelling of dispersed patterns is a significant concern [Sie23]. Consequently, the HRIC scheme has not been implemented in the current work. The VOF model can actually also be used with more than two phases. Therefore, the number of conservation equations equals M-1 when M denotes the number of phases. Numerical difficulties can arise at locations where three or more phases appear at the same time. Here the calculation of the volume fraction to determine the position of the interface becomes challenging [Pas04].

The VOF model has been applied for the examined counter-current flow, as presented in subsection 4.6.2 and 4.6.3.

Mixture Multiphase (MMP) model

The mixture multiphase model assumes completely miscible flow behaviour in the whole domain for all involved phases. It can be applied to dispersed flows, e.g., bubbly and droplet flows, but also for evaporation and condensation processes. The transport equations of volume fraction, mass and momentum are similar to the VOF model. They are calculated for a phase mixture as a whole while averaging the fluid properties using the volume fraction of the involved phases according to Eqs. (4-16)-(4-18). Nevertheless, a representation of a free surface of the involved phases is not possible. Consequently, this model does not fit the flow requirements for our flow of interest and is rejected.

Optional Models

Optional models can only be selected in combination with the VOF model. The *Dispersed Multiphase model* (DMP) is suitable for simulating dispersed phases in a continuous background with lower computational effort than the *Lagrangian approach*. The Lagrangian approach provides more options for droplet and/or wall interactions. Nevertheless, such simulations are only possible up to a phase fraction of 5% combined with high numerical costs for a sufficient number of particle trajectories for both models [Pas04]. The particle volume fraction was already determined in subsection 3.4.6 with $\varepsilon'_{exp} > 55\%$ (Table 3-21) which is computationally not feasible with DMP.

A further approach is the *Discrete Element Method* (DEM) which also considers the interaction forces between the particles [IBW+ 23], [MBI+ 24]. This would enable the simulation of sticking processes between the single A. annua particles, representing a bulk, as well as the sticking of leaves to the screw and to the wall of the extractor due to the rotation of the screw. However, DEM needs even more computational resources for calculating specific particle interactions and forces, compared to DMP and Lagrangian approach. Currently, the simulation of granular systems with more than 10^6 particles rapidly exceeds the computational limits of modern computers, even when employing highly parallelised and optimised DEM and DEM-CFD software on multi-core processors [DCK+22]. As an example, the number of particles for OP 2 is determined. Here, the ratio between the total solid phase retention volume $V_s = 5.9 \cdot 10^{-5} \text{m}^3$ (Table 3-21) and the single particle volume V_p {Eq. (4-20)} can be used.

$$V_p = \frac{4}{3} \left(\frac{D_p}{2}\right)^3 \pi = \frac{4}{3} \left(\frac{2 \cdot 10^{-4}}{2}\right)^3 \pi = 4.19 \cdot 10^{-12} \text{ m}^3$$
 (4-20)

The ratio V_s/V_p results in a particle number in order of 10^7 which is too high for using DEM in this work. Studies can be performed by bundling multiple particles into large-sized particles to reach industrial scale systems with up to 10^8 - 10^{12} particles. Here, the knowledge of interaction forces is crucial to obtain acceptable results [DND21], [BGJ+24]. Nevertheless, these studies are just a first approach to approximate these large-scale challenges. For applying the DEM method to the investigated screw extractor, a reduction to one single screw element would be necessary. This could enable a specific observation of phase interactions with high but acceptable computational costs. However, the overall flow properties of the involved phases, as well as the residence time distributions cannot be examined in such a simplified geometry. For that reason, optional models for the VOF model have not been selected in this thesis.

4.4.3 Eulerian Multiphase model

The Eulerian Multiphase (EMP) model, also known as the two-fluid model has proven its effectiveness in accurately representing both dispersed and separated flow patterns, especially in the context of multi-scale flows [Dre83], [IM84], [MSW22], [SW008]. It can resolve multiphase flows involving fluids and/ or particles by averaging flow behaviour considering quasi-fluids which are fully inter-penetrating and do not have phase discontinuities [SW008]. In contrast to the VOF, MMP and TPTE model their conservation equations of mass, momentum and energy are solved for each phase separately. An advantage of this formulation is that the interfacial forces are inherently present in the modelling. Nevertheless, they need to be accounted for using closure models and this averaging leads to a loss of flow details [SW008]. The phase-specific equations of motion involve the volume fraction α_i . The continuity equation for a generic phase i is shown in Eq. (4-21).

$$\frac{\partial}{\partial t} \int_{V} \alpha_{i} \rho_{i} dV + \oint_{A} \alpha_{i} \rho_{i} \mathbf{u}_{i} \mathbf{n} dA = \int_{V} \sum_{j \neq i} (m_{ij} - m_{ji}) dV$$
 (4-21)

The term on the right-hand side describes the mass transfer rate between phase i and phase j. The separated calculation of fluid motion for each phase increases the calculation effort of the EMP model. Furthermore, the representation of a stable and sharp interface is more difficult compared to VOF, especially in mixing procedures where a movement of the interface occurs

[Pas04]. As a consequence, simulating the full extractor appears currently impossible. The analysis would be limited to a single screw segment.

For representing the agglomerated solvent-soaked particles correctly, optional models need to be selected for the EMP model.

Optional models

The EMP model allows for several optional models to adapt the simulation to the real flow (Figure 4-6). This includes particulate flows represented by the *Suspension Rheology* model, the *Granular Pressure* and *Solid Pressure* model.

Particulate flows generally describe multiphase flows including gas/solid or liquid/solid phases, appearing for example in fluidised beds, pneumatic conveyors or cement products [Sie23]. Using the Eulerian approach for simulating particles limits the accuracy of representing particle size distributions compared to Lagrangian approaches. The particle phase is represented as a continuum phase rather than by single particles. Nevertheless, high particle loads, locally also packed beds, can be simulated while the numerical costs increased only slightly for higher particle fractions [Pas04].

For setting up a particulate flow simulation at least two Eulerian phases are required, namely a fluid phase and a solid particle phase. The particles in the particle phase share equal material properties and particle size by default. If the solid particles are suspended in a laminar fluid flow the *Suspension Rheology* model can be selected. Since the investigated flow simulation requires a high solid-fraction load representing the agglomerated solvent-soaked A. annua leaves (section 4.3) a suspension cannot be used for a proper representation.

For representing packed beds, the *Granular Pressure* model and the *Solid Pressure* model are available. While the *Granular Pressure* model is suitable for loosely packed particles, e.g., in fluidised beds, the *Solid Pressure* model can represent closely packed particles. This particle phase is represented by a Eulerian, homogeneous phase with a user-defined pseudo-viscosity. This allows the representation of high particle loads with acceptable computational costs, as required for the considered flow. Following, the theoretical definitions and flow requirements of the *Solid Pressure* model are presented.

Solid Pressure model

The representation of closely packed particles requires a user-given value of the maximum packing limit $\delta_{p,max}$, e.g., 0.624 for rigid spherical particles. To allow the physical representation of packed beds with the continuously-assumed particle phase this packing limit must not be exceeded. If the packing limit value is approached, a solid pressure force f_{int} becomes active in the momentum equations of all dispersed particle phases j=1- M {Eq. (4-22)}. This equation includes a model constant B_3 and the packing fraction in each cell $\delta_{p,i}$.

$$(f_{int})_{i} = -\frac{\delta_{p,i}}{\sum_{j=1}^{M} \delta_{p,j}} \left[e^{B_{3}(\delta_{p,max} - \sum_{j=1}^{M} \delta_{p,j})} \right] \nabla \left(\sum_{j=1}^{M} \delta_{p,j} \right)$$
(4-22)

This integrated compaction force term will spread the particles in the affected cell which will also influence the fluid flow around the cell trying to fill the void caused by the departing particles. Consequently, high velocities can occur and the solution might diverge.

To reach a good and stable solution without exceeding the maximum solid fraction small time steps and high inner iterations can be helpful. In this way the numerical system has more time to find a suitable solution in the critical cells and the velocity of particles cannot increase too fast. In this thesis the packing fraction $\delta_{p,i}$ can be visualised using the solid phase volume fraction α_s .

The selection of the EMP model allows extended boundary options. With a focus on the described flow simulation requirements (section 4.3), the definition of impermeable outlets for one fluid is helpful. This boundary condition allows a blockage of one phase (e.g., solvent water) without disturbing the flow of the other involved phases (e.g., solvent-soaked A. annua leaves). By selecting the optional Solid Pressure model, the dense packing of the agglomerated solvent-soaked leaves could be represented, allowing RTD measurement of liquid and solid phase. The application of the EMP and Solid Pressure model is presented in subsection 4.6.1.

4.4.4 Viscous Multiphase model

The Viscous Multiphase model is based on the Finite Element method (FEM) and can be applied for viscoelastic materials and other highly viscous non-Newtonian fluids, e.g. liquid plastics, rubber and molten glass As a result, this approach is in principle well-suited for simulating the investigated flow of a highly viscous fluid, representing the behavior of solvent-

soaked leaves. In newest versions of Simcenter StarCCM+ the *Viscous Multiphase Flow* model can represent several liquid phases. Optional flow models are not available.

The Viscous Multiphase model contains strict limitations for its implementation. This includes the Reynolds number which should be lower than 10 and mostly less than 1; so that the surrounding fluid is in Stokes regime [SB23]. Further the simulation of convection is not possible while the model is compatible with diffusion. The model is not compatible with overset meshes or conjugate heat transfer and does not work with radiation modelling. The implementation of a sliding mesh approach is not possible making unsteady rotations of the mesh impossible. The calculation mesh has to be generated with tetrahedral or quadrilateral cells which are extruded through the domain so that the element angles are as close as possible to 90°.

For our flow of interest, the restriction of Reynolds number can be satisfied concerning the particle Reynolds number {calculated as $Re_p = 0.1$, Eq. (4-10)}, while the solvent flow with a Reynolds number of Re = 28 {Eq. (3-1)} is actually already too large for this approach. Furthermore, the restriction of motion is highly undesirable for the examined flow simulation, since the rotation of the screw is a central part of process and cannot be neglected.

In summary the Viscous Multiphase model is a promising model to accurately simulate highly viscous flows but cannot be used for the investigated flow due to several limitations.

Note that it has also been checked if alternative simulation software could address the described limitations. Ansys Polyflow 2021 R1 [Ans21] appeared highly promising, as it is specifically designed for highly viscous flows. However, after a thorough evaluation of the available models, limitations related to moving parts were also identified. As a result, the motion of the screw cannot be accurately implemented, rendering the software unsuitable for this work.

4.4.5 General options for region definition

For all multiphase flow simulations Simcenter StarCCM+ provides the possibility to select between a fluid region and a porous region. A porous region can represent the flow behaviour of a fluid in a porous material, i.e. ceramic. Here, flow resistances occur due to the specific porosity of the porous material influencing the pressure drop inside the domain.

In the context of the investigated flow this porous region becomes especially important for

representing the induced pressure drop of the extraction cake caused by the perforated disk, without simulating this compression process itself. The actual flow behaviour of the fluid inside the extraction cake and the perforated disk (porous region) is not relevant for this work since it is not significant for the extraction process of ARTE (subsection 3.4.1).

When selecting a porous region, a user-specified volume porosity χ is included in the unsteady terms of the continuity equation describing the ratio between occupied volume by the fluid V_f and total volume V of a cell in the range of $0 \le \chi \le 1$ {Eq. (4-23)}. For the extraction process the porosity mimics the extraction cake. The extraction cake consists only of solvent-soaked leaves and the (internal) extract of water, but no gas phase ($V_f = V_l$, $V = V_l + V_s$). In this case, the porosity is similar to the liquid phase volume fraction ε' defined in Eq. (3-24). It ranges within the interval [0,1]:

$$\chi = \frac{V_f}{V} \qquad \widehat{=} \qquad \varepsilon' = \frac{V_l}{V_l + V_c} \quad \text{Eq. (3-24)}$$

Consequently, the porosity can be determined by using the equation for the extract mass flow rate \dot{m}_{ext} {Eq. (3-12)} along the phase-specific densities. For the reference case OP 2, which is the focus of the simulations, the mass flow rates can be obtained from Table 3-10, while the solvent density ρ_l (water) is provided in Table 3-3 and ρ_{ds} (dry leaves) in Table 3-5. The porosity then equals a value of 0.7 {Eq. (4-24)}.

$$\chi = \varepsilon' = \frac{\dot{V}_l}{\dot{V}_l + \dot{V}_s} = \frac{\dot{m}_{ext}/\rho_l}{\dot{m}_l/\rho_l + \dot{m}_{ds}/\rho_{ds}} \approx 0.7 \tag{4-24}$$

When a fluid enters a porous medium with user-defined porosity, its physical velocity increases due to the reduced open area. In the porous region approach, however, this velocity increase is not computed. Instead, a superficial velocity vector \mathbf{u}_{sf} is determined under the assumption that only the fluid passes through the porous medium, neglecting the solid portion. This superficial velocity vector depends on the physical velocity vector of the fluid \mathbf{u} {Eq. (4-25)}. The continuity equation is modified as shown in Eq. (4-26).

$$\mathbf{u}_{\mathbf{sf}} = \chi \cdot \mathbf{u} \tag{4-25}$$

$$\frac{\partial}{\partial t} \left(\int_{V} \rho \chi \right) dV + \oint_{A} \rho \mathbf{u}_{sf} \cdot \mathbf{n} dA = \int_{V} \sum_{j \neq i} (m_{ij} - m_{ji}) \ dV$$
 (4-26)

Pressure losses in porous regions are modelled as momentum sinks in the momentum equation, incorporating a porous medium force vector $\mathbf{f}_{\mathbf{p}}$. This vector accounts for flow

resistance caused by the porous medium and depends on the superficial velocity vector \mathbf{u}_{sf} and the porous resistance tensor \mathbf{P} which comprises the viscous (linear) resistance tensor \mathbf{P}_{v} and inertial (quadratic) resistance tensor \mathbf{P}_{i} [Sie23]:

$$\mathbf{f}_{\mathbf{p}} = \mathbf{P} \cdot \mathbf{u}_{\mathbf{sf}} = (\mathbf{P}_{\mathbf{v}} + \mathbf{P}_{\mathbf{i}} \mathbf{u}_{\mathbf{sf}}) \cdot \mathbf{u}_{\mathbf{sf}} \tag{4-27}$$

The resistance force always acts in counter-current direction to the flow direction. For laminar flows as in this work the inertial resistance tensor P_i can be neglected resulting in a linear function [Sie23]:

$$f_{p} = P_{v}u_{sf} \tag{4-28}$$

The viscous resistance tensor $\mathbf{P_v}$ can be defined as an orthotropic tensor with components $P_{v,x}, P_{v,y}$ and $P_{v,z}$. In this study, the porous region represents the flow resistance in the axial direction caused by the compressed extraction cake at the perforated disk. For this axial flow direction, only the x-component $P_{v,x}$ was defined, while the flow perpendicular to this direction is restricted by resistance coefficients 2-3 orders of magnitude larger than the primary coefficient. Although high resistance values do not affect the flow, they may influence convergence [Sie23]. The porous resistance is directly related to the pressure drop per length. This relation is well described by the generally used Ergun equation [Erg 52] which enables the calculation of the porous resistance coefficients based on experimental values. It is generally defined for spherical particles in a packed bed. Here only the linear form is introduced for laminar flows:

$$\frac{\Delta p}{\Delta L} = P_{v,x} u_{sf,x} = \frac{150(1-\chi)^2 \mu}{\chi^3 D_p^2} u_{sf,x}$$
 (4-29)

The viscous porous resistance $P_{v,x}$ increases significantly for decreasing particle sizes due to the smaller flow channels and typically ranges between $10^2 - 10^7$ Pa·s/m² [TL14], [BRV+07].

In conclusion, after analysing all the multiphase models in Figure 4-6, the MMP and TPTE models were found unsuitable for describing the physical configurations of our flows of interest. The Viscous Multiphase model, while promising, cannot account for the screw's rotating motion, the driving element of solid-phase motion, making it unusable. The two remaining approaches, (1) EMP and (2) VOF, will be implemented and compared to investigate our configuration.

4.5 Mesh-independence study

The impact of the computational mesh resolution on the numerical accuracy is significant. A discretisation error describes the difference between the exact solution of the differential equations and the exact solution of their discretised description. High discrepancies can occur due to insufficiently fine meshes. At the same time the computational effort is proportional to the number of discrete elements leading to a balance between solution accuracy and computation times [FP20]. For choosing sufficiently fine mesh sizes, a mesh-independence study with systematic mesh-refinements can be performed using Richardson extrapolation [Ric11].

Three different types of meshes were compared using the numerical geometry of the extractor: a block-structured mesh (hexahedral cells), an unstructured mesh with polyhedral cells and an unstructured mesh with tetrahedral cells. StarCCM+ offers the possibility of automatically generating unstructured meshes based on defined base sizes, which was used here. Each mesh type was assessed at four different levels of refinement, as indicated in Table 4-1. The number of prism layers, the height of the first cell adjacent to the wall, and the overall thickness of the prism block were maintained for all mesh types. The SD is meshed for all three mesh types with polyhedral cells, consisting of only two layers of thin cells filling the screw gap. This ensures the highest mesh quality.

The unstructured polyhedral and tetrahedral mesh were refined at the interfaces between SD and in- and outlet geometries to ensure an accurate transfer of flow parameters. For the block-structured mesh the thin layer cells from the SD are used to generate a structured mesh for the in- and outlet geometries by mesh extrusion. Figure 4-8 illustrates the investigated mesh topologies, displaying both a cross-sectional mesh and the central axial section of the extraction device at a mesh resolution of one million cells (Mesh #3).

Table 4-1: Number of finite-volume cells (in million) for three mesh types and four different resolutions.

Mesh #	1	2	3	4	
hexahedral/ block-structured	0.517	0.790	1.026	2.100	
polyhedral automated mesh	0.500	0.746	0.974	1.927	
tetrahedral automated mesh	0.525	0.739	1.062	2.000	

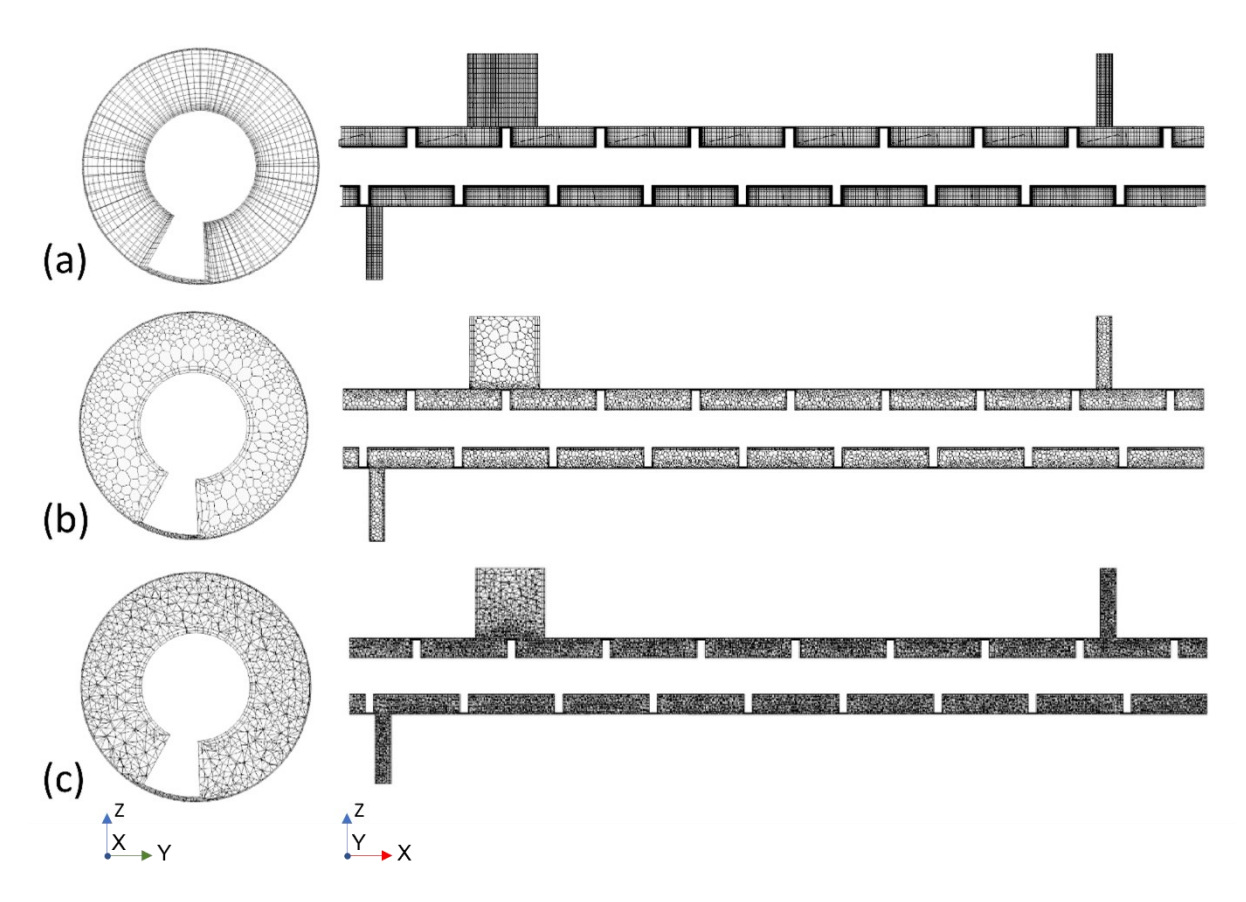


Figure 4-8: Representation of the three applied mesh topologies using a resolution of one million cells (Mesh #3): (a) block-structured, (b) (unstructured) polyhedral and (c) (unstructured) tetrahedral mesh.

A simplified model from previous work has been used to represent the basic counter-current flow behaviour of the solvent-soaked leaves and the solvent (water) concerning the ideal mesh topology [LJM+20]. A more specific model and adaption to the flow requirements and steady state operation points will be performed in section 4.6.

To speed-up the tests only a 60-second physical time solution run was conducted for all mesh types, corresponding to one full rotation of the screw at a rate of n=1 rpm with a solid inlet flow rate of $\dot{m}_{ds}=1$ g/min (1.67·10⁻⁵ kg/s). The solid-liquid ratio was first fixed to R=0.06 {Eq. (3-9)}. The inlet boundary conditions are set equal to the experimental setup as shown in Figure 3-3. Further, the raffinate outlet was defined as a simplified porous region for representing the pressure drop at the perforated disk and creating a counter-current flow field. In this simulation setup the pressure drop was not validated with experimental data from subsection 3.4.3, yet. A porous resistance for water in axial direction of $1\cdot10^4$ Pa·s/m² was retained, which is in the range of typical values from literature ($10^2 - 10^7$, [TL14], [BRV+07]) and fits to calculations with the Ergun equation {Eq. (4-29)} assuming wetted, agglomerated

particles with a diameter of 1 mm {Eq. (4-29), ε = 0.7, μ = 1·10⁻³ Pa·s D_p = 1 mm}. This definition of flow resistance prevents the water from escaping at the raffinate outlet and creates a counter-current flow.

Consistency was maintained between the three mesh types in terms of boundary conditions and node count. Since previous simulations of a fully-filled VOF simulation using water and highly-viscous A. Annua leaves ($\mu_s = 1 \cdot 10^3 \, \text{Pa·s}$, Table 3-5) showed a high sensitivity to the CFL number, an adaptive time step (ATS) model was chosen to ensure a CFL number below 1. The resulting time steps ranged between $1 \cdot 10^{-3}$ to $5 \cdot 10^{-3}$ s. Due to widely varying steps, a comparison of computation times between the three implemented meshes is not reasonable. Table 4-2 summarises the used parameters for this mesh-independence study.

Table 4-2: Physical models for the mesh-independence study at room temperature ($T = 20^{\circ}$ C).

Parameter	Settings	Unit
Multiphase flow model	Volume of Fluid (laminar)	
liquid phase (water)	ref. to Table 3-3	
highly-viscous liquid phase (A. Annua leaves)		
density	260	kg/m³
viscosity	1.10^{3}	Pa∙s
screw rotation rate	1	rpm
Boundary conditions		
leaves inlet	1.67·10 ⁻⁵	kg/s
solvent inlet	2.78·10 ⁻⁴	kg/s
extract outlet	101 325 (= p_{atm})	Pa
raffinate outlet	8.9·10 ⁻⁵ {Eq. (3-11)}	kg/s
porous viscous resistance in x-direction (water)	1.104	Pa·s/m²
Adaptive time step criteria		
convective mean CFL number	1	-
convective max CFL number	10	-
minimum time step	1.10^{-3}	S
maximum time step	0.05	S
Solver	implicit unsteady	
temporal discretisation	2 nd order	
discretisation scheme: momentum	2 nd order	
implicit scheme	SIMPLE	
under-relaxation factor		
velocity	0.4	-
pressure	0.2	-
discretisation scheme: volume fraction	2 nd order	
under-relaxation factor	0.2	-
Inner iterations	30	-

The main objective of the mesh independence study is to obtain accurate results for critical simulation parameters that should remain consistent regardless of mesh size variations. The focus here is on the water flow, starting from the right-hand inlet of the device. Figure 4-9 (a) illustrates the dimensionless axial length (x/L) for the water-front position, with x representing the current water position and L denoting the total length of the extractor. Figure 4-9 (b) presents the corresponding average liquid velocity.

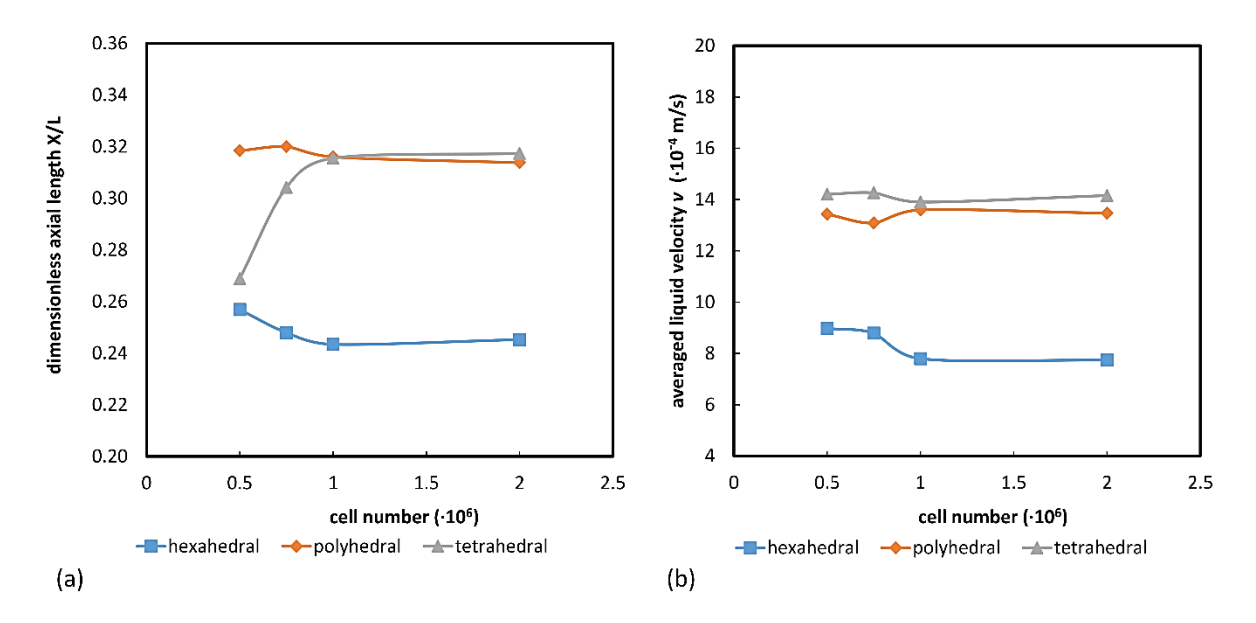


Figure 4-9: (a) Position of water front and (b) averaged liquid velocity. In total a physical time of 60 s for all three mesh types was simulated with a screw rotation rate of n = 1 rpm.

All three types of tested meshes exhibit convergent values as the number of cells increases, with final convergence achieved at a resolution of one million cells. However, the polyhedral and tetrahedral meshes yield higher values for the dimensionless axial position of the water front (1.3 times) and the average water velocity (1.8 times) in comparison to the hexahedral mesh. This observation aligns with Mansour et al. [MKK+20] who concluded that polyhedral and tetrahedral meshes introduce significant numerical diffusion during liquid mixing processes. To quantitatively determine the optimal mesh quality, a Richardson extrapolation has been conducted [Ric11]. For the block-structured mesh with a resolution of one million cells, a discretisation error of only 0.74% was computed based on the dimensionless water-front position.

As a result of this low error value and to avoid excessive numerical diffusion [MKK+20], a block-structured mesh with a million hexahedral cells has been chosen for all further CFD simulations, ensuring accurate results within reasonable computation times.

4.6 Multiphase flow simulations

This section presents simulations of multiphase flows using the two most-promising models – namely the general Eulerian Multiphase (EMP) model and the Volume of fluid (VOF) model. The goal of the simulations is to represent important flow characteristics with focus on the hydrodynamics at quasi-steady-state and to determine the residence time distribution (RTD) of both, the solid and liquid phase. The operating conditions of pressure and gravity are set constant in all simulations (Table 4-3).

Table 4-3: Reference values for all multiphase flow simulations.

Parameter	Value	Unit
operating pressure	101 325	Pa
gravity in z-direction	-9.81	m²/s

4.6.1 Eulerian Multiphase simulation

The Eulerian Multiphase model solves the transport equation separately for each phase as described in subsection 4.4.3. This provides advantages compared to the VOF model since each phase can show separate velocity and pressure fields.

Nevertheless, the appropriate representation of a free surface requires a sufficiently fine mesh at the interface. The required transient screw rotation speed leads to a position change after each time step and the mesh needs to be recomputed frequently to ensure a fine mesh at the interface position. This remeshing process combined with the highly complex flow requirements is computationally too expensive. Consequently, only a fully-filled process within one single screw segment, based on OS ($L=a=0.035~{\rm m}$), is computed with the EMP model, neglecting the existence of an additional gas phase ($V_g=0$). The geometry of the leaves inlet is neglected, resulting in a number of 128 983 finite volume cells. In this way computational costs could be decreased compared to Mesh #3 in section 4.5 with a million cells, while still investigating some important hydrodynamic features.

Initial and boundary conditions

The EMP model provides a boundary condition for defined outlets, known as an impermeable outlet, where a specific outlet can be completely impermeable to one phase, while other phases are unaffected. This impermeable outlet was used at the raffinate outlet for the

solvent phase (water) (Figure 4-10). Consequently, only A. annua leaves exit at the raffinate outlet while the solvent (water) flows through the extractor towards the extract outlet. This solvent enters the extractor through a back-rotated inlet pipe to ensure a direct entering to the initialised liquid phase.

The solvent-soaked leaves have been represented as a continuous, closely packed particle phase using the Solid Pressure model with a pseudo-solid viscosity of μ_s = $1\cdot10^3$ Pa·s. They have been initialised at the lower position of the screw segment for simplification. Since the gas phase is neglected, the solid phase volume fraction α_s can be estimated based on the liquid phase volume fraction calculated with ε' = 0.7 in Eq. (4-24). The volume fraction becomes

$$\alpha_{\scriptscriptstyle S} = 1 - \alpha_{\scriptscriptstyle l} = 1 - \varepsilon' = 0.3 \qquad \qquad \text{for } V_{\scriptscriptstyle g} = 0 \tag{4-14}$$

An inlet of this particle phase has not been defined at first. The mass flow rate of extract and raffinate outlet are set equal to the values calculated according to the mass flow balance for OP 2 (Table 3-9). This assumption already includes the soaking process of leaves by solvent and ensures the correct representation of the material flows.

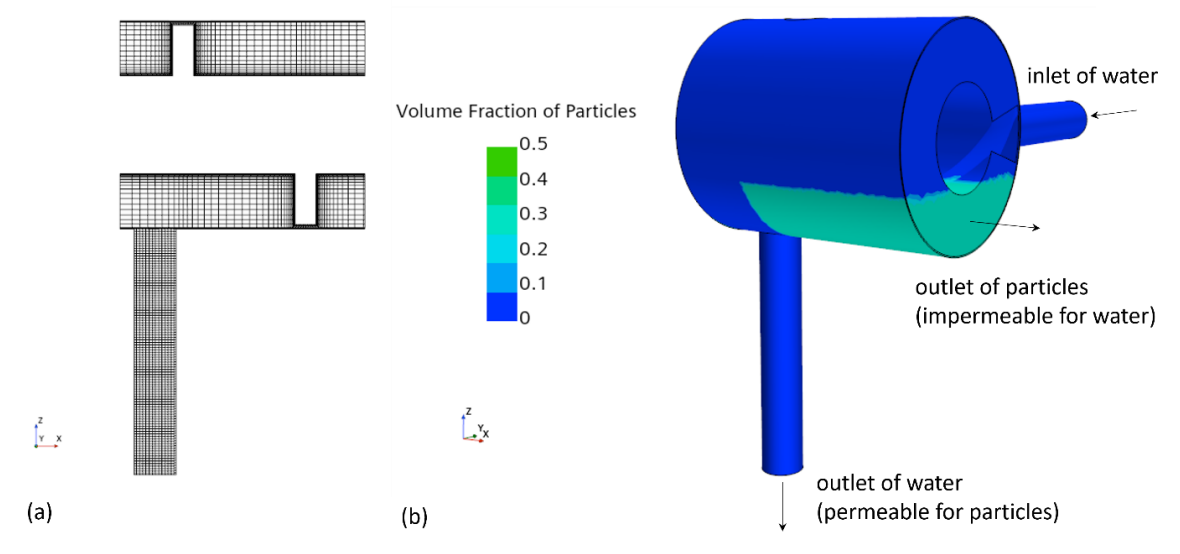


Figure 4-10: Mesh geometry, initial and boundary conditions for EMP model. (a) Mesh on the xz-plane for a single screw segment geometry excluding the leaves inlet geometry; based on Mesh #3 in section 4.5, (b) initial and boundary conditions, with the solvent phase (water) (blue) and the solvent-soaked A. annua leaves (green). Initially, the particles are present in the bottom-right corner of the screw segment with a volume fraction of $\alpha_s = 0.3$.

The simulated particle mass flow transported by the screw inside the extractor segment is higher than the desired raffinate mass flow rate fixed according to experiments. In the experiments, this effect leads to the formation of the extraction cake across the entire diameter of the extractor. In the simulations, a compression of the particles occurs, leading to

an increase of the particle packing. This compression process is actually not accepted by the solid pressure model. The default maximum packing limit of the solid phase, $\alpha_{s,max}$ = 0.624 represents the behaviour of rigid, spherical particles [Sie23]. When reaching this limit, the solid pressure force applies to maintain this value. This can influence the flow field around the particles, leading to instabilities in the simulation. To ensure stability, the time steps needs to be reduced strongly at this point ($\approx 1\cdot10^{-6}$ s).

However, in this simulation setup, the objective is not to achieve a physically accurate representation of the extraction cake but to ensure a stable, particle-only mass flow rate at the raffinate outlet including compression. To facilitate this, the maximum packing limit was increased artificially to $\alpha_{s,max}=0.9$, so that the solid pressure force should not be applied, leading to stable simulations during the compression process. Below this value the governing equations of the EMP model are not changed. The screw rotation speed was defined with n=2.2 rpm (OP 2). To reach a stable solution, a fixed time step of $\Delta t_1=1\cdot 10^{-3}$ s has been set with a number of 30 inner iterations. The CFL number was used as a stability criterion. Table 4-4 summarises the used parameters for the EMP simulation.

Table 4-4: Physical models for the EMP model at room temperature (T = 20°C) considering a single segment.

Parameter	Settings	Unit
Multiphase flow model	Eulerian Multiphase (laminar)	
liquid phase (water)	ref. to Table 3-3	
particle phase (A. Annua leaves)		
density	922	kg/m³
pseudo-solid viscosity	1.10^{3}	Pa∙s
screw rotation rate	2.2	rpm
Boundary conditions		
leaves inlet	wall	-
solvent inlet	2.78·10 ⁻⁴	kg/s
extract outlet	101 325 (= p_{atm})	Pa
raffinate outlet	0.09·10 ⁻⁴	kg/s
Solver	implicit unsteady	
time step	1.10^{-3}	S
temporal discretisation	1 st order	
discretisation scheme: momentum	2 nd order	
under-relaxation factor		
velocity	0.1	-
pressure	0.1	-
discretisation scheme: volume fraction	2 nd order	
under-relaxation factor	0.1	=
Inner iterations	30	<u>-</u>

Results

After a physical time of 7.17 s solver instabilities occur based on the CFL number, which increased rapidly in cells near to the front wall of the geometry to values >20 (Figure 4-11 a). At this position the particles are not present. The maximum packing limit of $\alpha_{s,max}$ = 0.9 was not close to being reached in the simulations (Figure 4-11 b). Consequently, even manipulating the packing limit will not lead to converging results.

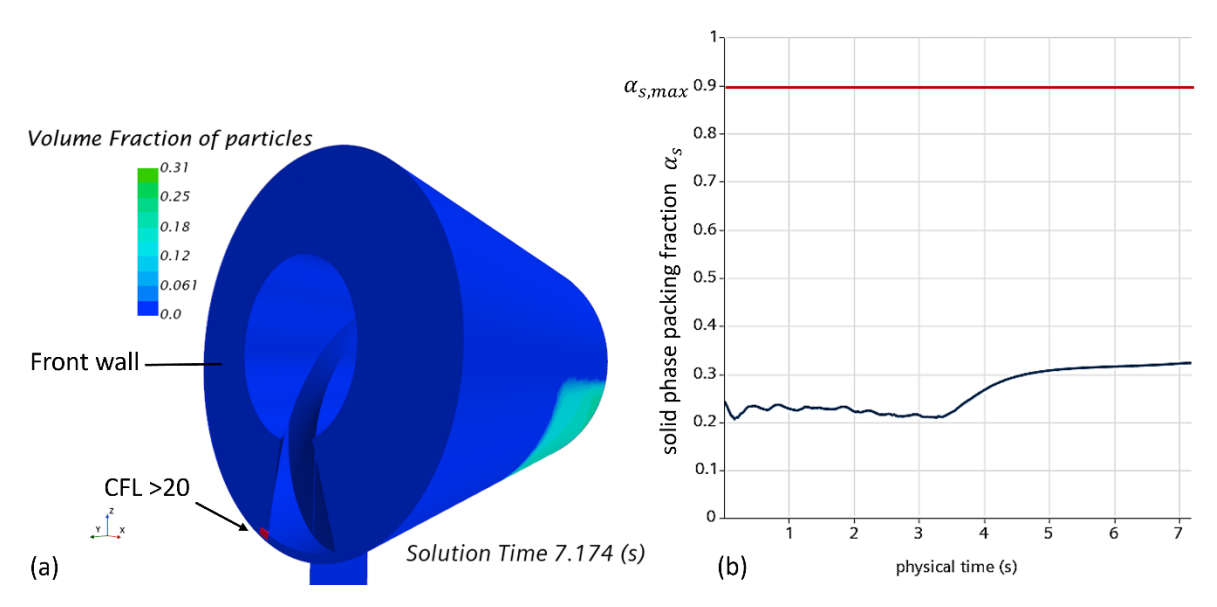


Figure 4-11: Solid phase packing fraction α_s in the EMP model. (a) Particle volume fraction in the screw segment shows that particles are located far from cells that first exceed a CFL value of 20 at the front wall. (b) Evolution in time shows low values of α_s < 0.4, not close to the defined maximum of $\alpha_{s.max}$ = 0.9.

To understand this divergence, the cell quality was monitored for the cells which firstly exceed the CFL value of 20 (in total 5 cells). It was found that the skewness angle θ for 4 of the 5 cells exceeds the recommended value of 85° (two cells: 100°, two cells: 111°) which often results in solver instabilities [Sie23]. By investigating the skewness angle for the total geometry, a value $\theta > 85^\circ$ only appears at the end surfaces of the extractor (Figure 4-12, blue marked cells). At this position the screwgeometry has been cut in previous construction processes to achieve the shorter cylinder-shaped geometry. Obviously, the high skewness angle values in the cut cells at the ends of the geometry cause solver instability problems resulting in high velocities, ultimately leading to a crash of the simulation.

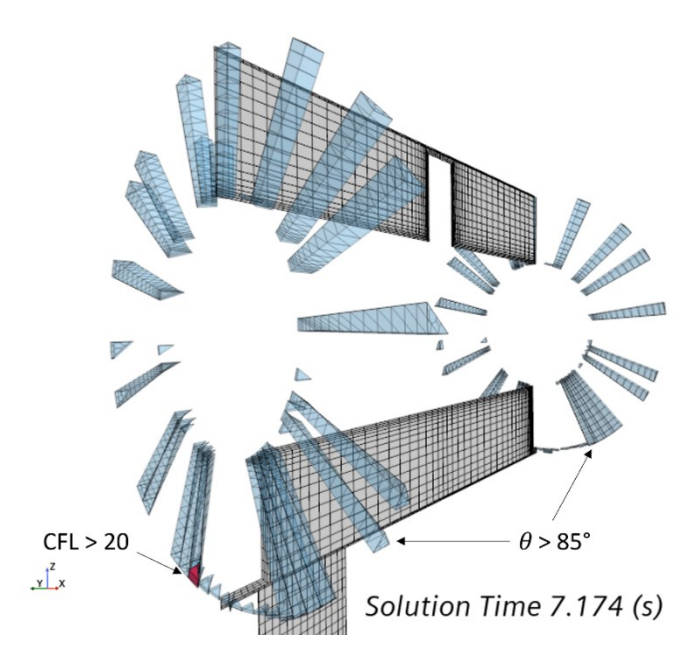


Figure 4-12: Skewness angle for the counter-current EMP model in a single screw segment. Cells exceeding the skewness angle $\theta > 85^{\circ}$ (blue) and with CFL number > 20 (red) introduce solver instabilities. All marked cells are located at the two end-surfaces of the geometry.

The implementation of an adaptive time step (ATS) ensuring low CFL numbers could stabilise the simulation but results in time steps between 10⁻⁵ down to 10⁻⁸ s This is computationally not feasible for achieving solution times over several screw rotations. To overcome the solver instabilities, a different mesh construction procedure would be required. Based on the performed mesh-independence study in section 4.5, this would result in a poorer overall mesh quality for the investigated screw geometry.

In conclusion the EMP model provides promising boundary conditions for reaching a countercurrent flow but cannot be used to simulate the process of interest due to numerical instabilities and extremely high computational requirements.

4.6.2 Volume of Fluid simulation - Fully-filled reactor

The Volume of Fluid model allows a stable representation of free surfaces between several phases. In this thesis a fully-filled two-phase flow and a partly-filled three-phase flow have been investigated. The flow complexity is very high, which is why the models need to be simplified to get acceptable results in a reasonable computing time. As the flow involves a gas phase which is actually not necessary for the extraction process, a first assumption is to neglect this gas phase and simulate a fully-filled process of solvent and solvent-soaked leaves.

In a preliminary work the VOF model was already found to achieve stable simulations of the fully-filled process [LJM+20] and it was also implemented in the mesh-independence study in section 4.5. These simulations can now be continued.

Initial and boundary conditions

In this flow simulation the complete extractor volume was initially filled with the solvent phase (water) and the solvent-soaked A. annua leaves. The A. annua leaves, fully-soaked with solvent, are represented by a liquid, highly-viscous Newtonian phase with a dynamic viscosity of $\mu_s = 1\cdot 10^3$ Pa·s (Table 3-5). The density is set constant to the experimentally derived value of $\rho_s = 922$ kg/m³ (Table 3-5). To reduce the computational time for reaching a quasi-steady-state, the two phases are initially distributed over the whole extractor length (Figure 4-13 b). The screw rotation speed is set to n = 2.2 rpm, as for operation point 2 with laminar flow regime. The boundary conditions for in- and outlets, sketched in Figure 4-13 (a), are set equal to the experiments (Figure 3-3) while the inlet mass flow rates correspond to the calculated extract and raffinate mass flow rates based on the mass flow balance of OP 2 (Table 3-10). The actual soaking process of leaves with solvent is not represented in the simulation but is included in these boundary conditions.

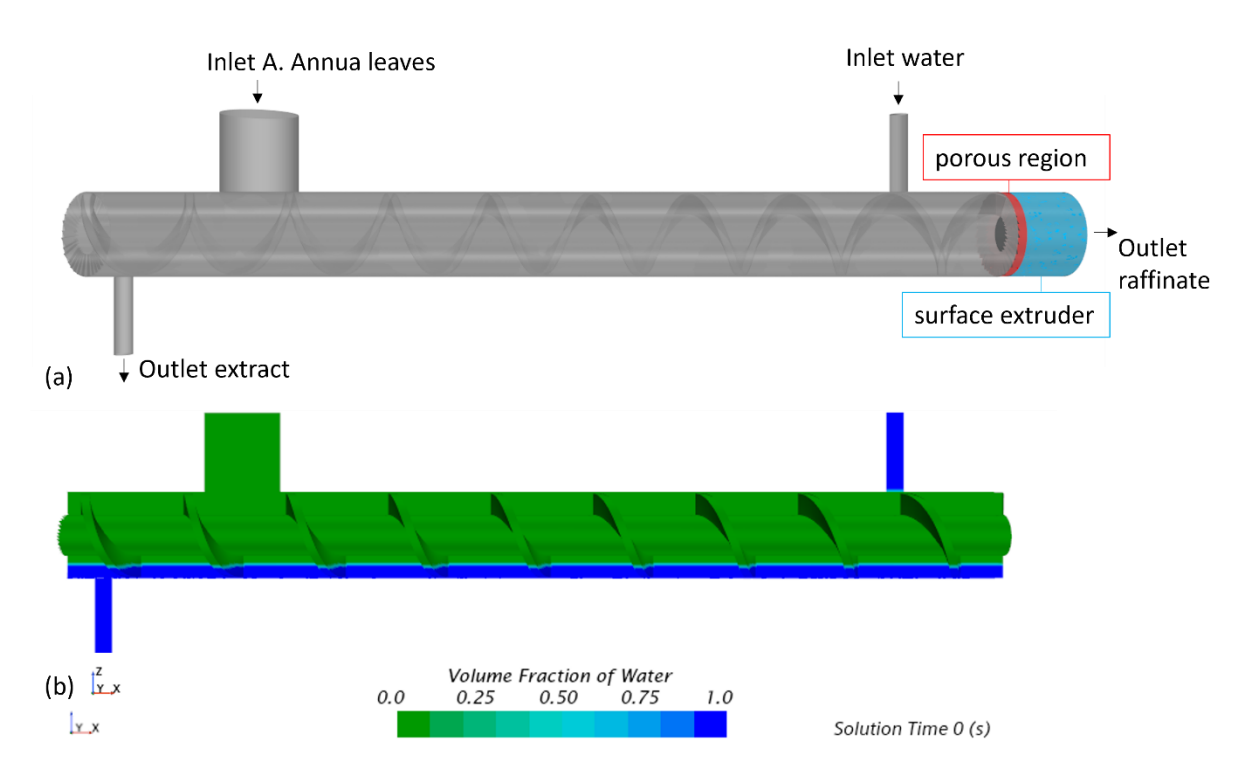


Figure 4-13: Initial and boundary conditions for a fully-filled VOF model, (a) geometry scene of the extractor with defined boundary conditions, (b) initial position of the interface between the solvent water (blue) and the solvent-soaked A. annua leaves (green).

To correctly measure the desired phase residence time distributions, the specific phase mass flow rates at the outlets of extract and raffinate need to fit the experimental measurements in Table 3-9. This implies a quasi-single-phase flow of water at the extract outlet and of the solvent-soaked A. annua leaves at the raffinate outlet. In particular, the definition of the raffinate outlet is complex due to the geometric contours of the perforated disk as well as the material properties of the solvent-soaked A. Annua leaves. For simplification the extraction cake is modelled as a porous region, as already used in the mesh-independence study in section 4.5. It mimics the flow resistance introduced by the disk. This needs to be set correctly now to achieve the desired flow pattern.

To define this flow resistance, a porosity and a viscous resistance can be used (subsection 4.4.5). The implementation of the porosity, calculated as $\chi=0.7$ {Eq. (4-24)}, was found to introduce solver instabilities especially when the highly-viscous A. Annua phase is present inside the porous region. However, this presence is a main flow requirement for reaching a counter-current regime. Since the accurate representation of the flow through the extraction cake itself is not required, and as the primary interest lies in the extractor's internal dynamics, the cake porosity was neglected in the simulations and set to a constant value of 1. The viscous resistance $P_{v,x}$ for water in flow direction of the raffinate outlet (x-direction) is fitted to the measured pressure at the perforated disk in subsection 3.4.3 ($p_{max}=2.2\cdot10^5$ Pa). The resulting value for the porous resistance equals $P_{v,x}=1\cdot10^{-3}$ Pa·s/m² which is several orders of magnitude lower than usual values in literature with 10^2-10^7 Pa·s/m² [TL14], [BRV+07]. This unexpectedly low value effectively reproduces the pressure drop across the porous region detected in experiments.

With a time step of $\Delta t = 0.02$ s and 15 inner iterations stable results could be obtained. For a physical time of 350 s (steady state) a calculation time of 26 hours using 240 CPU cores (15 nodes) was necessary. At this point the mass flow rate balance of all involved phases has to be fulfilled according to Eq. (3-10).

Table 4-5: Physical models for the fully-filled VOF simulation at room temperature (T = 20°C). The operation parameters are based on OP 2 (see Table 3-9).

Parameter	Settings	Unit
Multiphase flow model	Volume of Fluid (laminar)	
liquid phase (water)	ref. to Table 3-3	
highly-viscous liquid phase (A. Annua leaves)		
density	922	kg/m³
dynamic viscosity	1.10^{3}	Pa∙s
screw rotation rate	2.2	rpm
Boundary conditions		
leaves inlet	\dot{m}_{raff} in Table 3-10	kg/s
solvent inlet	$\dot{m}_{\it ext}$ in Table 3-10	kg/s
extract outlet	101 325 (= p_{atm})	Pa
raffinate outlet	\dot{m}_{raff} in Table 3-10	kg/s
porous viscous resistance in x-direction (water)	0.001	Pa·s/m²
Solver	implicit unsteady	
temporal discretisation	2 nd order	
time step	0.02	S
discretisation scheme: momentum		
implicit scheme	SIMPLE	
under-relaxation factor		
velocity	0.4	-
pressure	0.2	-
discretisation scheme: volume fraction	2 nd order	
under-relaxation factor		
volume fraction	0.2	-
Inner iterations	15	-

Results

Based on visual inspection, the distribution of the phases inside the extractor geometry is coherent after a solution time of 350 s, see Figure 4-14 (a). In each segment the A. annua phase appears more in the centre of the geometry while the water phase flows at the bottom and top of the extractor. The extract outlet is mainly filled by the solvent water while the raffinate outlet is dominated by the A. annua phase. The mass flow error e {Eq. (3-18)} is plotted in Figure 4-14 (b). The values range between 40 and 50% during each time step due to the selected solver (unsteady flow). By averaging the mass flow errors over each screw rotation (27.27 s), a decreasing trend is visible with final errors below 2% (Figure 4-14 c).

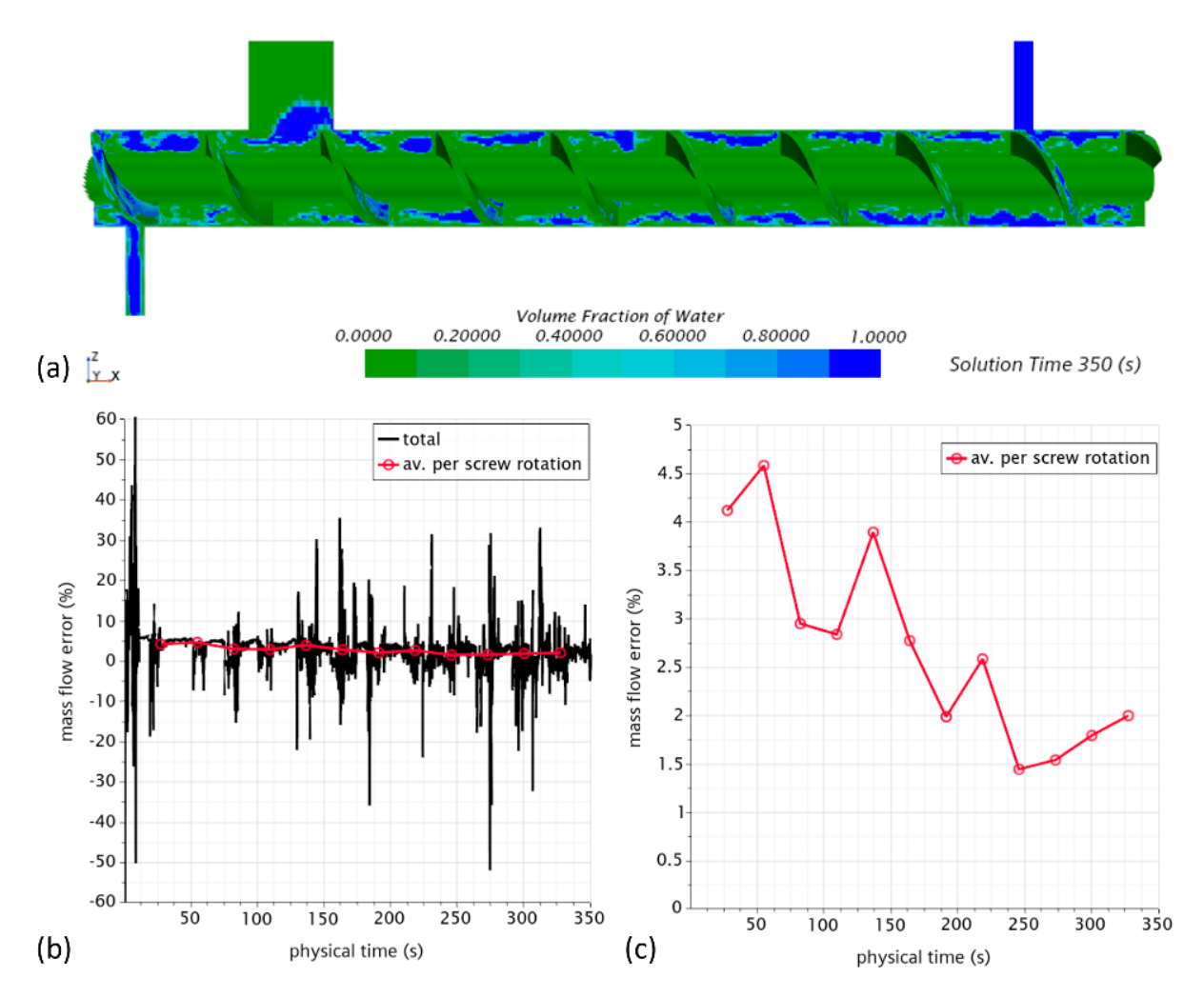


Figure 4-14: Quasi-steady-state of the fully-filled VOF model. (a) Phase distribution of water (blue) and A. annua leaves (green) in the extractor geometry after a solution time of 350 s, (b) total mass flow error e {Eq. (3-18)} based on the total mass flow inlet for each time step ($\Delta t = 0.02$ s) (black) and averaged over each screw rotation (27.27 s) (red), (c) averaged mass flow error over each screw rotation (27.27 s).

As stated previously, both the total mass flow balance and the correct phase mass flow rates at the extract and raffinate outlets are crucial for achieving the required RTD behaviour. To ensure the correct flow pattern, only A. annua leaves should be discharged at the raffinate outlet, while only water should exit at the extract outlet. According to Figure 4-15 this flow pattern could not be reached for both outlets. A. annua leaves (green) periodically exit through the extract outlet (27.27 s) (Figure 4-15 a). The corresponding mass flow rates are large up to $\dot{m}_s \approx 0.23$ g/s in quasi-steady state. This influences also the phase distribution at the raffinate outlet. Since not enough leaves are transported to this outlet, water exits here, despite its defined porous resistance, as seen in Figure 4-15 (b). Compared to experiments, this difference of behaviour prevents a correct measurement of phase RTDs.

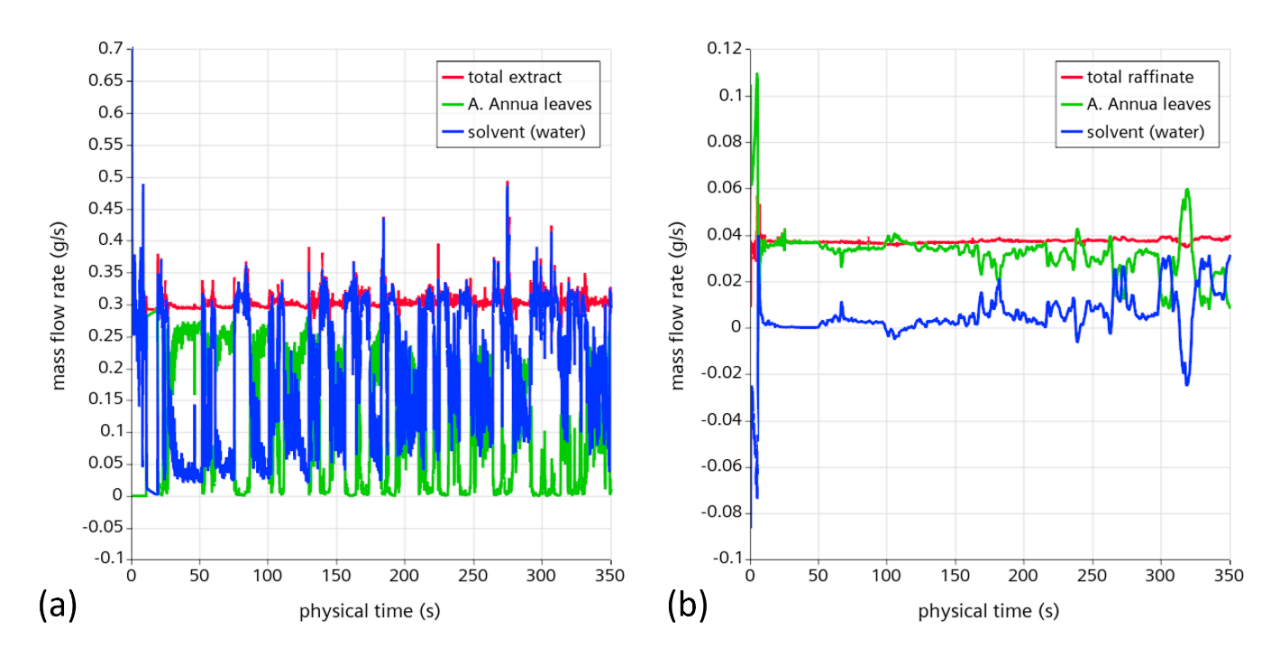


Figure 4-15: Mass flow rates in the fully-filled VOF model. Mass flow rate at (a) extract outlet and (b) raffinate outlet in total (red), and phase-specific for the A. annua leaves (green) and the solvent (water) (blue).

The obvious possibility of further increasing the viscous resistance for water at the raffinate outlet is not reasonable when observing the pressure field (Figure 4-16). With the lowest (atmospheric) pressure at the extract outlet, the pressure rises toward the raffinate outlet, reaching a value of $1.9 \cdot 10^5$ Pa, which was previously fitted to the maximum pressure of steady-state operation (subsection 3.4.3: $p_{max} = 2.2 \cdot 10^5$ Pa). This is already significantly higher than the experimentally measured pressure for OP 2 of $p_{st} = 1.2 \cdot 10^5$ Pa. A higher pressure at the raffinate outlet would affects leaf transport, shown by the streamlines in Figure 4-16 (black). Instead of moving towards the raffinate outlet, A. annua leaves would then be directed straight to the extract outlet upon entry.

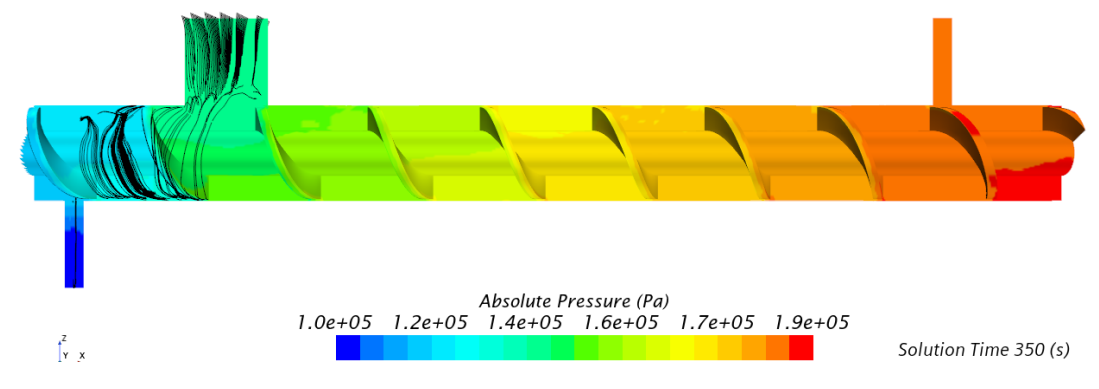


Figure 4-16: Absolute pressure field of the quasi-steady-state process. The streamlines (black) show the flow of solvent-soaked A. annua leaves towards the extract outlet instead of the desired direction towards the raffinate outlet.

Consequently, based on the results of this fully-filled VOF simulation model, not enough A. annua leaves will flow towards the raffinate outlet. The resistance required for the water phase at the raffinate outlet to maintain correct mass flow rates also affects the movement of A. annua leaves, preventing a correct counter-current flow of the phases. Unfortunately, the VOF model does not support a separate phase-specific definition of resistance for outlets. Therefore, another configuration must be adapted.

4.6.3 Volume of Fluid simulation - Partly-filled reactor

This section is partly based on:

[LJM+22b]

Lehr, A.; Janiga, G.; Seidel-Morgenstern, A.; Thévenin, D.: Numerical study on the solid-liquid residence time distribution in a counter-current screw extractor. Proc. Conference on Modelling Fluid Flow (CMFF'22), 30.08.-02.09.2022, Budapest, Hungary, pp. 278-286, 2022.

In the fully-filled process the pressure increase towards the raffinate outlet prevented the correctflow pattern for A. annua leaves and consequently for the solvent (water). By including a gas phase in the process, the pressure field can be strongly modified and adapted to the experiments. Nevertheless, this results in a highly complex and expensive three-phase flow with a free interface intersected by the rotation of the screw. So, further simplifications need to be implemented for representing such a multiphase flow.

In experiments the solvent-soaked A. annua leaves stick to the screw which transports them with constant axial velocity through the extractor. Consequently, they do not actually flow and have a stable, consistent position in each screw segment. Visually, the solid phase can be clearly separated from the solvent phase in the transparent extractor (subsection 3.4.2). These investigations suggest a simplified model where the A. annua phase is represented as a solid, not as a fluid. This corresponds indeed better to the measured rheological behaviour (Figure 3-9 a).

Initial and boundary conditions

The experimental position of the A. annua phase is represented by an additional rotating geometry distributed along the screw and turning with it in a solid movement of 2.2 rpm for OP 2. This implies that the solid inlet and raffinate outlet equals a value of zero in the mass

flow balance ($\dot{m}_s = \dot{m}_{raff} = 0$). A transient measurement of the solid phase RTD in this CFD model is not possible. Nevertheless, it is possible to represent the solvent mean residence time (MRT) appropriately.

The solvent MRT depends on the free volume and the volume flow rate of the solvent $\{\text{Eq. (2-35)}\}$. While the volume flow rate of the solvent can be adapted easily, the free volume does not correspond to the total extractor volume V_{tot} anymore but is now reduced by the solid phase retention volume $(V_{tot} - V_s = V_l + V_g)$. This solid phase retention volume V_s was already defined in subsection 3.4.6 and is now implemented in CFD.

The solid screw geometry is now built by defining the thickness of the A. Annua phase, turning around the screw rod. This thickness was adapted to a value of 16 mm reaching an agreement of the resulting volume with the desired retention volume V_s in subsection 3.4.6. This defined thickness fits to experimental observations. The defined total solid volume has been subtracted from the rotating domain to decrease the solvent flow field accordingly. This subtraction can only be performed within the cell size of the mesh, so that no cell is cut off. Consequently, slight variations could not be avoided and a final volume error of 3% was found to be acceptable (exp: $5.9 \cdot 10^{-5}$ m³, num: $6.1 \cdot 10^{-5}$ m³). The resulting free volume for solvent and gas phase in the extractor equals $V_l + V_g = 9.8 \cdot 10^{-5}$ m³ (Table 4-6). This value is only 2% lower than the experimentally derived volume in Table 3-21 ($V_l + V_g = 10 \cdot 10^{-5}$ m³).

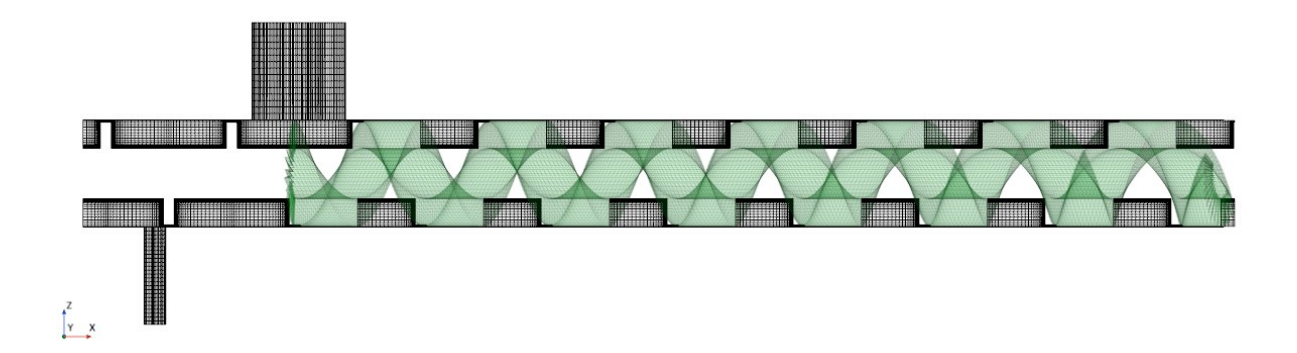


Figure 4-17: Reduced flow field on the xz-plane for the partly-filled simulation. The liquid solvent (water) and air flow in the meshed part (black-white). The flow region of the reactor is reduced by the volume of the rotating geometry representing the solvent-soaked A. Annua leaves (green), sticking on the screw.

Table 4-6: Numerical volume fit of A. annua phase and resulting free volume for the solvent. Since the cells in the CFD simulation cannot be cut there is a small difference between the experimental and numerical solid volume of 3%.

Parameter		experimental	numerical	Unit
total extractor volume	V_{tot}	15.9	15.9	$\cdot 10^{-5}~\mathrm{m}^{\mathrm{3}}$
exp. A. annua volume	V_s	5.90	6.10	$\cdot 10^{-5}~\text{m}^{\text{3}}$
free volume for solvent	$V_l + V_a$	10	9.80	$\cdot 10^{-5}~\mathrm{m^3}$

To ensure in the simulation that liquid solvent (water) directly enters the liquid phase inside the extractor, the inlet geometry of the solvent has been rotated by 90°, as shown in Figure 4-18 (a). Initially, this liquid phase is horizontally distributed over the total length of the extractor by half-filling the previously defined free volume (Figure 4-18 b). The gas phase (air) fills up the remaining extractor volume. The solvent inlet flow rate was set to the calculated extract mass flow rate according to Eq. (3-12). This includes the loss of solvent by leave absorption during the extraction process (\dot{m}_{int}).

The solvent-soaked A. annua leaves remain at their fixed (steady-state) position relatively to the screw movement and do not enter or exit the process. Consequently, the defined leaves inlet face of the basic numerical domain in the fully-filled process is used as a degassing outlet (pressure outlet) for the gas phase (air) in this model (Figure 4-18 a). The extract outlet exhibits varying mass flow rates of water and gas in experiments. To account for this variation, a flow split outlet has been defined, assigning 50% of the total mass flow to this boundary. The defined pressure outlet adapts naturally as proven in literature [GK08]. A mass balance validation confirmed compliance with the total mass balance.

The raffinate outlet face is not used as an outlet in this flow model, but is defined as a wall. The extraction cake is not represented in CFD, since it has a stable thickness in steady-state operation and does not play an important role for the extraction efficiency. An implicit unsteady solver with a 1st order temporal discretisation has been chosen to increase the stability of the simulation. The implementation of an adaptive time step model with a convective mean CFL number of 1 and a maximum of 80 ensures the stability of the simulation and an accurate representation of the free liquid surface. The minimum time step was defined with $\Delta t = 10^{-4}$ s, corresponding to final CFD values between $1 \cdot 10^{-4}$ and $1 \cdot 10^{-3}$ s and a mean CFL number of ≈ 0.2 . The highest CFL numbers occur in the small layer cells of the stationary domain at the transition from the screw extractor to the extract outlet. This is where the solvent velocities are increased. Further selected physical models and parameters

are listed in Table 4-7. A total physical time of 190.89 s was computed, representing 7 total screw turns until reaching a quasi-steady-state. For this simulation the high-performance computer (HPC) cluster with 240 CPU cores (15 nodes) was used to achieve results after 4.5 days.

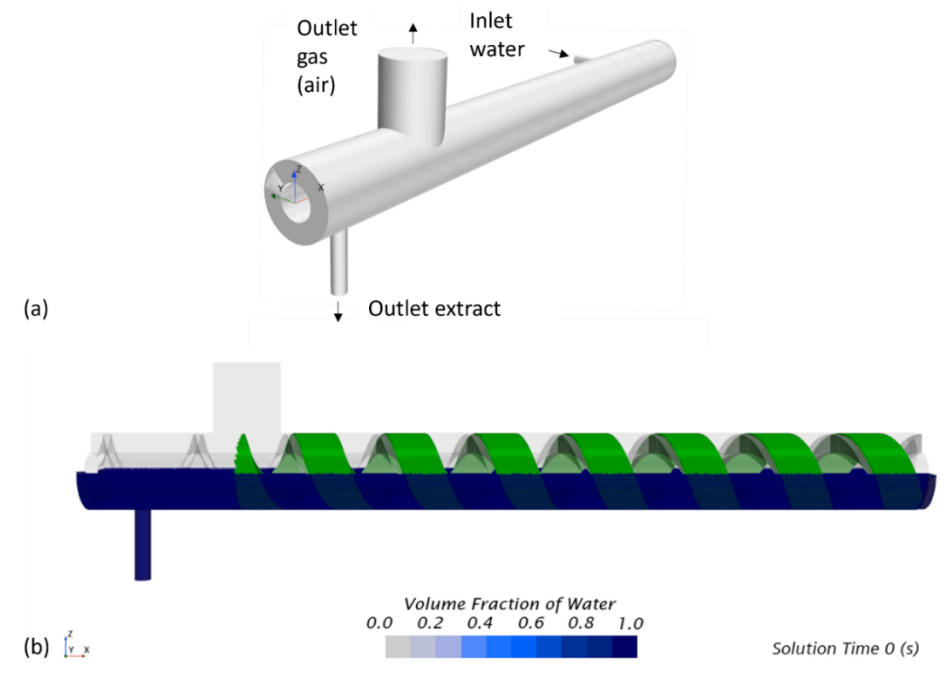


Figure 4-18: Initial and boundary conditions for the partly-filled VOF model. (a) Boundary conditions with flow directions for the water/gas flow. The solvent (water) inlet position is rotated by 90° to directly enter the liquid phase inside the extractor (following [LJM+22b]), (b) initial position of the solvent (water) phase (blue) and the gas (air) phase (white) with fixed position of the A. annua geometry (green) at the x-z-plane.

To analyse the residence time distribution (RTD) of the solvent at the extract outlet, the species method is a computationally efficient, precise, and widely used approach [CBB+19]. This method solves a single species transport equation during a numerical tracer experiment, accounting for both convection and diffusion processes [DSJ+09], [CBB+19], [ZWJ+15]. The species method could already be effectively used in a preliminary simulation to model the RTD behaviour of a single-phase flow of A. Annua leaves within the screw extractor [LJM+22a]. The species method has been implemented in the quasi-steady-state simulation, where each screw revolution is intended to deliver a similar velocity field. The flow field at this quasi-steady-state was frozen and a tracer species has been initialised, tracking only convection processes. Diffusion processes were neglected, as implementing the calculated experimental axial diffusion coefficients led unrealistic results. Further studies will be necessary to understand the origin of this problem. A constant time step of $\Delta t = 0.5 \, \mathrm{s}$ has been implemented for this post-processing step, which is higher by a factor 5 000 compared to the

simulation time step for reaching a quasi-steady-state. Finally, only one transport equation for the tracer species was solved in the domain leading to results of liquid RTD after a simulation time of only 5 min on 64 CPU cores (4 nodes).

Table 4-7: Physical models for the partly-filled VOF simulations (T = 20°C).

Parameter	Settings	Unit		
Multiphase flow model	Volume of Fluid (laminar)			
liquid phase (water)	ref. to Table 3-3			
gas phase (air)				
density	1.20	kg/m³		
dynamic viscosity	1.7	$\cdot 10^{-5}$ Pa \cdot s		
screw rotation rate	2.2	rpm		
Boundary conditions				
leaves inlet = outlet gas	101 325 (= p_{atm})	Pa		
solvent inlet	2.71	$\cdot 10^{-4}~{ m kg/s}$		
extract outlet	split ratio: 0.5	-		
raffinate outlet	wall	-		
Adaptive time step criteria				
convective mean CFL number	1	-		
convective max CFL number	80	-		
minimum time step	1.10^{-4}	S		
maximum time step	0.01	S		
Solver	implicit unsteady			
temporal discretisation	1 st order	-		
discretisation scheme: momentum	SIMPLE	-		
under-relaxation factor				
velocity	0.4	-		
pressure	0.2	-		
discretisation scheme: volume fraction	single-step			
under-relaxation factor	0.2			
Inner iterations	10	-		
Species method – passive scalar				
discretisation scheme: convection	2 nd order	-		
transport	convection only	-		
under relaxation factor	0.9	-		
time step	0.5	S		

Results and validation

Steady-state

Figure 4-19 (a) shows an increased water surface compared to the initial position in Figure 4-18 (b). The water surface drops at the position of the degassing outlet where the fixed A. annua volume decreases to zero. This results in a nearly gas-filled screw segment at the left

side of the extractor where the extract outlet is located. Consequently, not only solvent but also gas exit at the extract outlet. Figure 4-19 (b) shows the extract mass flow rate of water which stabilises after a solution time of 30 s (\approx 1 screw turn) and equals nearly zero until a solution time of 80 s (\approx 3 screw turns). After this time the extract mass flow rate starts to gently fluctuate showing the real flow pattern of the two-phase flow. This fluctuation is similar to the experimentally observed dripping at the extract outlet. The mass flow rate error e {Eq. (3-18)} of water, shown in Figure 4-19 (c), decreases to a value of 1.7% after a solution time of 190.89 s (7 screw turns), revealing a quasi-stationary flow.

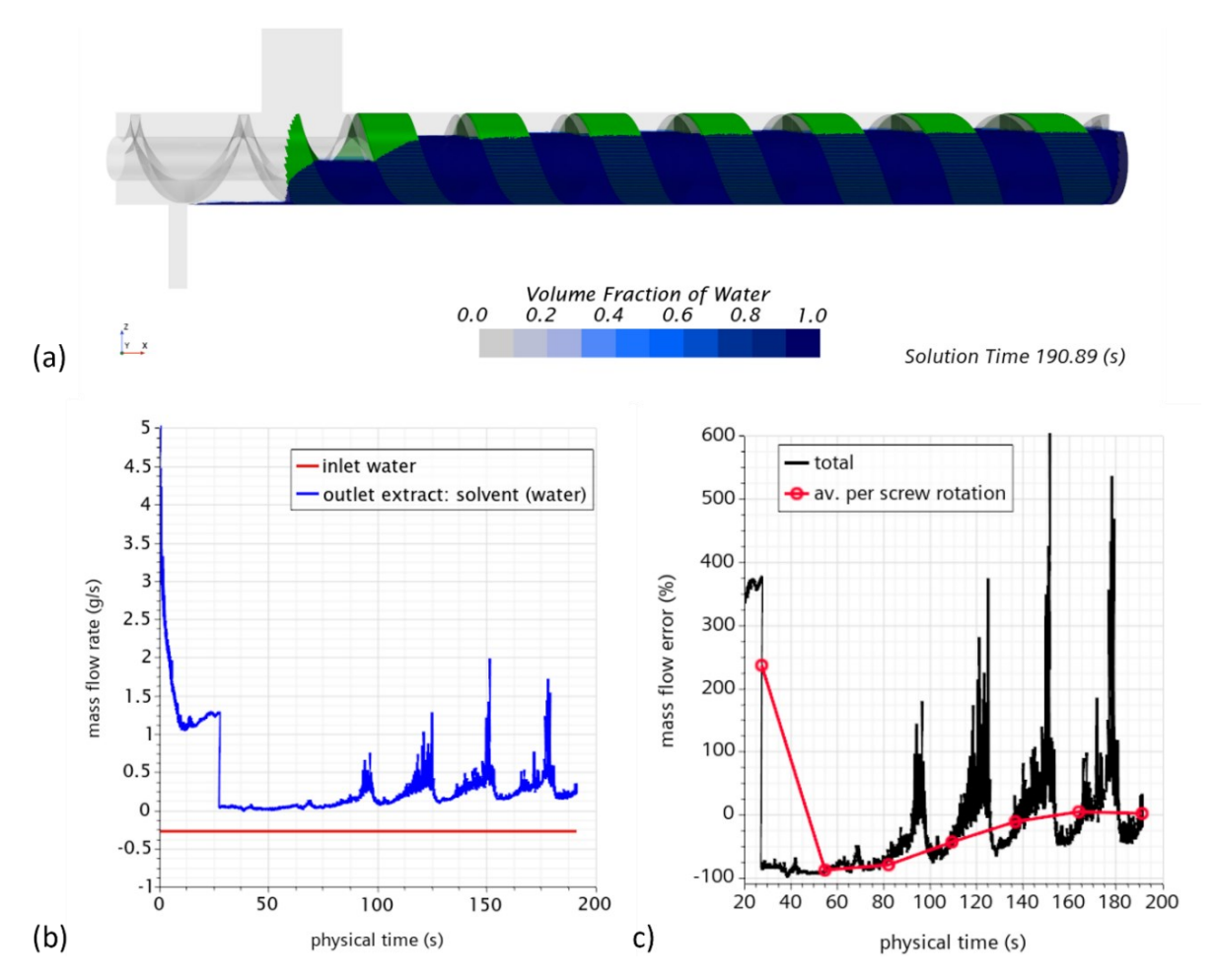


Figure 4-19: Quasi-steady-state of the partly-filled VOF model. (a) Phase distribution of water (blue), air (transparent) and A. annua leaves (green) in the extractor geometry after a solution time of 190.89 s (7 screw turns). The water surface increases from left to right due to the rotation of the screw with the fixed A. annua phase and resulting pressure variations, (b) mass flow rates of solvent inlet and extract outlet, (c) mass flow error e {Eq. (3-18)} of the solvent between in- and outlet (black) and averaged values for every screw rotation (27.27 s) (red) showing a decrease to a final error of only 1.7% for the considered solution time.

The numerical phase distribution of gas, liquid and A. annua leaves is optically compared to the experimental setup in Figure 4-20. For one screw segment in the centre of the extractor,

very similar phase distributions can be qualitatively detected. At the position of the extract outlet in both setups the gas phase dominates while the solvent is located only at the bottom of the extractor. A. annua leaves are only present at the wall of the experimental setup at this position and are not needed to be represented by the numerical setup.

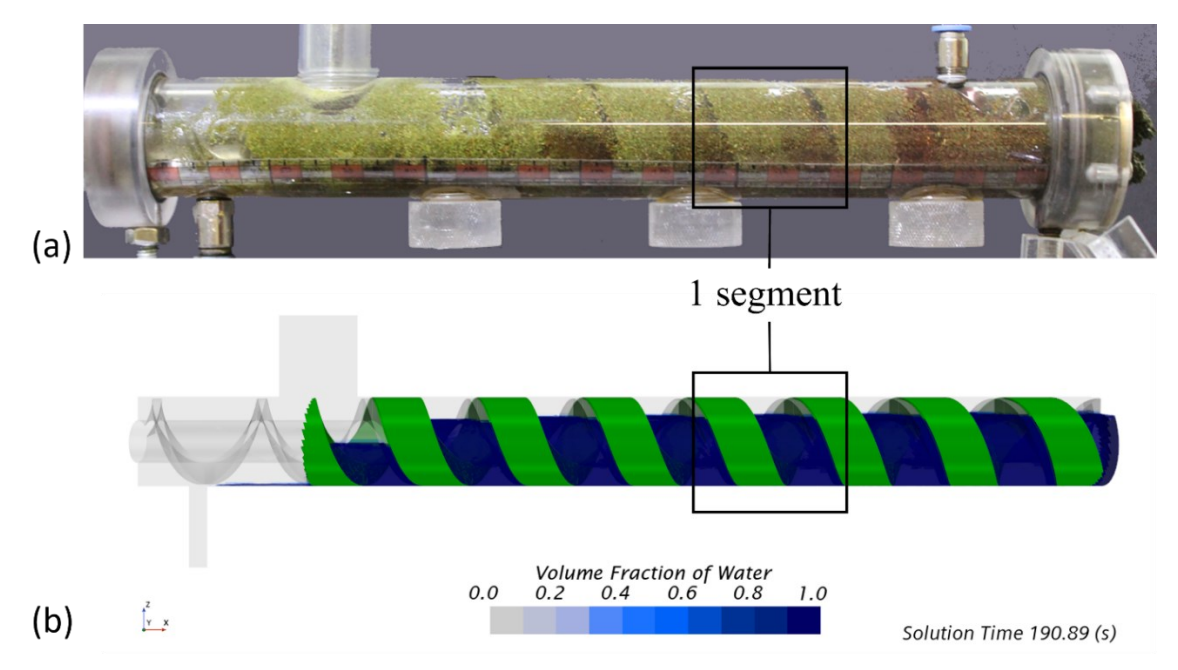


Figure 4-20: Visual comparison of phase distribution. The position of the solvent-soaked A. annua leaves and solvent (water) is similar in (a) the experimental extraction process at continuous operation (green- A. annua leaves, red- coloured solvent) and (b) the numerical quasi-steady-state after 190.89 s, i.e., 7 screw turns (green – A. annua leaves, blue – solvent). In both cases, the air phase is transparent.

RTD of the solvent

The resulting RTD of the solvent phase based on the species method in CFD is compared with the experimentally measured RTD curve (subsection 3.4.4) with the same screw rotation speed (n = 2.2 rpm) in Figure 4-21. Since a numerical time step of 0.5 s was used, the resulting values of E(t) were summarised over each minute to enable comparison with the experimental data, where sampling occurred at one-minute intervals (Figure 4-21 a). A good agreement can be observed in shape. Both curves reach their maxima after a physical time of 3 min. Nevertheless, the numerical curve increases and decreases faster and shows a higher maximum peak compared to the experimental one (experimental: 0.173 1/min, numerical: 0.275 1/min). This could be attributed to the fact that diffusion processes have been switched off when analysing the CFD with the species method. In a dimensionless comparison using the dimensionless time t_0 {Eq. (4-30)} and the dimensionless normalised

RTD function E_0 {Eq. (4-31)} a good agreement in shape is found (Figure 4-21 b). This shows that the ratios between the normalised RTD function at a specific time E(t) and the (constant) value for the calculated mean residence time at SP 4 $E(\bar{\tau})$ are very similar compared to the experimental ratios.

$$t_0 = \frac{t}{\bar{\tau}} \tag{4-30}$$

$$E_0 = \frac{E(t)}{E(\vec{\tau})} \tag{4-31}$$

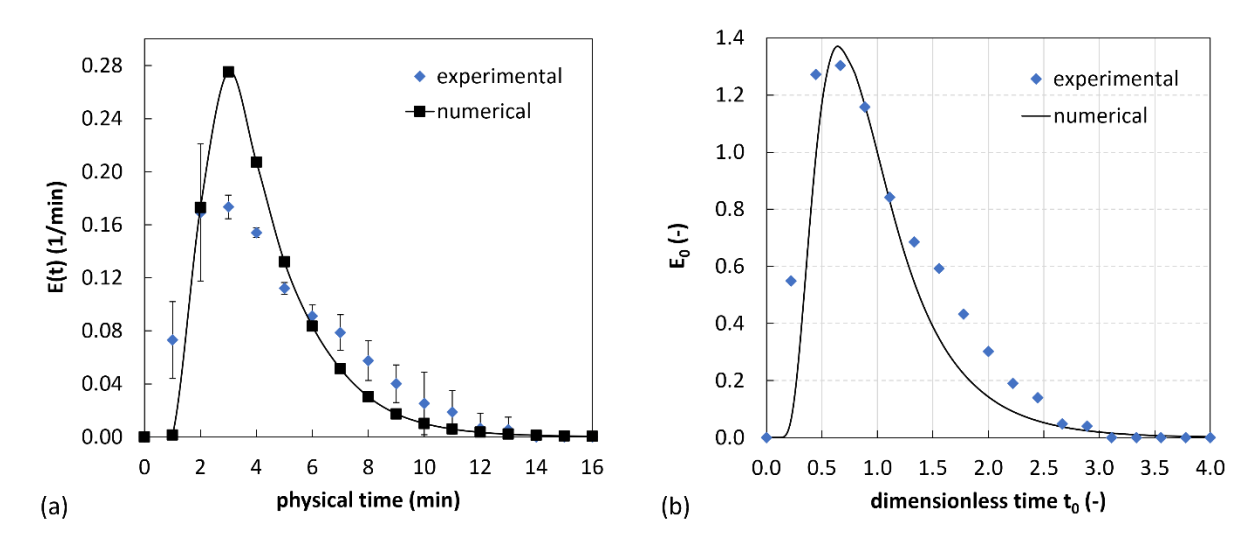


Figure 4-21: Results from the solvent RTD study at operation point 2 (n = 2.2 rpm). The deviations detected when repeating three experimental runs are compared with a quasi-steady-state of the CFD simulation showing good agreement.

The numerical mean residence time and the variance are calculated based on Eqs. (2-31) and (2-32), while the standard deviation derives from the square root of the variance. The time duration for the calculation of the MRT and variance has been set equal to that in the experimental procedures to allow for a comparison. For the steady-state conditions, the obtained agreement is again very good (

Table 4-8). The numerical MRT is lower by only 2.2% compared to the experimental one (exp: 4.5 min, num: 4.4 min). This error is in the range of the mass flow error of water, calculated with 1.7% (Figure 4-19). Considering additionally the standard deviation, the numerical result still fits very well into the experimentally measured range. Further, the calculated stage number N_l results in a value of three for both, experiments and CFD. Consequently, also the Bodenstein numbers are identical. This indicates an excellent representation of the liquid RTD behaviour by the implemented CFD model.

Table 4-8: Results of numerical RTD study of the liquid solvent for OP 2 (ref) and comparison with experiments. Operation conditions are listed in Table 3-9 and experimental measurements in subsection 3.4.4.

Parameter		experimental	numerical	Unit
mean residence time	$ar{ au}_l$ {Eq. (2-31)}	4.5	4.4	min
standard deviation	σ_{l} {Eq. (2-32)}	± 2.5	± 2.4	min
theoretical number of stages	N_{I} {Eq. (2-33)}	3	3	-
Bodenstein number	Bo _l {Eq. (2-44)}	6	6	-

To validate the model for several steady-state operation points, similar simulations have been performed with the conditions of operation point 1 and 3 (Table 3-9). Since the estimated retention volume of the solid leaves in the experiments was found to be very constant for all operation points (<5% variation, Table 3-21), the rotating geometry representing the solid phase was kept constant. Consequently, only the rotation rate and the inlet mass flow rate of solvent were adapted, by considering the assumed loss by absorption of leaves (\dot{m}_{int}) using Eq. (3-12) (similar to the previously investigated OP 2). For OP 1 with a screw rotation speed of 1.3 rpm (one rotation = 46.15 s) the mass flow error already converges after 5 screw rotations and results in an error of 6% (Figure 4-22). As the computational cost for one screw rotation is particularly high for OP 1 due to the low rotation rate, it is recommended to stop the simulation after 5 screw rotations assuming a quasi steady-state. The RTD was analysed at the corresponding solution time (230.8 s).

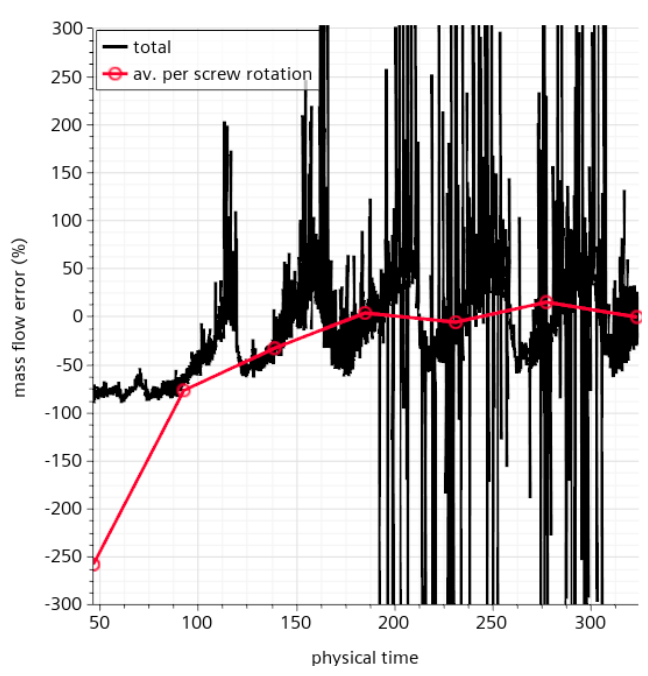


Figure 4-22: Mass flow error e {Eq. (3-18)} of the solvent (water) for OP 1 between in- and outlet (black) for a duration of 7 screw rotations and averaged values for each screw rotation (1 rotation = 46.15 s) (red) showing a convergence after 5 screw rotations (230.8 s) to an error of only 6%.

The resulting solvent-phase RTD curves for both setups (OP 1 and OP 3) show good agreements (Figure 4-23). For both operation points the curve peaks in Figure 4-23 (a) and Figure 4-23 (c) are numerically overestimated (e.g., OP 3: exp: 0.196 1/min, num: 0.275 1/min). When time and E(t) function are normalised according to Eqs. (4-30) and (4-31) small peak overestimations remain (Figure 4-23 b and Figure 4-23 d). The differences are larger for OP 1, probably due to the slow screw rotation speed and resulting higher diffusion effects which are neglected in the CFD model.

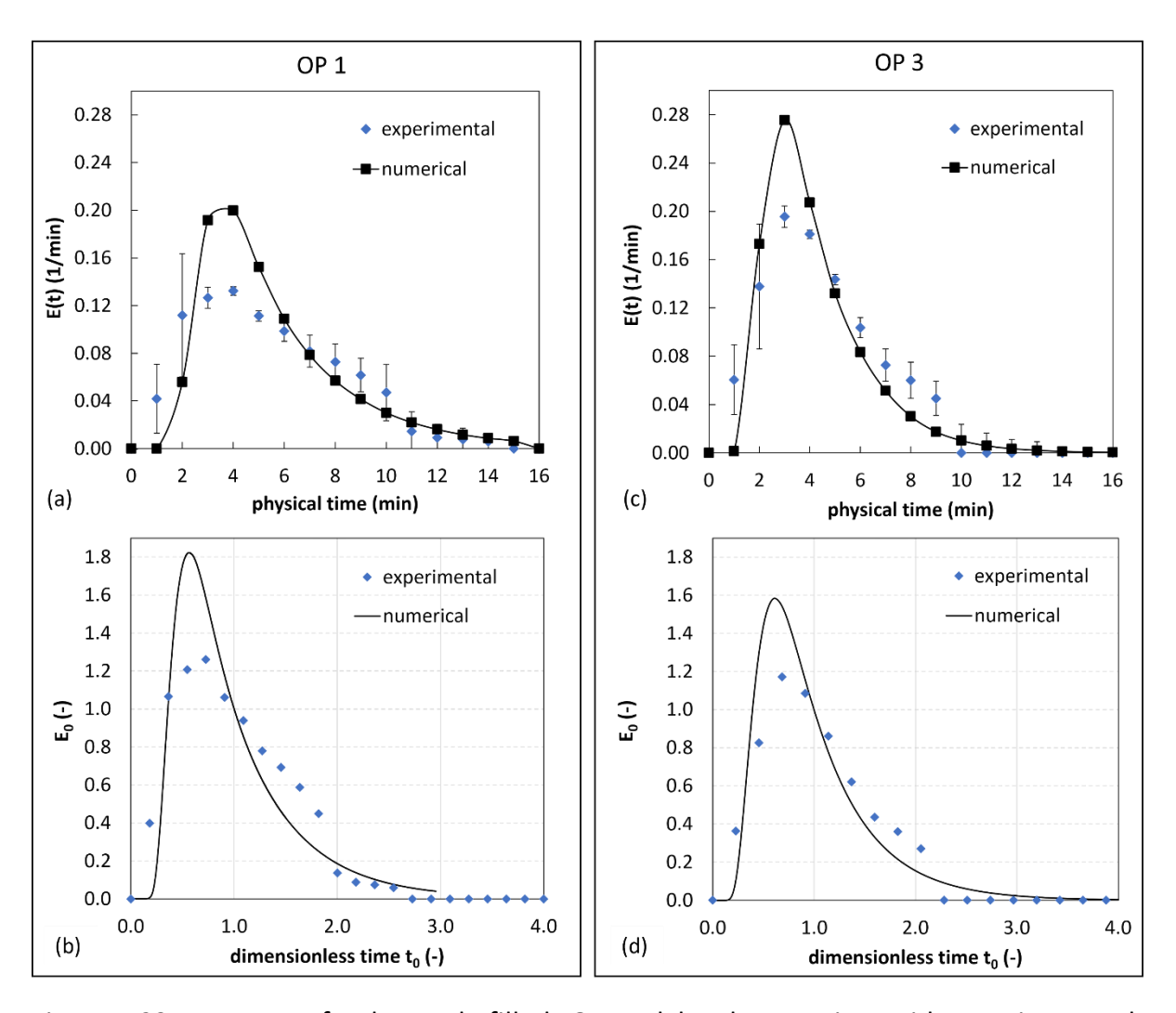


Figure 4-23: RTD curves for the partly-filled VOF model and comparison with experiments. The RTD curves of the numerical model (black) and experimental measurements (blue) are shown for OP 1 (n = 1.3 rpm) (a) with dimensions, and (b) dimensionless. The RTD curves for OP 3 (n = 2.5 rpm) are shown in (c) with dimensions and (d) dimensionless. For the dimensional experimental measurements deviations are shown, detected when repeating three experimental runs.

Nevertheless, the estimated mean residence time and variance are very similar between experiments and numerical simulations (Table 4-9). For OP 1 the MRT comes with an error of

only 4%, which is in the range of the mass flow error of 6% for this solution time (OP 1: exp: 5.5 ± 2.8 min, num: 5.3 ± 3.3 min) (Table 4-9). The standard deviation differs slightly which can again be attributed to neglecting diffusion effects in the CFD simulation. This results in small differences of the theoretical number of stages and the Bodenstein number (OP 1: exp: Bo_l = 8, num: Bo_l = 6). However, the order of magnitude is identical. For OP 3 a good fit of the MRT and standard deviation is obtained numerically showing a high accuracy of the model for higher screw rotation speeds (OP 3: exp and num: 4.4 ± 2.3 min). Consequently, also the theoretical number of stages N_l and the Bodenstein number Bo_l are identical.

The nearly constant Bodenstein numbers found in the numerical model for OP 1, OP 2, and OP 3 align with the previously investigated constant Bodenstein numbers in the experiments, as discussed in subsection 3.4.4. This indicates an accurate representation of the solvent-phase flow behaviour in the counter-current extractor using the partly-filled VOF model.

Table 4-9: Results of numerical RTD study of the liquid solvent for OP 1 and OP 3 and comparison with experiments. Operation conditions are listed in Table 3-9 and experimental measurements in subsection 3.4.4.

Parameter		Operation Point (OP) Unit			Unit	
		1		3		
		ехр	num	exp	num	
mean residence time	$ar{ au}_l$ {Eq. (2-31)}	5.5	5.3	4.4	4.4	min
standard deviation	σ_l {Eq. (2-32)}	± 2.8	± 3.3	± 2.3	± 2.3	min
th. number of stages	N_l {Eq. (2-33)}	4	3	4	4	-
Bodenstein number	Bo ₁ {Eq. (2-44)}	8	6	8	8	-

In conclusion, the Volume of Fluid model is very helpful to represent the complex flow pattern in a simplified way and allow for very good predictions of the solvent RTD behaviour. Nevertheless, it is not suitable for representing all three phases (gas, liquid, solvent-soaked-leaves) in a counter-current flow due to its mass and momentum definitions.

The developed simulation setup can easily be adapted to different solvents by only changing the material properties. This was later used in this thesis for compartment modelling using toluene as solvent accounting also for extraction kinetics (see chapter 5).

4.7 Summary

Based on systematic experiments a multiphase CFD model has been developed to describe important features of the continuous solid—liquid counter-current extraction process while neglecting any mass exchange. The aim of numerical simulations is to represent this flow based on phase distribution and RTD behaviour in order to provide a model for later optimisation. Further, information from CFD can support the improvement of a compartment model to consider also mass transfer and extraction kinetics, as discussed next.

The Eulerian Multiphase (EMP) model was first used to represent the solid-liquid multiphase flow. Due to high computational costs, only one screw segment was represented. The A. annua leaves are considered as solid phase with a pseudo-viscosity ($\mu_s = 1 \cdot 10^3 \, \text{Pa·s}$). The EMP should actually be able to represent a counter-current flow due to appropriate boundary conditions. Nevertheless, the model is found to be very sensitive to cell quality factors, especially the skewness angle. As a consequence, the model could not be used for the investigated screw-driven reactor in this work.

Another approach using the Volume of Fluid (VOF) method was implemented to represent a fully-filled two-phase multiphase flow by first neglecting the gas phase. This simulation could be performed in a quasi-steady-state reaching an acceptable total mass flow rate balance. Nevertheless, the required phase separation at the outlets in counter-current flow conditions could not be reached. The pressure gradient implemented at the perforated disk to prevent the pure water phase from exiting also influences the flow behaviour of the solvent-soaked leaves. The mass flow rates of solvent (water) and solid (A. annua) phase at extract and raffinate outlet did not correspond to the experimental mass flow rates. These facts prevent the correct representation of the counter-current flow and the RTD behaviour in a configuration without gas phase. A continuous counterflow of three phases is not possible due to stability problems and very high computational costs.

Finally, a partly-filled VOF multiphase flow involving solvent and gas phase, with leaves treated as a solid phase, provides a good agreement of the phase-specific mass flow rates at the outlets in a quasi-steady state. A good prediction of the liquid RTD is obtained for several operation points, validated with experimental measurements. Nevertheless, this model strongly approximated the transportation process of the A. Annus leaves and has an increased computational load compared to the fully-filled process.

Figure 4-24 shows a comparison of the calculation times for reaching two screw rotations

(with n = 2.2 rpm) on 10 CPUs for VOF (fully-filled and partly-filled), and the EMP model. Since the EMP model could not be used to reach several screw rotations, its calculation time is extrapolated. Also the simulation domain was extended from one screw segment to the full extractor length. The cheapest approach (VOF fully-filled) does not deliver physically correct flow directions. The EMP model could not be used in a stable manner. Even if the partly-filled VOF model requires at least 7 screw rotations for reaching a quasi-steady state making the simulation very cost-intensive on HPC clusters, this approach is recommended for further investigations.

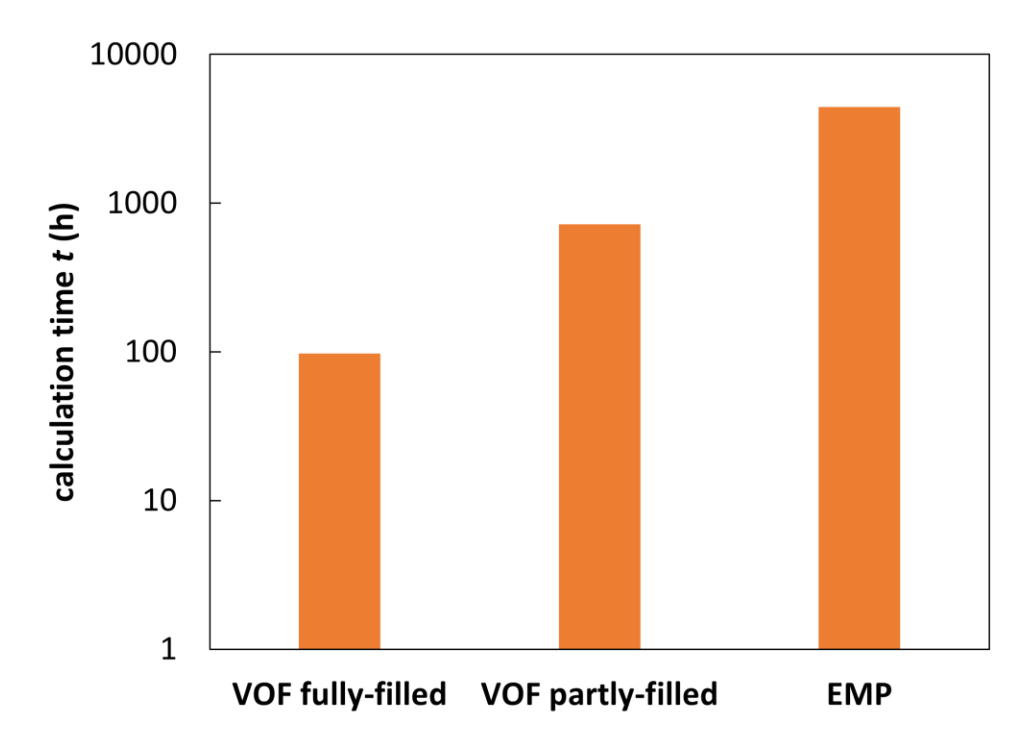


Figure 4-24: Comparison of the calculation times for two screw rotations (10 CPUs, n = 2.2 rpm). The calculation time for VOF fully-filled, VOF partly-filled and EMP (extrapolated from one screw segment) shows a significant increase concerning the computational time.

Answers:

- 1. Which multiphase flow models are available to simulate the complex counter-current process regarding its main flow requirements?
- The Volume of Fluid (VOF) model and the Eulerian Multiphase (EMP) model provide appropriate conditions for representing the investigated flow in a quasi-steady-state. Nevertheless, both models show specific limitations and come with high computational requirements.
- 2. What is the specific distribution of the involved phases at steady-state?
- ➤ Using the partly-filled VOF model a uniform phase distribution between A. annua leaves and solvent can be detected in the middle segments of the screw extractor. The solvent is slightly retained by the screw rotation until reaching the extract outlet. Here a dripping is detected, similar to experiments.
- 3. Is it possible to accurately represent the residence time behaviour of both solid and liquid phases using CFD?
- The solvent RTD can be well represented by a partly-filled VOF model considering only gas and liquid solvent. The solvent-soaked A. annua leaves are represented as a fixed, rotating geometry. A good agreement between numerical results and experiments was determined for several operation points. The solid RTD, mainly driven by the screw rotation, could not be represented in a continuous multiphase process. However, the mean residence time of solvent-soaked leaves in a continuous process can be calculated by using the experimentally derived transport efficiencies in section 3.5.

5 CFD-based compartment model

The implementation of compartment models (CPT), also called "network-of-zones" or "multizonal" modelling approach is much less demanding in terms of computational time compared to full CFD simulations [BMP03], [BM04]. They are often applied to highly complex flows such as bioreactors [GBM+09], [DDC+10], [DCC+14], [TSB+19], bubble columns [RJ03], [ASG13], loop reactors or extraction columns [WSG+20], [WCM+19]. CPT models divide the domain into several smaller volumes, called compartments, which share similar and approximately homogeneous flow properties such as turbulence, velocity, concentration, etc. These compartments allow for easy implementation of reaction, breakage and coalescence models. However, fluxes between the individual compartments may be underestimated if the number of compartments is too small. This can lead to inaccuracies in the prediction of mixing behaviour [DCC+14]. Recently, the combination of CFD with CPT models has emerged. Here, the flow field is first calculated by a CFD model neglecting any reactions or mass transfer. Based on these results a compartment model is developed or fitted [DCC+14], [WSG+20], [SFH+23], [TBN20].

For the investigated solid-liquid extraction process Vu has already developed a simple theoretical counter-current compartment model to predict the mass fraction of artemisinin at the extract outlet, as presented in subsection 2.3.2 [Vu23]. The model is already in rather good agreement with experiments. The main assumptions of this reduced CPT-model for selected parameters are compared in Table 5-1 with the experimental conditions and the detailed CFD model.

The reduced compartment model developed by Vu considers only the extraction kinetics of artemisinin transport between phases, without accounting for volume fluxes between compartments. In the CPT model, mass transfer is represented by a constant linear driving force, k_E {Eq. (2-16)}. However, this assumption is inaccurate, as k_E does not apply at the beginning of the process when fresh leaves and solvent first come into contact. Additionally, the model assumes thermodynamic linearity between the leaves and solvent, expressed by K_E^{eq} {Eq. (2-17)} which presumes a constant equilibrium.

The counter-current extraction process consists of four phases: (1) dry leaves, (2) solvent-soaked leaves due to soaking processes, (3) liquid solvent, and (4) gas (air). The gas phase is unavoidable in experiments since the solid-liquid ratio, R, between dry leaves and solvent must remain constant for a steady-state process (subsection 3.4.1). The reduced CPT model neglects the gas phase, as it is irrelevant for extraction. However, assuming full extractor filling leads to incorrect volume flow rates and phase residence times τ , as defined in Eq. (2-35). In contrast, the CFD model includes the gas phase, enabling a more accurate representation of the filling degree and liquid phase residence times. The solvent-soaked leaves are not simulated as a fluid but are instead defined as a solid rotating geometry, moving at the same speed as the screw.

Furthermore, experimental investigations reveal a counter-current flow with backflow through the screw gaps, which the CFD model can represent. However, due to its simplified structure, the CPT model cannot account for such flow behaviour. Additionally, the CPT model assumes equal residence times for leaves and solvent, which contradicts experimental findings (subsection 3.4.4). Consequently, the theoretical number of stages differs for liquid and solid phases but is assumed identical in the CPT model. Despite the higher degrees of freedom in the models, parameter variations are limited to the experimentally defined operating window.

In conclusion the reduced CPT model is a very cost-effective and accurate model to describe the counter-current process. However, it includes several simplifications e.g. neglecting the gas phase, and cannot account for back-flow effects. Here, the CFD model offers significant advantages, as the gas phase can be represented using the partly-filled VOF model. This model also accounts for back-flow effects, which influence the flow behaviour of the solvent. To observe these effects in more detail a compartmentalisation is useful. Further, the transfer to different geometries will be performed in order to find the optimal operating points regarding back-flow conditions.

Scientific questions:

- 1. How can the liquid phase volume fraction be described and which effect does it have on the flow field?
- 2. Which backflow effects are present in the different designs of the screw extractor?

Table 5-1: Comparing experiment with model assumptions of CPT and CFD model.

Parameter	Experiment (steady-state)	reduced CPT model by [Vu23]	detailed CFD model (partly-filled VOF)
thermodynamics	phase equilibrium	linear	ignored
·	for long residence	phase equilibrium	_
	times	with constant	
		K_E^{eq}	
mass transfer	non-linear rate	one rate constant $k_{\it E}$	ignored
	constant $k_{\it E}$	(linear driving force)	
	affected by mixing		
	(driving force)		
phases	-gas (air)	-liquid solvent	-gas (air)
(affected by wetting)	-liquid solvent	-solvent-soaked	-liquid solvent
	-dry leaves	leaves	-solvent-soaked
	-solvent-soaked		leaves as a solid
	leaves		
liquid phase volume		$\varepsilon' = \frac{V_l}{V_l + V_s} \{ \text{Eq. (3-24)} \}$	
fraction			
material	-liquid: $ ho$, μ , c^0	-liquid: $ ilde{c}^0$	$ ho$, μ for gas and liquid
properties	-dry leaves:	-solvent-soaked	phase
	$ ho$, D_p , q^0	leaves: S , \tilde{q}^{0}	
	-solvent-soaked		
	leaves: ρ , μ , S		
flow behaviour	counter-current	counter-current	counter-current
	operation,	operation by	operation,
	backflow-specific	connecting inlets and	backflow-specific for
	for phases	outlets of pseudo-	the solvent
		homogeneous stages	
MRT	$\bar{\tau}_l \neq \bar{\tau}_s$	$\bar{\tau}_l = \bar{\tau}_s$	$ar{ au}_l$, calculated $ar{ au}_{\scriptscriptstyle S}$
			$\bar{\tau}_l \neq \bar{\tau}_s$
results	$ar{ au}_l \pm \sigma_l$	c_{out} , q_{out}	$\bar{ au}_l \pm \sigma_l$
	$ar{ au}_{\scriptscriptstyle S}$ ± $\sigma_{\scriptscriptstyle S}$		\dot{V} through planes
	\dot{m}_{ext} , \dot{m}_{raff}		\boldsymbol{u}_l at each position
	c_{out} , q_{out}		arepsilon' including gas phase
number of stages	$N_s \neq N_l$	$N = N_s = N_l$	$N_{l,} (N_s \neq N_l)$
degrees of freedom			
liquid phase	\dot{m}_l	\dot{m}_l via ε $(x_l^{in}=0)$	\dot{m}_l, ho , μ
solid phase	$\dot{m}_{ds}, F_{ds}, R(\dot{m}_l, \dot{m}_{ds})$	x_s^{in} , S , \dot{m}_{ds} via $arepsilon$	$V_s(S,\dot{m}_{ds})$
extractor	n	m_{tot} , N	V_{tot} , n
further		K_E^{eq} , k_E	

5.1 Refinements of the reduced CPT model based on experimental investigations

As mentioned above the reduced CPT model by Vu [Vu23] includes one single value for the stage number of liquid and solid phase N which could only be estimated. Based on experimental investigations in chapter 3 this value can now be set accurately and strengthen the significance of the CPT model.

For validation of the model with more experimental data, extraction experiments have been conducted in cooperation with Vu by using the solvent toluene in the steel setup. Thereby, the reference operation point 2 was used (renamed as Exp 0), as well as a newly examined upper (Exp 1) and lower (Exp -1) operation point by keeping the solid mass flow rate constant and varying the solvent mass flow rate. This leads to a variation of the liquid phase mass fraction ε in an interval of [0.6, 0.7, 0.8]. The final ARTE mass flow rates in extract/ raffinate can be calculated based on the total mass flow rate $\dot{m}_{ext}/\dot{m}_{raff}$ and the final ARTE mass fraction x_l^N/x_s^1 , respectively:

$$\dot{m}_{ARTE,ext} = x_l^N \cdot \dot{m}_{ext} \tag{5-1}$$

$$\dot{m}_{ARTE,raff} = x_s^1 \cdot \dot{m}_{raff} \tag{5-2}$$

The operation conditions and the final mass flow of ARTE in the extract $\dot{m}_{ARTE,ext}$ are listed in Table 5-2. The extended operation window will be addressed in the outlook of this thesis.

Table 5-2: Extended operation window and ARTE mass flow in the extract using the solvent toluene (in cooperation with Vu). The reference operation point OP 2 was renamed for simplification as Exp 0 (operation conditions see Table 3-31). The upper (Exp 1) and lower (Exp -1) operation points have been performed with identical solid mass flow rate, but varied liquid (solvent) mass flow rate. Note that the employed units are not in SI.

Parameter		Operation point		Unit	
		Exp -1	Exp 0	Exp 1	
			(ref)		
liquid phase mass fraction	$arepsilon$ {Eq. (2-22)}	0.6	0.7	0.8	-
solid-liquid ratio	R {Eq. (3-9)}	0.13	0.1	0.07	g/g
mass flow rate of dry leaves	\dot{m}_{ds}	1.2	1.2	1.2	g/min
mass flow rate of solvent	\dot{m}_l	9.4	11.7	16.1	g/min
mass flow rate of extract	\dot{m}_{ext} {Eq. (3-12)}	6.7	9	13.4	g/min
mass flow rate of raffinate	\dot{m}_{raff} {Eq. (3-11)}	3.9	3.9	3.9	g/min
ARTE mass fraction in	N	0.400	0.445	0.116	
extract	x_l^N	0.186	0.145	0.116	wt.%
ARTE mass flow at extract	$\dot{m}_{ARTE,ext}$ {Eq. (5-1)}	0.0125	0.0131	0.0155	g/min

The model parameters used in cooperation with Vu to solve the linear equation system in Eq. (2-23) are listed in Table 5-3, based on material characterisation by Vu [Vu23]. To fit the model to the three ARTE extraction experiments with toluene in the steel extractor, only the theoretical number of stages N is adjustable. Initially, N is set to 5 as a first estimate. Additionally, a stage number of N=18 was applied to the model, equal to the experimentally investigated value in the glass extractor between the liquid and solid phase (Table 3-33). Since the steel setup is longer by factor 2 compared to the glass extractor, the stage number is expected to double to a value of N=36, following the relation $N/L_{ch}=$ const. {Eq. (2-44)} which also has been implemented.

Table 5-3: Modelling parameter for the counter-current CPT model using toluene as solvent in cooperation with Vu.

Parameter		Value	Unit
initial ARTE mass fraction in leaves	$\chi_{_{S}}^{in}$	0.013	kg/kg
soaking factor for toluene	S_{tol}	2.25	
total reactor mass capacity (steel setup)	m_{tot}	0.4	kg
thermodynamic equilibrium	K_E^{eq}	0.4	_
extraction rate constant	$k_{\scriptscriptstyle E}$	0.05	1/min
liquid phase mass fraction	$arepsilon_{CPT}$	[0.6, 0.7, 0.8]	-
theoretical number of stages	N	[5, 18, 36]	-

The inner profiles of the ARTE mass fractions of extract and raffinate (based on Exp 0) along the stage number N=5 are visualised in Figure 5-1. The real inlet mass fractions of ARTE in the solvent $x_l^{in}=0.013$ and solid phases $x_s^{in}=0$ are marked with red stars (*). The calculated mass fractions in the CPT model according to Eq. (2-23) between stages 1 to N are simulated with the separated mass fractions \tilde{x}_l (blue cross) and \tilde{x}_s (green circle). A linear increase in the ARTE extract mass fraction through the stages is observed, while the ARTE raffinate mass fraction decreases simultaneously. This behaviour is strongly influenced by the thermodynamic equilibrium coefficient K_E^{eq} and the extraction rate constant k_E . The final outlet mass fractions for the pseudo-homogeneous system x_l^N and x_s^1 are calculated using the liquid phase mass fraction $\varepsilon=0.7$ according to Eqs. (2-25) and (2-26), respectively:

$$x_l^N = \frac{\tilde{x}_l^N}{\varepsilon}$$

$$\chi_s^1 = \frac{\tilde{\chi}_s^1}{1 - \varepsilon}$$

The outlet mass fractions are indicated by red triangles (\triangle).

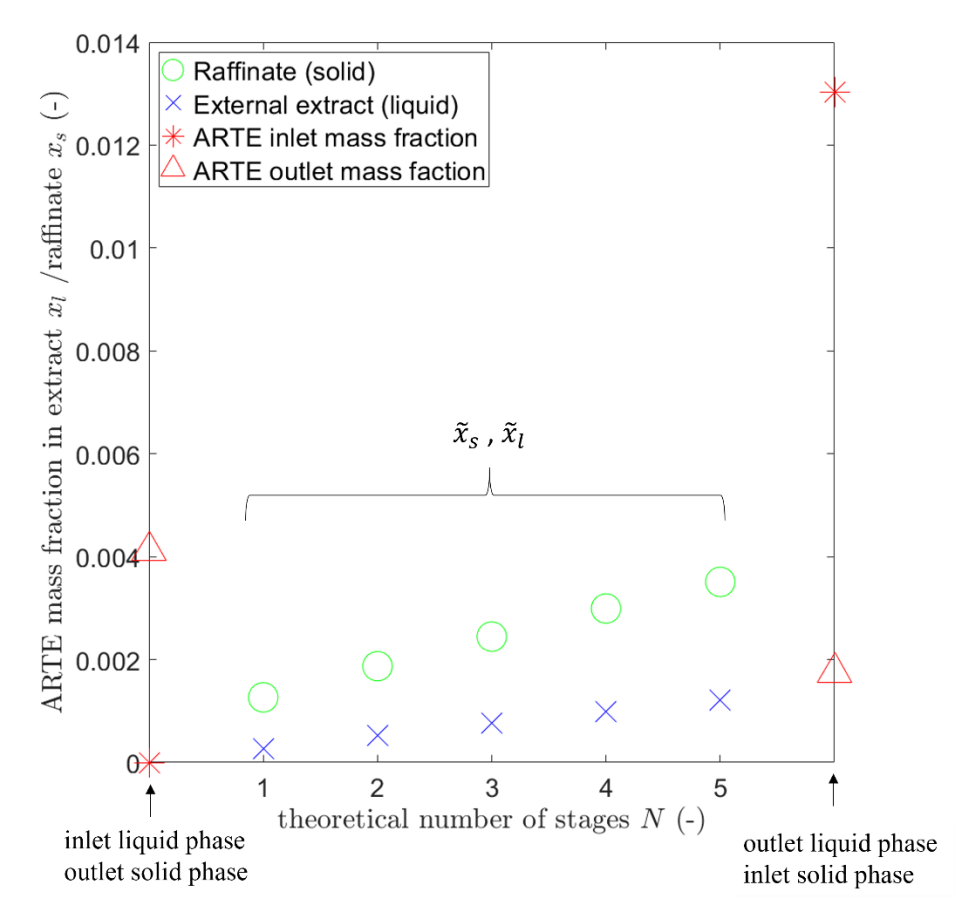


Figure 5-1: ARTE mass fractions along a CSTR cascade with N=5 using the reduced CPT model of Vu [Vu23]. The separated ARTE extract (blue cross) and raffinate (green circle) mass fractions \tilde{x}_l and \tilde{x}_s increase/ reduce linearly from inlet (red *) to outlet (red \triangle) in countercurrent directions. The inlet and outlet mass fractions represent the pseudo-homogeneous system based on the liquid phase mass fraction ε .

When calculating the total ARTE outlet mass flows at extract and raffinate based on Eqs. (5-1) and (5-2), Figure 5-2 (a) shows the dependency on the solvent inlet mass flow (variation of ε) for a stage number of N=5. The three performed extraction experiments Exp -1 ($\varepsilon=0.6$), Exp 0 ($\varepsilon=0.7$), and Exp 1 ($\varepsilon=0.8$), as presented in Table 5-2 are not fitted by this low model complexity (red cross). It clearly underestimates the final ARTE extract mass flow.

For a stage number of N = 18 (Figure 5-2 b) the model predicts the experimental ARTE mass flow rates more accurately, demonstrating the high transferability of results from the glass extractor with the solvent water to actual extraction experiments.

Increasing the stage number to N=36 for the steel setup does not result in a significant change in the predicted ARTE mass flow rates (Figure 5-2 c). The equilibrium between the phases is obviously already reached for N=18.

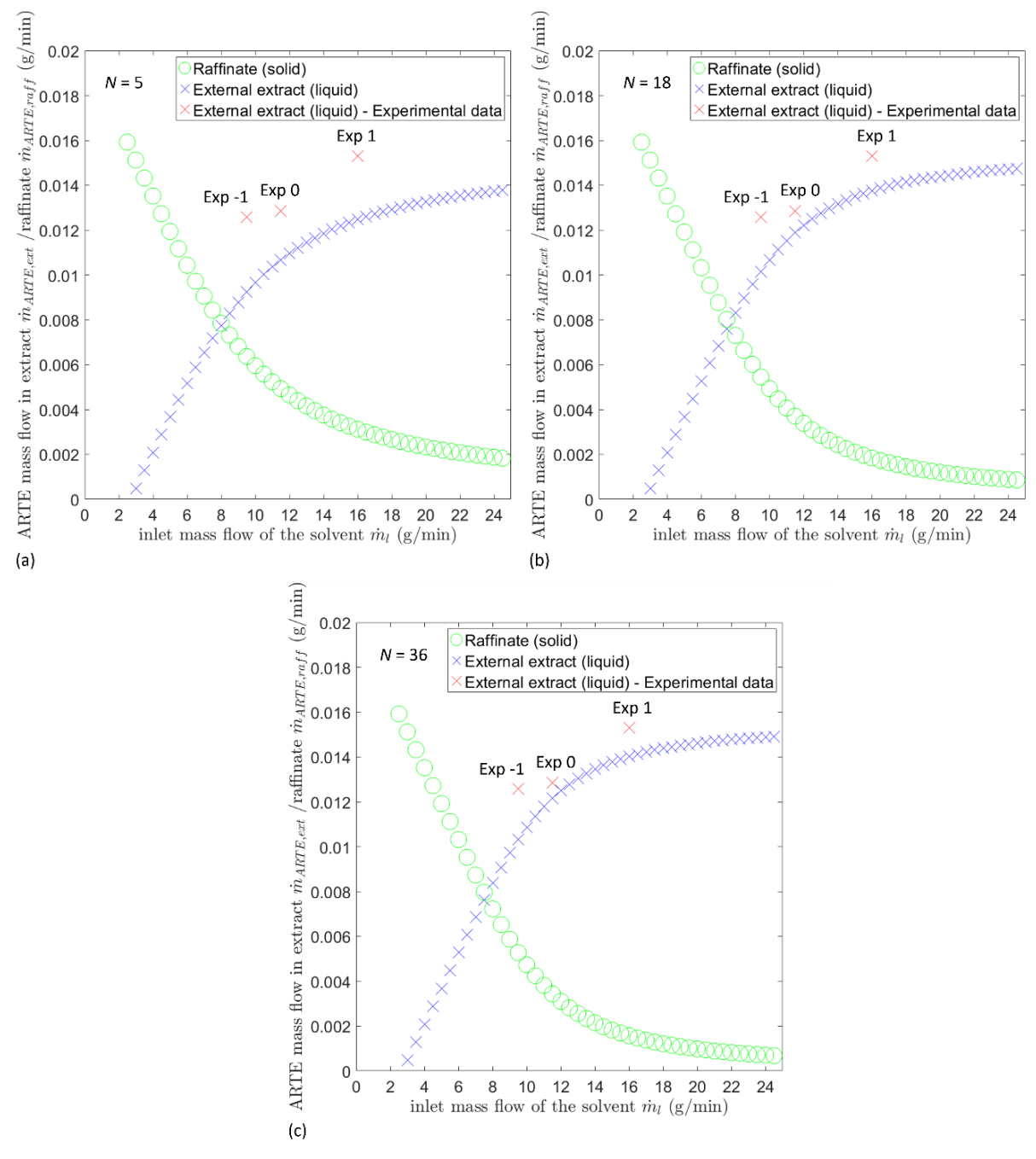


Figure 5-2: Reduced CPT model of Vu validated with experimental data [Vu23]. The ARTE mass flow rate \dot{m}_{ARTE} (y-axis) for the (external) extract (blue cross) and solvent-soaked leaves (raffinate, shown with green circle) depend on the inlet mass flow rate of the solvent, toluene (x-axis). Three experimentally derived ARTE mass flow rates in the extract are shown for validation (red cross) at a reference point (Exp 0) and a lower (Exp -1) and upper (Exp 1) operation point. The model was run with different stage numbers of (a) N=5, (b) N=18 (similar to the averaged stage number, see subsection 3.4.4) and (c) N=36 (estimated for the longer steel setup). A good fit with the averaged stage number N=18 is visible.

As a small conclusion, the stage number examined in experimental investigations by using the glass extractor with the solvent water can also describe the extraction process with toluene in the longer steel setup very precisely.

5.2 Compartmentalisation of the screw extractor for CFD-CPT coupling

The compartmentalisation step is a key step to identify sufficiently large compartment volumes, where the flow conditions are homogeneous. This process can either be performed automatically, based on the flow field [SFH+23], [BM04] or geometrically based on the coordinates [DCC+14]. An automatic procedure can ensure homogeneous flow conditions, but often results in a high number of compartments. A geometrical compartmentalisation by knowledge of the flow field allows a much faster and easier compartmentalisation process [DCC+14] and is used in this work.

The quasi-steady-state flow field of the partly-filled VOF model (subsection 4.6.3) using toluene as solvent with properties listed in Table 3-3 was analysed. The inlet mass flow rate of the solvent toluene was again reduced by the internal extract which is soaked by the leaves according to Eq. (3-12) and (3-13), resulting in a total mass flow rate of \dot{m}_{ext} = 9 g/min or \dot{V}_{ext} = 1.73·10⁻⁷ m³/s (ρ_{tol} = 867 kg/m³).

$$\dot{m}_{ext} = \dot{m}_l - (\dot{m}_{ds} \cdot S_{tol}) = 11.7 \text{ g/min} - (1.2 \text{ g/min} \cdot 2.25) = 9 \text{ g/min}$$
 (5-3)

Figure 5-3 (a) visualizes the quasi-steady state in the extractor along the xy- and xz-plane based on the axial velocity of the solvent only. As visible, x is the axial streaming direction, y the horizontal transverse direction and z the vertical transverse direction. A xy-plane is a horizontal cut through the extractor while a xz-plane is a vertical cut. Figure 5-3 (b) and (c) show a repetition of the velocity values for each screw segment, while the black lines visualize the screw position. The grey region on the left is filled with gas (air). The representation of the vertical xz-plane (Figure 5-3 c) shows that the free surface of the solvent goes up along the extractor from extract outlet (left) to the solvent inlet (right). A correct representation of the extractor with only one screw segment is not feasible due to these evolutions. A geometrical compartmentalisation was performed based on the periodic solvent velocity field and the screw segment length α using configuration OS. The resulting nine segments are separated by an interface (red), as illustrated in Figure 5-4.

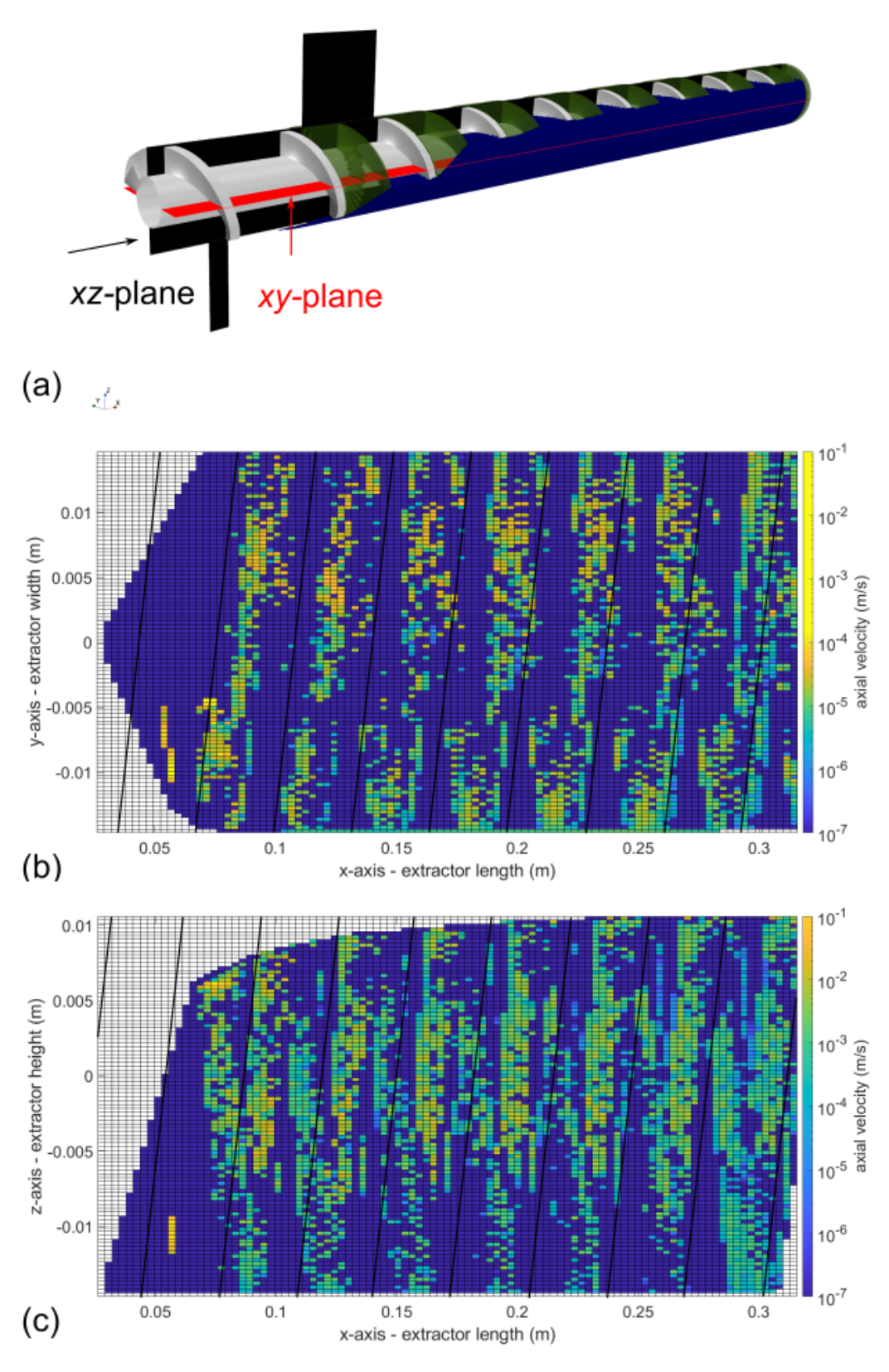


Figure 5-3: Axial velocity field of the solvent (toluene) (a) in 3D view, (b) along the horizontal *xy*-plane and, (c) along the vertical *xz*-plane. The black lines visualize the position of the screw.

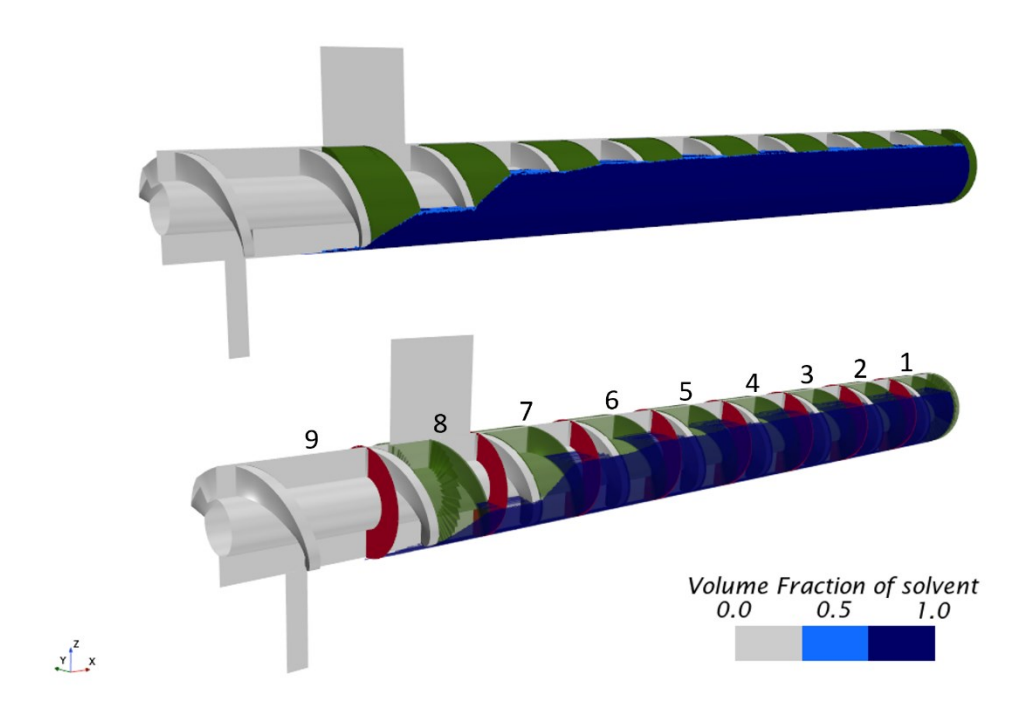


Figure 5-4: Geometrical compartmentalisation of the flow field for OS at steady state. Based on the screw segment length α = 0.035 m, in total 9 compartments are defined starting at the solvent inlet (#1) up to the extract outlet (#9). The separating faces of the compartments are shown as red planes.

The CFD-CPT coupling is quite challenging for the investigated counter-current flow. Similar studies in the literature decoupled the simulation of solid particles and of the continuous phase to simplify the flow (one-way coupling). The continuous flow profile was then used for developing a compartment model which calculates fluxes between identical velocity regions to simulate drop movement, breakage or mixing behaviour [WJ20], [DCC+14]. However, for our flow of interest the continuous liquid phase is strongly influenced by the solid phase and a decoupling would not be reasonable. Further, the rotating elements of the screw change the flow field for each time step, even after finding a steady-state. At the same time the consideration of only one screw segment does not represent the flow field of the total extractor due to the varying free surface. The development of a dedicated CFD-based compartment model for this very complex flow can only be proposed for future work, as discussed in the outlook. Since Vu already developed a reduced CPT model which showed good agreement to experiments, it is reasonable to improve this model by extending it using the CFD model as described in the next section.

5.3 Simplified CFD-CPT coupling

The developed CPT model by Vu simplifies the liquid phase mass fraction ε {Eq. (2-22)} inside the extractor as evenly distributed and neglects the gas phase. This is not the case in the experiments as already optically determined in chapter 3. Further, the model cannot represent the actual flow through the single compartments including backflow effects. These simplifications can be accounted for in the compartmentalised CFD model in this section.

Phase volumes in the compartments

Analysing the CFD results of a steady-state process, the averaged phase volumes between 7 and 8 screw turns in the single compartments for operation point 2 (n = 2.2 rpm) show differences depending on the extractor position, similar to experimental investigations (Figure 5-5 a). The phase volumes from CPT #2 in front of the solvent inlet ($x/L \approx 0.89$) towards CPT #6 are quite constant for all involved phases. The filling degree of the extractor with leaves and solvent nearly equals 90% in the central region. From CPT #6 to CPT #9 the solvent surface decreases towards the extract outlet. In CPT #9 only the gas phase (air) is present in the extractor. The liquid phase volume fraction (red dashed line) in the central extractor part (CPT #2 - CPT #6) equals a value of ε'_{CFD} = 0.50 which is lower by only 9% compared to the experimentally calculated value in Table 3-21 using water as solvent (ε'_{exp} = 0.55). This deviation can be attributed to the difference in the solid-liquid ratio R for water and toluene in steady state operation (Table 3-31). In the reduced CPT model of Vu the constant liquid phase mass fraction of ε = 0.7 can be transformed to the liquid phase volume fraction ε'_{CPT} {Eq. (3-24)} using the phase specific densities ho_l for toluene (Table 3-3) and ho_{ds} for dry ARTE leaves (Table 3-5), the external mass of solvent \dot{m}_{ext} {Eq. (3-12)} (reduced by the soaking factor S_{tol} , Table 3-5) and the inlet mass flow rates for OP 2 (Table 3-31):

$$\varepsilon'_{CPT} = \frac{\dot{V}_l}{\dot{V}_l + \dot{V}_s} = \frac{\dot{m}_{ext}/\rho_l}{\dot{m}_l/\rho_l + \dot{m}_{ds}/\rho_{ds}} \approx 0.57$$

The resulting liquid phase volume fraction of ε'_{CPT} = 0.57 is very similar to the experimental value (ε'_{exp} = 0.55) and higher by only 14% compared to the CFD results (Figure 5-5). This effect might come from the influence of the gas phase in CFD simulations, leading to lower liquid volume fractions. The definition of a constant value is only advisable for the central part of the extractor, but does not apply for the total extractor length, since especially at the extract outlet the gas phase dominates.

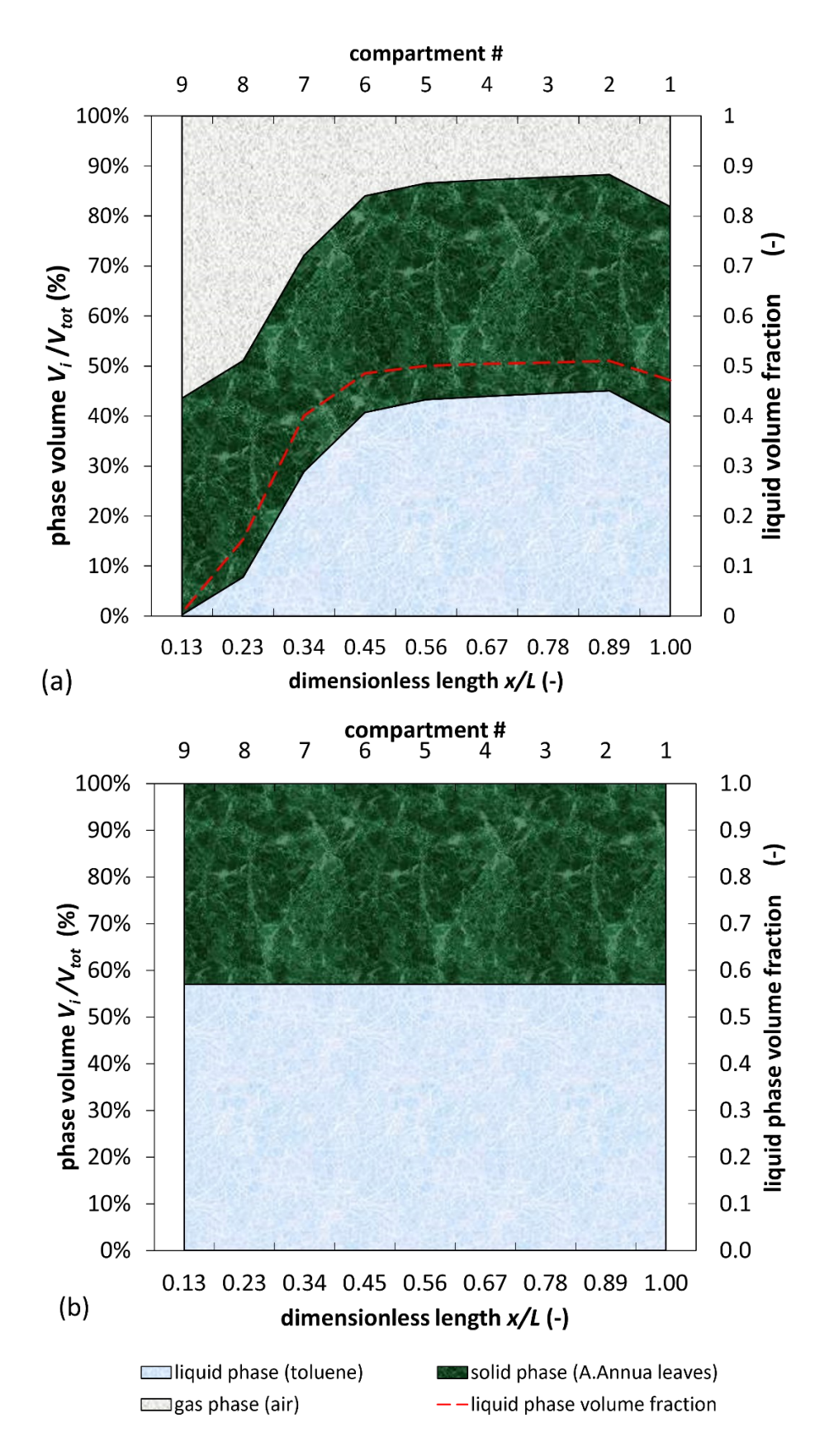


Figure 5-5: Phase volume and liquid phase volume fraction, (a) Analysis in the compartmentalised CFD model with n=2.2 rpm in the compartments along the dimensionless length of the extractor (x/L=1 defines the raffinate outlet), (b) model assumption of the liquid phase volume fraction in the reduced CPT model by Vu [Vu23].

RTD of the solvent (toluene) in each compartment

The mean residence time for each compartment defines the contact time between the solvent (toluene) and the solvent-soaked A. Annua leaves in each stage. Figure 5-6 demonstrates that the mean residence time (MRT) for each compartment increases nearly linearly from CPT #1 (inlet) to CPT #6 and then converges to one value. This implies a high solvent velocity between CPT #6 and the extract outlet (end of CPT #9). The total MRT of toluene with $\bar{\tau}_l=5.2$ min is higher compared to water for the same OP 2 (Table 3-17). This results from the lower solid-liquid ratio R with toluene (section 3.3). Regarding the solvent flow time $\Delta \tau$ through each compartment, CPT #1 exhibits the longest time, nearly one minute, accounting for approximately 20% of the total residence time in the extractor. This optimises the extraction efficiency by providing prolonged contact between nearly exhausted ARTE leaves and fresh solvent at this position. The flow time per compartment remains relatively constant between CPT #2 and CPT #5, while it decreases to below 0.2 minutes for CPT #6 and CPT #7, where only a wetting process of the dry fresh leaves with loaded solvent appears, ensuring a rapid start of extraction.

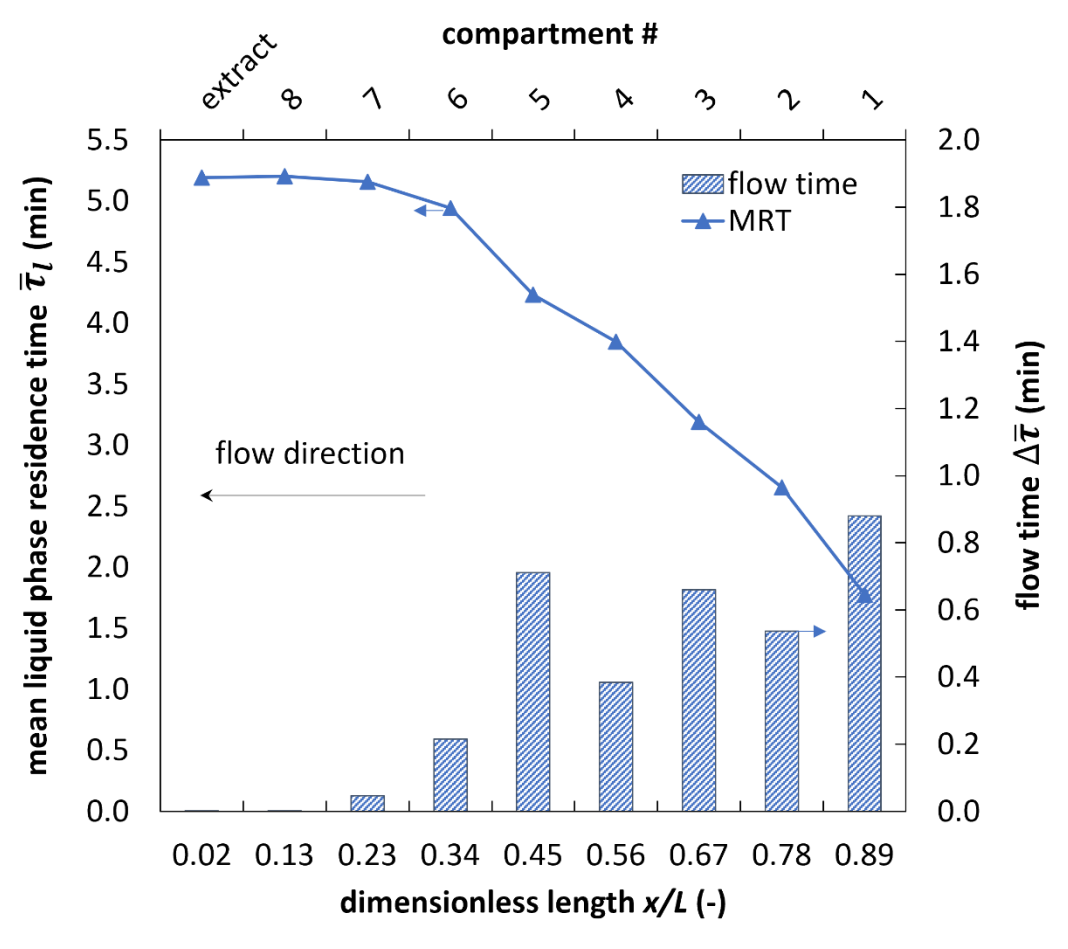


Figure 5-6: Mean liquid phase residence time $\bar{\tau}_l$ and flow time ($\Delta \bar{\tau}$) per compartment at a simulation time of 190.89 s (=7 screw rotation rates).

The CPT model developed by Vu assumes constant volume flow rates through the extractor, and is thus not able to consider backflow effects. In CFD the specific volume flow rate transferred between each compartment can be analysed giving more information about the actual process. Backflow effects can be distinguished for a various number of operation points and screw geometries.

Figure 5-7 illustrates the averaged liquid volume flow rates through the CPTs averaged between two screw rotation (between 7 and 9 screw turns) along the axial direction, from right (inlet) to left (extract outlet, between CPT #8 and CPT #9). The volume flow rates are analysed based on their direction relative to the extract outlet, distinguishing between forward and backward flows. These are presented alongside the total volume flow rate, which is the sum of both components. The total volume flow rate through the extractor (represented by the dashed red line) remains relatively constant across the compartments and predominantly flows in the forward direction (from inlet to outlet), as expected. The low flow rate detected at CPT #1 is attributed to its proximity to the solvent inlet, where the incoming flow splits—partly moving forward through CPT #1 and partly flowing backward. However, this backward component is undetectable in this simulation setup.

In absolute terms, the total flow rate is significantly lower than the forward flow rate of toluene (depicted by the blue line). This discrepancy indicates the presence of backflow (black line), which occurs across the entire contact area between compartments but is minimal within the screw gap (only 10^{-10} m³/s). Due to its low magnitude, the screw gap backflow is not visible in Figure 5-7.

The impact of backward solvent flow must be considered when characterising the extractor's flow behaviour. A higher backward flow is beneficial as it increases the contact time between the solvent and A. Annua leaves, thereby enhancing extraction efficiency.

To quantify this effect, the ratio between the backward ($\dot{V}_{l,back}$) and forward liquid volume flow ($\dot{V}_{l,for}$) is calculated for each compartment (i=1 to N) using Eq. (5-4). The resulting mean value of $\bar{b}=0.45$ indicates that approximately half of the total liquid volume flow moves in the backward direction. This aligns with the experimentally determined low stage number ($\bar{N}_l=4$) indicating a near-CSTR behaviour (Table 3-17).

$$\bar{b} = \frac{1}{N} \sum_{i=1}^{N} \frac{\dot{V}_{l,back}}{\dot{V}_{l,for}} \tag{5-4}$$

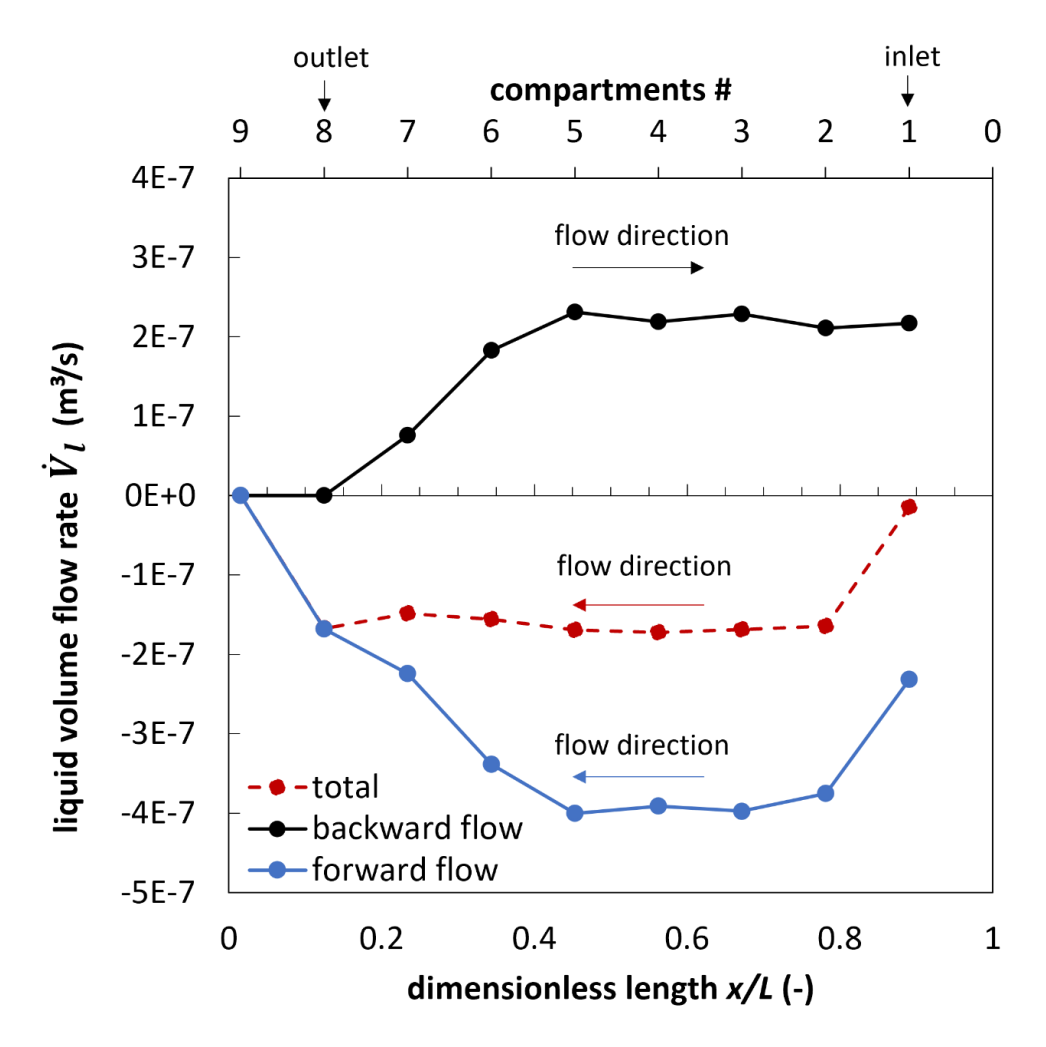


Figure 5-7: Volume flow rates of the liquid phase (toluene) in OS with OP 2 from compartment #1 (inlet) to #9. The extract outlet is located beyond #8. The total volume flow (red) is compared to the forward flow towards the extract outlet (blue) and the backward flow (black), highlighting the significant influence of backward flow.

The developed CFD model can further be applied to evaluate different screw geometries. In this study, the modified screws MS 1 and MS 2 are analysed with respect to their backflow effects on the solvent. Due to the varying length scales of the screw segments (Table 3-1), the compartmentalisation process results in a different number of compartments for each screw configuration. Figure 5-8 illustrates that MS 1 (red line) exhibits similar backflow effects compared to the original screw design OS (black line) (\bar{b} (MS 1) = 0.41, \bar{b} (OS) = 0.45). This suggests similar mixing ratios.

In contrast, MS 2 (blue line) shows significantly lower backflow effects compared to OS $(\bar{b} \text{ (MS 2): 0.3; } \bar{b} \text{ (OS): 0.45})$. In previous investigations MS 2 was already found to be inefficient for transporting the leaves (section 3.5) and should therefore not be considered in future analysis.

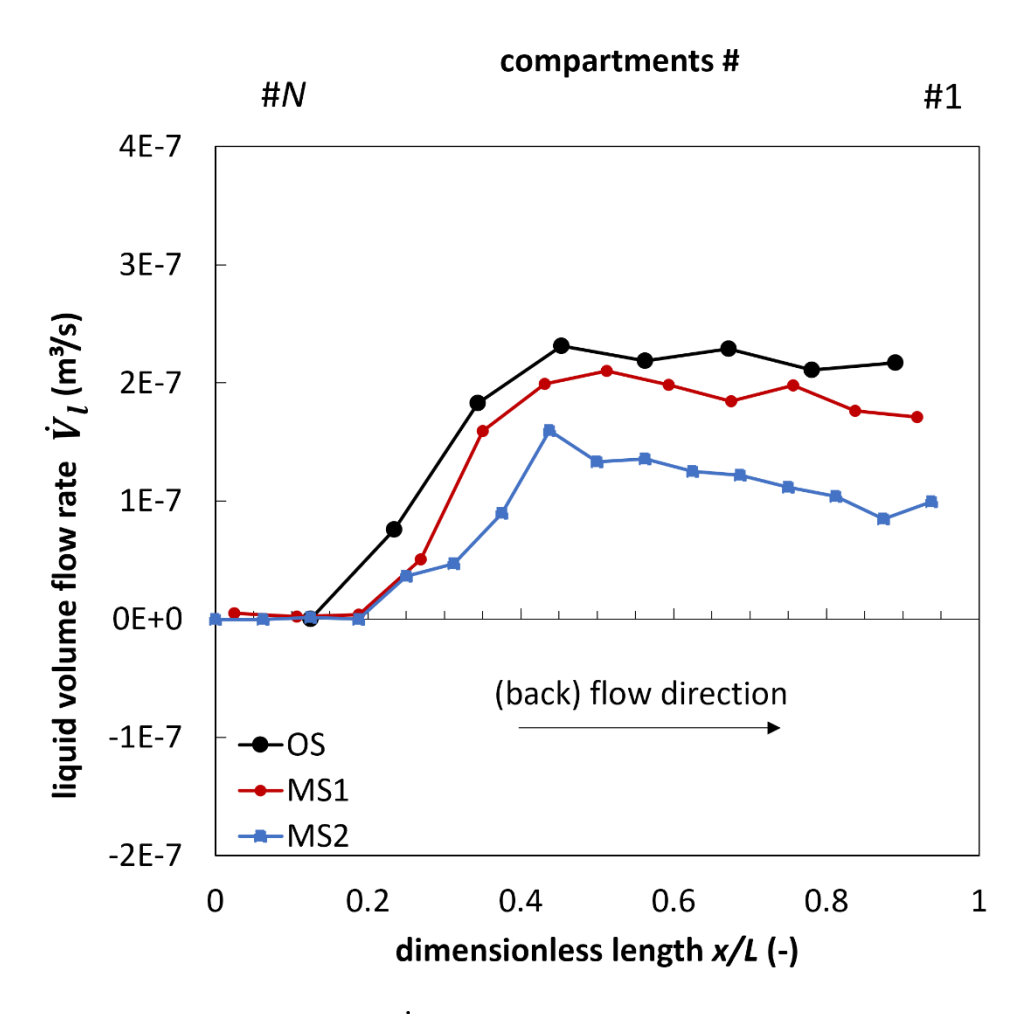


Figure 5-8: Liquid volume flow rate \dot{V}_l in x-direction (backward flow) for OS, MS 1 and MS 2. The backward flow was analysed at each compartment face, while the total number of compartments #N varies between 9 (OS) and 16 (MS 2) due to the different screw designs. The desired backflow for the liquid solvent (toluene) is similar between OS and MS 1 while the lowest value is reached with MS 2. The latter design should not be used for optimal operation.

Combined with a higher extract mass flow for MS 1 of 8% due to a lower cake bulk humidity (section 3.5), and a more efficient transport of solvent-soaked leaves (section 3.4.5) the implementation of this design modification appears promising for increasing the final extraction efficiency of artemisinin during the continuous extraction process, compared to the original screw (OS), with the same operation conditions. Therefore, extraction experiments with toluene need to be performed in future using MS 1 to specify quantitatively the final ARTE mass fraction.

5.4 Summary

The development of models to describe the investigated three-phase counter-current screw extractor is very complex and simplifications had to be made in the reduced CPT model by Vu [Vu23] as well as in the presented CFD simulations. The coupling of CFD simulations with compartment models is a promising approach to achieve more accurate results in reasonable computation times. Nevertheless, more detailed considerations are required and proposed for future work.

A simplified CFD-CPT coupling was performed using a CFD model representing a partly-filled flow with toluene as the solvent, computed with VOF. Geometrical compartmentalisation based on the segment length revealed that phase volumes within the extractor are not constant, contrary to Vu's reduced CPT model [Vu23]. A significant decrease in solid and liquid volumes was observed near the extract outlet, affecting solvent residence times. These remain relatively constant in the central part of the extractor but drop sharply behind CPT #6. The longest residence time was found in CPT #1, where fresh solvent contacts nearly exhausted leaves to extract residual ARTE. The analysis of solvent volume transport revealed that the backward flow corresponds to about 45% of the forward flow, significantly influencing the flow field. This behaviour suggests a near-CSTR condition, consistent with the RTD analysis presented in subsection 3.4.4. Applying the simplified CFD-CPT coupling to modified screws revealed that MS 1 offers similar back-mixing effects compared to OS, while MS 2 is unsuitable for further use.

Answers:

- 1. How can the liquid phase volume fraction be described and which effect does it have on the flow field?
 - The liquid phase volume fraction decreases along the extractor from inlet to outlet, averaging 50% in the central region. This results in consistently high liquid MRT in the central part, dropping to a few seconds near the extract outlet.
- 2. Which backflow effects are present in the different designs of the screw extractor?
 - For OP 2 and the OS geometry, backflow corresponds to more than 45% of forward flow, indicating near-CSTR behaviour consistent with RTD analysis (subsection 3.4.4). MS 1 results in similar backflow which is in combination with experimental investigations promising for ARTE productivity. MS 2 should not be used further.

6 Conclusion

To isolate valuable target components from natural products continuous counter-current extraction processes attract increasing interest. This is essentially due to the facts that extraction efficiencies are higher compared to standard batch extraction, the steady state operation is easier to implement and the product quality is improved. However, the understanding of such processes needs to be further improved and optimised. The use of CFD models can provide valuable insights into process hydrodynamics and support optimisation strategies without the need for extensive experiments. Nevertheless, research on multiphase flows is still incomplete, with key mechanisms and dynamics not fully understood. Hereby, validation of predictions with experiments is crucial.

This thesis focused on the analysis of a continuous counter-current extraction process performed in screw-type extractors. Experiments in a glass extractor have been performed to improve the understanding of the process. The extraction of artemisinin (ARTE) from leaves of *Artemisia annua L.* is considered as a relevant case study. Instead of the efficient solvent toluene, in the experiments devoted to study the hydrodynamics water was used.

According to experimental investigations the counter-current process can be operated under steady state conditions only in a small operation window. This window can be extended performing geometrical or material variations. The solvent-soaked leaves can be described as a highly viscous fluid. Their bulk density is nearly constant in the total extractor and equals the equilibrium state between solid and liquid material. Their actual rheological behaviour is closer to a solid. Consequently, the leaves are mainly transported by the screw. The solid-phase residence time distribution (RTD) was matched to the extraction kinetics explored in a preliminary study in batch experiments carried out to efficiently extract ARTE. As expected, the stage and Bodenstein numbers increased with transportation length revealing a constancy of the axial dispersion coefficient. Sharp RTD curves and low back-mixing effects support the assumption of an almost PFTR-behaviour of the leaves. Reducing the screw angle by using modified screws could even sharpen the solid phase RTD curve, but introduced larger back-mixing effects. The solvent RTD showed significantly lower stage and Bodenstein numbers approaching more a CSTR behaviour. To model the heterogeneous system with a pseudo-homogeneous model proposed in a preliminary work, a mean stage number of 18 was

identified. It was proven that the experimental results examined with the solvent water can be transferred to toluene considering the difference of viscosities and soaking factors.

Based on this experimental information a suitable multiphase model was implemented in the CFD software StarCCM+. General multiphase flow models offer various options for representing specific flow conditions, but also have limitations in capturing all important flow properties. In the end two models have been tested to represent the main flow properties, namely the Eulerian Multiphase (EMP) model and the Volume of Fluid (VOF) model. Both models allowed the prediction of the most important hydrodynamic flow conditions in a twophase flow but are not able to represent a full representation of the counter-current threephase flow. Further, the VOF model was the only approach able to simulate the full reactor. It could represent the correct phase distribution of Artemisia annua L. leaves and solvent in the middle segments of the screw extractor. The solvent was retained by the screw rotation until dripping out at the extract outlet, similar to experiments. With the VOF model the solvent RTD was correctly predicted in a partly-filled simulation for several operation points. This enabled a reliable estimation of the liquid phase stage number N_I . The solid-phase RTD could not be represented due to the flow complexity of the solvent-soaked leaves and limited computational resources. Nevertheless, the mean residence time of the solid phase can be estimated using a constant transport efficiency for each screw design.

The partly-filled VOF CFD model could finally be used to develop a simplified compartment model, able to consider also extraction kinetics [Vu23]. The CFD-CPT model effectively represented the phase distribution inside the extractor including the gas phase as well as the backflow behaviour and the liquid phase residence time for each screw segment. Along the extractor length, the liquid phase volume fraction decreases from inlet to outlet, averaging 50% in the central region. This value reflects the conditions used in the experimental investigations. It resulted in a local, consistently high liquid phase mean residence time (MRT) in the middle sections, which reduced to just a few seconds near the extract outlet. Consequently, the solvent flow velocity near the extract outlet is higher compared to the inlet region. Further, the solvent phase backflow is approximately half of the forward flow reflecting near-CSTR behaviour, aligned with experimental RTD analysis. While reducing the screw angle by up to 10% (MS1) could keep this CSTR behaviour, lower screw angles are unsuitable for further use

7 Outlook

In this thesis important parameters and limitations for performing continuous solid-liquid counter-current extraction processes were investigated. Systematic experiments have been performed to determine the impact of parameter variations. CFD simulations based on the VOF model represent the specific flow fields of the involved phases during the transportation process. With this information model parameters for a compartment model could be improved allowing to calculate the product mass fraction in the extract. In all sections of this thesis further additional steps can be implemented to improve the quality of the process description.

Regarding the experimental investigations there are the following four tasks for further optimisation:

- 1. As a result of experimental investigations, the extraction can be performed continuously in its optimal steady-state condition with half of the length of the steel reactor applied to extract ARTE. Using a modified screw geometry with a 10% reduced screw angle compared to the original geometry (MS 1) and a perforated disk with a 5 mm hole diameter operating with OP 2 allows for further optimisation for achieving sharp RTD curves and approaching PFTR behaviour. This should improve the ARTE extraction efficiency and minimise solvent waste. Extraction experiments in the steel reactor are needed for validation. While further reducing the screw angle sharpens the RTD and enhances PFTR behaviour, it also introduces back-mixing effects for the solvent-soaked leaves. Therefore, the second modified screw geometry (MS2), with a 20% reduced screw angle compared to the original, is not recommended.
- 2. In cooperation with Vu, the operation window, particularly OP 2 conditions, could already be modified to a lower (Exp -1) and upper (Exp 1) operation point by adjusting the solvent mass flow rate (section 5.1). This approach is promising as it increases the ARTE mass fraction in the extract from 0.145 wt.% (OP 2) to 0.186 wt.% (Exp -1). Exp -1 was already successfully run in the glass extractor using the solvent water, with flow parameters adjusted after 20 min of stability. With this procedure the identified small

- operation window in this thesis could be extended in future work.
- A further increase of the currently available operation window can be achieved by modifying the shape of the perforated disk, especially the hole diameter and the number of holes, to optimise the induced pressure.
- 4. For long-term-performance of the continuous extraction, fouling needs to be avoided.

 It is recommended to clean the total extractor after a maximum run time of 2 days.

The next step in the continuous production of artemisinin is to scale up the process from laboratory to industrial scale. However, enlarging the tube diameter will cause broader residence time distributions and may reduce extraction efficiency [HÇL+14]. This will be due to the larger deviations from the ideal plug flow reactor behaviour [Lev99]. Here, the use of the modified screw with a 10% reduced screw angle (MS 1) can sharpen the solid phase RTD again, as found in this thesis.

The developed CFD models can predict flow characteristics by only changing the corresponding geometrical parameter in the simulation. However, the complexity of the three-phase flow remains high, requiring further development of multiphase models for more accurate counter-current flow representation. Simcenter StarCCM+continuously enhances its multiphase flow models with each new version. The increase in computational capacities will enable more detailed and comprehensive simulations. The following steps are recommended:

- With more computational capacities, especially the EMP model is highly promising as
 it provides appropriate boundary conditions for reaching a counter-current flow. In
 this way a combination of the gas-liquid flow considered in this thesis and a solid-liquid
 flow could be represented with acceptable computational times.
- 2. Until these computing capacities are achieved, the recurrence method has the potential to significantly reduce the computational time of multiphase flow simulations [LP16], [APL 20]. This method needs to be precisely implemented in the CFD code to achieve appropriate results and this is the subject of our current work.
- 3. An alternative approach could rely on Smoothed Particle Hydrodynamics (SPH) simulations, which do not require a classical mesh. Consequently, computational effort for multiphase flow simulations can be decreased and accurate modelling of complex flows becomes possible, in particular when involving a free surface [WCW+16].

The compartment model should be further developed in combination with the adapted CFD simulations to predict the mass fraction of extracted ARTE for different extractor geometries and operation points:

- 1. Additional variations in the liquid phase mass fraction ε can be included to potentially identify further optimal operation points.
- 2. Validation with additional extraction experiments using the modified screw MS 1 should be performed to identify model applicability to different screw geometries.
- As an extension, volume flow rates in forward and backward directions and phase fractions across the geometry, computed by CFD simulations, could be incorporated to the compartment model.

After performing these additional investigations a powerful tool should be available for optimisation and upscaling of continuous solid-liquid counter-current extraction of artemisinin. The general approach will be applicable to the extraction of other natural products, supporting the promising transition from batch to continuous processing.

8 References

- [AEB99] Agtmael, M. A. van; Eggelte, T. A.; Boxtel, C. J. van: Artemisinin drugs in the treatment of malaria: from medicinal herb to registered medication. Trends in Pharmacological Sciences 5/20, pp. 199–205, 1999.
- [AlH24] Al Hamadi, R.: Experimentelle Untersuchung der Festphasen-Verweilzeitverteilung in einem Schneckenextraktor für verschiedene Schneckendesigns. Bachelor thesis, Magdeburg, 2024.
- [Ans21] ANSYS Inc.: Ansys Polyflow 2021 R1: User's Guide. Canonsberg, PA.
- [AP23] Anton Paar GmbH: Anton Paar Wiki. https://wiki.anton-paar.com/en/tables/, accessed 4 Nov 2024.
- [APL 20] Abbasi, S.; Pirker, S.; Lichtenegger, T.: Application of recurrence CFD (rCFD) to species transport in turbulent vortex shedding. Computers & Fluids 196, 104348, 2020.
- [APS+09] Anandakumar, A. M.; Paulsamy, S.; Sathish kumar, P.; Senthilkumar, P.: Preliminary phytochemical studies for the quantification of secondary metabolites of medicinal importance in the plant, Acalypha fruticosa Forssk.

 Journal of Applied and Natural Science 1/1, pp. 41–43, 2009.
- [ASG13] Abel, N. H.; Schlusemann, L.; Grünewald, M.: Beschreibung von Blasensäulen mithilfe von Kompartment-Modellansätzen. Chemie Ingenieur Technik 7/85, pp. 1112–1117, 2013.
- [BAB04] Basara, B.; Alajbegovic, A.; Basara, D.: Simulation of single- and two-phase flows on sliding unstructured meshes using finite volume method. International Journal for Numerical Methods in Fluids 45, pp. 1137–1159, 2004.
- [BGJ+24] Brandt, V.; Grabowski, J.; Jurtz, N.; Kraume, M.; Kruggel-Emden, H.: DEM and DEM-CFD modeling of systems with geometric constrictions using a new particle location based multi-level coarse graining approach. Powder Technology 436, 119447, 2024.

- [BM04] Bezzo, F.; Macchietto, S.: A general methodology for hybrid multizonal/ CFD models Part II. Automatic zoning. Computers & Chemical Engineering 28, pp. 513–525, 2004.
- [BMP03] Bezzo, F.; Macchietto, S.; Pantelides, C. C.: General hybrid multizonal/CFD approach for bioreactor modeling. AIChE Journal 8/49, pp. 2133–2148, 2003.
- [BP11] Bart, H.-J.; Pilz, S.: Industrial Scale Natural Products Extraction. Wiley-VCH, Weinheim, 2011.
- [BRV+07] Belforte, G.; Raparelli, T.; Viktorov, V.; Trivella, A.: Permeability and inertial coefficients of porous media for air bearing feeding systems. Journal of Tribology 129 (4), pp. 705–711, 2007.
- [BS13] Böckh, P. von; Saumweber, C.: Fluidmechanik. Springer Berlin Heidelberg, Berlin, Heidelberg, 2013.
- [CBB+19] Chen, K.; Bachmann, P.; Bück, A.; Jacob, M.; Tsotsas, E.: CFD simulation of particle residence time distribution in industrial scale horizontal fluidized bed. Powder Technology 345, pp. 129–139, 2019.
- [CBD+23] Chatre, L.; Bataille, M.; Debacq, M.; Randriamanantena, T.; Nos, J.; Herbelet, F.: Modelling of powder hydrodynamics in a screw reactor. Powder Technology 420, 118367, 2023.
- [CG98] Choudhary, G. S.; Goutam, A.: Online measurement of residence time distribution in a food extruder. Journal of Food Science 63/3, pp. 529–534, 1998.
- [CLT15] Chanioti, S.; Liadakis, G.; Tzia, C. Eds.: Food Engineering Handbook: Food Process Engineering. Solid-Liquid Extraction. CRC Press, Taylor & Francis Group, 2015.
- [Con08] Conzen, C.: Numerische und experimentelle Untersuchungen zu Transportvorgängen in Schneckenmaschinen. PhD thesis, Kassel, 2008.
- [CRR+17] Castillo-Santos, K.; Ruiz-López, I. I.; Rodríguez-Jimenes, G. C.; Carrillo-Ahumada, J.; García-Alvarado, M. A.: Analysis of mass transfer equations during solid-liquid extraction and its application for vanilla extraction kinetics modeling. Journal of Food Engineering 10/192, pp. 36–44, 2017.

- [CSB+23] Caré, F.; Sangaré, D.; Bostyn, S.; Atwi-Ghaddar, S.; Lafite, P.; Buron, F.: Computational Fluid Dynamics (CFD) modeling of static maceration in view to optimize continuous flow extractions of robinetin and dihydrorobinetin from Robinia pseudoacacia wood. Food and Bioproducts Processing 141, pp. 185–198, 2023.
- [CSW+90] Charles, D. J.; Simon, J. E.; Wood, K. V.; Heinstein, P.: Germplasm Variation in Artemisinin Content of Artemisia Annua Using an Alternative Method of Artemisinin Analysis from Crude Plant Extracts. Journal of natural products 1/53, pp. 157–160, 1990.
- [DCC+14] Delafosse, A.; Collignon, M.-L.; Calvo, S.; Delvigne, F.; Crine, M.; Thonart, P.; Toye,
 D.: CFD-based compartment model for description of mixing in bioreactors.
 Chemical Engineering Science 106, pp. 76–85, 2014.
- [DCK+22] De, T.; Chakraborty, J.; Kumar, J.; Tripathi, A.; Sen, M.; Ketterhagen, W.: A particle location based multi-level coarse-graining technique for Discrete Element Method (DEM) simulation. Powder Technology 398, 117058, 2022.
- [DDC+10] Delafosse, A.; Delvigne, F.; Collignon, M.-L.; Crine, M.; Thonart, P.; Toye, D.: Development of a compartment model based on CFD simulations for description of mixing in bioreactors. Biotechnology, Agronomy, Society and Environment S2/14, pp. 517–522, 2010.
- [DGU23] Deutsche Gesetzliche Unfallversicherung (DGUV): GESTIS-Stoffdatenbank, Tabelle für Toluol. https://gestis.dguv.de/data?name=010070, accessed 23 Oct 2023.
- [DLM99] Dudukovic, M. P.; Larachi, F.; Mills, P. L.: Multiphase reactors revisited. Chemical Engineering Science 54, pp. 1975–1995, 1999.
- [DND21] Di Renzo, A.; Napolitano, E. S.; Di Maio, F. P.: Coarse-Grain DEM Modelling in Fluidized Bed Simulation: A Review. Processes 9, 279, 2021.
- [DP90] Demirdžić, I.; Perić, M.: Finite volume method for prediction of fluid flow in arbitrarily shaped domains with moving boundaries. International Journal for Numerical Methods in Fluids 10/7, pp. 771–790, 1990.

- [DPE+94] Duke, M. V.; Paul, R. N.; Elsohly, H. N.; Sturtz, G.; Duke, S. O.: Localization of Artemisinin and Artemisitene in Foliar Tissues of Glanded and Glandless Biotypes of Artemisia annua L. International Journal of Plant Sciences 155/3, pp. 365–372, 1994.
- [Dre83] Drew, D. Ed.: Continuum Modeling of Two-Phase Flows, in: Theory of Dispersed Multiphase Flow, Academic Press, 1983.
- [DSJ+09] Deshmukh; S.S.; Sathe, M.J.; Joshi, J. B.; Koganti, S. B.: Residence Time Distribution and FLow Patterns in the Single-Phase Annular Region of Annular Centrifugal Extractor. Industrial & Engineering Chemistry Research 48, pp. 37–46, 2009.
- [DSS24] DSSE Danish Sugar Sweetener Engineering A/S: Sugar Equipment, DSSE Diffusers, Available from: https://www.dsse.biz/, accessed 10 Jun 2024.
- [Erg 52] Ergun, S.: Fluid flow through packed columns. Chemical Engineering Progress 48, pp. 89–94, 1952.
- [FGB+22] Ferreira, M. C.; Gonçalves, D.; Bessa, L.; Rodrigues, C.; Meirelles, A.; Batista, E.: Soybean oil extraction with ethanol from multiple-batch assays to reproduce a continuous, countercurrent, and multistage equipment. Chemical Engineering and Processing Process Intensification 170, p. 108659, 2022.
- [FLD+05] Ferreira, J.; Laughlin, J. C.; Delabays, N.; Magalhães, P. M.: Cultivation and genetics of Artemisia annua L. for increased production of the antimalarial artemisinin. Plant Genetic Resources 2/3, pp. 206–229, 2005.
- [Fot23] Fotovati, M.: Isolating valuable ingredients of saffron using extraction and preparative chromatography. PhD thesis, Magdeburg, 2023.
- [FP20] Ferziger, J. H.; Perić, M.: Numerische Strömungsmechanik. Springer Vieweg, Berlin, Heidelberg, 2020.
- [GBM+09] Gresch, M.; Brügger, R.; Meyer, A.; Gujer, W.: Compartmental models for continuous flow reactors derived from CFD simulations. Environmental Science & Technology 7/43, pp. 2381–2387, 2009.
- [GIM12] Gao, Y.; Ierapetritou, M.; Muzzio, F.: Periodic section modeling of convective continuous powder mixing processes. AIChE Journal 1/58, pp. 69–78, 2012.

- [GJM+96] Gupta, M. M.; Jain, D. C.; Mathur, A. K.; Singh, A. K.; Verma, R. K.; Kumar, S.: Isolation of a High Artemisinic Acid Containing Plant of Artemisia annua. Planta Medica 62, pp. 280–281, 1996.
- [GK08] Grinberg, L.; Karniadakis, G. E.: Outflow boundary conditions for arterial networks with multiple outlets. Annals of biomedical engineering 9/36, pp. 1496–1514, 2008.
- [GMI12] Gao, Y.; Muzzio, F. J.; Ierapetritou, M. G.: A review of the Residence Time Distribution (RTD) applications in solid unit operations. Powder Technology 228, pp. 416–423, 2012.
- [GO01] Ghezzehei, A.; Or, D.: Rheological properties of wet soils and clays under steady and oscillatory stresses. Soil Science Society of America Journal 65, pp. 624–637, 2001.
- [GWB00] Gao, J.; Walsh, G. C.; Bigio, D.: Mean residence time analysis for twin screw extruders. Polymer Engineering and Science 1/40, pp. 227–237, 2000.
- [GY94] Gogoi, B. K.; Yam, K. L.: Relationships between residence time and process variables in a corotating twin-screw extruder. Journal of Food Engineering 21, pp. 177–196, 1994.
- [Hal18] Halford, B.: Looking for cheaper routes to malaria medicines. https://cen.acs.org/articles/96/i11/in-search-of-a-universal-flu-vaccine.html, accessed 24 Oct 2019.
- [HC97] Hahn, S.; Choi, H.: Unsteady Simulation of Jets in a Cross Flow. Journal of Computational Physics 134, pp. 342–356, 1997.
- [HÇL+14] Holbach, A.; Çalışkan, E.; Lee, H.-S.; Kockmann, N.: Process intensification in small scale extraction columns for counter-current operations. Chemical Engineering and Processing: Process Intensification 80, pp. 21–28, 2014.
- [HFS+06] Haynes, R. K.; Fugmann, B.; Stetter, J.; Rieckmann, K.; Heilmann, H. D.; Chan, H. W.; Cheung, M. K.; Lam, W. L.; Wong; H.N.; Croft: Artemisone A highly active antimalarial drug of the artemisinin class. Angewandte Chemie International Edition 13/45, pp. 2082–2088, 2006.

- [HKR+07] Hale, V.; Keasling, J. D.; Renninger, N.; Diagana, T. T.: Microbially derived artemisinin: A biotechnology solution to the global problem of access to affordable antimalarial drugs. American Society of Tropical Medicine and Hygiene 6/77, pp. 198–202, 2007.
- [HN81] Hirt, C. W.; Nichols, B. D.: Volume of Fluid (VOF) Method for the Dynamics of Free Boundaries. Journal of Computational Physics 39, pp. 201–225, 1981.
- [Hor19] Horosanskaia, E.: Strategien zur kristallisationsbasierten Aufreinigung von pharmazeutisch relevanten Naturstoffen und organischen Mehrkomponentengemischen. PhD thesis, Magdeburg, 2019.
- [IBW+23] Illana Mahiques, E.; Brömmer, M.; Wirtz, S.; van Wachem, B.; Scherer, V.: Simulation of Reacting, Moving Granular Assemblies of Thermally Thick Particles by Discrete Element Method/Computational Fluid Dynamics. Chemical Engineering & Technology 7/46, pp. 1317–1332, 2023.
- [IM84] Ishii, M.; Mishima, K.: Two-fluid model and hydrodynamic constitutive relations.

 Nuclear Engineering Design 82, pp. 107–126, 1984.
- [KFG+22] Kinghorn, A. D.; Falk, H.; Gibbons, S.; Asakawa, Y.; Liu, J.-K.; Dirsch, V. M.: Antimalarial Natural Products. Springer International Publishing, Cham, 2022.
- [KJS+10] Kassing, M.; Jenelten, U.; Schenk, J.; Strube, J.: A New Approach for Process Development of Plant-Based Extraction Processes. Chemical Engineering Technology 3/33, pp. 377–387, 2010.
- [Kun12] Kunik, C.: CFD-Simulationen turbulenter konvektiver Strömungen bei überkritischen Drücken. Dissertation, Karlsruhe, 2012.
- [Lac85] Lack, E. A.: Kriterien zur Auslegung von Anlagen für die Hochdruckextraktion von Naturstoffen. PhD thesis, Graz, 1985.
- [LPC06] Lapkin, A. A.; Plucinski, P. K.; Cutler, M.: Comparative assessment of technologies for extraction of artemisinin. Journal of Natural Products 11/69, pp. 1653–1664, 2006.
- [Lec11] Lecheler, S.: Numerische Strömungsberechnung. Schneller Einstieg durch anschauliche Beispiele. Vieweg + Teubner, Wiesbaden, 2011.

- [Lev12] Levenspiel, O.: Tracer Technology. Modeling the flow of fluids. Springer New York, New York, NY, 2012.
- [Lev99] Levenspiel, O.: Chemical Reaction Engineering. Third Edition. John Wiley & Sons, New York, NY, 1999.
- [LJM+20] Lehr, A.; Janiga, G.; Seidel-Morgenstern, A.; Thévenin, D.: CFD Simulation of a Solid-Liquid Counter-Current Screw Extractor. Computer Aided Process Engineering 48, pp. 223–228, 2020.
- [LJM+22a] Lehr, A.; Janiga, G.; Seidel-Morgenstern, A.; Thévenin, D.: Numerical study on the solid phase residence time distribution in a counter current screw extractor.

 Computer Aided Chemical Engineering 51, pp. 13–18, 2022.
- [LJM+22b] Lehr, A.; Janiga, G.; Seidel-Morgenstern, A.; Thévenin, D.: Numerical study on the solid-liquid residence time distribution in a counter-current screw extractor. Proc. Conference on Modelling Fluid Flow (CMFF'22), 30.08.-02.09.2022, Budapest, Hungary, pp. 278-286, 2022.
- [LIP09] Liu, Y.; lü, H.; Pang, F.: Solubility of Artemisinin in Seven Different Pure Solvents from (283.15 to 323.15) K. Journal of Chemical & Engineering Data 3/54, pp. 762–764, 2009.
- [LO18] Laurien, E.; Oertel, H.: Numerische Strömungsmechanik. Grundgleichungen und Modelle Lösungsmethoden Qualität und Genauigkeit. Springer Vieweg Wiesbaden, Wiesbaden, 2018.
- [LP16] Lichtenegger, T.; Pirker, S.: Recurrence CFD A novel approach to simulate multiphase flows with strongly separated time scales. Chemical Engineering Science 153, pp. 394–410, 2016.
- [LVJ+23] Lehr, A.; Vu, G. T.; Janiga, G.; Seidel-Morgenstern, A.; Thévenin, D.: Experimental investigation of the residence time distribution in a screw-type apparatus designated to extract artemisinin. Chemical Engineering and Processing Process Intensification 187, 109337, 2023.
- [LW12] Lübke, M.; Wünsch, O.: Two-phase flow in single-screw extruders. Proceedings in Applied Mathematics and Mechanics 1/12, pp. 509–510, 2012.

- [Mar00] Martin, A. D.: Interpretation of residence time distribution data. Chemical Engineering Science 23/55, pp. 5907–5917, 2000.
- [Mat24] The MathWorks, Inc.: Matlab Toolbox numerical solver "linsolve".

 MATLAB2024b, accessed 3 Feb 2025.
- [MBI+ 24] Mieg, L.; Bergold, T.; Illana Mahiques, E.; Scherer, V.; Mönnigmann, M.: A reduced model for particle calcination for use in DEM/CFD simulations. Particuology 93, pp. 316–327, 2024.
- [Mez14] Mezger, T. G.: Angewandte Rheologie. Anton Paar GmbH, Österreich, 2014.
- [MGL92] Meuser, F.; Gimmler, N.; van Lengerich, B.: A system analytical approach to extrusion. Food Extrusion Science and Technology, New York: Marcel Dekker, pp. 619–630, 1992.
- [MKK+20] Mansour, M.; Khot, P.; Kováts, P.; Thévenin, D.; Zähringer, K.; Janiga, G.: Impact of computational domain discretization and gradient limiters on CFD results concerning liquid mixing in a helical pipe. Chemical Engineering Journal 383, p. 123121, 2020.
- [MM97] Mas, R.; Magnin, A.: Experimental validation of steady shear and dynamic viscosity relation for yield stress fluids. Rheologica Acta 36, pp. 49–55, 1997.
- [Mon17] Montgomery, D. C.: Design and analysis of experiments. John Wiley & Sons, Arizona, 2017.
- [MSW22] Michaelides, E.E.; Sommerfeld, M.; van Wachem, B. Eds.: Multiphase Flows with Droplets and Particles. CRC Press, Boca Raton, 2022.
- [MW12] Munz, C.-D.; Westermann, T.: Numerische Behandlung gewöhnlicher und partieller Differenzialgleichungen. Springer Berlin Heidelberg, Berlin, Heidelberg, 2012.
- [MW35] MacMullin, R.; Weber, M.: The theory of short-circuiting in continuous-flow mixing vessels in series and kinetics of chemical reactions in such systems. Transactions of American Institute of Chemical Engineers 2/31, pp. 409–458, 1935.
- [Noo10] Noorden, R. van: Demand for malaria drug soars. Nature 466, pp. 672–673, 2010.

- [NSV+23] Neubauer, M.; Steiner, M.; Vogi, M.; Rudelstorfer, G.; Wallek, T.; Lux, S.: Continuous separation and purification of glycerol distillation residues in the sense of circular economy: Experimental proof-of-concept and techno-economic assessment. Chemical Engineering and Processing Process Intensification 191, p. 109465, 2023.
- [NvR+15] Nachenius, R. W.; van de Wardt, T. A.; Ronsse, F.; Prins, W.: Residence time distributions of coarse biomass particles in a screw conveyor reactor. Fuel Processing Technology 130, pp. 87–95, 2015.
- [ONO+24] Ocan, M.; Nambatya, W.; Otike, C.; Nakalembe, L.; Nsobya, S.: Copayment mechanism in selected districts of Uganda: Availability, market share and price of quality assured artemisinin-based combination therapies in private drug outlets. PloS one 3/19, e0295198, 2024.
- [Pas04] Paschedag, A. R.: CFD in der Verfahrenstechnik. Allgemeine Grundlagen und mehrphasige Anwendungen. Wiley-VCH Verlag GmbH & Co. KGaA, Weinheim, 2004.
- [PP13] Picardo, J. R.; Pushpavanam, S.: On the conditional superiority of counter-current over co-current extraction in microchannels. Microfluidics and Nanofluidics 5/15, pp. 701–713, 2013.
- [Rap17] Rapp, B. E.: Microfluidics: Modelling, Mechanics and Mathematics. Elsevier, 2017.
- [Ric11] Richardson, L. F.: The approximate arithmetical solution by finite differences of physical problems involving differential equations, with an application to the stresses in a masonry dam. Philisophical Transactions of the Royal Society of London 210, pp. 307–357, 1911.
- [Riz13] Rizvi, S.: Separation, Extraction and Concentration Processes in the Food, Beverage and Nutraceutical Industries. Woodhead Publishing, 2013.
- [RJ03] Rigopoulos, S.; Jones, A.: A hybrid CFD—reaction engineering framework for multiphase reactor modelling: basic concept and application to bubble column reactors. Chemical Engineering Science 14/58, pp. 3077–3089, 2003.

- [RL08] Rahimpour, M. R.; Lotfinejad, M.: A comparison of co-current and counter-current modes of operation for a dual-type industrial methanol reactor. Chemical Engineering and Processing: Process Intensification 9-10/47, pp. 1819–1830, 2008.
- [RM94] Roberts, A. W.; Manjunath, K. S.: Volumetric and torque characteristics of screw feeders. Proceedings of the Powder and Bulk Solids Conference, Rosemont, USA, pp. 189–208, 1994.
- [RMM93] Roberts, A. W.; Manjunath, K. S.; McBride, W.: The Mechanics of Screw Feeder Performance for Bulk Solids Flow Control. Transactions of Mechanical Engineering, Institution of Engineers, Australia ME18 #1, 1993.
- [Rod21] Rodrigues, A. E.: Residence time distribution (RTD) revisited. Chemical Engineering Science 230, p. 116188, 2021.
- [RP13] Rostagno, M.A.; Prado, J.M. Eds.: Natural Product Extraction. Royal Society of Chemistry, Cambridge, 2013.
- [RPO+06] Ro, D.-K.; Paradise, E. M.; Ouellet, M.; Fisher, K. J.; Newman, K. L.; Ndungu, J. M.; Ho, K. A.; Eachus, R. A.; Ham, T. S.; Kirby, J.; Chang, M. C. Y.; Withers, S. T.; Shiba, Y.; Sarpong, R.; Keasling, J. D.: Production of the antimalarial drug precursor artemisinic acid in engineered yeast. Nature 7086/440, pp. 940–943, 2006.
- [SB23] Subramaniam, S.; Balachandar, S. Eds.: Computation and Analysis of Turbulent Flows: Modeling Approaches and Computational Methods for Particle-Laden Turbulent Flows. Academic Press, 2023.
- [SFH+23] Schwarz, S.; Frey, T.; Hoffmann, M.; Grünewald, M.; Schlüter, M.: CFD-Based Compartment Modeling of Continuous Polymer Reactors in Milli-Structured Apparatuses by Use of the Mean Age Theory. Industrial & Engineering Chemistry Research 31/62, pp. 12109–12119, 2023.
- [Sie23] Siemens PLM Software, Inc.: Simcenter StarCCM+ 2302 Documentation 18.02. Plano, TX, USA. 2023.
- [SMW10] Salmi, T.O.; Mikkola, J.-P.; Warna, J.P. Eds.: Chemical Reaction Engineering and Reactor Technology. CRC Press, 2010.

- [SP02] Steffani, K.; Platzer, B.: Influence of velocity profile and diffusion on residence time distributions: mesoscopic modeling and application to Poiseuille flow. Chemical Engineering and Processing: Process Intensification 2/41, pp. 143–155, 2002.
- [SS18] Sievers, D. A.; Stikel, J. J.: Modeling residence-time distribution in horizontal screw hydrolysis reactors. Chemical Engineering Science 175, pp. 396–404, 2018.
- [SSS20] Schmidt-Traub, H.; Schulte, M.; Seidel-Morgenstern, A. Eds.: Preparative chromatography. Wiley-VCH, Weinheim Germany, 2020.
- [SWO08] Sommerfeld, M.; van Wachem, B.; Oliemans, R.: Best practice guidelines for computational fluid dynamics of dispersed multiphase flows. European Research Community On Flow, Turbulence And Combustion (ERCOFTAC), 2008.
- [TBN20] Tobo, Y. M.; Bartacek, J.; Nopens, I.: Linking CFD and Kinetic Models in Anaerobic Digestion Using a Compartmental Model Approach. Processes 6/8, p. 703, 2020.
- [Tes13] Teschner, R.: Glasfasern. Springer Berlin Heidelberg, Berlin, Heidelberg, 2013.
- [TGG+14] Turconi, J.; Griolet, F.; Guevel, R.; Oddon, G.; Villa, R.; Geatti, A.; Hvala, M.; Rossen, K.; Göller, R.; Burgard, A.: Semisynthetic Artemisinin, the Chemical Path to Industrial Production. Organic Process Research & Development 3/18, pp. 417–422, 2014.
- [TGV+18] Triemer, S.; Gilmore, K.; Vu, G. T.; Seeberger, P. H.; Seidel-Morgenstern,
 A.: Literally green chemical synthesis of artemisinin from plant extracts.

 Angewandte Chemie International Edition 19/57, pp. 5525–5528, 2018.
- [TL14] Tang, G. H.; Lu, Y. B.: A Resistance Model for Newtonian and Power-Law Non-Newtonian Fluid Transport in Porous Media. Transport in Porous Media 2/104, pp. 435–449, 2014.
- [Tre80] Treybal, R. E.: Mass-transfer operations. Mc Graw Hill International Book Company, 1980.
- [TSB+19] Tajsoleiman, T.; Spann, R.; Bach, C.; Gernaey, K. V.; Huusom, J. K.; Krühne, U.: A CFD based automatic method for compartment model development. Computers & Chemical Engineering 123, pp. 236–245, 2019.

- [Vu23] Vu, T. G.: Experimental investigations and modeling of extracting natural products from plants: from batch to continuous processes. PhD thesis, Magdeburg, 2023.
- [WCM+19] Weber, B.; Campenhausen, M. von; Maßmann, T.; Bednarz, A.; Jupke, A.: CFD based compartment-model for a multiphase loop-reactor. Chemical Engineering Science: X 2, 100010, 2019.
- [WCW+16] Wang, Z. B.; Chen, R.; Wang, H.; Liao, Q.; Zhu, X.; Li, S. Z.: An overview of smoothed particle hydrodynamics for simulating multiphase flow. Applied Mathematical Modelling 23-24/40, pp. 9625–9655, 2016.
- [Wen08] Wendt, J. F.: Computational fluid dynamics. An introduction. Springer, Berlin, London, 2008.
- [WHO24] World Health Organization: World Malaria Report 2024. World Health Organization, Geneva, 2024.
- [Wil03] Willner, K.: Kontinuums- und Kontaktmechanik: Synthetische und analytische Darstellung. Springer, Berlin, 2003.
- [WJ20] Weber, B.; Jupke, A.: Compartment-model for the simulation of the separation performance of stirred liquid–liquid-extraction columns. AIChE Journal 8/66, pp. 1–11, 2020.
- [WPT+07] Waje, S. S.; Patel, A. K.; Thorat, B. N.; Mujumdar, A. S.: Study of Residence Time Distribution in a Pilot Scale Screw Conveyor Dryer. Drying Technology 1/25, pp. 249–259, 2007.
- [WR01] Wu, Z.Y.; Raven, P.H. Eds.: Flora of China, Volume 8: Brassicaceae through Saxifragaceae. Science Press, Beijing and Missouri Botanical Garden Press, St. Louis, 2001.
- [WSC+07] Wang, L.-H.; Song, Y.-T.; Chen, Y.; Cheng, Y.-Y.: Solubility of Artemisinin in Ethanol + Water from (278.2 to 343.2) K. Journal of Chemical & Engineering Data 3/52, pp. 757–758, 2007.
- [WSG+20] Weber, B.; Schneider, M.; Görtz, J.; Jupke, A.: Compartment Model for Liquid-Liquid Extraction Columns. Solvent Extraction and Ion Exchange 1/38, pp. 66–87, 2020.

- [You09] Youyou, T.: Artemisia Annua and Artemisinin Drugs. Chemical Industry Press, pp. 187–194, 2009.
- [ZWJ+15] Zhang, Y.; Wang, Z.; Jin, Y.; Li, Z.; Yi, W.: CFD simulation and experiment of residence time distribution in short-contact cyclone reactors. Advanced Powder Technology 4/26, pp. 1134–1142, 2015.

List of Figures

Figure 1-1: Countries with endemic status in 2000 and their status by 2023	2
Figure 1-2: (a) Artemisia Annua L. plant, (b) chemical structure of Artemisinin	2
Figure 1-3: Extraction setup of the continuous counter-current apparatus	4
Figure 2-1: Phytoextraction of solute from solid leaves to liquid solvent	7
Figure 2-2: Ideal continuous tank reactor models,	7
Figure 2-3: Process scheme of co-current extraction with two stages ($N = 2$)	11
Figure 2-4: Process scheme of a counter-current extraction process with N stages	12
Figure 2-5: Linear equation system with 2 N equations in the form of $0 = By + B0$	13
Figure 2-6: Methods of tracer input	16
Figure 2-7: Typical RTD curves for CSTR, PFTR and non-ideal reactor	19
Figure 2-8: Classification of screw extractors, reproduced from [Con08]	20
Figure 2-9: Theoretical axial velocity at one screw element	21
Figure 3-1: Dimensions of the screw extractor (in mm).	23
Figure 3-2: Original (OS) and modified screws (MS 1, MS 2)	24
Figure 3-3: (a) Glass extraction device (left) and perforated disk (PD) in a front view (right)	. 24
Figure 3-4: Experimental setup for the glass extractor	26
Figure 3-5: (a) A. annua leaves (raw material), (b) particle size distribution	27
Figure 3-6: (a) grinded A. annua leaves, (b) particle size distribution	28
Figure 3-7: Absorption study of dry A. Annua leaves with the solvent water	30
Figure 3-8: Bulk humidity in screw segments	32
Figure 3-9: Rheological measurements for the solvent-soaked leaves	35
Figure 3-10: Mass fraction of ARTE in the extract during batch extraction with toluene	37
Figure 3-11: Mass fluxes in a continuous steady-state process	39
Figure 3-12: Critical regions in the extractor	40
Figure 3-13: Operation window for the counter-current process	43
Figure 3-14: Steady-state operation of the counter-current solid-liquid extraction process	. 45
Figure 3-15: Mass flow rates in three identical repetitions of steady-state	46
Figure 3-16: Pressure measurement device,	
	48
Figure 3-17: Pressure distribution in the screw extractor at steady-state for OP 2	

Figure 3-19: Upper pressure limit measurement,	52
Figure 3-20: Mass flow rates of steady-state operation with the modified disk PD 5	53
Figure 3-21: Mass flow rates of OP 2 with PD 4.5	53
Figure 3-22: Experimentally determined RTD curve of the liquid phase (water)	56
Figure 3-23: Experimental RTD curve for the solvent-soaked leaves	59
Figure 3-24: (a) Mean residence time and (b) variance for the solvent-soaked leaves	60
Figure 3-25: Stage number and Bodenstein number for solvent-soaked leaves	61
Figure 3-26: Evolution of the axial velocity for leaves along the extractor at OP 2	64
Figure 3-27: Mass of extract and raffinate over time for OS, MS 1 and MS 2 at OP 2	68
Figure 3-28: RTD curves for (a) MS 1 and (b) MS 2 for sampling points LSP 1 - SP 4	70
Figure 3-29: Averaged solid phase RTD curves with screw designs OS, MS 1 and MS 2	70
Figure 3-30: RTD curves of the solvent (water) at $T=20^{\circ}\text{C}$ (blue) and at $T=38^{\circ}\text{C}$ (black)) 75
Figure 3-31: Averaged solid phase RTD curves	76
Figure 4-1: Unstructured mesh blocks before connection through interface	87
Figure 4-2: Scheme of the skewness angle $ heta$ between two adjacent cells	90
Figure 4-3: Types of numerical 3D meshes.	90
Figure 4-4: Screw extractor in xz-plane	92
Figure 4-5: Example of several flow regimes in one domain, reprinted from [Sie23]	94
Figure 4-6: Multiphase flow models in Simcenter StarCCM+	95
Figure 4-7: Interface capturing with the Volume of Fluid model illustrated on a 2D grid.	97
Figure 4-8: Representation of the three applied mesh topologies	107
Figure 4-9: (a) Position of water front and (b) averaged liquid velocity	109
Figure 4-10: Mesh geometry, initial and boundary conditions for EMP model	111
Figure 4-11: Solid phase packing fraction $lpha s$ in the EMP model	113
Figure 4-12: Skewness angle for the counter-current EMP model	114
Figure 4-13: Initial and boundary conditions for a fully-filled VOF model	115
Figure 4-14: Quasi-steady-state of the fully-filled VOF model	118
Figure 4-15: Mass flow rates in the fully-filled VOF model	119
Figure 4-16: Absolute pressure field of the quasi-steady-state process	119
Figure 4-17: Reduced flow field on the xz-plane for the partly-filled simulation	121
Figure 4-18: Initial and boundary conditions for the partly-filled VOF model	123
Figure 4-19: Quasi-steady-state of the partly filled VOF model.	125
Figure 4-20: Visual comparison of phase distribution	126

Figure 4-21: Results from the solvent RTD study at operation point 2 (n = 2.2 rpm)	127
Figure 4-22: Mass flow error e {Eq. (3-18)} of the solvent (water) for OP 1	128
Figure 4-23: RTD curves for the partly-filled VOF model	129
Figure 4-24: Comparison of the calculation times for two screw rotations	132
Figure 5-1: Internal ARTE mass flow rates along a CSTR cascade	139
Figure 5-2: Reduced CPT model of Vu validated with experimental data [Vu23]	140
Figure 5-3: Axial velocity field of the solvent (toluene)	142
Figure 5-4: Geometrical compartmentalisation of the flow field for OS at steady state	143
Figure 5-5: Phase volume and liquid phase volume fraction,	145
Figure 5-6: Mean liquid phase residence time $ au l$ and flow time (Δau) per compartment	146
Figure 5-7: Volume flow rates of the liquid phase (toluene) in OS with	148
Figure 5-8: Liquid volume flow rate Vl in \emph{x} -direction (backward flow)	149
Figure A-1: Perforated disk structure and dimensions (in mm)	174

List of Tables

Table 3-1: Characterising parameters for the three screw geometries	24
Table 3-2: Diameter and axial location of the upper and lower sampling points	25
Table 3-3: Material properties of water and toluene at a temperature of 20°C [AP23]	29
Table 3-4: Measuring data of soaked-leaves density in a batch process	33
Table 3-5: Summary of material properties at $T = 20^{\circ}\text{C}$.	35
Table 3-6: Normalised extraction efficiency of artemisinin in %	37
Table 3-7: Range of experiments for finding steady-state operation.	42
Table 3-8: Identified exploitable limits for successful steady-state operation	44
Table 3-9: Selected operating parameters for RTD measurements	45
Table 3-10: Input and output mass flow rates for steady-state operation	47
Table 3-11: Bulk humidity of the steady-state operation points	47
Table 3-12: Pressure distribution in the screw extractor for operation point OP 2	49
Table 3-13: Pressure at the perforated disk for three steady-state operation points	50
Table 3-14: Upper pressure limit operating conditions	51
Table 3-15: Comparison of mass flow rates for original (PD 5.5) and modified disk (PD 5).	52
Table 3-16: Conductivity measurement of OP 2.	55
Table 3-17: Effect of the screw rotation speed on the liquid-phase Bodenstein number	57
Table 3-18: Stage number Ns and Bodenstein number Bos for solvent-soaked leaves	62
Table 3-19: Transport efficiency by the screw for three different operation points	64
Table 3-20: Calculated mean solid-phase residence times	66
Table 3-21: Retention volume and phase ratio of solid and liquid phases	67
Table 3-22: Mass flow rates of extract and raffinate for OS, MS 1 and MS 2	69
Table 3-23: Filling degree of dry leaves in one screw segment for OS, MS 1 and MS 2	69
Table 3-24: Mean residence time and standard deviation for OS, MS 1 and MS 2	71
Table 3-25: Stage number and Bodenstein number for OS, MS 1 and MS 2	72
Table 3-26: Screw-driven transport efficiency for OS, MS 1 and MS 2 for OP 2	72
Table 3-27: Retention volume of solid leaves with OS, MS 1 and MS 2	73
Table 3-28: Adaption of kinematic viscosity of water to the efficient solvent toluene	74
Table 3-29: Residence time distribution of the solvent water at $T = 20^{\circ}\text{C}$ or 38°C	75
Table 3-30: RTD of the A. annua leaves with water as solvent at $T = 20^{\circ}\text{C}$ or 38°C	76

Table 3-31: Steady-state operation conditions with $n = 2.2$ rpm using water or toluene	78
Table 3-32: Steady-state operation conditions with n = 2.5 rpm using water or toluene	78
Table 3-33: Summary of important parameters after experimental investigations	80
Table 4-1: Number of finite-volume cells (in million)10	06
Table 4-2: Physical models for the mesh-independence study at room temperature 10	80
Table 4-3: Reference values for all multiphase flow simulations	10
Table 4-4: Physical models for the EMP model at room temperature ($T=20^{\circ}\text{C}$)12	12
Table 4-5: Physical models for the fully-filled VOF simulation at room temperature12	17
Table 4-6: Numerical volume fit of A. annua phase12	22
Table 4-7: Physical models for the partly-filled VOF simulations12	24
Table 4-8: Results of numerical RTD study of the liquid solvent for OP 2 (ref)12	28
Table 4-9: Results of numerical RTD study of the liquid solvent for OP 1 and OP 313	30
Table 5-1: Comparing experiment with model assumptions of CPT and CFD model13	36
Table 5-2: Extended operation window and ARTE mass flow in the extract13	37
Table 5-3: Modelling parameter for the counter-current CPT model	38

A. Appendix

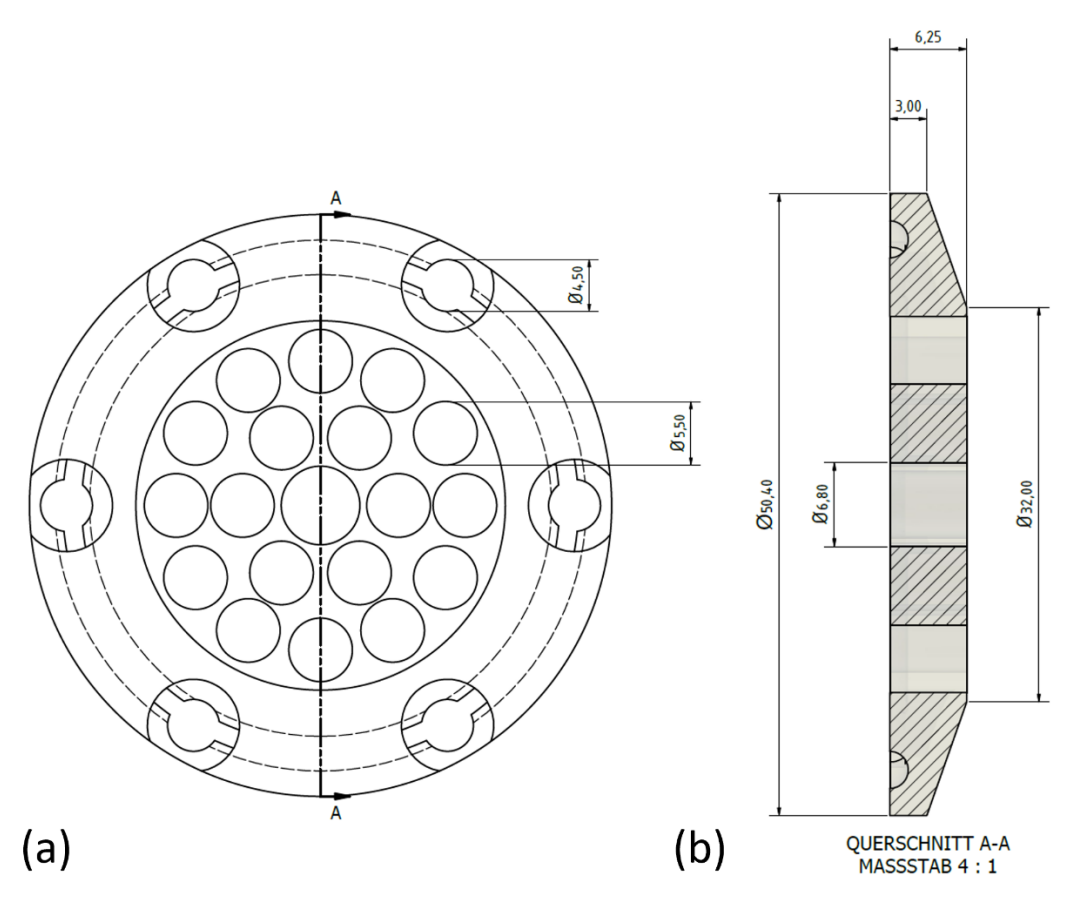


Figure A-1: Perforated disk structure and dimensions (in mm).